The role of excited state electron-impact ionization and configuration mixing in the population modeling of neutral Ne and W in fusion-capable plasmas using large-scale *R*-matrix collisional data

by

Connor James Favreau

A dissertation submitted to the Graduate Faculty of
Auburn University
in partial fulfillment of the
requirements for the Degree of
Doctor of Philosophy

Auburn, Alabama
December 14, 2019

Keywords: Tungsten, Electron-Impact Ionization, Generalized Collisional-Radiative Theory

Approved by

Stuart Loch, Professor of Physics
Mitch Pindzola, Professor of Physics
Michael Fogle, Associate Professor of Physics
David Ennis, Associate Professor of Physics
Hans-Werner van Wyk, Assistant Professor of Mathematics

Abstract

This work reports on large-scale non-perturbative *R*-matrix quantum mechanical calculations for neutral neon and tungsten. In addition, generalized collisional-radiative modeling of neutral neon and tungsten is conducted for fusion relevant plasma temperatures and densities. The generalized collisional-radiative coefficients produced are important for impurity transport modeling and in the case of tungsten for measuring erosion rates of tungsten plasma facing components.

Neon is being used in the W7-X stellarator for divertor cooling and spectral diagnostics. The electron-impact *R*-matrix calculations of the present work include cross sections for the excited states of neutral neon ($2p^5nl$ through nl = $6p$) and the $5d^46s^2$ (^5D) ground, $5d^56s$ (^7S) metastable, and a number of excited states arising from the $5d^6$, $5d^56s$, $5d^56d$, $5d^46s6p$, $5d^56s6d$, and $5d^36s^26p$ configurations of neutral tungsten. Ionization from the excited states of neutral neon was found to obey an n-scaling law allowing the data to be extrapolated to higher excited states. In addition, the generalized collisional-radiative modeling showed that ionization from the excited states is an important contribution to the effective ionization of neutral neon for fusion plasma divertor and edge densities, contributing up to a factor of 3 more than the direct ground state ionization. The atomic data for neutral neon has been archived and made available to the fusion and astrophysical communities.

Tungsten is important because it has been selected as a plasma-facing component (PFC) for the divertor region of ITER and is being used in a number of current tokamaks. Therefore, an accurate real-time diagnostic is needed of tungsten's erosion rate. The S/XB coefficient specifies the "ionizations per photon" of the atomic species and depends upon an effective ionization rate coefficient, related to the electron-impact ionization out of both the ground and excited states. The work on tungsten reported here is focused on improving the electron-impact ionization data for the ground, metastable, and excited states of neutral tungsten.

The electron-impact ionization calculations for neutral tungsten found a number of important effects. Configuration-mixing present in the target tungsten atom's levels leads to contributions from configurations of lesser mixing percentages, such as from the $5d^5nl$ series for the ground state ionization cross section. These contributions can arise from configuration-mixing in either the initial or final target states or both. Additionally, relative differences in the ground and metastable $5d$ and $6s$ ionization cross sections exist when compared to perturbative and semi-classical calculations. These differences can be attributed to channel coupling of the incident electron-atom system due to a shared W^+ $5d^46s$ core between the $5d^46snl$ and $5d^5nl$ series, which was not reflected in previous calculations. The mixing did not allow the *R*-matrix calculation to be split up into smaller calculations for each set of direct ionizations, but instead had to be evaluated as one large calculation. One of the findings for neutral tungsten that should also help guide future high-Z ionization calculations was that the $N + 1$ partial waves for a given total spin value produced similar sized cross sections when summed over all of the L-values of the partial waves. This allowed the states on the target with the highest spin values to be evaluated relatively quickly and for the case of neutral tungsten, it allowed the ground ^5D term to be evaluated.

Tungsten ground and excited state ionization cross sections were fitted with a scaled form of the semi-classical Exchange Classical Impact Parameter (ECIP) method. The scale factors from the ECIP fits demonstrate a scaling with ionization potential that allowed ionization rate coefficients to be generated for two strong separate linear correlations with respect to the term-specific ionization potentials. These linear correlations are distinguished by the parity of the initial target state.

Excited-state ionization for neutral tungsten contributes more than a factor of 12 than the ground state to the effective ionization for low electron temperatures (0 - 30 eV) and 10^{14} cm^{-3} electron density. Subsequent tests on the effect of the $6p$ orbital scaling parameter of the tungsten structure on the ECIP scale factors, as well as a ground-resolved S/XB coefficient that is several orders of magnitude higher than previous measurements, suggests ionization cross sections from odd-parity configurations are particularly sensitive to the $6p$ orbital scaling parameter. A continued exploration of the sensitivity of the excited state cross sections to

the underlying atomic structure is part of the future work of this project. In addition, other processes may affect the S/XB value in tokamak plasmas, including non-steady state metastable values (particularly if the sputtered tungsten atoms come off the wall with populations greater than the steady state value), sheath effects, and non-Maxwellian electron distributions.

Acknowledgments

The work presented was funded through the U.S. Department of Energy, grant DE-SC0015877, in relation to DIII-D tokamak experiment located in San Diego, CA. Many invaluable computational resources were utilized, including the local Auburn University Hopper Cluster, the High-Performance Computing Center at Stuttgart's "Hazel Hen, and the Titan and Rhea supercomputers at Oak Ridge National Laboratory. A special thanks is also owed to the IT departments of both Auburn University and Oak Ridge for their help and agreeableness in assisting our computational needs.

I would like to thank the people who made this dissertation possible. From the Auburn and University of South Alabama physics departments, I was given a well-rounded and highly personal learning environment that both challenged me and pushed me towards success. To Connor Ballance, one of my committee members, of Queen's University at Belfast, thanks for making yourself available so regularly and patiently walking me through the *R*-matrix codes and various insights into atomic physics. Also to the Queen's University at Belfast at large, including Cathy Ramsbottom, for their incredible hospitality. Thanks to my advisor David Ennis for his help guiding me through the inner workings of presentations, writing, and existence in the realm of physics. Also, to my other committee members, Michael Fogle, Hans-Werner van Wyk, and Mitch Pindzola for their help dissecting the work here and their overall support throughout my time in graduate school. I would like to make a special shout out to my main advisor Stuart Loch for his overwhelming support. I learned a lot from his humility, optimism, and patience, and I hope I can reflect that in my own life.

Finally, thanks to all of my incredible family and friends, who stood by me through both the best and worst moments. To my mom Barbara Favreau, my number one fan, for her overwhelming love and support over the years and for teaching me that value can sometimes only come from sacrifice. To my dad Peter Favreau, for teaching me that some things really are worth speaking up about: the happy, the sublime, the nostalgic, the serious, and the unjust.

Even though he is no longer here to speak for himself, the things that he did have the courage to voice are the ones that I carry with me to this day. To my brothers Peter, Thomas, and Jeremy, for always having my back. To my niece and nephew, Gemma and Max: it's been a real treat getting to watch you grow up so far. To all the cool cats: Boris, Arya, and Igor. Coolest. Cats. Ever. I am very lucky to have been surrounded by so many amazing people.

Table of Contents

List of Figures

List of Tables

Chapter 1

The Need for Atomic Population and Spectral Modeling of High-Z Elements in Plasmas: Tungsten and Neon

Recent developments in fusion- and astrophysical-relevant plasmas have created a need for more accurate modeling of high-Z atomic collision and population modeling in plasmas. For example, the simultaneous observation of a neutron star merger from both gravitational and electromagnetic spectra was achieved in 2017 [1]. Such cosmological events are believed to produce high-Z elements such as Au, Ag, and Pb [2]. In fusion research, with the successful completion of the W7-X stellerator [3] and the construction of ITER tokamak underway [4], concurrent advancements in atomic population and spectral modeling are needed to properly assess both their spectral and plasma impurity transport data. Of particular relevance for these devices are neon and tungsten, both of which have shown useful for plasma facing and as potential diagnostics.

1.1 Tungsten and the S/XB Ratio for Erosion Diagnostics

Tungsten, an open $d-$shell element with 74 protons, has many properties that make it highly suitable as a plasma facing component (PFC) for fusion experiments, including a high melting point, high thermal conductivity, and low sputtering and tritium retention rates [5, 6]. Figure 1.1 illustrates a cross-section of the DIII-D tokamak that includes tungsten inserts in the lower divertor, as well as the installation of an ultraviolet spectrometer and its viewing range (red) over the tile. Plasma is intentionally directed into the divertor region, where it comes into contact with the PFCs. Proper diagnosis and control of the divertor region is therefore crucial to ensure long-term efficacy of these devices as well as flushing impurities from the divertor

region. The Joint European Torus (JET) has experienced decreased erosion rates as a result of switching from carbon to tungsten divertors and beryllium first walls [7]. In addition to experiments involving the DiMES probe and W-coated divertor tiles in DIII-D [8,9], the erosion and plasma transportation of tungsten have been investigated at TEXTOR [10, 11], JET [7, 12], C-Mod [13, 14], DIII-D [8], ASDEX-Upgrade [15, 16], and recently at Auburn University in the Compact Toroidal Hybrid (CTH) [17].

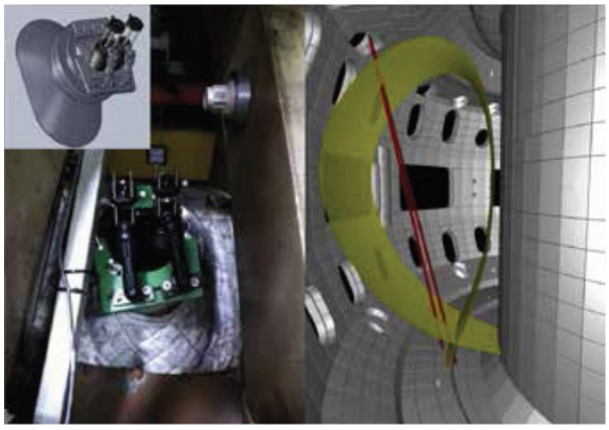

Figure 1.1: Illustration of an ultraviolet spectrometer lines of sight within the DIII-D tokamak measuring emission from tungsten inserts in the lower divertor region. A collection of optics mounted on the tokamak is shown (left).

While tungsten's significant radiation cooling makes it an effective PFC in the divertor region, it can quench the fusion reaction if eroded tungsten transports into the plasma core: the ionization of electrons from high-Z atomic impurities and spectral emission from excited states depletes the energy of the core plasma. Unlike lighter elements such as beryllium and carbon, which have far fewer electrons to ionize and therefore radiate less power from the plasma, tungsten has 74 electrons that can be ionized. Even at fusion relevant plasma conditions, W atoms would not be fully stripped in the plasma core, meaning the continued potential for radiation losses exists. Additionally, the resultant changes in surface topology from its redeposition can weaken thermo-mechanical resilience [13, 14, 18]. At ITER, where tungsten is planned for the divertor components [16, 19], a 10 percent relative accuracy of the tungsten influx measurement is needed [11, 20], requiring precise spectral diagnostics.

One such diagnostic method that relates the erosion rate of a PFC to the intensity of an associated spectral line was developed in Behringer *et al.* [21]. The diagnostic utilizes fundamental atomic data comprising the S/XB ratio, which quantifies the 'ionizations per photon.' Under the assumption that all eroded material becomes ionized within the observation line of

sight, the measured intensity of a spectral line and the S/XB can then be used to calculate a gross erosion flux.

Calculation of the S/XB coefficient requires (1) the spontaneous emission rate for the chosen line as well as the effective electron-impact (2) ionization and (3) excitation rates. The latter two rates can be determined through a comprehensive generalized collisional-radiative modeling, which quantifies the populations of atomic species as a result of expected atomic processes in the plasma. Such processes can include electron-impact ionization and excitation, spontaneous emission, and dielectronic and radiative recombination. Rate coefficients for these processes often assume a Maxwellian distribution of electrons, which is used to convolve a cross section, a measure of the probability of a single process, over the free electron distribution. Cross sections represent fundamental quantum mechanical probabilities and can be generated through measurements, theoretical calculations, or both.

Attempts to experimentally determine the S/XB ratio for tungsten have been conducted previously for a set of tungsten spectral lines by comparing spectral line intensities and eroded tungsten. Measurements at TEXTOR [10] were obtained with a pure tungsten source by injecting WF_6, which dissociates at low temperatures [22, 23]. Brezinsek *et al.* 2011 first developed this dissociation technique [23], and Laengner *et al.* demonstrated its feasibility in limiter conditions [22]. Other S/XB measurements have been made via tungsten mass loss [8, 24, 25] and WCO_6 sublimation [26, 27]. The most common neutral tungsten line for these measurements is the 400.88 nm spectral line arising from $5d^5 6s\ ^7S_3$ - $5d^5 6p\ ^7P_4$ [8, 10, 11, 22–28] because it is easily accessible in the visible region. Use of this line is problematic, however, because of the presence of a W II line at 400.88753 nm [29, 30]. The 429.5 nm ($5d^5 6s\ ^7S_3$ - $5d^5 6p\ (^7P_2)$ is another spectral line being considered [8, 10, 11, 22, 24, 25].

Results from these experiments suggest (1) that current theoretical atomic data either underestimates or overestimates the S/XB at higher electron densities, depending on the method used for calculating electron-impact excitation and ionization cross sections and associated rates, (2) the S/XB is highly dependent on metastable and excited state populations [11], and (3) the S/XB is highly sensitive to density above n_e=10^{19} m^{-3}, based on measurements [8] and current ADAS theoretical atomic data [31]. Brezinsek *et al.* 2017 [10], measuring the S/XB in

the 20 to 85 eV temperature range, fit their results with previous experiments from 2 to 20 eV at ASDEX-Upgrade [27], PISCES-B [24, 25], and PSI [28]. The experimentally measured S/XB is 25% higher than current ADAS predictions [31] for densities between 10^{18} to 10^{19} m^{-3} [10]. The DIII-D DiMES experiment found similar discrepancies in the same density range [8].

All previous comparisons of the S/XB have been of semi-classical or perturbative electron-impact rate coefficients. The ADAS data uses the semi-classical Exchange Classical Impact Parameter method (ECIP) [32] for electron-impact ionization and Plane-Wave Born for electron-impact excitation [31]. Beigman *et al.* [11], on the other hand, use the perturbative Born and Born-Ochkur approximations from the ATOM code [33] for $5d$ and $6s$ ionization from the ground state. For electron-impact excitation, Beigman *et al.* used the semiempirical van Regemorter formula [34] and compared with experiments [26–28] in the 2.5 to 5 $\times$ 10^{19} m^{-3} range. For temperatures above 10 eV, measurements fall below theoretical values by a factor of 1.5 to 5 depending on how excited populations are modeled. The Born and Born-Ochkur approximations tend to produce higher cross sections than expected, thus increased effective ionization rates. Another experiment at TEXTOR, specifically measuring ionization rates [35] also suggests that the ionization rather than the excitation calculations are responsible for differences in the S/XB ratio observed at TEXTOR in a separate experiment investigating the 400.88, 498.3, and 522.5 nm lines [10].

Other complications for tungsten S/XB and atomic modeling include sensitivites to metastable and excited-state populations as well as electron densities beyond 10^{19} m^{-3}, as seen in Figure 1.2. Metastable atomic states describe populations that do not quickly reach equilibrium often because there does not exist a rapid radiation pathway to the ground state. Beigman *et al.* demonstrated the effect of varying metastable populations on possible W S/XB values [11], an effect that is both hard to distinguish from and also directly affected by the electron-impact ionization rates. A set of S/XB ratios were obtained based on a tungsten temperature parameter T_W, which is related to tungsten metastable populations (considered as $5d^4 6s^2\ {}^5D_{0,1,2,3,4}$ and $5d^5 6s$ ($^7S_3$ levels) under Maxwell-Boltzmann statistics (the different green lines in a)). The range of T_W considered was based on observed spectral line intensities, and the S/XB ratios obtained within this range were found to differ by as much as a factor of 82, suggesting a need for

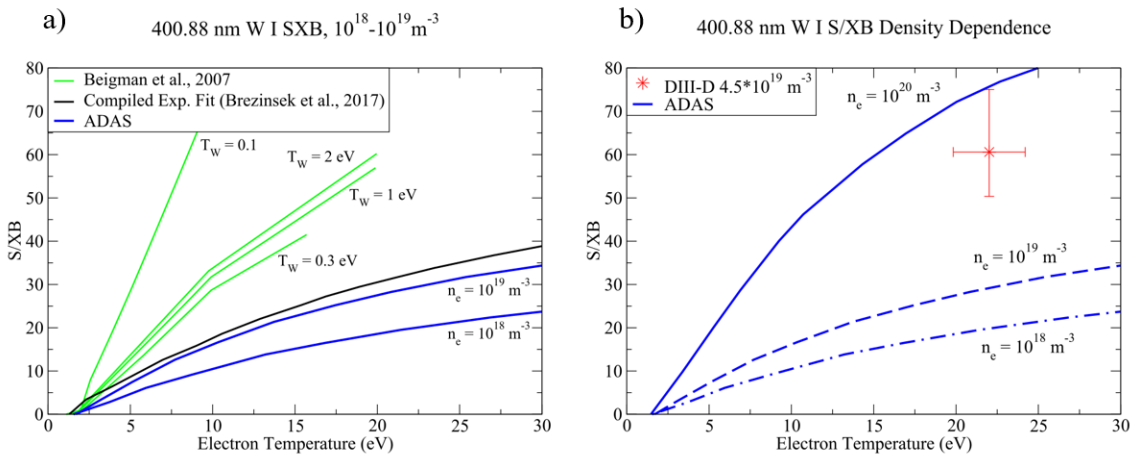

Figure 1.2: Effect of a) metastable populations and b) electron density on the 400.88 nm tungsten S/XB. In a) the green lines reflect different assumed metastable populations. The blue lines are from using the approximate electron-impact data available from ADAS [36], while the black line is a fit made from compiled measurements of the S/XB [28]. As b) shows, the S/XB becomes highly sensitive to electron density above 1×10^{19} m^{-3}.

an accurate account of metastable populations. Additionally, while most measurements have been performed at electron densities under 10^{19} m^{-3}, an S/XB measurement in DIII-D at 4.5×10^{19} m^{-3} shows a sharp increase compared to lower densities [8].

One of the factors contributing to increased effective ionization rates at higher electron densities is ionization from excited states. Light atomic species such as He, Li, and B have demonstrated strong contributions by high-n excited states to the effective ionization in the low temperature and moderate to high density regime, indicated by a noticeable rise in the effective rate coefficients [37–39]. An experiment with Li in the divertor region of the DIII-D tokamak, for example, showed good agreement of the effective ionization rate with theoretical calculations that include all of the excited-state ionization [40]. Excited-state ionization of higher Z elements beyond B has currently not been studied, though included within the ADAS suite is the ability to use ECIP rates for atomic states without electron-impact ionization data [31]. Because the ionization potential of excited states is always lower than the ground state, the effect of excited state ionization is particularly relevant in low temperature plasmas, such as in the divertor region of fusion relevant plasmas, where the average electron temperature might be below the ground state ionization potential.

Many factors therefore influence the S/XB, particularly at higher electron densities. It is thus of critical importance to develop accurate theoretical neutral tungsten atomic data and employ atomic population modeling that encompasses metastable and excited states to determine accurate S/XB diagnostics over a range of electron temperatures and densities for fusion-relevant devices. Non-perturbative atomic data for both the electron-impact excitation and ionization of neutral tungsten is needed to replace the current perturbative and semi-classical data.

A non-perturbative Dirac *R*-Matrix (DARC) calculation was recently completed by R. Smyth *et al.* for the electron-impact excitation of neutral tungsten [41]. The relativistic structure used in this calculation was made with experimental guidance about which configurations were emitting strong lines, based on a tungsten probe inserted into the Compact Toroidal Hybrid (CTH) at Auburn University [17] and shows an 11% average percent error compared to compiled experimental energy levels [42]. The *R*-matrix method yields an exact solution to Schrodinger's equation for the collision of an electron with an atom that includes all possible ways that the two can couple in terms of overall quantum numbers, as well as both exchange and correlation effects. To fit the relativistic structure within available computational resources, the DARC calculation did not include transitions of electrons into the continuum states, i.e., "pseudostates," that would correspond to electron-impact ionization.

The primary motivation of the present work is to complete the set of non-perturbative atomic data (ionization) necessary to model the S/XB of neutral tungsten accurately at both low and high electron densities. An electron-impact ionization *R*-Matrix with pseudostates (RMPS) calculation is performed that includes both configuration mixing and ionization from the $5d^5 6s$ ($^7S_3$) metastable as well as from excited states, in addition to the ground. The combination of the previous DARC electron-impact excitation and the present RMPS electron-impact ionization calculation should thus help clarify inconsistencies reported in S/XB measurements from various lines [8, 10, 11, 24, 25].

1.2 Neon: A Bridge between Light and Heavy Elements with Divertor Applications

Neon, at the heavier end of the light elements, can serve as an important benchmark in gauging the importance of excited-state ionization for collisional-radiative modeling of both heavier atomic species and noble gases. Applications including divertor cooling and spectral diagnostics also make neutral neon important in its own right for proper GCR modeling.

Neon is also a useful element in many plasma applications related to astrophysics [43–45], low-temperature laboratory plasmas [46], and fusion research [47–51]. In fusion devices, neon has been effective at mitigating disruptions [48, 49] (sudden termination of the plasma) as well as for divertor cooling [50, 51]. Recently, the spectrum of neutral neon, along with helium, has been investigated as a diagnostic for electron temperature and density in the edge region of the W7-X stellerator from a gas injection [47]. Unlike helium, neutral neon is expected to emit measurable spectral lines for high electron densities ($> 10^{20}$ m^{-3}) and low temperatures (< 10 eV). A well-developed collisional-radiative model of neon in this regime would thus provide greater coverage and lower the uncertainty of the temperature and density profiles in the edge region.

The electron-impact excitation and ionization of neutral neon have previously been calculated and demonstrated good agreement with most measurements for the ground and lower-energy excited states [52]; however, ionization from a large number of excited states is still missing. Currently, cross sections for the $2p^6$ and $2p^5 3s$, $2p^5 4s$, $2p^5 5s$ ionizations have been calculated [53–57]. Obtaining accurate cross sections, and thus rate coefficients, requires non-perturbative approaches, such as the *R*-matrix technique, coupled with the inclusion of an adequate number of pseudo-states to the atomic structure in order to account for target electrons in the continuum state. The previous calculation for ionization from the $2p^5 ns$ configurations was limited in the number of pseudo-states that could be included. Our main objective is thus both to check for convergence of the *ns* results and also to calculate new cross sections and rate coefficients for the *np*, *nd*, and 4*f* states, which can then be used in collisional-radiative modeling.

A related goal is to provide a full account of the electron-impact excitation of neutral neon from all *LSJ*-resolved levels. Neutral neon has previously been used to study the contribution of pseudostates to cross sections, showing that the presence of more pseudo-states can significantly lower excitation cross sections for neutral species [52, 55, 58]. Excitation into higher valence orbitals such as the $3d$ has only been examined in one other study [52]. Thus, we seek to generate rate coefficients from a new non-perturbative calculation that will also serve as a check upon the previous one.

With a full account of the electron-impact excitation and ionization from all excited states, the most accurate set of collisional-radiative data for neutral neon to date is compiled. Further, the importance of excited-state ionization, particularly ones that can be excited from the ground via a electric-dipole allowed transition is demonstrated.

1.3 Unresolved Questions for High-Z Elements in Atomic Physics and Generalized Collisional Radiative Theory

The completion of non-perturbative electron-impact ionization calculations for neutral neon and tungsten should cover new frontiers in atomic physics not previously addressed in lighter elements. Of particular relevance is how relativistic effects, configuration mixing, and shared ionization pathways among configuration series impact electron-impact ionization cross sections and the effective ionization rate.

The configurations of W are all open $d-$shell and exhibit a high degree of mixing. Figure 1.3 shows a Grotrian diagram, with an emphasis on the 5d^{4}6s*nl*, 5d^5 *nl*, and $5d^36s^2nl$ series. The metastable $5d^56s$ (^{7}S$_3$) falls within the energy span of the ground $5d^46s^2$ (^{5}D) levels, blurring the distinction between "ground" and "metastable." Wyart, through parametric fitting of compiled experimental measurements [42] with a Relativistic Hartree Fock (HFR) calculation that includes core polarization effects, found that only six of the low odd parity energy levels between $5d^36s^26p$, $5d^46s6p$, and $5d^56s6p$ have a configuration percentage of $5d^36s^26p$ greater than 60% [59]. The ground and metastable configurations for W$^+$ include $5d^46s$, $5d^5$, and $5d^36s^2$, where the $5d^46s$ (^{6}D) ground term can can be reached directly from W via either ground $6s$ or metastable $5d$ ionization.

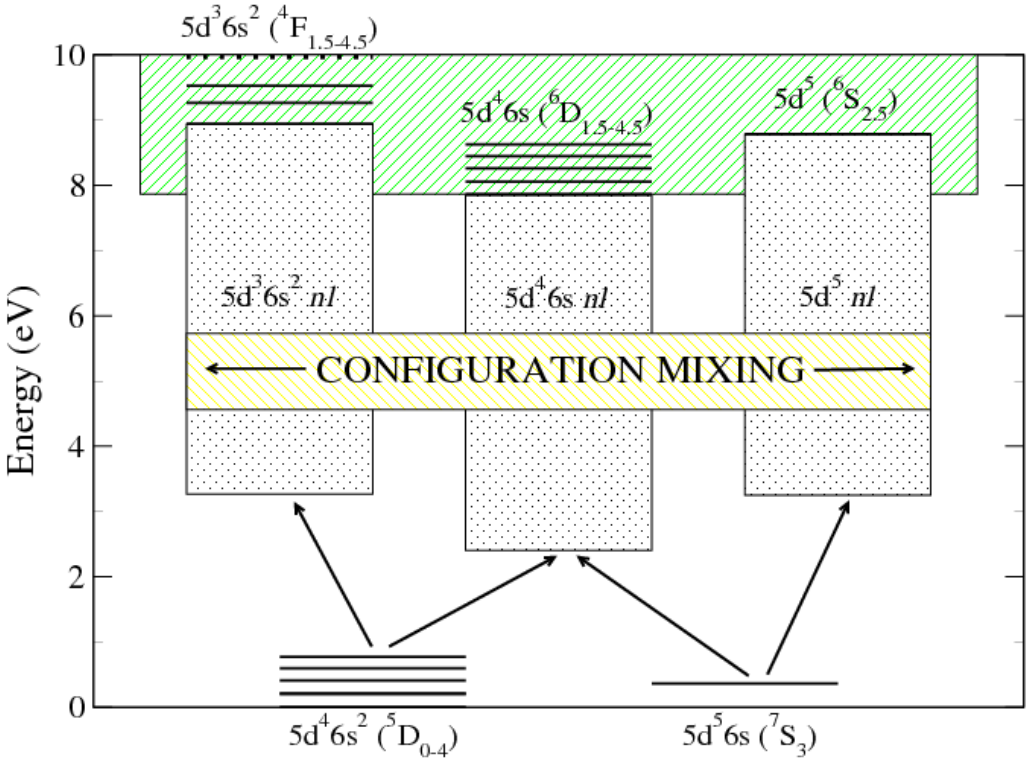

Figure 1.3: Grotrian diagram of selected neutral tungsten levels, with an emphasis on the ionization pathways between the three main series, $5d^46snl$, $5d^5nl$, and $5d^36s^2nl$. The ground and metastable levels can be excited into two of the three series each, and the configurations are all heavily mixed.

Configuration-averaged methods such as Distorted Wave, Exchange-Classical Impact Parameter, and Time Dependent Close Coupling consider different ionization configuration pathways as separate problems. For example, a calculation for the $6s$ ionization from the ground state would have no information regarding the $5d$ ionization from the metastable state, despite their shared W^+ core. Put differently, interference effects between different initial and final state ionization processes are not included. An *LS*- or *LSJ*-resolved *R*-matrix calculation, on the other hand, can simultaneously include both neutral tungsten's ground and metastable state ionizations in addition to any other possible transitions into the continuum, as long as the target structure includes the configuration series corresponding to the ionization pathway. An open

question to be answered is therefore **(1) Do all ionization pathways need to be considered in a single calculation for accurate electron-impact ionization cross section results, or can they be treated separately?**

A related but slightly different question is **(2) What is the effect of configuration mixing on term- and level-resolved electron-impact ionization cross sections?** The $5d^5nl$ series, for example, mixes strongly with the $5d^46s\ nl$ series; however, the former cannot be reached via the ground state from a conventional one-electron transition. Understanding the effects of mixing is therefore important in guiding adequate target structure candidates and interpreting their results.

A major challenge associated with non-perturbative electron-impact calculations of tungsten and other open $d-$ and $f-$ shell elements is that they require expensive computational resources in terms of RAM, I/O, and runtime. These computational constraints are further exacerbated by the requirements imposed by the nature of the ionization problem itself. The *R*-matrix with pseudostates (RMPS) method takes an exhaustive approach to the electron-atom collision problem: for a given target-incident electron "N + 1" set of conserved quantum numbers, the method requires calculating Hamiltonian matrix elements corresponding to each set of possible coupled target and electron quantum numbers. Further, a given target quantum number set (of one N + 1 symmetry and one Hamiltonian element within that set) values for all corresponding mixed configurations must be calculated separately and summed together, weighted by their mixing coefficients. The angular algebra associated with open $d-$ and $f-$ shell elements results in many more energy levels than open $s-$ or $p-$ shell elements, corresponding to much larger Hamiltonian sizes. Electron-impact ionization calculations further require a large number of additional discrete pseudostates to represent the continuum, the energy levels of which can far exceed the regular optical energy levels associated with the target atom.

Aside from requiring a large number of pseudostates, RMPS calculations for electron-impact ionization further requires a larger basis set to describe the continuum electron compared to electron-impact excitation calculations. The basis set approach of the Belfast *R*-matrix suite of codes [60] builds a continuum electron representation of orthogonal states from low

incident electron energies upwards. So, a basis set covering an incident energy beyond the ionization potential will necessarily be larger than one only covering electron-impact excitation of a target state. Each extra member of the set corresponds to a multiplying of the dimensions of the Hamiltonian. The *R*-matrix itself consists of a multiplication between two matrices, which are of dimensions of the Hamiltonian size versus the number of target-electron channels for a given N + 1 symmetry.

The RMPS method is therefore a computationally demanding one, made more so by the necessity of pseudostates and larger basis sets for electron-impact ionization, and in some cases might not even be feasible, at least for certain N + 1 symmetries with a large number of target-electron channels. The present work is thus in part concerned with **(3) how can the size or computational burden of more expansive non-perturbative calculations be reduced while maintaining accuracy in the results?**

Finally, the electron-impact ionization results from neutral neon and tungsten should yield new insights into atomic population modeling of plasmas. Here, modeling of both atoms should answer **(4) how important is excited-state ionization for accurate GCR modeling, particularly as concerns the effective ionization rate coefficient?** Regarding the relativistic and configuration mixing effects associated with tungsten and relativistic and configuration mixing effects: **(5) how important is LSJ- and LS-resolved electron-impact data for accurate GCR modeling of high-Z elements?**

Regarding these five questions, the present work on the electron-impact ionization and Generalized-Collisional-Radiative modeling of neutral neon and tungsten will arrive at the following three overall conclusions:

1. **Due to configuration mixing and multiple ionization pathways, at least term-level resolution and the inclusion of all sizeably contributing pathways in the target structure are required for accurate electron-impact ionization cross sections of open $\mathrm{d}-$shell high-Z.**
2. **At present, computationally expensive LS-resolved non-perturbative methods are required to obtain accurate electron-impact ionization cross sections for high-Z open $\mathrm{d}-$shell elements.** However, as the incoming electron can couple to a given term

either as spin up or down, it is reasonable to assume the two spin symmetries contribute roughly equal to a term's ionization cross section, and across all incident energies. This will be demonstrated with neutral tungsten's metastable cross section, in which the higher and lower spin sets of N + 1 symmetries yield contributions within 10% of each other, as well as with an analysis of scaling Exchange-Classical Impact Parameter [32] cross sections with the obtained neutral tungsten excited state cross sections.

3. **Excited-state ionization contributes more than the ground state to the effective ionization rate for both neutral neon and neutral tungsten, particularly at low temperatures and high densities. While the photon-emissivity coefficient (PEC) requires precise LSJ-resolved excitation rates, the effective ionization rate (SCD) demonstrates nearly negligible change between LS- and LSJ-resolved rates.**

The rest of this work is divided as follows: Chapter 2 provides a theory overview spanning atomic structure, electron-atom collisions, and Generalized-Collisional Radiative theory, with an emphasis on ionization and the S/XB coefficient for erosion diagnostics. Chapter 3 details the results of neutral neon electron-impact excitation and ionization calculations, as well as a study of the effects of excited-state ionization on the effective ionization rate. Chapter 4 describes the neutral tungsten *LS*-resolved electron-impact ionization calculation, including structure details and cross section results for the ground and metastable states. Chapter 5 analyzes the ionization cross sections out of excited states from the neutral tungsten RMPS calculation and concludes with SCD and S/XB modeling using the new ionization data. Chapter 6 summarizes the current findings as well as suggests various strategies for future high-Z electron-impact ionization calculations and future computational and atomic physics directions. A number of code developments were required for the R-matrix calculations, and these are described, along with excerpts, in Chapter 6 and Appendix B.

Chapter 2

From Schrodinger's Equation to Spectral modeling of plasma emission: R-matrix scattering theory and Generalized Collisional-Radiative Modeling

2.1 Introduction

The goal of the R-matrix calculations reported in this dissertation is to generate reliable atomic data for spectral modeling in plasma devices. For example, one such application involves the spectral emission of neutral Ne to measure the electron temperature in the edge region of fusion plasmas. The W-7X experiment in Germany is developing such a diagnostic and requested electron-impact excitation and ionization data for use in the diagnostic (to be used in the 0-40 eV electron temperature and 10^{12} - 10^{14} cm^{-3} electron density ranges [47]). In this chapter we describe the theoretical methods that bridge the gap between the quantum mechanical cross sections and the modeling of the observed spectra. Similarly, the tungsten cross section data will be the same theoretical framework.

The theoretical methods that will be used to calculate electron-impact excitation and ionization cross sections in this dissertation will be described. These cross sections are for single collisions of electrons at a specified energy. In order to obtain overall spectral rates in a plasma, we must understand both the limitations of these cross sections and how they can be applied beyond a single-electron collision. In addition, other possible atomic processes in the plasma, such as electron recombination, radiative decay, and proton collisions, also need to be considered. We will show that for neutral tungsten modeling in tokamak divertors, that electron recombination is not important in the modeling, while proton collisions for Ne may be important.

2.2 Theory of Atomic Structure

Accurate spectroscopic modeling of an atomic species in a plasma requires a well-informed model of the atom's structure. Metrics guiding the quality of an atomic structure include 1) an adequate inclusion of configurations to account for both the atomic processes involved and the observed lines seen in the spectrum, 2) the accuracy of the term/level energies, and 3) the oscillator strengths (Einstein A_{ij} coefficients).

The atomic processes to be modeled and available spectra can often guide the set of electronic configurations used to describe the atom. For smaller atomic species such as He or Li with less computational constraints for collision calculations, larger sets of configurations can be used to describe both fine-structure electron-impact excitation and ionization, as well as the lines over a large wavelength range. To make collision calculations for heavier elements computationally feasible, priorities must be assigned when generating the atomic structure based on the kind of collision and the spectral wavelength range. For example, Smyth *et al.* [41], in their calculation for neutral W electron impact excitation, use a subset of configurations in part corresponding to strong transitions from 200-500 nm, which includes potential line candidates for the W I S/XB diagnostic [11]. The spectral lines for which their data need *LSJ*-resolution, as fine-structure transitions can easily be resolved in the spectral observations. Pseudo orbitals, which can account for ionization from the target, were therefore not included. A proper electron-impact ionization calculation, on the other hand, would require a set of pseudo orbitals extensive enough to converge the ionization cross sections, yet, because ionization from the J-resolved levels within an LS-term are unlikely to show large differences, performing an LS-resolved ionization calculation allows one to reduce the size of the calculation. This is in part because ionization cross sections are a summation of individual transitions above the ionization potential, rather than of one transition.

The configuration set used as well as a set of orbital scaling parameters will determine the accuracy of the structure, as noted through the resulting energy terms/levels and oscillator strengths. In the next subsection, an overview of atomic structure theory and the program AUTOSTRUCTURE is given.

2.2.1 Atomic Structure through Configuration State Functions and the Variational Principle

Schrodinger's equation for *N* particles and their wavefunction Ψ,

$$\frac{-\hbar^2}{2}\sum_{n=1}^{N}\frac{1}{m_n}\nabla_n^2\Psi(r_1,r_2,...,r_N)+V(r_1,r_2,...,r_N)\Psi(r_1,r_2,...,r_N)=E\Psi(r_1,r_2,...,r_N) \tag{2.1}$$

can be solved analytically only for a few V(r) potentials, one of which is for the hydrogen atom. Yet, all quantum systems have the special property of being describable by any orthonormal, complete set of functions ψ_i:

$$\Psi(r_1,r_2,...,r_n)=\sum_i c_i\psi_i$$

In accordance with $\langle\Psi\mid\Psi\rangle=1$, $\sum_i c_i^2=1$. That is, the square of a coefficient represents the probability of measuring that state. Thus, wavefunctions for atoms of one or more electrons can be described as a superposition of a single centered basis. In addition, a further assumption known as the *self-consistent field approximation* considers the total wavefunction for the *N* electrons as the product of one-electron spin-orbitals. To obey particle indistinguishability, the set of spin-orbitals corresponding to the set of quantum numbers, nlm_lsm_s for non-relativistic, are cast into Slater determinants, where each element represents a different interchanging of $r_1,...,r_N$ coordinates. The possible γnlM_lsm_s sets of quantum numbers of a given configuration must obey the Pauli exclusion principle (reflected in the Slater determinants), limiting the possible total quantum numbers, γLM_LSM_S.

A *configuration state function* $\Phi(\gamma LM_LSM_S)$ for a given electron configuration $(n_1l_1)^{w_1}(n_2l_2)^{w_2}...(n_ml_m)^{w_m})$, where $N=\sum_{a=1}^{m}w_a$, can then be formed from the linear combination of Slater determinants of all m_l and m_s spin-orbitals leading to the total quantum number set γLM_LSM_S. These CSFs are eigenfunctions of the N-electron Hamiltonian:

$$\mathcal{H}=\sum_{i=1}^{N}-\frac{1}{2}\nabla_i^2-\frac{Z}{r_i}+\sum_{i<j}^{N}\frac{1}{r_{ij}} \tag{2.2}$$

The first two expressions on the right hand side correspond to the electron kinetic energies and attraction to the nucleus respectively. The last expression accounts for electron-electron interactions, where $r_{ij} = |\vec{r_i} - \vec{r_j}|$ is the distance between an i,j electron pair. The Thomas-Fermi-Dirac-Amaldi potential utilized by the program AUTOSTRUCTURE assumes that, rather than needing to calculate each individual electron-electron interaction separately, an electron cloud density can be used to account for the effect of the other N - 1 electrons. This cloud density, in accordance with the self-consistent field approximation, is spherically symmetric and thus contains no angular dependence between the position of an electron versus its effective N - 1 electron cloud. Further, the interaction expression,

$$\frac{1}{r_{ij}} = \sum_{l=0}^{\infty} \frac{r_<^l}{r_>^{l+1}} P_l(cos\theta),$$

converges reasonably well within the first few values of l. Here P_l denotes the radial function and θ the angle between the two electrons. $r_>$ and $r_<$ correspond to the radial position of the either the i^{th} electron or a j^{th} electron from the cloud, whichever is farther or closest from the nucleus, respectively.

The Thomas-Fermi-Dirac-Amaldi potential arises from considering the first three moments of the expansion:

$$V(r_i) = \frac{-2(Z-N)}{r_i} + \int_0^{r_0} \rho(r_i)[\frac{2}{r_>} + C_1\frac{r_<}{r_>^2} + C_2\frac{r_<^2}{r_>^3}]4\pi r_j^2 \, dr_j \tag{2.3}$$

The interaction terms are integrated over the electron cloud radius r_0. These interaction terms correspond to the monopole, dipole, and quadrupole moments respectively. Starting with the dipole moment, the positions of the electron with the rest of the cloud are now *correlated*, where C_1 and C_2 account for the angular terms of the i^{th} and j^{th} electron. Unlike the monopole moment, the succeeding moments all reflect a dependence of an electron's position on the rest of the electrons. An expression for the charge density can be solved for by minimizing the total kinetic and potential energy of the system:

$$\rho(r) = \frac{1}{2\pi^2}\left\{\frac{1}{\pi} + \left[\frac{1}{\pi^2} + V_0 - V(r)\right]^{1/2}\right\}^3 \tag{2.4}$$

where

$$V_0 = -\frac{15}{16\pi^2} - \frac{2(Z-N)}{r_0}.$$

The use of the Thomas-Fermi-Dirac-Amaldo potential in AUTOSTRUCTURE further employs a *variational principle*, a technique to find the upper bound of the lowest energy state. It can be shown that, for an arbitrary trial wavefunction ϕ with a parameter or parameters λ, the "variational" parameters, an upper bound ϵ can be obtained satisfying

$$\epsilon = \frac{\langle\phi|\mathcal{H}|\phi\rangle}{\langle\phi|\phi\rangle}$$

such that $\epsilon \geq E_0$ where E_0 is the lowest eigenstate of the Hamiltonian. ϵ is solvable by optimizing the expectation value of the Hamiltonian with respect to the variational parameters:

$$\frac{d\,\langle\phi|\mathcal{H}|\phi\rangle}{d\lambda} = 0 \tag{2.5}$$

This principle *prima facie* makes the method very promising; however, not all trial wavefunctions are created equal, some resulting in upper bounds much farther away than E_0. Wavefunctions already close in form to the actual wavefunction will be able to achieve a tighter bound. The energies for all states, including ground and excited, are then obtained through diagonalization of the Hamiltonian.

The Thomas-Fermi-Dirac-Amaldi potential also allows for variational scaling parameters λ_d and λ_q for the dipole and quadrupole terms respectively per atomic orbital, under the assumption of a spherically symmetric electron cloud density and the truncation of the interaction expression:

$$\begin{aligned} V(r_i) = \frac{-2(Z-N)}{r_i}\int_0^{r_0}\rho(r_i)\frac{2}{r_>}4\pi r_j^2\,dr_j + \lambda_d\frac{8}{3\pi}[\frac{1}{r^2}\int_0^r \rho r_i^3\,dr_i + \int_r^{r_0}\rho\,dr_i] \\ +\lambda_q\frac{8}{3\pi}[\frac{1}{r^2}\int_0^r \rho r_i^4\,dr_i + r^2\int_r^{r_0}\frac{\rho}{r_i^2}\,dr_i]. \end{aligned} \tag{2.6}$$

In addition to solving for an atom's term and/or level energies with the TFDA potential, AUTOSTRUCTURE incorporates another set of λ_{nl} scaling parameters, one per orbital. Functionally, these parameters can shift the average position of the wavefunction closer or farther away from the nucleus, allowing for closer agreement to NIST. These parameters can either be manually tuned by the user, or else a subset can be chosen to be optimized with the other λ_d and λ_q parameters.

A mathematically complete set of configurations is required to yield an exact solution to the atom's eigenfunctions and eigenenergies. Recall, the configuration state functions (CSF's) assume a radially symmetric potential, the simplest case of course being a hydrogenic potential. A proper solution to Hamiltonians with electron-electron interactions, then, requires a superposition of CSF's,

$$\Psi(\gamma LS) = \sum_{i=1}^{M} c_i \Phi(\gamma LS).$$

The coefficients c_i, termed *mixing coefficients*, reflect the presence of configuration interaction (CI) observed as off-diagonal elements of the Hamiltonian. For cases in which the wavefunctions are on their own exact eigenfunctions of the Hamiltonian, corresponding to unique energy levels, all off-diagonal elements will be zero due to orthonormality. A detailed discussion on the rules governing which configurations will interact and to what degree can be found in [61]. They can be summarized as follows:

1. CI is zero unless both the bra and ket have the same parity.
2. Configurations can differ in at most two orbitals.
3. Configurations must have a common *LS* value (for *LS*-resolution).
4. CI is large for configurations that are close in energy.
5. CI is large between configurations whose shared Coulomb matrix elements are large.

These rules are related to which conditions will yield non-zero off-diagonal elements. 1) results from the Hamiltonian operator being even. 2), 4), and 5) relate to the off-diagonal Coloumb elements. Mixing will of course be large as a result of the off-diagonal elements between configurations being large. Further, the Coulomb elements involve summing the possible interactions between two electrons of either the same or different orbitals, hence 2). Finally,

from orthonormality, configurations must have the same total angular momentum quantum numbers. These rules are often used as a rule of thumb for guiding which configurations to include in a structure: one includes all of the single-electron promotion configurations within the same complex (i.e., same n-shell), and if this is not sufficient, then one includes the double-electron promotions within the same complex.

Accuracy of an atomic structure can be gauged both from the generated series of term/level energies from the variational procedure with the TFDA potential as well as by the *oscillator strengths* describing transitions between states. The Einstein A_{ji} coefficient and oscillator strength f_{ji} describing the rate of spontaneous emission of a photon corresponding to a transition from state ϕ_j down to ϕ_i can be calculated from

$$A_{ji} = \frac{2e^2 w_{ji}^3}{3\epsilon_0 hc^3} \frac{1}{g_j} \sum_{\phi_i} | < |\phi_i|\vec{r}|\phi_j > |^2, \tag{2.7}$$

and

$$f_{ij} = -\frac{e^2 w_{21}^2}{18\pi\epsilon_0 mc^3} \frac{g_j}{g_i} A_{ji}.$$

Here, w_{ji} is the oscillation frequency between the two states, proportional to the difference in their energies. The $\vec{r}$ operator is related to the dipole operator of an electric field, the dominant term of electromagnetic radiation. Obtaining accurate A_{ij}'s and oscillator strengths therefore requires optimizing transitions where this expression is expected to be large, i.e., *dipole-allowed* transitions. g_i and g_j are the statistical weights of the lower and upper levels respectively. Given that the operator has an odd parity, the two states must therefore have *opposite* parities in order for the term to be non-zero. From the spherical harmonic functions, opposite parities will occur if the difference in angular momenta between the states ΔJ equals ± 1. Where *LS*-coupling is appropriate, this additionally corresponds to $\Delta L = \pm 1$. In developing an accurate atomic structure, therefore, configurations representing possible strong dipole transitions should be included and their oscillator strengths optimized to match NIST values. Of course, in the multi-configurational case, the atomic states are superpositions of CSFs. Furthermore, other transitions, such as magnetic dipole and electric quadrupole, are also

possible, complicating defining transitions by a simple set of rules. Thus, a more rigorous test on the structure would be to check the spontaneous emission rates of the non-dipole transitions. Rigorous and tentative rules regarding possible transitions can be found in [61].

2.2.2 Semi-relativistic and Relativistic Structures

For heavier elements, including neon and tungsten, relativistic effects must be included in calculating the atomic structure. The equation governing the relativistic structure of an atom is the Dirac equation. Though this equation was used in the electron-impact excitation calculation of W, where the fine structure led to fine resonances in the cross sections, we restrict ourselves to a semi-relativistic and *LS*-resolved structure for the neutral neon electron-impact excitation and for all electron-impact ionization calculations respectively.

For a semi-relativistic structure, the Breit-Pauli Hamiltonian may be used, which incorporates new relativistic shift (RS) and fine stucture (FS) terms [62]:

$$\mathcal{H}_{\mathcal{BP}} = \mathcal{H}_{\mathcal{NR}} + \mathcal{H}_{\mathcal{RS}} + \mathcal{H}_{\mathcal{FS}}$$

Equations for each $\mathcal{H}_{\mathcal{RS}}$ and $\mathcal{H}_{\mathcal{FS}}$ term can be found in [62]. Important relativistic shift terms include the mass, velocity, and Darwin terms, as well as the spin-orbit interaction. The fine structure spin-orbit interaction term,

$$\mathcal{H}_{\mathcal{SO}} = \frac{\alpha^2 Z}{2} \sum_{i=1} N \frac{1}{r_{ij}^3} l_i \cdot s_i, \tag{2.8}$$

where $\alpha = \frac{1}{c}$ explicitly depends on the total angular momentum operator J^2. The final wavefunctions can now be described as superpositions of *LS* states leading to overall JM_J values:

$$\Psi(\gamma J M_J) = \sum_{i=1}^{M} c_i \Phi(\gamma_i L_i S_i J M_J). \tag{2.9}$$

2.2.3 Pseudostates

For neutrals, for which the coulomb force of attraction of an electron with the nucleus is roughly equal to the force of repulsion felt by the other N - 1 electrons, the electronic states are less

tightly bound, and coupling of states to those in the continuum can occur. Recall, mixing between different configurations will be greater when the configurations are closer in energy. Therefore, bound states that are higher and energy, i.e., closer to the ionization potential, are more likely to experience mixing with continuum states.

Pseudostates serve an additional purpose in account for ionization of an electron into the continuum. A regular structure calculation only allows for transitions between bound states. Ionization can be considered as a summation of the pseudostates whose energies are above the ionization potential, provided an adequate number of pseudostates are included to converge the cross section.

The functions known as Sturmian-type orbitals [63] can used to represent these states and are expressible as $r^i e^{-\alpha r}$. Their shape is similar to continuum orbitals, except that they dissipate to zero as the radial coordinate approaches infinity. The parameter α, different from the previous $\alpha = \frac{1}{c}$, becomes defined through diagonalization of the Hamiltonian.

Figure 2.1 depicts a generic energy level diagram with pseudostates included (blue lines), representing the kinds of energies one might expect from an atomic structure calculation. Here, two configuration series, nl_1 and nl_2 are shown, for which the ionization potential is relative to the first series. The energies of levels from these optical orbitals converge at the ionization potential. A series of pseudostates, used to represent the continuum, $n\bar{l}_1$ and $n\bar{l}_2$ extend from just below the ionization potential into the continuum. Though the continuum itself is not discrete, the energy levels resulting from the pseudostates are. As shown, the lines from the configuration series on the left and right is in groups of five and three respectively, each group corresponding to one configuration. If assuming *J*-resolution, the lines would correspond to the 2J + 1 states.

2.2.4 Summary of Atomic Structure Theory and Practice

Generating an accurate atomic structure requires first deciding upon a set of configurations. Because the configuration state functions form a complete set, more configurations will result in a more accurate structure. In reality, particularly for more complex atoms with many terms/levels, configurations must be decided upon judiciously based on 1) the atomic process

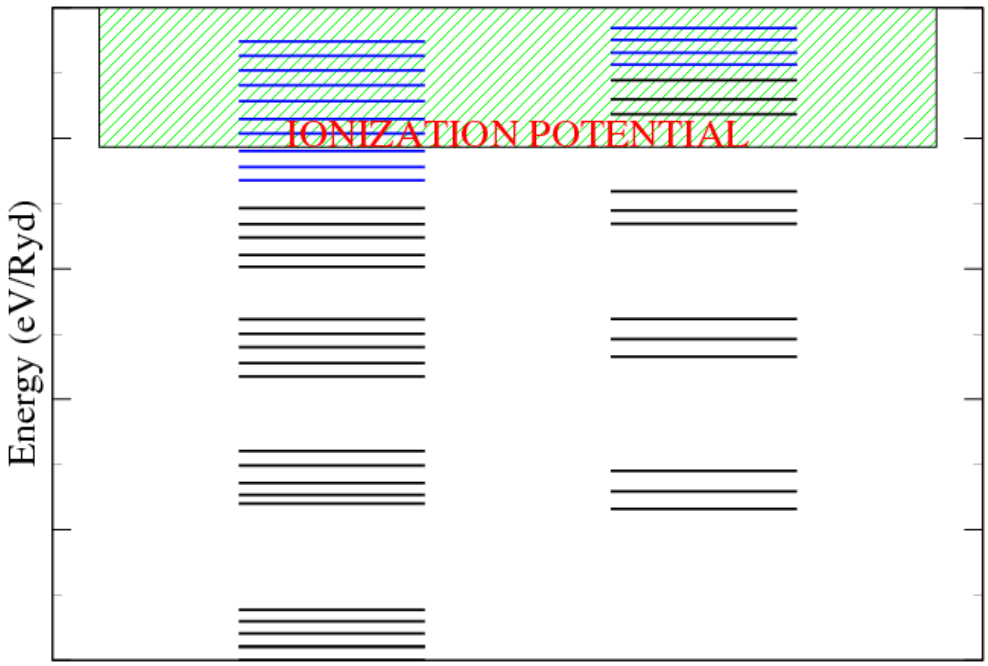

Figure 2.1: An example diagram of the resultant energies of an atomic structure calculation. Two series of optical configurations are shown. The pseudostate energies (blue) are discrete and used to represent the continuum.

being modeled (more pseudostates for ionization), 2) which configurations will mix heavily, and 3) which configurations will correspond to strong transitions observed in a spectrum. Aside from changing the set of electron configurations, one can also vary the set of λ_{nl} orbital parameters in AUTOSTRUCTURE. These parameters can either be adjusted manually or else a subset can be included in the variational procedure.

2.3 Atomic Collisions and Cross Sections

The dominant atomic processes for neon and tungsten that determine the main spectral features are due to electron-impact collisions. Accurate rates for electron-impact excitation and ionization, and these processes for neutral systems require non-perturbative methods that give the collision proper consideration of its inherently quantum-mechanical nature and account for the many-body effects in the collision process. This section is organized as follows: 1) A description is provided of the parameters involved in a collision process, such as the cross section, 2) an overview of semi-classical and perturbative methods is given, and 3) a detailed description of *R*-matrix, the non-perturbative method to be used in the present work, is given.

2.3.1 Basic Collision Model

Figure 2.2 shows a classical picture of the collision of a particle, such as an electron, with an arbitrary central potential $V(r)$ as a function of radial distance r. Of primary importance is an impact parameter b, the perpendicular distance from the radial axis. From the classical kinetic energy, the impact parameter is related to the angular momentum l and energy E of the projectile through, $b = \frac{l}{\sqrt{2mE}}$. b can further be related to the probability $d\sigma$ of the particle being scattered through an angular area $d\Omega = \sin\theta d\theta d\phi$, where $d\phi$ is the azimuthal angle. From the relation $d\sigma = bd\phi db$, the differential cross section can be calculated as

$$\frac{d\sigma}{d\Omega} = \frac{b}{\sin\theta}\left|\frac{db}{d\theta}\right|.$$

The differential cross section can further be integrated to give the total cross section. For example, integration of the differential cross section for a classical hard sphere of radius *r*

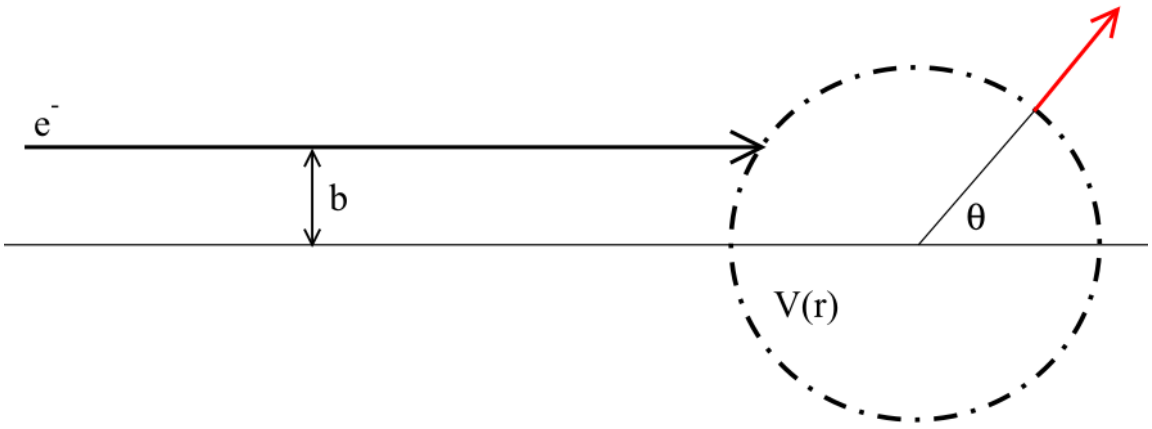

Figure 2.2: Classical diagram of the scattering problem of a particle of perpendicular distance b away from the radial axis. b can be related to the differential cross section $d\sigma$, the probability of the particle distending through an angular range $d\Omega = \sin\theta d\theta d\phi$.

would yield πr^2, indicating that all incident particles striking the face of the sphere – an area of πr^2– are scattered.

In quantum mechanical collisions, the picture of the particle as a point striking a sphere is no longer valid. Instead one can imagine a plane wave interacting with a spherical potential, yielding the following general form of a wavefunction for the incident and scattered particle:

$$\Psi \approx e^{ikz} + f(\theta)\frac{e^{ikr}}{r} \tag{2.10}$$

The left and right expressions indicate the incident and scattered wavefunctions respectively. $f(\theta)$ is a function that will contain the problem-specific scattering information: the goal of quantum mechanical scattering calculations is to solve for this function. One can think of the differential cross section as the probability density per unit time for a scattered particle of incident velocity v passing through $d\Omega = 2\pi \sin\theta d\theta$:

$$d\sigma = v|f(\theta)|^2 d\Omega = 2\pi \sin\theta |f(\theta)|^2 d\theta,$$

where the incident wavefunction is normalized to the velocity. A further complication of quantum mechanical collisions is the treatment of inelastic effects. For an inelastic collision, the energy of the scattered electron will change as a result of an internal change of state of the target. For example, in an electron-atom collision, energy in the form of a photon might be used for a target transition into or out of an excited state. The present work on electron-impact excitation and ionization shall therefore be concerned with inelastic collisions.

For both inelastic and elastic atomic collisions, the wavefunction u_l of a continuum electron of l angular momentum and $k^2 = 2E$ will be solved through considering a spherically symmetric potential $U(r)$:

$$\left(\frac{d^2}{dr^2} - \frac{l(l+1)}{r^2} - U(r) + k^2\right) u_l(r) = 0. \tag{2.11}$$

It can be shown [64] that as $r \to \infty$,

$$u_l \approx s_l(kr) + c_l(kr)\tan\delta_l(k), \tag{2.12}$$

where s_l and c_l are related spherical Bessel and Neumann functions $j_l(r)$ and $n_l(r)$ respectively and represent the solution when no potential is present. With proper choice of normalization constant, u_l can be rewritten as,

$$u_l \approx exp(-i\theta_l) - exp(-i\theta_l)S_l(k), \tag{2.13}$$

where $\theta_l = kr - \frac{1}{2}l\pi$ and $S_l(k)$ is the diagonal elements of the S-matrix:

$$S_l(k) = exp[2i\delta_l(k)] = \frac{1 + iK_l(k)}{1 - iK_l(k)}. \tag{2.14}$$

$K_l(k)$ is in turn the diagonal elements of $K_l(k) = \tan\delta_l(k)$. δ_l can be understood as a phase shift of the continuum electron as a result of the potential $U(r)$. From 2.12 and 2.10, one can further derive an expression of the scattering amplitude $f(\theta, \phi)$ in terms of δ_l [64]:

$$f(\theta, \phi) = \frac{1}{2ik}\sum_{l=0}^{\infty}(2l+1)\{exp[2i\delta_l(k)] - 1\}P_l(\cos\theta) \tag{2.15}$$

Obtaining quantum mechanical cross sections therefore requires solving for the phase shift δ of the continuum electron u_l.

Scattering properties will be determined based on the differences in the electron wavefunction as a result of $U(r)$. Therefore, one way to conceptualize the scattering problem is to consider the projection of the wavefunction without $U(r)$ onto the Hamiltonian operator with $U(r)$, and vice versa. That is,

$$\langle v_l(r)|H_u|u_l(r)\rangle \text{ and } \langle u_l(r)|H_v|v_l(r)\rangle \,,$$

where v_l refers to the solution to the wavefunction of a continuum electron absent any potential. Carrying out the Hamiltonian operators and subtracting the latter from the former,

$$\int_0^\infty \left(v_l(r)\frac{d^2u_l}{dr^2} - u_l(r)\frac{d^2v_l}{dr^2} \right) dr = \int_0^\infty v_l(r)U(r)u_l(r)dr \tag{2.16}$$

The left-hand side admits use of Green's theorem. Using the boundary conditions for u_l and v_l, as specified in 2.12, it becomes

$$\int_0^\infty \left(v_l(r)\frac{d^2u_l}{dr^2} - u_l(r)\frac{d^2v_l}{dr^2} \right) dr = v_l(r)\frac{du_l}{dr} - u_l(r)\frac{dv_l}{dr} = -k\tan\lambda_l(k). \tag{2.17}$$

Inserting the solution of v_l and Equation 2.17 into Equation 2.16 and simplifying,

$$\tan\delta_l(k) = -\int_0^\infty j_l(r)U(r)u_l(r)rdr. \tag{2.18}$$

2.3.2 Perturbative and Non-Perturbative Methods

Most $U(r)$ potentials cannot be solved analytically. In certain circumstances, however, perturbative and semi-classical methods can be employed to simplify the scattering problem. These methods are normally valid when the potential is sufficiently small or when the scattered particle passes quickly.

The Born approximation is the most traditional way of calculating scattering amplitudes. At first order, it's fundamental assumption is that the scattered term of Equation 2.10 is much weaker and can be solved as a perturbation of the incident plane wave. That is, u_l becomes replaced by the free particle solution v_l in Equation 2.18:

$$\tan \delta_l^B(k) = -\int_0^\infty j_l^2(r)U(r)r^2dr. \tag{2.19}$$

The corresponding scattering amplitude from $\delta_l^B(k)$ will be,

$$f(\theta,\phi)^B = -\frac{m}{2\pi\hbar^2}\int_0^\infty e^{i(\vec{k'}-\vec{k})\cdot\vec{r}}U(\vec{r})d^3\vec{r}, \tag{2.20}$$

where $\vec{k'} = k\vec{z}$ and $\vec{k}$ are in the directions of the incident and scattered wavefunctions respectively. For inelastic collisions between an electron and an atom in which the atom is excited from state n_i to n_f, the following equation for the differential cross section can be derived [65]:

$$\frac{d\sigma}{d\Omega} = \frac{k_f}{k_i}\frac{m^2}{4\pi^2\hbar^4}|\left\langle k_f n_f|U|k_i n_i\right\rangle|^2, \tag{2.21}$$

where

$$U(\vec{r},\vec{r_j}) = \sum_{j=1}^{N}\frac{e^2}{|\vec{r_j}-\vec{r}|} \tag{2.22}$$

represents the Coulomb repulsion of between the scattered electron and each of the N electrons of the atom.

Another perturbative approach, known as the distorted wave method, builds upon Equation 2.21 by Fourier transforming a "distorted" wavefunction under a Coulomb potential into momentum space. A more detailed version of the following derivation can be found in [65]. Let $\psi_{k_i}^{(+)}(r)$ and $\psi_{k_f}^{(-)}(r)$ represent the incoming and scattered electron wavefunctions respectively given a Coulomb potential. Importantly, the wavefunctions no longer assume that the incoming wave function experiences no effect from the potential, in which case it would be

a simple plane wave. Compared to Equation 2.20, the scattering amplitude of the Coulomb potential solutions contain a distortion in the form of a phase factor $e^{-i\eta_i ln(\sin^2\frac{\theta}{2})}$, where

$$\eta_i = \frac{mZZ'e^2}{\hbar^2 k_i} \tag{2.23}$$

A Fourier transform into momentum space is performed:

$$\phi_k^{(+)}(p) = \frac{1}{(2\pi)^3}\int e^{-ip\cdot r}\psi_k^{(+)}(r)dr \tag{2.24}$$

The full Coulomb wavefunctions in both position and momentum space can be found in [65]. The distorted wave approximation involves expressing the Coulomb potential of Equation 2.22 as a Fourier integral:

$$U = \frac{e^2}{2\pi^2}\sum_{j=1}^{N}\int \frac{-iq\cdot(r-r_j)}{q^2}dq. \tag{2.25}$$

where q is over all of generalized spherical coordinate space. Inserting this Fourier integral into the differential cross section of Equation 2.21 leads to the following equation:

$$\frac{d\sigma}{d\Omega} = \frac{k_f}{k_i}\frac{m^2}{4\pi^2\hbar^4}|\frac{e^2}{2\pi^2}\int d^3\vec{q}\frac{1}{q^2}\left\langle k_f|e^{-iq\cdot r}|k_i\right\rangle\left\langle n_f|\sum_{j=1}^{N}e^{-iq\cdot r_j}|n_i\right\rangle|^2. \tag{2.26}$$

In the distorted wave approximation, the distorted Coulomb wavefunction in momentum space is used to calculate the first braket inside the integral, while the second braket involves the (separate) atom wavefunction. As the Coulomb wavefunction assumes no electron-electron interaction, the distorted wave approximation is most accurate when: 1) The atom is an ion, such that the nuclear attractive force is much greater than the overall electron repulsive force, 2) The incoming electron interacts quickly with the atom, and 3) The incoming electron's trajectory is at a far distance (high impact parameter b from the atom.

Consequently from 2) and 3), the distorted wave method becomes more accurate with increasing angular momentum. The method therefore proves useful when used in conjunction with non-perturbative collisions calculations in that a distorted-wave 'top-up', as described in [66], can be used to account for partial waves above a certain angular momentum threshold.

Furthermore, distorted wave calculations can provide a simple and accurate method for calculating atomic collision data of the higher charge states of ions. For example, a distorted wave calculation done in tandem with an *R*-matrix calculation for W^{3+} revealed that the two were converged for that ion [67].

Most of the work presented here is regarding neutral Ne and W, for which, as will be shown, the distorted wave method does not yield accurate data. Distorted wave calculations can further produce diverging (asymptotic) cross sections at lower energies for ionization from excited states. In addition, approximate methods tend to disagree with each other. The distorted wave method, which does not account for exchange or correlation effects between the incident and target electrons, typically overestimates cross sections, while another method, the semi-classical Exchange Classical Impact Parameter (ECIP) method [32], underestimates. This disagreement will be shown explicitly for tungsten. Non-perturbative methods, such as the *R*-matrix method described in the next section, are required.

2.4 *R*-Matrix Theory for Electron-Impact Excitation and Ionization of Atoms

As discussed, perturbative and semi-classical methods, despite being efficient solutions and accurate for highly charged ions and fast-moving incident electrons, can be inaccurate by large factors for lower charge states, such as will be shown for neutral neon and tungsten. Accurate atomic data for these species requires a more comprehensive quantum mechanical approach that accounts for exchange and correlation effects between the incident and all target N electrons. The *R*-matrix is one such non-perturbative method, in that it makes no approximations: the exact solution to Schrodingers equation is solved by including all possible states, or channels, of the total (N + 1) electron system. Unlike approximate methods, however, which can usually be calculated in minutes, the *R*-matrix method carries with it a much larger computational cost in terms of RAM, disk space, I/O, and time to completion. This cost in part arises from using more finely *LS*- and *jK*-resolved atomic structures and from allowing channels to be coupled.

This section is organized as follows: 1) an overview of R-matrix theory for electron-atom collisions is given and 2) brief summaries of the Belfast *R*-matrix code stages [60] are given. Other non-perturbative methods include the Time-Dependent Close-Coupling (TDCC)

method [68], and the Exterior complex scaling method [69, 70]. These methods are not used in the calculations of this dissertation. However, TDCC results from a previous paper for the electron impact ionization of neutral W [71] results are used and converted to LS-term and LSJ-resolution' using angular factors that are described in Section 2.5 of this dissertation.

2.4.1 Sketch of *R*-Matrix Theory for Electron-Impact Ionization and Excitation

A thorough description of R-matrix for electron-impact collisions with atoms can be found in Burke [64]. Figure 2.3 depicts the setup of the *R*-matrix problem. One of the main distinguishing characteristics of the R-Matrix method, with or without pseudostates, is that the wavefunction is solved in two distinct regions, whose boundary is defined by the *R*-matrix box or radius a. This boundary is set far enough from the target atom such that all bound orbitals have dissipated, and the incoming (continuum) electron is therefore effectively distinct from the target N electrons.

In the inner region, the continuum electron is considered indistinguishable from the other N electrons: for a given N + 1 partial wave *LS* (or *J*) symmetry, Hamiltonian H_{N+1} elements for each possible $LS\Pi_{TARGET}$ + $ls\pi$ channel are calculated, where the first and second terms correspond to the total target and incident electron's quantum numbers respectively. The N + 1 Hamiltonian in the *LS* case includes the kinetic energy of the incident electron, as well as its nuclear attraction to the nucleus and repulsion from the N electrons:

$$H_{N+1} = \sum_{n=1}^{N+1} \left(-\frac{1}{2}\nabla_n^2 - \frac{Z}{r_n} + \sum_{m>n}^{N+1} \frac{1}{r_{nm}} \right) \tag{2.27}$$

Regarding the incident electron, the Queen's University at Belfast *R*-Matrix suite of codes make a further assumption that the orbitals describing it are orthogonal to the target orbitals [72]. Because the incoming electron orbitals must form a complete set, i.e., account for all possible states, additional bound orbitals for the incoming electron must also be included to account for states where it is bound to the target. Most of the *R*-matrix calculation therefore

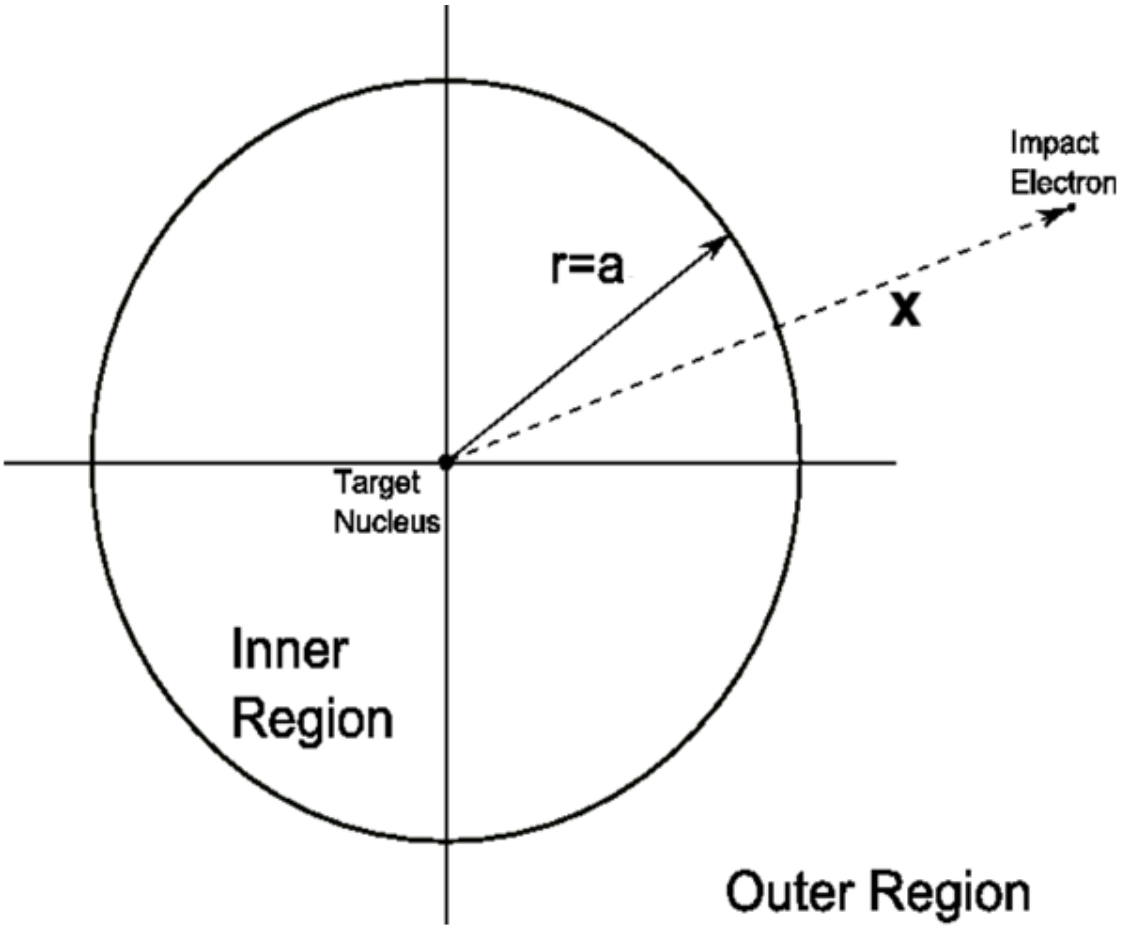

Figure 2.3: Depiction of the *R*-matrix problem. Schrodinger's equation is solved separately in the inner and outer region, separated by the "box" radius a. Computing the *R*-matrix from the inner region determines the boundary conditions of the continuum electron wavefunction in the outer region at r = a.

consists of 1) calculating the continuum-continuum, bound-continuum, and bound-bound elements of a Hamiltonian matrix and 2) diagonalizing the Hamiltonian. Upon diagonalization, the following energy-independent basis states are obtained:

$$\psi_k(x_1...x_{N+1}) = \mathcal{A}\sum_{ij} c_{ijk}\bar{\Phi}_i(x_1...x_N;\hat{r}_{N+1}\sigma_{N+1})\frac{1}{r_{N+1}}u_{ij}(r_{N+1}) + \sum_j d_{ij}\chi_j(x_j...x_{N+1}). \tag{2.28}$$

Equation 2.28 is known as the close coupling equation. The first and second terms signify the continuum and bound contributions respectively. For a given set of quantum numbers of the system *k*, such as total *L*, *S* and parity Π, the continuum orbital u_{ij} can couple to a target term/level through a certain set of combinations, referred to as channels $\bar{\Phi}_i$. To be specific, the expression $\bar{\Phi}_i$ includes a target term wavefunction as well as the angular momentum factors resulting from recoupling the continuum electron wavefunction. The bound contribution reflects the possibilities in which the incident electron becomes bound to the atom and leads to resonances in the cross sections. The N + 1 Hamiltonian matrix therefore consists of continuum-continuum, continuum-bound, and bound-bound elements. Importantly, the quantum numbers of the continuum electron must be recoupled to those of the target to ensure indistinguishability from the target electrons. The coefficients c_{ijk} and d_{ij} are determined from diagonalization of the N + 1 Hamiltonian.

The result from H_{N+1} diagonalization does not yield a full solution to the scattered electron wavefunction. The integration of Hamiltonian elements is not performed across all radial space, only up to the *R*-matrix box at a. The solution in the inner region is therefore energy-independent up to this point: its full solution as well as the solution outside of the box must be obtained from matching the solutions of each region at the box r = **a**. An additional complication from the truncated integration is that H_{N+1} is not unitary. Its eigenvalues and eigenvectors will therefore not be probability conserving. Full diagonalization is therefore performed on the unitary expression H_{N+1} - $\mathcal{L}$, where

$$\mathcal{L}(a, b_0) = \delta(r-a)\left(\frac{d}{dr} - \frac{b_0}{r}\right) \tag{2.29}$$

is the Bloch operator and b_0 is a arbitrary constant generally set to 0 [64].

The continuum electron in the outer region will not require indistinguishability but will be subject to the long-range multiple potential. Projecting channel *i* onto the total N + 1 wavefunction leads to a solution of the reduced radial wavefunction F_i(r) such that, $\langle\bar{\Phi}_i|\Psi\rangle$ = $\frac{1}{r}F_i$(r), describing the incident and scattered wavefunction. The full N + 1 wavefunction in the outer region will now lack the antisymmetrization $\mathcal{A}$ operator as well as the bound terms:

$$\Psi_{EXT}(x_1, ..., x_N) = \sum_i \bar{\Phi}_i(x_1, ...x_N; \hat{r}_{N+1}\sigma_{N+1})\frac{1}{r^{N+1}}F_i(r_{N+1}) \tag{2.30}$$

From projecting the channels functions onto Ψ_{EXT}, one can derive [60] the following differential equation for F_i(r):

$$\left(\frac{d^2}{dr^2} - \frac{l_i(l_i+1)}{r^2} + \frac{2z}{r} + k_i^2\right)F_i(r) == 2\sum_{\lambda=1}^{\lambda_{max}}\sum_{j=1}^{n}\frac{a_{ij}^{\lambda}}{r^{\lambda+1}}F_j(r) \tag{2.31}$$

where z = Z-N and a_{ij}^{λ} represents the long-range potential coefficients:

$$a_{ij}^{\lambda} = \langle\bar{\Phi}_i|\sum_{m=1}^{N} r_m^{\lambda}P_{\lambda}(cos\theta_{m,N+1})|\bar{\Phi}_j\rangle \tag{2.32}$$

As with the case of a general collision of a radially symmetric potential, cross sections, in this case regarding transitions of the target atom, can be obtained by asymptotically expanding this function to infinity $F_i(r \to \infty)$. These asymptotic conditions will depend on the k_i^2 of the continuum electron of a particular channel. If $k_i^2 < 0$, the channel is said to be *closed*, and its solution will diminish exponentially. Conversely, if $k_i^2 > 0$, the channel is said to be *open*, and its asymptotic solution will be oscillatory.

Obtaining the full outer region solution will require imposing boundary conditions both at infinity and at the *R*-matrix box. Determining the boundary at the box is accomplished via the *R*-matrix. In the preceding discussion on scattering in a radial potential, Green's theorem was used to describe differences between a free particle solution v_l and solution in the presence of a potential u_l. A similar technique can be applied in deriving the *R*-matrix boundary condition.

Given the eigenstates of H_{N+1} diagonalization, ψ_k, the total energy-dependent wavefunction can be written as a superposition of these states at a given energy E:

$$\Psi_{N+1} = \sum_k A_{Ek}\psi_k \tag{2.33}$$

Starting from 2.33 and using the following projection relation, in which () reflects no radial integration performed,

$$(\psi_k|H^{N+1}|\Psi_{N+1}) - (\Psi_{N+1}|H^{N+1}|\psi_k) = (E - E_k)(\psi_k|\Psi_{N+1}), \tag{2.34}$$

one can show [60]:

$$-\frac{1}{2}\sum_i[(w_{ik}|\frac{d^2}{dr^2}|F_i) - (F_i|\frac{d^2}{dr^2}|w_{ik})] = (E - E_k)A_{Ek}. \tag{2.35}$$

Here, the $w_{ik} = \sum_j c_{ijk}u_{ij}$ reflect the eigenvectors from H_{N+1} diagonalization. From Green's theorem and using the boundary conditions for u_{ij}, 2.35 becomes

$$-\frac{1}{2}\sum_i w_{ik}(a)\left(\frac{dF_i}{dr} - \frac{b}{a}F_i\right)_{r=a} = (E - E_k)A_{Ek}. \tag{2.36}$$

Solving for the A_{Ek} coefficients, an expression for F_i(a) can then be obtained:

$$F_i(a) = \sum_j R_{ij}(E)(a\frac{dF_j}{dr} - bF_j)_{r=a}, \tag{2.37}$$

where R_{ij} is finally the shining ***R***-matrix:

$$R_{ij}(E) = \frac{1}{2a}\sum_k \frac{w_{ik}(a)w_{jk}(a)}{E_k - E}. \tag{2.38}$$

E_k represents the eigenvalues from H_{N+1} diagonalization and E the incident electron energy. Upon obtaining the boundary conditions of F_i at r = a and asymptotically expanding the solution, cross sections corresponding to transitions between all of the target states can be obtained relative to the energy of the incident electron. Ionization cross sections can be obtained through a summing of transitions going into a targets pseudostates above the ionization

potential. These discrete states are included in the target structure to account for the continuum, and their inclusion can dramatically increase the size of electron-impact ionization calculations compared to an excitation calculation.

2.4.2 The Basis Set Representation of the Continuum Electron

Knowledge of the continuum electron prior to N + 1 Hamiltonian diagonalization is somewhat limited; however, from the fundamental principles of quantum mechanics, that a solution can be represented by any complete set of states, the problem becomes determining the best complete set for the atomic scattering problem. While, for example a superposition of sine and cosine waves could suffice, an excessively high number of them would be required to converge the solution. Recall that for representing target states, configuration state functions arising from the hydrogenic solution are used. The *R*-matrix basis set u_{ij}, in keeping with the scattering problem, will assume a solution to a scattered particle in the presence of a radially symmetric potential V_0(r). For the RMATRX I codes [60], a further assumption is made that this basis set is mutually orthogonal to each other and to the target bound and pseudo orbitals [60]. They represent solutions of the following:

$$\left(\frac{d^2}{dr^2} - \frac{l_i(l_i+1)}{r^2} - V_0(r) + k_{ij}^2\right) u_{ij}(r) = \sum_{n_b=l_i+1}^{l_i+n_{l_i}} \lambda_{ijn_b} P_{n_b l_i}(r), i = 1, ..., n, j = 1, ..., n_c, \tag{2.39}$$

where k_{ij} represent the eigenvalues and V_0 is represents the static potential of the target, typically in its ground state. A Thomas-Fermi potential for the atom may be used instead [64]. An angular momentum l_i is assumed for each orbital. The right-hand side reflects the use of Lagrange multipliers to orthogonalize to the bound orbitals $P_{n_b l_i}$, where n_b is the total number of bound orbitals, though Gram-Schmidt orthogonalization can be performed instead. The continuum orbitals are subject to the following boundary conditions:

$$u_{ij}(0) = 0 \tag{2.40}$$

and

$$\frac{a}{u_{ij}(a)}\frac{du_{ij}}{dr}|_{r=a} = b \tag{2.41}$$

where b is the same constant, typically set to 0, that was used with the Bloch operator.

The size of the basis set n_c will determine the range of the incident electron energy, relative to the ground state, for which converged cross sections can be obtained. The larger the basis set, the farther in incident energy that the calculation can cover. A common metric for judging the basis set coverage prior to the full calculation is to take 2/3rd of the lowest last energy eigenvalue, relative to each angular momentum l_i, as the farthest the calculation can extend [60].

A practical constraint of the continuum basis set is that a limited number of orbitals are used to represent it, while in reality a complete set representing the continuum would be infinitely large. A correction known as the Buttle correction [73] to the *R*-matrix can account for the continuum orbitals not included. For more complex atoms, heavy configuration mixing is present such that the process of both orthogonalizing to the bound orbitals and applying the Buttle correction is not feasible for larger sets of configurations. The structure used for the tungsten calculation of the present work, for example, was restricted to include only up to n = 11; a solution could not be obtained if including orbitals beyond this such that target optical state, pseudostate, and continuum wavefunction orthogonality could be maintained, in addition to the Buttle correction. In such cases, an orthogonal basis set may not be desirable, and another complete, yet non-orthogonal, basis set still solving Equation 2.39 might prove more effective. One such basis set is the *B*-Spline set [74], which has been used in the past for elements such as neon [75]. Because the *B*-splines form a complete set, no Buttle correction is required. Nevertheless, non-orthogonal methods face the more generalized singular value decomposition of the N + 1 Hamiltonian, rather than eigenvalue decomposition of a Hermitian matrix, and therefore requires more memory at this stage.

2.4.3 Short Description of the Belfast *R*-matrix Suite of Codes

The Belfast *R*-matrix codes can be broken down into four main stages [60], which will be referenced throughout the rest of this work. Below is a description of each in order:

Stage 1: Setting up the continuum basis and calculating the radial integrals

The continuum basis set is calculated using equation 2.39. The orbitals are orthogonalized to each other, the bound orbitals, and the pseudo orbitals. The radial integrals of the target structure, obtained from a prior AUTOSTRUCTURE run, are required as input. All radial integrals to be used for the (N+1) system are also calculated and written to a set of files to be accessed in the next stage. This stage generally runs in no more than an hour depending on the size of the basis set and number of target states.

Stage 2: Calculation of the Target and (N + 1) Hamiltonian Matrix Elements

Both the target and N + 1 Hamiltonians H_N and H_{N+1} are calculated, using both the results from the former and the close-coupling equations for the latter. H_{N+1} is done *per partial wave* N + 1 $LS\Pi$ symmetry. Given that they are symmetric, the N + 1 Hamiltonians are stored as their upper triangles, and they include the continuum-continuum, bound-continuum, and bound-bound elements resulting from the inner product of the close-coupling equation.

Stage 3: Diagonalization of the Inner Region N + 1 Hamiltonian

The N + 1 Hamiltonian, with the inclusion of the Bloch operator, of each partial wave is diagonalized separately using ScaLAPACK's parallel divide and conquer algorithm PDSYEVD [76]. The eigenvalues and eigenvectors are stored.

Stage f: R-matrix (Matrix-Matrix Multiplication) to Solve the Outer Region

The outer region is solved, using the *R*-matrix to determine $F_i(a)$. Cross sections for all possible target transitions over a set of user-supplied energy points are obtained.

The *R*-matrix method thus generates fundamental atomic data describing the general cases of electron-impact, as well as photoionization. These atomic processes are used in modeling codes that determine the resultant spectrum of a plasma. To bridge the gap between singular processes and spectra, an understanding of these processes given an overall population of electrons will be required, detailed in Section 2.6.

2.5 Sampson Branching Ratios for Configuration-Averaged, *LS*, and *LSJ* Rates

In certain cases, such as for electron-impact ionization of heavy elements, in which *LSJ*-resolution of both the structure and atomic processes is appropriate, performing the full non-perturbative calculation in *LSJ*-resolution might yield relatively small gains in accuracy. Unlike electron-impact excitation, with which we are concerned with fine structure and elucidating the N + 1 resonances, electron-impact ionization cross sections are much coarser, having been summed over all pseudostates above the ionization potential. To avoid unnecessary computational burden, performing a configuration-averaged or *LS*-resolved calculation might be more desirable.

Sampson [77] derive formulas for calculating branching ratios, in order to convert a configuration-averaged cross section into a set of constituent *LSJ*- or *LS*-resolved cross sections, arising from the target configuration. For example, an ionization cross section of the $3s$ from the neutral neon $2p^5 3s$ configuration can be split into separate cross sections for each possible *LSJ* level: ${}^3P_{0,1,2}$ and ${}^1P_1$. In contrast with a classical statistical weighting of each unique *LS* or *LSJ* state, these branching ratios are derived from the wavefunctions used to represent the collision and from angular algebra. They are thus distinctly quantum mechanical. If statistically-weighted, all the degenerate states, e.g. $(2S+1)(2L+1)$ total for a given *LS* term, contribute the same to the configuration-averaged cross section σ_{CA} such that,

$$\sigma_{LS_i} = \frac{(2S_i+1)(2L_i+1)}{\sum_i (2S_i+1)(2L_i+1)} \times \sigma_{CA} \tag{2.42}$$

where the sum is over all of the *LS* states. A similar expression can be obtained from *LSJ*-multiplicity.

In discussing the Sampson branching ratios, and for many other discussions to follow, reference will be made to a quantity known as the *collision strength* Ω_{ij} representing a transition from i to j:

$$\Omega_{ij} = \frac{g_i E(Ry)}{\pi a_0^2} \sigma_{ij} \tag{2.43}$$

where a_0 is the Bohr radius, g_i the statistical weight of i, $E(Ry)$ the incident electron energy in Rydbergs, and σ_{ij} the corresponding cross section. This quantity can be useful for integration of cross sections to yield rate coefficients [78], as discussed in the next section. Whereas excitation cross sections exhibit a sharp peak followed by a sharp decrease, collision strengths are slowly varying, often flat, over the incident energy range. The collision strength carries an additional meaning as a ratio between the cross section and the square of the de Broglie wavelength of the relative motion of the collision [78].

Derivation of the branching ratios involves using angular algebra to manipulate the collision wavefunctions. These wavefunctions formulate the reactance matrix R, similar to Equation 2.18. R includes both direct and exchange effects R^d and R^e, such that $R = R^d - R^e$, though Sampson shows the exchange effects do not affect the final branching ratios [77]. The direct part of the reactance matrix can be calculated through,

$$\begin{aligned} ZR^d(\beta_t J_t k l j J; \beta_t' J_t' k' l' j' J) = 2 \sum_{M_t, m, M_t', m'} & C(J_t j M_t m; JM) C(J_t' j' M_t' m'; JM) \\ & \times \int dx_1 \int dx_2 \cdots \int x_{N+1} \Psi_{\beta_t J_t M_t} * (x_i^{-1}) u_{kljm} * (x_i) \\ & \times (\sum_{q(\neq i)} \frac{1}{r_{qi}}) \Psi_{\beta_t' J_t' M_t'} (x_i^{-1}) u_{k'l'j'm'} (x_i) \end{aligned} \tag{2.44}$$

where Z is the atomic number ;J_t, j, and J are the angular momenta of the target ion, incoming electron, and total system respectively; β_t is any additional angular momentum quantum numbers of the target ion; k and l are the wavenumber orbital angular momentum quantum number of the impact electron respectively; and the C's are Clebsch Gordon coefficients. The primes designate quantum numbers after the collision has occurred. Psi and u represent the target and

continuum wavefunctions respectively, integrated over the coordinates x_i of all N + 1 electrons. The reactance matrix can be related to the cross section through

$$Z^2\Omega_{ij}(\beta_t J_t - \beta'_t J'_t) = 2\sum_J (2J+1) \sum_{l,l',j,j'} |ZR|^2. \tag{2.45}$$

Formulas for the branching ratios can then be obtained from angular algebra manipulations of the wavefunctions in Equation 2.44, inserted back into Equation 2.45. These manipulations themselves are exact; however, the wavefunctions are assumed to be hydrogenic or by extension configuration-averaged. Two shortcomings result from the above formalism, however. First, the accuracy of both the target structure and resultant cross sections will depend on the accuracy of the wavefunctions corresponding to the original cross section for the particular collision. The branching ratios would not account for atomic processes of higher angular momentum resolution, such as spin-orbit interaction, in either the target ion or the collisional Hamiltonians. Another problem is that the branching ratios assume only one hydrogen-like or configuration-averaged wavefunction; configuration mixing is not considered. The following equation denotes conversion of a configuration-averaged cross section of an active subshell $Q(n_a l_a j_a - n'_a l'_a j'_a)$ into *LSJ*-resolution via branching ratios:

$$\begin{aligned}
&\sum_{J'_a} Q(n_a l_a^w \alpha_a S_a L_a J_a - n_a l_a^{w-1} \alpha''_a S''_a L''_a J''_a n'_a l'_a j'_a J'_a) \\
&= \begin{bmatrix} l_a & L''_l & L_l \\ L_{l-1} & L_a & L''_a \end{bmatrix} \begin{bmatrix} \frac{1}{2} & S''_l & S_l \\ S_{l-1} & S_a & S''_a \end{bmatrix} \\
&\times w[(l_a^{w-1}\alpha''_a S''_a L''_a|\}l_a^w \alpha_a S_a L_a)]^2 \times \sum_{j_a} (2S_a+1)(2L_a+1)(2J''_a+1)(2j_a+1) \\
&\times \begin{bmatrix} S''_a & L''_a & J''_a \\ \frac{1}{2} & l_a & j_a \\ S_a & L_a & J_a \end{bmatrix}^2 Q(n_a l_a j_a - n'_a l'_a j'_a)
\end{aligned} \tag{2.46}$$

The primes denote final states of both the scattered electron and the target ion, whose quantum numbers are denoted by the subscript a. The target subshell in losing an electron changes from

l_a^w to l_a^{w-1}. The sum over J_a' on the left-hand side is thus over the total final angular momentum of both the l_a^{w-1} subshell, $J_a'' = L_a'' + S_a''$ and the ionized electron $j_a = l_a + 1/2$. The first two bracketed terms and the last bracketed term on the right-hand side are known as $6-j$ and $9-j$ symbols, to account for recoupling of three and four angular momentum quantum numbers respectively. The $6-j$ symbols are not included in the original Sampson formulation [77], in which hydrogen orbitals with effective atomic numbers are used, but the symbols are needed for configuration-averaged cross sections in which the angular momentum quantum numbers of the ionized electron must be recoupled out from the active subshell's quantum numbers. The $9-j$ symbol reflects recoupling of S_a'', L_a'', s_a, and l_a for a total target angular momentum J_a. The term $[(l_a^{w-1}\alpha_a'' S_a'' L_a''|\}l_a^w \alpha_a S_a L_a)]$, known as a coefficient of fractional parentage, accounts for the number of ways, here the double primed quantum numbers, that l_a^{w-1} can be recoupled up to l_a^w. Through summing over the possible total angular momenta of the ionized electron and shell, the following branching ratio formula for an *LS*-resolved cross section can be obtained:

$$\sum_{J_a', j_a', J_a''} Q(n_a l_a^w \alpha_a S_a L_a J_a - n_a l_a^{w-1} \alpha_a'' S_a'' L_a'' J_a'' n_a' l_a' j_a' J_a') = w[(l_a^{w-1}\alpha_a'' S_a'' L_a''|\}l_a^w \alpha_a S_a L_a)]^2 \times Q(n_a l_a^w \alpha_a S_a L_a - n_a l_a^{w-1} \alpha_a'' S_a'' L_a'' n_a' l_a') \tag{2.47}$$

In the present work, *LS*-resolved electron-impact ionization cross sections for both neutral neon and tungsten needed to be converted to *LSJ*-resolved cross sections, having to convert back to configuration-averaged cross sections via statistical weights. A modification of the Sampson branching ratios [77] to attain *LSJ* resolution from the *LS*-resolved ionization cross sections was derived. For an *LS*-resolved *R*-matrix with pseudostates calculation, the pseudostates with energy E above the ionization potential IP are summed:

$$Q(nl^w LS - nl^{w-1} L'' S'') = \sum_{n'l'L'S'} Q(nl^w LS - n'l'^{w-1} L'' S'' n'l'L'S') \qquad (\mathrm{E} > \mathrm{IP})$$

Recoupling to *LSJ* leads to the following relation:

$$
\begin{aligned}
Q(nljLSJ - nlj^{w-1}L''S''J'') = &\begin{bmatrix} l_a & L''_l & L_l \\ L_{l-1} & L_a & L''_a \end{bmatrix} \begin{bmatrix} \frac{1}{2} & S''_l & S_l \\ S_{l-1} & S_a & S''_a \end{bmatrix} \\
&\times \sum_{j_a} (2S_a+1)(2L_a+1)(2J''_a+1)(2j_a+1) \\
&\times \begin{bmatrix} S''_a & L''_a & J''_a \\ \frac{1}{2} & l_a & j_a \\ S_a & L_a & J_a \end{bmatrix}^2 Q(nlLS - nl^{w-1}L''S'')
\end{aligned} \tag{2.48}
$$

Importantly, this *LSJ*-resolution for ionization of an N-electron target requires that the N - 1 ion also be in *LSJ* and also that the *LS* state of the final N - 1 ion is known.

2.6 Generalized Collisional Radiative Modeling

To bridge the gap between the quantum mechanics of the atomic collisions and what we are able to measure, i.e., the spectrum, we need an understanding of the fundamental collisional processes given a population of electrons and their dynamics in a plasma environment. That is, we must first calculate rate coefficients from the cross sections atomic processes over a range of electron temperatures. From these rate coefficients, we can then account for the expected simultaneous rates of atomic and collisional processes through Generalized Collisional Radiative modeling, described in detail in [79].

The rate coefficients are generated from a combination of the fundamental atomic data, i.e., cross sections for each atomic process, and also from assuming an energy distribution function of the free-electrons in the plasma. In general, a Maxwellian electron-distribution function is assumed, given by

$$
f_{T_e}(E) = \frac{1}{kT_e} \frac{2}{\sqrt{\pi}} \left(\frac{E}{kT_e} \right)^{1/2} exp\left(-\frac{E}{kT_e} \right). \tag{2.49}
$$

The Maxwellian assumption depends on certain criteria regarding the magnitude of the timescales τ of the plasma, collisional, and atomic processes, namely the following [80]:

$$\tau_P \approx \tau_m \approx \tau_{ion} \gg \tau_O \gg \tau_{ee}. \tag{2.50}$$

τ_P represents the timescale for plasma dynamics (e.g., temperature fluctions, edge localized modes). It is roughly of the same magnitude as τ_m and τ_{ion}, the "metastable" and ionization time scales respectively (which are determined by collisional ionization and recombination time-scales). The populations of excited states will in general radiatively decay down to a lower state faster than can be populated and will therefore reach steady-state in a shorter timescale, τ_O. The term "metastable" refers to atomic states that require a longer time scale to reach steady state. These states might be the result of forbidden transitions to populated states. For example, neutral tungsten's metastable $5d^5 6s$ ($^7S_3$) state is both close to the ground state energy and also forbidden to the ground $5d^4 6s^2$ ($^5D_0$) from $\Delta J = 0$, thus its only radiative decay is relatively slow, leading to long equilibrium time-scales.. A greater mathematical distinction between metastable and excited states with regards to the rates will be made in the generalized collisional-radiative modeling discussion. Discussions on metastable states often implicitly include the ground state as well, as it is on the same timescale. Free-electron thermalization, related to the electron distribution function, is assumed the smallest timescale, τ_e. *If τ_e is in fact of the order of the plasma τ_P, then the Maxwellian distribution function is no longer valid.*

If a cross section is quantifying the probability of each transition given collision with a single electron, the rate coefficient is providing a statistical account of how often the transition occurs given a distribution of electrons. To generate rate coefficients from cross sections, cross sections can be converted into effective collision strengths, given by

$$\Upsilon_{i\to f}(T_e) = \int_0^\infty w_i \frac{\epsilon_i}{I_H} \frac{\sigma_{i\to f}}{\pi a_0^2} e^{-(\frac{\epsilon_f}{kT_e})} d\left(\frac{\epsilon_f}{kT_e}\right) \tag{2.51}$$

for a Maxwellian electron distribution. $\sigma_{i\to f}$ is the cross section from state i to f, T_e the temperature (eV), ϵ_i the incident electron energy, and I_H the binding energy of hydrogen, 13.606 eV. The effective collision strength arises from integrating the collision strength from Equation 2.43 over ϵ_i/kT_e. As discussed in the previous section, integrating over the collision strength

can provide greater numerical stability than over a cross section. Electron-impact excitation rate coefficients can then be calculated through

$$q_{i\to f}(T_e) = 2\sqrt{\pi}\alpha c a_0^2 \frac{1}{w_f}\frac{I_H}{kT_e}\Upsilon_{i\to f}(T_e) \tag{2.52}$$

where α the fine structure constant is $\frac{1}{137}$ and c the speed of light. For the ionization rate coefficients from cross sections $\sigma_{i\to\gamma^+}$,

$$S_{i\to\gamma^+}(T_e) = \frac{2\alpha c}{\sqrt{\pi}}\left(\frac{1}{I_H}\right)^{\frac{1}{2}}\left(\frac{1}{kT_e}\right)^{3/2}\int_{I_p}^{\infty}\epsilon_i\sigma_{i\to\gamma^+}e^{-\frac{\epsilon_i}{kT_e}}\,d\epsilon_i \tag{2.53}$$

Three other atomic processes have so far been neglected for which rate coefficients can be obtained: radiative, dielectric, and three-body recombination. All involve a state in which the incident electron is captured. In radiative recombination, the electron remains captured, and a photon is released:

$$\mathcal{A}^{z+1}(\rho) + e(\epsilon_i) \to \mathcal{A}^{z}(\gamma) + e(\epsilon\text{`}) \to \mathcal{A}^{z+}(i) + h\tilde{v} \tag{2.54}$$

A photon is similarly ejected for dielectric recombination, but an additional resonance step of the atom-electron system results in one of the electrons of the atom being promoted:

$$\mathcal{A}^{z+1}(\rho) + e(\epsilon_i) \to \mathcal{A}^{z+}(\rho' nl) \to \mathcal{A}^{z+}(\rho nl) + h\tilde{v}_{\rho'\to\rho} \tag{2.55}$$

In three-body recombination, two electrons collide with the atom, one of which is captured. This recombination is therefore the reverse process of electron-impact ionization:

$$\mathcal{A}^{(z+1)+}(\gamma) + e(\epsilon') + e(\epsilon\text{"}) \to \mathcal{A}^{z+}(i) + e(\epsilon) \tag{2.56}$$

Rate coefficients can be derived for these processes as well, found in [80]. Other atomic processes exist, described in [79], but that will be neglected for present purposes of fusion plasmas. Ion-ion collisions can also cause excitation and ionization. In charge exchange, an

electron or electrons are transferred from one ion to another. In more optically dense plasmas, photo-excitation and ionization, i.e, from photons, can also occur.

The change in population density of each level with respect to time will thus depend on the collection of radiative, excitation, ionization, and recombination rates either transitioning into or out of the level, as in the following equation:

$$\begin{aligned}\frac{dN_i}{dt} &= \Sigma_\gamma N_\mathrm{e} N_\gamma^+ (\alpha^{(r)}_{\gamma\to i} + \alpha^{(d)}_{\gamma\to i} + N_\mathrm{e}\alpha^{(3)}_{\gamma\to i}) + \Sigma_{j<i} N_j N_\mathrm{e} q_{j\to i} \\ &+\Sigma_{j>i} N_j (N_\mathrm{e} q_{j\to i} + A_{j\to i}) \\ &-N_i[\Sigma_{j<i}(N_\mathrm{e} q_{i\to j} + A_{i\to j}) + \Sigma_\gamma N_\mathrm{e} S_{i\to\gamma}]\end{aligned} \tag{2.57}$$

where N_e is the total electron population, and N and N^+ are the populations of the current z+ and z+1 ion states. The equation, in which each term is a population density *rate*, reflects spontaneous radiative decay A_{ij} from a higher level or down to a lower level; excitation q_{ij} into or out of the level; ionization $S_{i\to\gamma}$ out of a level; and radiative $\alpha^{(r)}_{\gamma\to i}$, dielectric $\alpha^{(d)}_{\gamma\to i}$, and three-body $\alpha^{(3)}_{\gamma\to i}$ recombination into a level.

Collisional-radiative theory, first outlined in [81], describes the basic method of modeling ion populations in plasmas given the rates of atomic processes in 2.57. Without making any assumptions, the level populations would be solved from the system of rate equations. The rates of these atomic processes can be described via a matrix, C_{ij}, whose elements represent the sum of the different rates from level i to level j. This system of equations is Markovian: the level populations depend only on the previous time step. So, given an initial population, perhaps every atom in the ground state for example, one can examine the evolution of the populations over time. A steady-state solution would correspond to solving the eigenvalue problem for the C_{ij} matrix.

The solutions to the collisional-radiative matrix can depend heavily on both electron temperature and density, and various approximations can be made, particularly for low or high densities. In low-density plasmas, electron-impact collisions causing transitions between excited states occur much less frequently, causing the bulk of the atom population to remain in the

ground state. Accordingly, the *coronal approximation* for low-density plasmas assumes only collisional excitation from the ground can populate the excited states and only spontaneous emission from those states can depopulate them:

$$\frac{dN_i}{dt} = N_e N_1 q_{1\to i} - N_i \sum_j A_{i\to j}. \tag{2.58}$$

For high electron density plasmas, the populations are in *local thermodynamic equilibrium*, in which case the levels populations do not change, i.e., $dN_i/dt = 0$. The levels are thus statistically populated according to the electron temperature.

In other cases, within the *collisional-radiative* density region, the *quasi-static* approximation can be used. In the collision-radiative theory first proposed in [81], all of the levels except the ground state considered to be in steady state. The rate of change of the population of each level dN_i/dt besides the ground state is therefore set to 0. This approximation is in accordance with the timescales discussed earlier.

In *Generalized* Collisional Radiative (GCR) theory, proposed in [82], the longer-lived metastable levels are also assumed not to be in steady state. Starting with the C_{ij} collisional radiative matrix, separate expressions for the metastable and for the excited state populations can be derived from the elements of C_{ij}. The excited state populations can be solved directly, while the metastable state populations must either be propagated through time or solved for at steady state.

Solving the GCR matrix can reveal larger trends in how atomic processes are driving the level populations. An effective ionization rate $\mathcal{S}_{\beta\to\gamma}$, or SCD, from a ground or metastable state can be obtained:

$$\mathcal{S}_{\beta\to\gamma} = S_{\beta\to\gamma} - \Sigma_j S_{j\to\gamma} \Sigma_{j'} (C^z_{jj'})^{-1} C^z_{j'\beta} \tag{2.59}$$

This rates includes both direct ionization from the ground (or metastable) as well as through the intermediary excited states. A photon emissivity coefficient, or PEC, proportional to the spectral line intensity I for a transition from level i to j can be obtained,

$$PEC_{\sigma,(j\to i)} = A_{j\to i}\frac{N_j}{N^\sigma} \tag{2.60}$$

where σ designates a metastable level and N^σ its population. If there are no metastables other than the ground, the denominator would reflect the overall ion population N^z. In the general case of metastables, N^z will correspond to the sum of all of the metastable populations. The intensity of a spectral line will correspondingly be the total light emitted as a result of a transition, given the ion's total population:

$$I = \frac{\Sigma_\sigma PEC_{j\to i}N^\sigma}{\Sigma_\sigma N^\sigma}, \tag{2.61}$$

The PEC therefore reflects how often a spontaneous emission transition will occur, relative to the upper level's population ratio to the overall ion population N^z. A spectrum can then be obtained from the collection of PECs over a wavelength range, with the spectral lines being of heights relative to each other. Both the PEC and SCD depend on electron temperature and density. An important application of collisional-radiative modeling is therefore line ratio diagnostics: determining the electron temperature and density of a plasma given a set of line ratios that are sensitive to different electron temperatures and densities.

Of particular interest for tungsten is the ratio of the SCD and PEC: the S/XB. This ratio was originally proposed as a diagnostic for plasma surface erosion in [21]. The diagnostic assumes that all of the material eroded from a surface becomes ionized. The total erosion flux Γ therefore obeys the following relation to the SCD:

$$\Gamma = \int_0^\infty n_e N^z \mathcal{S}_{z\to z+1} dx \tag{2.62}$$

From some mathematical reimagining on the right-hand side, the equation can be written,

$$\Gamma = \int_0^\infty n_e \frac{\mathcal{S}_{z\to z+1}}{PEC_{j\to i}}(PEC_{j\to i}\times N^z)dx. \tag{2.63}$$

From Equation 2.61 and from the expression for the S/XB,

$$SXB^z_{j\to i} = \frac{\mathcal{S}_{z\to z+1}}{PEC_{j\to i}}, \tag{2.64}$$

Equation 2.63 becomes,

$$\Gamma = \int_0^\infty n_e SXB^z_{j\to i} I dx. \tag{2.65}$$

In other words, the erosion rate from a plasma surface material can be determined from the S/XB and measured spectral line of a transition $j \to i$. If more than one metastable is present, than both the SCD and PEC must be metastable-resolved. As discussed in the introduction chapter, the work of Beigman *et al.* suggests that the S/XB for the neutral tungsten 400.88 nm line is highly sensitive to metastable populations, in which case metastable resolution will be required.

Problems in accurate modeling the SCD, PEC, and, by extension, the S/XB, can come from 1) their temperature and density dependence, 2) how many metastable states are included, 3) how much ionization from excited states is included, and 4) the accuracy of the atomic data. These problems will be delineated further in the next two chapters and observed for both neutral neon and tungsten.

2.7 Conclusions

An overview of theoretical atomic physics, from atomic structure to generating a spectrum has been provided. For both neutral tungsten and neon, we are ultimately interested in understanding the relationship between an observed spectrum and the underlying atomic processes of the plasma. Atomic structures can be calculated with codes such as AUTOSTRUCTURE [83], which use configuration-state functions as building blocks for more complex terms. From the self-consistent field approximation and the variational principle, a series of *LS*-resolved terms or *LSJ*-resolved levels, *jK*-resolved for relativistic structures, are calculated, corresponding to a set of radial orbital solutions. This structure also results in a set of oscillator strengths, each quantifying the spontaneous emission rate between two levels. The atomic structure can then

be used in programs such as the Belfast *R*-matrix suite of codes [60] to determine electron-impact and/or photoionization and photoexcitation cross sections. Cross sections can then be converted into rate coefficients corresponding to the likelihood of an atomic process, given an energy distribution of electrons in the plasma. Level and ion populations can then found through generalized collisional-radiative modeling with the set of rate equations describing the set of atomic processes going into and out of a level. The ADAS suite of codes [36] or the recently developed ColRadPy [84] can be used for GCR modeling. In the next two chapters we will describe work on Ne (Chapter 3) and then on W (Chapter 4) that goes from cross sections through to quantities used in plasma modeling.

Chapter 3

Generating Accurate Neutral Neon Atomic Data using Electron-Impact Excitation and Ionization R-matrix Calculations

For its applications in the W7-X stellerator divertor [47] and as a benchmark for excited-state ionization in higher Z elements, the following study was performed regarding the electron-impact excitation and ionization of neutral neon along with a generalized collisional-radiative treatment of its effective ionization rate. When impurity transport codes track the charge state balance for an element in a plasma, they use 'effective ionization' rate coefficients. These coefficients include all of the ways that electrons can ionize from one charge state to the next. Historically, there has been a focus on calculating and measuring ground state ionization cross sections. However, it is now well known that the excited states can contribute significantly to the total ionization for a charge state, particularly for near neutral systems. This has been shown in H [85], He [37], Li [38], B [39]. Thus, an important topic in this chapter will be to use the atomic data that is generated to investigate the role of excited state ionization on the total ionization of neutral neon at different plasma conditions.

An overview of previous electron-impact excitation and ionization calculations for neutral neon is provided in Section 3.1. The new structure and electron-impact calculations are described in detail in Section 3.2. The electron-impact excitation and ionization cross sections and rate coefficients resulting from the new RMPS calculations are presented in Sections 3.3 and 3.4 respectively and are compared with previous results. Various checks of convergence of the calculation are also given. Finally, the results from GCR modeling with the new cross section data and the role of excited state ionization are presented in Section 3.5.

3.1 Literature Review of Neutral Neon Collisional Data

3.1.1 Review of the electron-impact excitation of neutral neon

Previous studies, particularly by Zatsarinny and Bartschat, have investigated the disagreement between the theoretical calculations and measurements of neutral neon electron-impact collisions [52]. Zatsarinny and Bartschat attributed a major source of this discrepancy, especially in the 20 to 40 eV range, to an undervaluing of the number of pseudostates to accurately reflect intermediate coupling to the continuum [52]. For their excitation calculation, the most recent, they utilize the non-orthogonal B-Spline R-matrix (BSR) method [74] for configurations 2p^{5}3s, $2p^5 3p$, and $2p^5 3d$, spanning an incident electron energy range from the threshold to 300 eV and representing 457 states, 87 bound and 370 in the ionization continuum, henceforth referred to as BSR-457. This calculation builds upon their previous LS-resolved one [56] by employing the semirelativistic Breit-Pauli approximation and jK-coupling. Their energy levels differ by less than 0.2 eV from those listed in NIST [86].

Aside from Zatsarinny and Bartschat, the most large-scale electron-impact excitation calculation of neutral neon was performed by Ballance and Griffin [58], whose Breit-Pauli calculation's bound states cover from $2p^5 3s$ to $2p^5 4f$, and for $2p^5 5s$ and $2p^5 5p$. Their pseudostates include $2p^5\ \bar{5d}$; $2p^5\ \bar{5f}$; $2p^5 \bar{nl}$, as well as from $\bar{n}$ = 6 to $\bar{n}$ = 8 and $\bar{l}$ = 0 to $\bar{l}$ = 3; $2p^5 \bar{9s}$; $2p^5 \bar{9p}$; and $2p^5 \bar{10s}$. 235 levels were thus included, 79 of which were spectroscopic, 28 bound and 128 continuum pseudostates. Their results at the time did not converge due to a lack of computational power. Ballance and Griffin also performed nonrelativistic, LS-coupled calculations with pseudostates to illustrate the effect of adding pseudostates, the most extensive of these calculations having pseudostates with valence orbitals spanning from $\bar{n}$ = 6 to $\bar{n}$ = 12.

Other calculations obtained excitation cross sections from the ground to bound spectroscopic states up through n = 3 [87, 88]. Similar to Ballance and Griffin [58], these calculations incurred computational limitations of the time. Further, they did not fully match experimental measurements beyond the $3s$ cross section, nor have any experiments measured excitations past $2p^5 3p$ [52, 89]. Zatsarinny and Bartschat made comparison cross sections of their BSR-457 and

BSR-31 with that of Ballance and Griffins' unconverged calculation and of Chilton *et al.*'s measurements in the 20 to 100 eV range for the $3p$ states [52]. Though the BSR-457 calculation agrees for the $3s$ cross section, it falls below Chilton's and outside of the error bar range; yet, Ballance and Griffins' limited calculation appears to agree with Chilton *et al.* Zatsarinny and Bartschat [52] and Ballance and Griffin [58] include the only available ground to $3d$ excitation cross section calculations, and the two do not match.

Hoshino *et al.* [90] recently measured cross sections for the electron-impact excitation from ground into the $3s[3/2]_1$ and $3s'[1/2]_1$ states using incident energies from 20 to 300 eV, and BSR-457 fell within their uncertainty [90]. Other measurements from [88,91–93] are either partially or completely above Hoshino *et al.*'s and Zatsarinny and Bartschats' cross sections in the 20 to 100 eV region at and after the ionization limit [52,90]. Suzuki *et al.* [94] and Allan *et al.* [95], who make measurements above 300 eV and around the threshold respectively, match both Hoshino *et al.* and BSR-457.

Hoshino *et al.* thus help clarify the discrepancy in that previous measurements fall somewhere in between calculations with and without pseudostates for the $3s$ cross sections. Zatsarinny and Bartschat compare their pseudostate-inclusive BSR-457 angle-integrated cross section with recent experiments [88, 92, 94], as well as to one of their previous calculations of 31 states that lacked continuum coupling, BSR-31 [75], and to a simple 5-state BSR calculation [52]. The cross sections without pseudostates exhibit a large peak, BSR-5 greater than BSR-31, not seen experimentally in the 20 to 40 eV range, while the 457-state cross sections lack this extra peak [52]. Previous measurements typically fall in between BSR-457 and BSR-31 [52,90], but the measurements of Hoshino *et al.* agree well with BSR-457 [90].

Other experimental benchmarks include an angle-integrated cross section by Chilton *et al.* [89] measuring the electron-impact excitation from the ground state to the $2p^5 3s$ levels with an incident energy range from 0 to 200 eV. Boffard *et al.* [96] reports the integrated cross section from the metastable $2p^5 3s$ state to a few of the $2p^5 3p$ levels from 0 to 450 eV. Khakoo *et al.* [88] offer an integrated cross section in the range 0 to 400 eV that has been compiled to include their measurements as well as those of Register et al. [93] and Kanik *et al.* [91] from the ground state to the $2p^5 3s$ levels.

A converged semi-relativistic Breit-Pauli calculation including pseudostates both below and above the ionization threshold and similar to that of Griffin and Ballance can thus provide a more complete, accurate picture of the electron-impact excitation of neutral neon beyond the $3s$ valence shell, with previous measurements and calculations serving as benchmarks. Reliable rate coefficients can then be derived from the resultant cross sections, and this is the aim of the work in this chapter.

3.1.2 Review of the electron-impact ionization of neutral neon

Past work determining the cross sections of the electron-impact ionization of neutral neon has been fruitful overall, particularly with the use of programs that account for the large continuum coupling effect of neutral atoms, though cross sections are missing for states beyond $2p^5 3s$, $4s$, and $5s$ that, as will be shown, have a significant impact on the effective ionization rate ceofficient [55].

In neutral atoms, the force of attraction to the nucleus for each electron is of the same order as the force from the other electrons. Thus, the coupling terms from the electron coulomb repulsions should have a higher impact on the dynamics of neutral collisions compared to those involving ions. This coupling can also occur between electrons in spectroscopic orbitals and electrons in the continuum. As previously mentioned, Ballance and Griffin [58] demonstrated the effect of continuum coupling through a comparison of an R-matrix calculation for neutral neon both with and without pseudostates. The pseudostates play a further role in accounting for ionization; that is, the transitions are summed whose upper energies are above the ionization threshold. Convergence of ionization cross sections therefore requires that enough pseudostates be present to account for all electron transitions into the continuum.

Previous theoretical work has focused on the electron-impact ionization from the ground state [53–56] and the $3s$ [56, 57], $4s$ [55], and $5s$ [55] excited state orbitals. The most recent and complete calculation, also by Zatsarinny and Bartschat [56] and which employs the same BSR with pseudostates method as their excitation calculation, is LS-resolved and includes 679 terms, 55 bound and 624 above the ionization threshold, covering the 0.1 to 200 eV energy range with the pseudostates reaching 85 eV. Partial waves extended to L = 25, and a top-up

approximation was used to account for the contributions of higher angular momenta. Zatsarinny and Bartschat provide integrated cross sections for ionization from the $2s^2 2p^6(^1S)$ ground state and the $2p^5 3s(^3P)$ configurations. Ballance *et al.* (2009) performed an LS-resolved BPRM calculation of the ground state, $2p^5 3s$, $2p^5 4s$, and $2p^5 5s$ configurations, over energy ranges of 0 to 100 eV for the ground-state ionization and 0 to 45 eV for the excited-state ionization [55]. The ground-state ionization converged by L = 9, while the excited-state ionizations' partial waves extended to L = 21, and a top-up approximation was also used [55]. Their pseudostate range included $2p^5\ \bar{n}\bar{l}$ and $2s2p^6\ \bar{n}\bar{l}$ configurations from $\bar{n}\bar{l}$ = $5\bar{d}$ to $16\bar{g}$.

Theoretical calculations mostly agree with measurements, though a slight discrepancy exists between Zatsarinny and Bartschat [56] and Ballance *et al.* [57] The BSR-679 cross section of [56] lies below all of the measurements [97, 98] in the roughly 30-130 eV energy range but matches the most recent experiment by Rejoub *et al.* [97] from 130-200 eV [56]. Yet, the cross section of Ballance *et al.* [57] matches Krishnakumar and Srivastava [98] but is slightly higher than Rejoub *et al.* for all energies [55]. The $2p^5 3s(^3P)$ ionization cross sections agree between BSR-679, that of Ballance *et al.* [57], and the measurements of Johnston *et al.* [99].

Aside from the ground and the $2p^5 3s$, $4s$, and $5s$ states, no data could be found in the literature for ionization cross sections from other excited states. We seek both to verify the existing excited-state ionization cross sections and to provide new converged cross sections from the ionization of excited states through $2p^5 5p$.

3.2 Description of New Neutral Neon Structure and *R*-Matrix Calculations

3.2.1 Neutral neon atomic structure calculations

Badnell [83] describes in detail the program AUTOSTRUCTURE that we used to create the atomic structure for this paper. This program utilizes the Thomas-Fermi-Dirac-Amaldi (TFDA) statistical potential for the spectroscopic orbitals. The $2p$ orbital was modified with a scaling parameter to give good agreement with experimental energies [86]. For both the electron-impact excitation and ionization models, configurations included the $2p^6$, $2p^5 nl$, and $2s2p^6 nl$ series. The target structures were each composed of twelve optical orbitals, up to 5p. Laguerre

pseudo-orbitals were used for the remaining orbitals, extending to $\bar{n}$ = 12 and $\bar{l}$ = 4 and to $\bar{n}$ = 12 and $\bar{l}$ = 6 for the electron-impact excitation and ionization models respectively.

The structure used for the electron-impact excitation calculation, which included intermediate coupling, yielded 633 *jK*-resolved levels from 337 *LS* terms. As will be discussed in the next section, 233 of these levels were removed from the calculation before *LS*-*jK* recoupling, leaving 400 levels for the N + 1 Hamiltonian diagonalization. A comparison of our energy levels to those of NIST [86] can be found in Table 3.2.1. All energy levels agree within 0.3 percent, and A-values had an average of 27 percent difference to those available on NIST. The electron-impact ionization calculation used the same base structure but without intermediate coupling and including more pseudostates, from $\bar{5}d$ through $\bar{n}$ = 12, $\bar{l}$ = 6, resulting in 545 *LS* terms.

31 and 24 continuum orbitals were used to represent the scattering electron for the excitation and ionization respectively. These sizes were chosen to make the energy ranges of each calculation as large as possible while still fitting within computational constraints. The ionization incident energy range extended past the excited-state ionization peaks, about 20 eV for the $3s$ metastable, enabling an accurate fit of the cross sections for higher energies. To ensure accurate spectral modeling, we compared the calculated oscillator strengths to those from the B-spline method [100] and NIST values [86] for dipole transitions to the ground state, as shown in Table 3.2.

3.2.2 Scattering calculations

We perform a similar semi-relativistic Breit-Pauli RMPS (BPRM) calculation to that of Ballance and Griffin [58] for the electron-impact excitation cross sections, but with additional pseudostates extending to $\bar{l}$ = 6. A parallel BPRM suite [58] was used that is based on modified versions of the RMATRX I suite [60, 72]. Similar to the standard R-matrix, the BPRM breaks apart the collision into an inner and outer region. The two regions are divided by a box of radius 74 atomic units for the present calculations. The inner region assumes that the continuum electron is indistinguishable from the target N electrons, the N + 1 basis set describable by the close coupling equations [64]. The Breit-Pauli N + 1 Hamiltonian includes

Table 3.1: Atomic structure NIST comparison to first 40 levels.

Configuration	Term	J-Value	NIST Energy (eV)	Theoretical Energy (eV)	Percent Difference
$2s2.2p6$	$1S$	0	0	0	0
$2s2.2p5.(2P*<3/2>).3s$	2[3/2]*	2	16.619	16.607	0.07
		1	16.671	16.675	0.02
$2s2.2p5.(2P*<1/2>).3s$	2[1/2]*	0	16.716	16.729	0.08
		1	16.848	16.946	0.58
$2s2.2p5.(2P*<3/2>).3p$	2[1/2]	1	18.382	18.324	0.32
		0	18.712	18.527	0.99
$2s2.2p5.(2P*<3/2>).3p$	2[5/2]	3	18.556	18.554	0.01
		2	18.576	18.598	0.12
$2s2.2p5.(2P*<3/2>).3p$	2[3/2]	1	18.613	18.631	0.1
		2	18.637	18.699	0.33
$2s2.2p5.(2P*<1/2>).3p$	2[3/2]	1	18.694	18.716	0.12
		2	18.704	18.723	0.1
$2s2.2p5.(2P*<1/2>).3p$	2[1/2]	1	18.727	18.74	0.07
		0	18.966	19.081	0.61
$2s2.2p5.(2P*<3/2>).4s$	2[3/2]*	2	19.664	19.645	0.1
		1	19.689	19.683	0.03
$2s2.2p5.(2P*<1/2>).4s$	2[1/2]*	0	19.761	19.767	0.03
		1	19.78	19.802	0.11
$2s2.2p5.(2P*<3/2>).3d$	2[1/2]*	0	20.025	20.011	0.07
		1	20.027	20.013	0.07
$2s2.2p5.(2P*<3/2>).3d$	2[7/2]*	4	20.035	20.022	0.06
		3	20.035	20.023	0.06
$2s2.2p5.(2P*<3/2>).3d$	2[3/2]*	2	20.037	20.025	0.06
		1	20.041	20.029	0.06
$2s2.2p5.(2P*<3/2>).3d$	2[5/2]*	2	20.049	20.037	0.06
		3	20.049	20.038	0.05
$2s2.2p5.(2P*<1/2>).3d$	2[5/2]*	2	20.137	20.123	0.07
		3	20.137	20.15	0.06
$2s2.2p5.(2P*<1/2>).3d$	2[3/2]*	2	20.138	20.15	0.06
		1	20.14	20.151	0.05
$2s2.2p5.(2P*<3/2>).4p$	2[1/2]	1	20.15	20.154	0.02
		0	20.26	20.165	0.47
$2s2.2p5.(2P*<3/2>).4p$	2[5/2]	3	20.189	20.176	0.06
		2	20.197	20.193	0.02
$2s2.2p5.(2P*<3/2>).4p$	2[3/2]	1	20.211	20.198	0.06
		2	20.215	20.26	0.22
$2s2.2p5.(2P*<1/2>).4p$	2[3/2]	1	20.291	20.295	0.02
		2	20.298	20.303	0.02

Table 3.2: A selection of oscillator strengths for comparison to previous results from B-spline [100] as well as NIST [86].

Configuration	Level	Oscillator Strength	B-Spline [100]	% Diff.	NIST	% Diff.
$2p^5(^2P^*<3/2>)3s$	$2[3/2]_1$	0.0088	0.0118	29.61	0.0118 ± 0.0030	29.61
$2p^5(^2P^*<1/2>)3s$	$2[1/2]_1$	0.1693	0.159	6.26	0.1490 ± 0.0373	12.74
$2p^5(^2P^*<3/2>)4s$	$2[3/2]_1$	0.0143	0.0126	12.30	0.0086 ± 0.0022	49.46
$2p^5(^2P^*<1/2>)4s$	$2[1/2]_1$	0.0239	0.0174	31.30	0.0130 ± 0.0033	58.91
$2p^5(^2P^*<3/2>)3d$	$2[1/2]_1$	0.0039	0.00479	19.28	0.0057 ± 0.0014	36.33
$2p^5(^2P^*<3/2>)3d$	$2[3/2]_1$	0.0131	0.0146	10.70	0.0160 ± 0.0040	19.80
$2p^5(^2P^*<1/2>)3d$	$2[3/2]_1$	0.0066	0.00718	8.47	0.0065 ± 0.0016	1.48

additional mass-velocity, Darwin, and spin-orbit relativistic effects not present in standard LS formulations [62]. The target state interactions are initially calculated in *LS* coupling but are then recoupled into the *jK* states before diagonalizing the Hamiltonian. N + 1 partial wave symmetries, described with $J\Pi$, extended from $2J$ = 1 to $2J$ = 43. Exchange effects were excluded for $2J$ = 15 and above. To account for higher partial waves beyond $2J$ = 43, a Burgess 'top-up' was applied [66]. Additionally, only the first 400 levels were kept at the recoupling stage to fit within our computational resources. These 233 levels, including primarily pseudostates and some $2s2p^5nl$ states, covered a 2.70 to 6.69 Ryd energy range, roughly 0.75 Ryd above the maximum incident electron energy cross section that we calculated.

At the diagonalization stage for the electron-impact excitation calculation, we additionally set the energies of the Hamiltonian to match NIST energies. This stage has further been parallelized such that partial waves can be diagonalized concurrently [55]. Dimensions of the partial wave Hamiltonians reached a maximum of 78,670. From the inner region solution, a boundary condition at the box radius can be obtained through the R-matrix, which can then be matched to an outer region solution that considers the continuum electron as distinguishable from the target. An absolute integrated cross section is then generated from an asymptotic expansion of the matched solution. Cross sections for the electron-impact excitation were obtained over an incident electron energy mesh from 1.12 to 1.93 Ryd, in 0.0012 Ryd increments.

The electron-impact ionization cross sections were performed using the same suite of codes but without *LS*-*jK* recoupling. Using *LS*-coupling both reduced the size of the calculation and allowed for more pseudostates. Our model improves upon that of Ballance *et al.* [55] by

increasing the pseudostate orbital angular momentum range from $\bar{l}$ = 4 to $\bar{l}$ = 6, increasing the number of possible transitions of the excited-state electrons into the continuum.While the *LS* energies from the RMPS ionization calculatoin were not shifted to NIST energies, a NIST shift was applied when the *LS* cross section data was split into *LSJ* resolution using the appropriate angular factors. No terms were cut prior to diagonalizing the N + 1 Hamiltonian. The inclusion of more pseudostates required diagonalization of larger Hamiltonians, the partial wave Hamiltonians reaching 114,459 dimension size. The calculation included partial waves from L = 0 to L = 20 with exchange effects, and a 'top-up' was applied for partial waves beyond L = 20. 100 energy mesh points were computed in the range 1.1 to 3.1 Ryd, encompassing the 1.5850 Ryd $2p$ ionization potential [86].

The electron-impact excitation and ionization calculations extended to maximum energies of 26 eV and 20 eV respectively, just past the ionization peaks of the chosen terms for the latter. These ranges were chosen to fit our computational capabilities. Though we are primarily concerned with lower temperatures, we wanted to extend the results to as wide of a temperature range as possible. Using the method proposed by Burgess and Tully [78], we extrapolated our excitation cross sections to an infinite energy point limit. For ionization, Rost-Pittard [101] and Younger [102] fits were used in the energy range below and above twice the ionization potential, respectively. The parameters fit the data well, allowing us to push the ionization cross sections beyond 20 eV. Bethe high-energy limit points obtained from Configuration-Averaged Distorted Wave runs were used in the Younger fits.

3.2.3 Generalized Collisional-Radiative modeling

The main goal of these new R-Matrix calculations is to generate reliable atomic data for spectral modeling in plasma devices. One such application is in creating plasma temperature and density diagnostics from the ratio of different emitted spectral lines. The W7-X fusion energy experiment in Germany is pursuing such a diagnostic in the 0 - 40 eV and $10^{12} - 10^{14}$ cm^{-3} ranges [47]. Another important area of study for neon in fusion plasmas is tracking the transport of neon and its charge states as it gets transported through the plasma. Neon is often used to cool the divertor, but it is important that it not get into the core plasma and radiate power. One

of the coefficients used in impurity transport codes is the effective ionization rate coefficient, representing the total ionization from one charge state to the next. Given the new ionization data, it is possible to determine the impact that high quality excited-state ionization data will have on the effective ionization rate coefficients.

Rate coefficients for all available electron-impact excitation and ionization cross sections were calculated and GCR modeling performed using a recently developed suite, ColRadPy [84]. The effective ionization rate coefficient, or SCD, was then examined at different electron temperatures and densities to assess the impact of excited-state ionization.

3.3 Electron-impact excitation cross sections and rate coefficients

3.3.1 Convergence Checks

We first consider the electron-impact excitation of neutral neon. A series of convergence checks were run to ensure:

1) enough partial waves were included,
2) energy points were included up as far as the basis set was valid,
3) false energy points resulting from numerical instability were removed, and
4) the cross sections tended towards their infinite energy points at higher energies.

Figure 3.1 shows the results of a convergence check on the first transition cross section, excitation from the ground $2p^6$ ($^1S_0$) to $2p^5 3s$ ($^3P_2$). Cross sections going up to varying partial waves are included: to 2*J*=13, 27, and 43. As shown, the set of partial waves converged at $2J$ = 13. The red line indicates the last incident energy that was considered in the final calculation. After roughly 26.2 eV, the cross section starts to oscillate, an indication that the basis set is no longer adequate in this energy region. Furthermore, around 25 eV the cross section begins turning downwards, another indication of an incomplete basis set at these higher energies. In other examined cross sections, this oscillation as well as the downward slant are not as noticeable. To ensure accurate extrapolation towards the infinite energy limits at

higher energies, the decision was made to consider only points up to 26.24 eV. It is common within the *R*-matrix community to consider energies up to two-thirds of the smallest final energy eigenvalue of the continuum orbitals with respect to the angular momentum as safe. In this case, *l*=0 had the smallest last energy eigenvalue, at 33.50 eV, two-thirds of which is 22.33 eV. The choice in the incident energy range thus represented a compromise between the safe choice dictated from the Stage 1 continuum orbital eigenvalues and where from observation the calculation started to oscillate and trend downward.

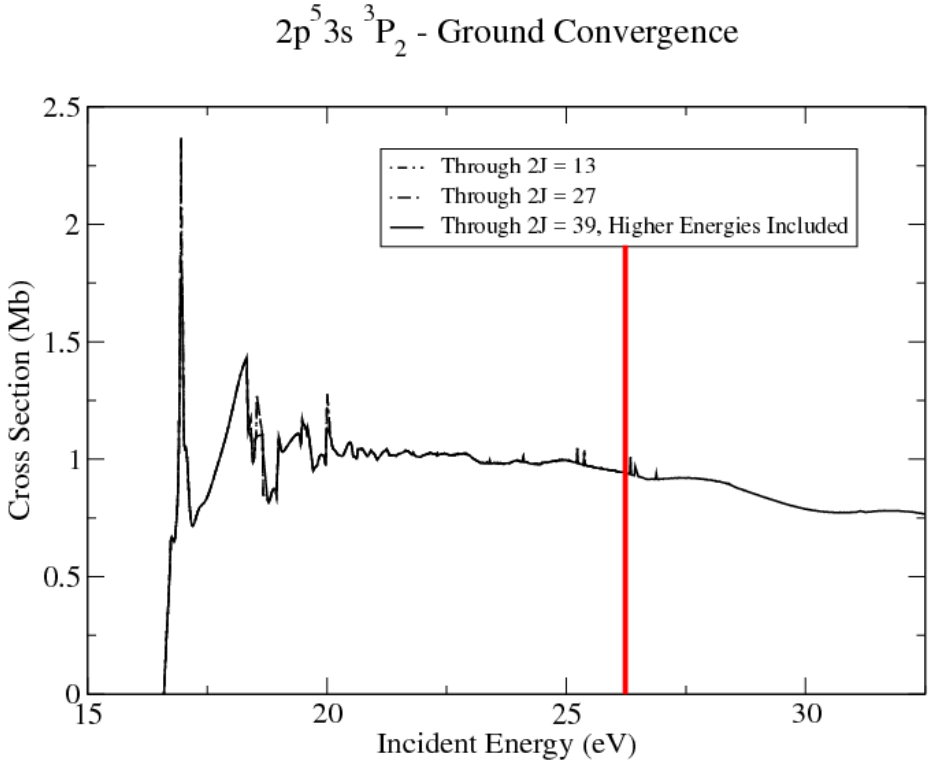

Figure 3.1: Electron-impact excitation of neutral neon from the ground state to $2p^5 3s$ ($^3P_2$). Partial wave convergence is demonstrated at $2J$=13. The red line indicates the last point considered accurate, above which the cross section trends downwards and begins to oscillate.

Another consideration when processing the cross sections was the criteria for removing points due to numerical instability. The *R*-matrix method elucidates resonances, or peaks, in the cross section at energies corresponding to the presence of N + 1 configurations. Other points, typically isolated, are artificially higher as a result of their energies occurring on poles

of *R*-Matrix, in which its denominator approaches zero. These points must be removed from the cross section, while retained as many of the N + 1 resonances as possible. The presence of numerical noise in the cross section is problematic for generating rate coefficients, in which the integration now assumes the presence of high, albeit thin, triangles, artificially raising the rate coefficient. This excess contribution can further prevent convergence of rates in partial waves. Figure 3.2 illustrates the $2p^5 4f$ ($^3D_3$) - $2p^5 5s$ $^1P_1$ cross section, which, without any cross section processing, demonstrated the worst convergence between the rate coefficients q_{ij} if including up to $2J$=41 and 43 respectively, as measured by the taking the ratio $\frac{q_{41}}{q_{43}}$. The numerical noise is clearly skewing two cross sections otherwise in agreement, as well as artificially raising the rate coefficients.

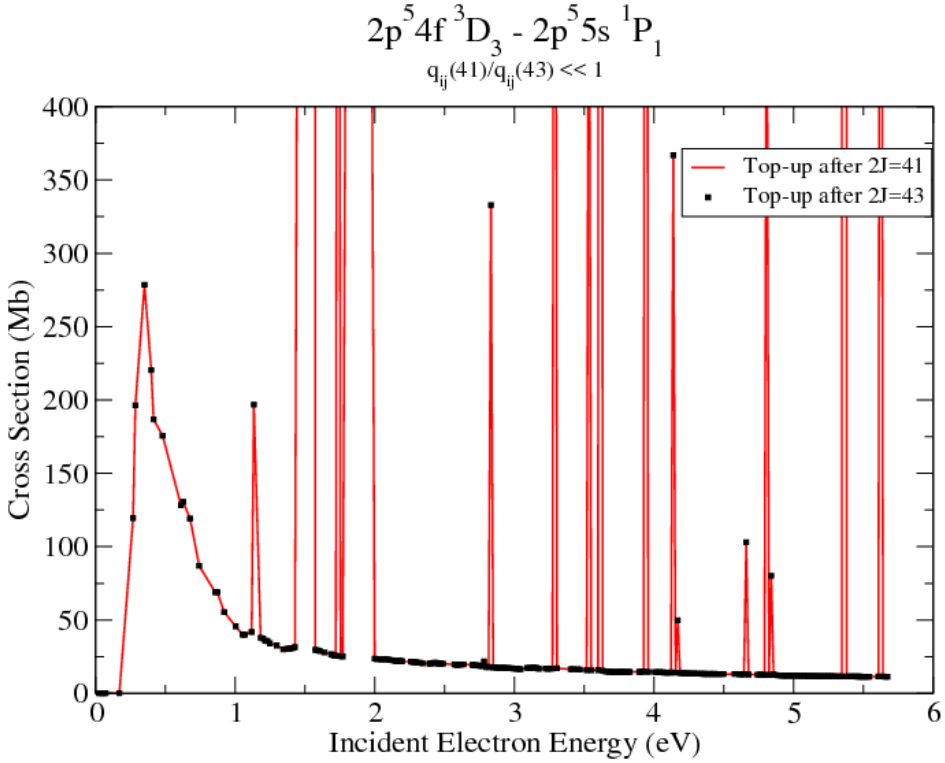

Figure 3.2: The $2p^5 4f$ ($^3D_3$) - $2p^5 5s$ $^1P_1$ cross section. The red line and black dots indicate the raw cross sections if including up to $2J$=41 and 43 respectively. This transition had the most numerical noise, as measured by the ratio of rate coefficients $\frac{q_{41}}{q_{43}}$.

A threshold for adjacent points was chosen such that points more than 20% higher than previous points were removed. Other thresholds were explored as well, from 5% to 40%. The 20% threshold removed all of the spikes in 3.2 while keeping the peak at 0.5 eV. Figure 3.1 further suggests the validity of this threshold, in which its large, thin peak is also kept.

Figures 3.3 and 3.4 show transitions from the ground to $2p^5 3p\ (^3P_1)$ and $2p^5 3d\ (^1P_1)$, spin-forbidden and dipole transitions respectively. As with Figure 3.1, cross sections if including up to 2*J*=13, 27, and 43 are included, and convergence is seen at $2J = 13$. Some small numerical noise is still observed at higher energies, despite the threshold criteria, though the amount is relatively small. A coarse energy mesh at high energies at been considered; however, the range of the calculation would ideally extend past the N + 1 resonances for use of a coarse mesh. The N + 1 resonances of neutral systems are typically of a wider energy spread than ionic states, and the $2p^5 3d$ excitation cross section in particular exhibits resonances up through 25 eV, at the upper end of the energy mesh.

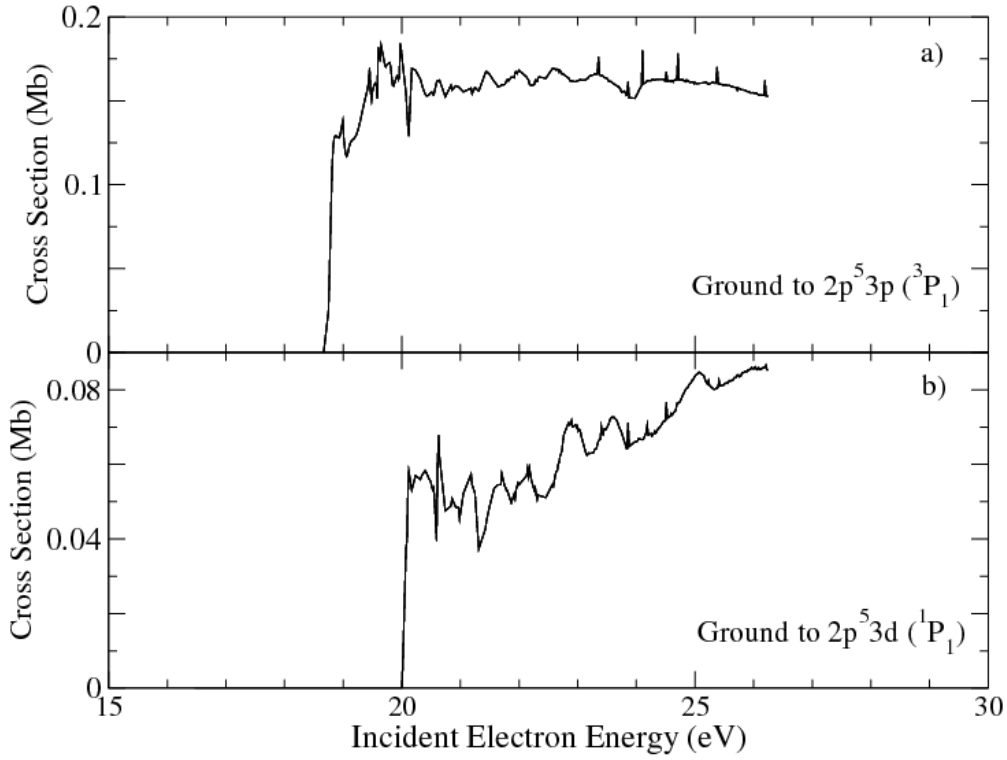

Figure 3.3: Electron-impact excitation cross sections from the ground to the spin-forbidden $2p^5 3p$ ($^3P_1$) and dipole-allowed $2p^5 3d$ ($^1P_1$) states. Separate cross sections for partial waves through $2J$=13, 27, and 43 are shown, and convergence is demonstrated at $2J$=13.

Excitation from excited states generally required more partial waves for convergence of cross sections and rates. Figure 3.4 shows two excitation cross sections from the metastable $2p^5 3s$ ($^3P_2$) to the $2p^5 3p$ ($^3D_3$) and ($^1D_2$) states. Despite ground state excitation convergence at $2J$=13, the metastable excitations converged much higher, with $2J$=41 and $2J$=43 (black line). The final calculation therefore included through $2J$=43 with top-up. Figure 3.5 shows a convergence check on the rate coefficients for all the transitions of the 79 levels. If converged, the ratio of the rate coefficients from including through $2J$=41 versus $2J$=43, $\frac{q_{41}}{q_{43}}$, should be close to 1. Less than a percent of the transitions have ratios either above 1.05 or below 0.95, suggesting convergence. In most cases where the ratio is farther from 1, the $2J$=41 rates are less than the $2J$=43 rates, and typically for excitation from higher excited states (higher transition numbers), in keeping with increased partial wave convergence of $2J$=43.

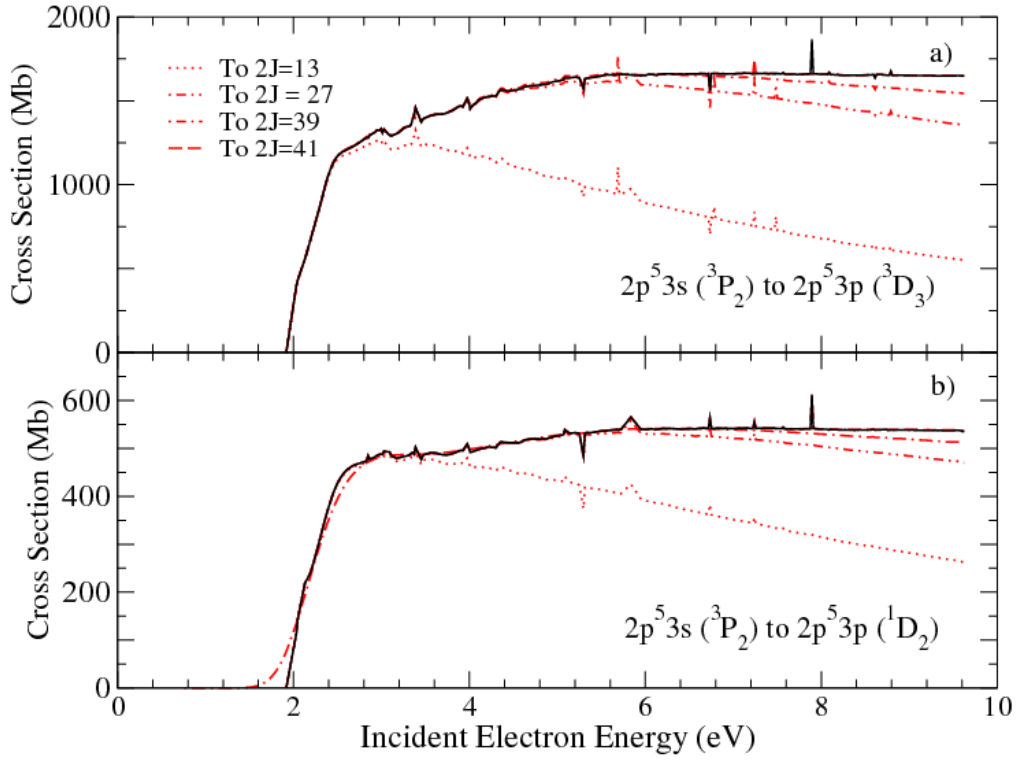

Figure 3.4: Electron-impact excitation cross sections from the metastable $2p^5 3s$ ($^3P_2$) to the $2p^5 3p$ a) ($^3D_3$) and b) ($^1D_2$) states. Convergence required much more partial waves, up to $2J$=43 (black line).

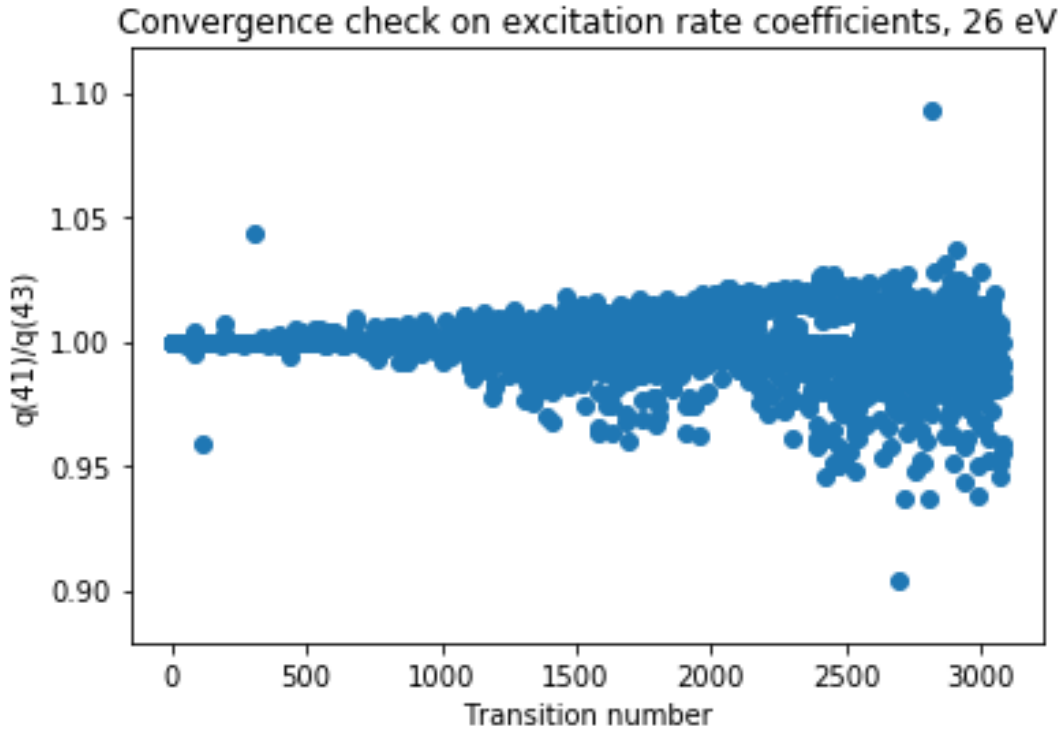

Figure 3.5: Convergence check on the electron-impact excitation rates, as measured by taking the ratio of the rate coefficients from including partial waves up to $2J$=41, q_{41}, and up to $2J$=43, q_{43}, for ever transition. More than 99% of transitions have ratios within 0.05 of 1. The rates were taken at an electron temperature of 26 eV, where the cross sections should experience the least partial wave convergence.

Figures 3.6, 3.7, and 3.8 show comparisons of the new RMPS-400 cross sections from the ground state excitation to four levels each of the $2p^5 3s$, $3p$, and $3d$ configurations. The cross sections are close to those of BSR-457 for every transition. Further, transitions from the ground state to $3s$ and $3p$ orbitals often agree more closely with experiments. Our original structure included a total of 524 pseudostates and 109 spectroscopic levels, though, due to processing capability, we cut down the number of levels before *jK*-recoupling to a total of 400: 319 pseudostates and 81 spectroscopic levels. The energy range of the cut levels extends from 36.59 eV to 91.07 eV. We used a fine energy mesh of a roughly 0.016 eV increment that reached 26.260 eV, well below the range of these levels. Therefore, the structure of the 400 remaining levels offers greater inclusion of continuum coupling. All shown cross sections are convolved

to an energy width of 0.5 eV. Particularly for the $3s$ orbital transitions, the new RMPS results exhibit the same peaks and resonances as BSR-457.

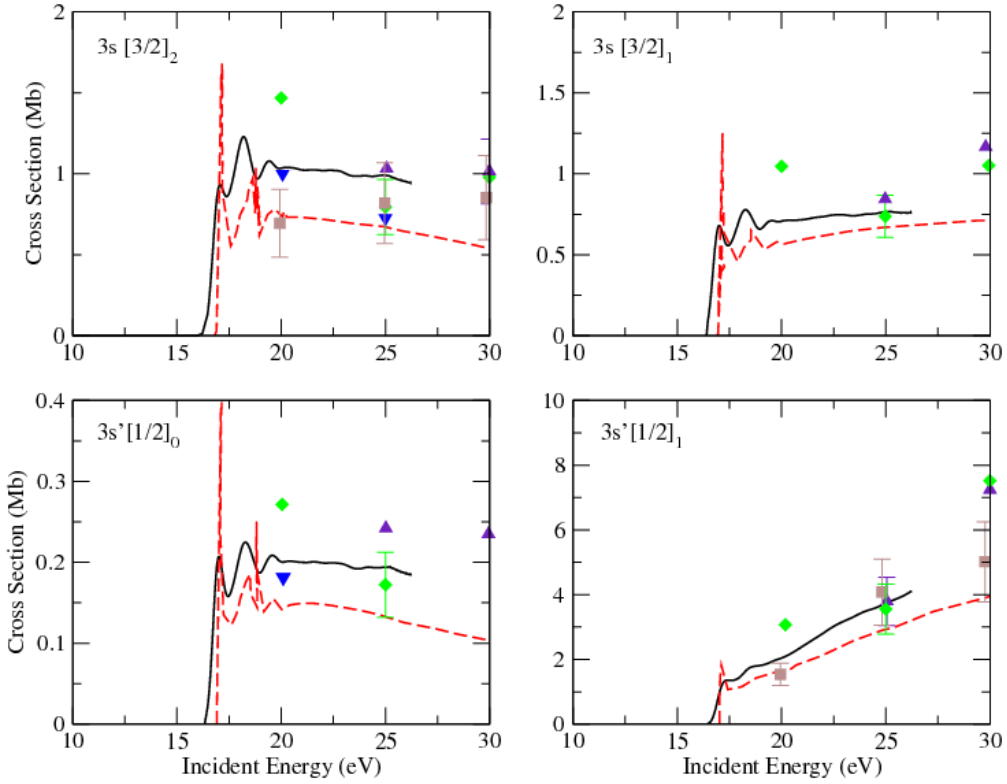

Figure 3.6: Ground state angle-integrated excitation to $2p^5 3s$ cross sections (solid black). Though our calculation only extended to 26 eV, we show results of previous measurements by Khakoo *et al.* (green diamond) [88], Phillips *et al.* (blue flipped triangle) [92], Register *et al.* (purple triangle) [93], Hoshino *et al.* (brown square) [90], and the most recent *B*-Spline (BSR-457) calculation [52] (red dashed), with whom our results are within range.

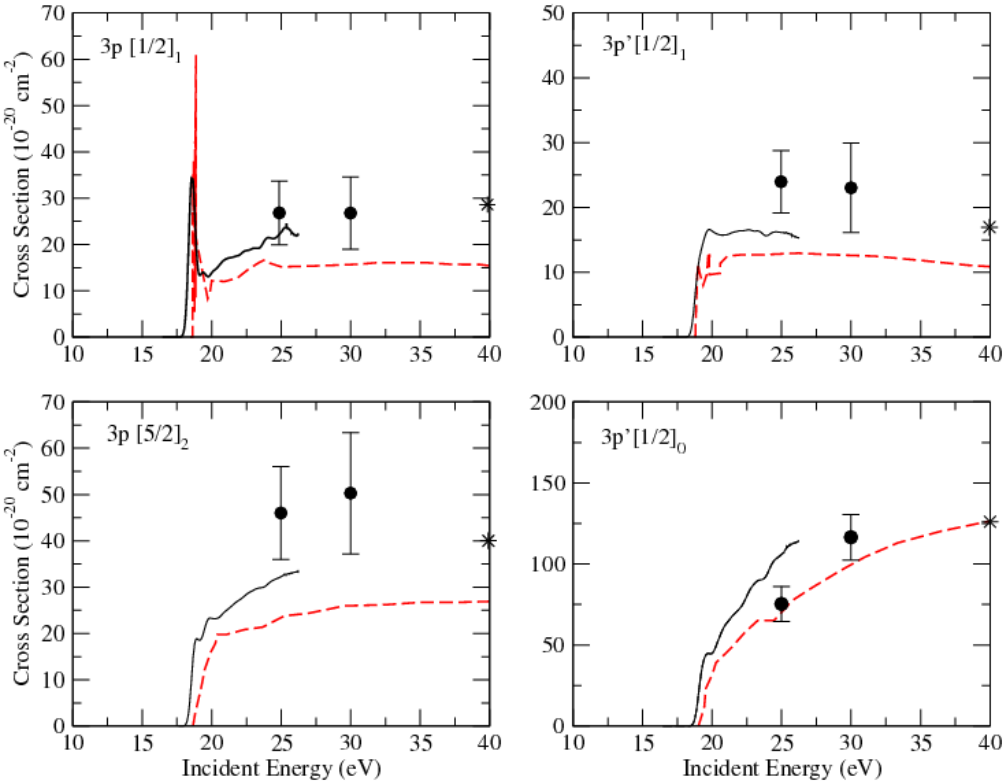

Figure 3.7: Ground state angle-integrated excitation to $2p^5 3p$ cross sections (solid black), including previous measurements by Chilton *et al.* (black circle) [89], the *R*-Matrix with Pseudostates (RMPS-235) calculation by Ballance and Griffin (black star) [58], and the most recent *B*-Spline (BSR-457) calculation (dashed red) [52], with whom our results are within range.

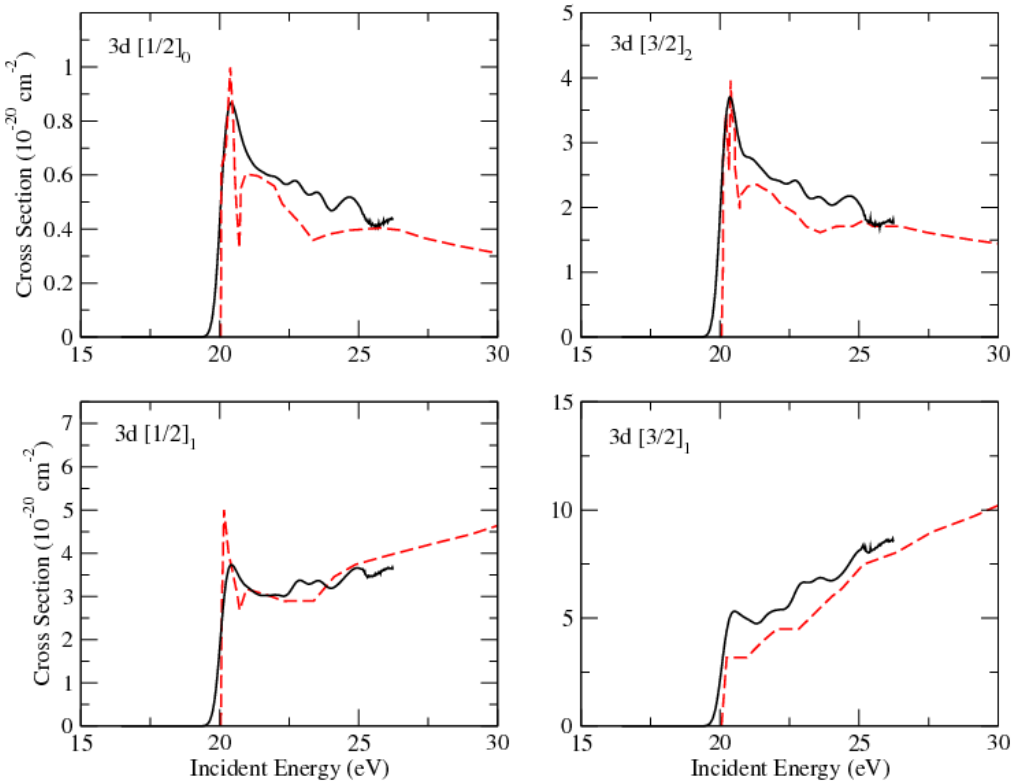

Figure 3.8: Ground state angle-integrated excitation to $2p^5 3d$ cross sections (solid black), including the *B*-Spline (BSR-457) (dashed red) results [52], with whom ours are within range.

Figure 3.9 shows cross sections for excitation from the metastable $3s[3/2]_2$ level. For the sake of clarity, comparison points before 2 eV are omitted. Of all cross section comparisons, the metastable RMPS-400 cross sections differ the most from previous results, falling slightly below the BSR-457 that do not include cascade effects [52] and a factor of two below the measurements of Boffard *et al.* [96] for excitation to $3p[3/2]_2$ and $3p'[3/2]_2$. Cascade effects are not shown for the RMPS-400. BSR-457 also disagrees with these two measurements, even if including cascade effects. The addition of more pseudostates might contribute to the RMPS-400 cross sections being 10-20% lower than BSR-457. In previous results [56], adding more pseudostates led to a decrease in cross section, in connection to a greater representation of continuum coupling. These metastable excitations, closer to the ionization potential, should be

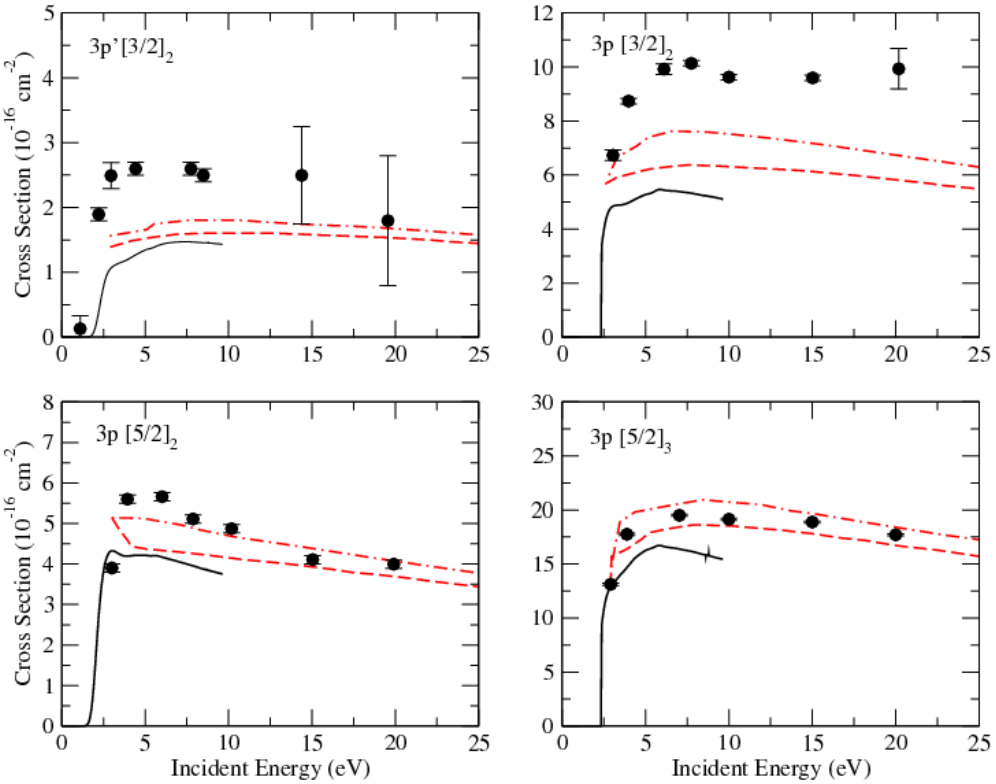

Figure 3.9: *R*-Matrix with Pseudostates (RMPS-400) metastable $3s[3/2]_2$ state angle-integrated excitation to $2p^5 3p$ cross sections (solid black), including the previous *B*-Spline (BSR-457) both with and without cascade effects (dashed and dashed-dot red respectively) [52] and experimental results [96] (black circle). RMPS-400, cascade effects not shown, agrees reasonably well with BSR-457 without cascades for all states, but differs by a factor of two for the $3p[3/2]_2$ and $3p'[3/2]_2$ states. Cross sections are relative to the metastable level energy, which is 16.607 eV above the ground. For the sake of clarity, comparison points with BSR-457 before 2 eV are omitted.

more affected by continuum coupling than ground state transitions. Overall, the strong agreement of our excitation cross sections with results for most previously modeled and measured transitions indicates the suitability of our calculation for accurate rate coefficients.

3.4 Electron-impact excited state ionization cross sections

The overall goal of our ionization calculation was to determine accurate cross sections for extending up to $2p^5 5p$, our last optical configuration. To test the accuracy of our model, we also compare to previous metastable cross sections for the ^3P states from the $3s$, $4s$, and $5s$ configurations [55, 99].

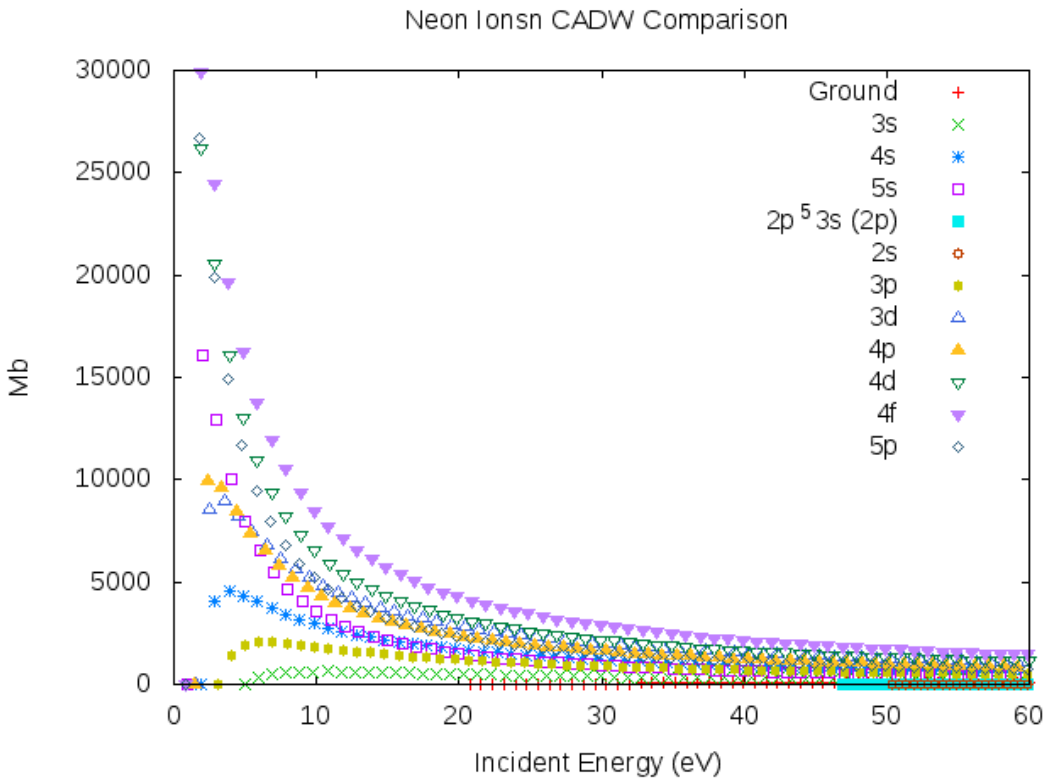

Figure 3.10: Configuration-averaged (CADW) results for the electron-impact ionization of neon.

Prior to running the *R*-matrix calculation, cursory configuration-averaged distorted wave (DW) calculations were run for valence ionization from each of the $2p^5nl$ configurations as well as ground state ionization of $2s$. Figure 3.10 shows a comparison of the electron-impact ionization of these states. The cross sections increase dramatically going to higher excited states, with the 4f valence ionization being the largest. The ground state ionization cross section falls well below the excited states and starts at a much higher energy as well, 21.56 eV. Ionization of $2s$, which begins much farther at around 46 eV and is much smaller than the rest, was factored into the atomic structure of the *R*-matrix calculation, but was not considered otherwise.

Figure 3.10 also demonstrates a problem for distorted wave calculations for the ionization of neutral systems in that the excited states diverge after $4p$, becoming asymptotic at low energies.

As previously discussed, we set up our model to represent the continuum as accurately as computationally feasible at energies below 20 eV through an inclusive set of Rydberg series, pseudostates, and partial waves. These parameters were at the cost of fewer continuum basis

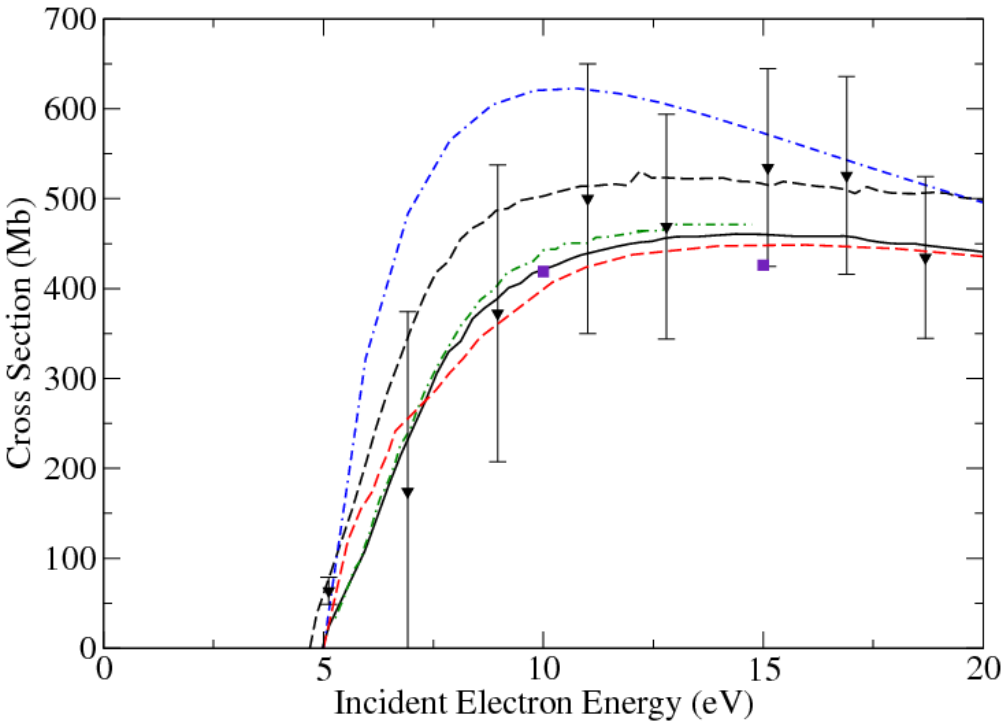

Figure 3.11: Ionization cross sections from the $2p^5 3s$ (^{3}P) state. The solid black, dashed-dotted green, and dashed red lines designate our *R*-Matrix with Pseudostates (RMPS-545) model, RMPS-297 [55], and the second-most recent *B*-Spline (BSR-679) model respectively [56]. Our model agrees well other calculations, including time-dependent close-coupling (TDCC) results (purple square) [57] and measurements by Johnston *et al.* (brown flipped triangle) [99]. The RMPS-545 ^1P ionization is also shown.

orbitals, and this trade-off was reflected in the results. Figure 3.11 shows the cross sections for the $3s(^3P)$ valence shell ionization, including a comparison to previous calculations [55, 57] and the measurements of Johnston *et al.* [99]. As shown, our RMPS-545 calculation agrees well with past theoretical and experimental data up to 20 eV, after which, the continuum basis set is not adequate. A cross section for the ground state was also extracted, but ours clearly does not match previous calculations, due to the limited energy range coverage. To extract ionization rate coefficients from the ground state, we instead used the BSR-679 ground state cross section [56].

Figure 3.12 shows cross sections from the $2p^5 3s$, $4s$, and $5s(^3P)$ and (^1P) states) from 0 to 20 eV, compared to the previous *R*-Matrix with Pseudostates (RMPS-297) ^3P results [55]. The two models agree well, particularly for the $3s$, with a steady increase in percent difference

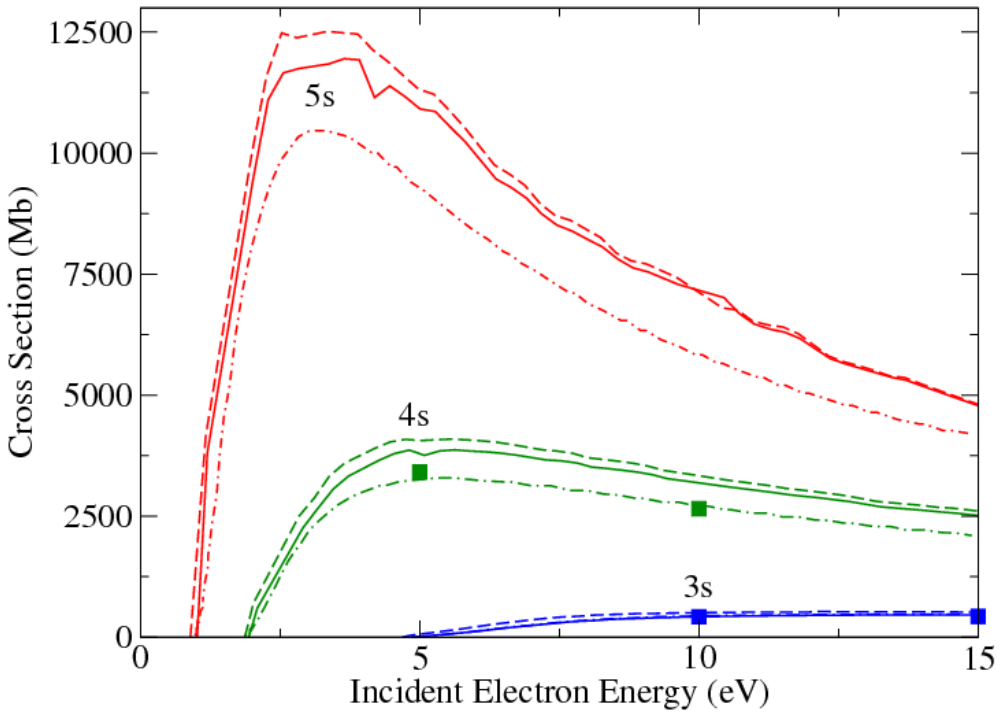

Figure 3.12: Ionization cross sections from the $2p^5 3s$ (blue), $4s$ (green), and $5s$ states (red), compared with the 2009 *R*-Matrix with Pseudostates (RMPS-297) model (dot-dashed) for ^3P states [55] and the configuration-averaged TDCC results (squares) [57]. ^3P and ^1P states are indicated by solid and dashed lines respectively. Percent difference between the two models steadily rises with increasing n-shell.

with the increase in *n*-shell. The RMPS-545 $5s(^3P)$ cross section peaks about 15% higher than the previous model. The cross sections from the new model, then, generally agree for lower states and become increasingly greater for higher state ionization, consistent with an increased pseudostate coverage for higher excited-state ionizations.

Table 3.3 describes some of the basic characteristics of the $2p^5 np$, *nd*, and $4f$ term-resolved ionization cross sections out of the respective shells. The $2p^5 np$, *nd*, and $4f$ configurations all give rise to six total singlet or triplet term each, ranging from $L = 0$ to 2, $L = 1$ to 3, and $L = 2$ to 4 respectively. Peak spread refers to the difference in Mb from the highest to the term-resolved cross section at the peak.

The cross sections from the higher $nl = 2$ and 3 orbitals were much closer together than those from the *np* orbitals, as indicated by the peak spread. The ^1S and ^3S, the highest and

Table 3.3: Descriptions of the term-resolved ionization peaks for each *l* = 1 - 3 optical configuration. Cross section measurements are rounded to the nearest hundred Mb.

Ionized Orbital	Highest Cross Section Term	Lowest Cross Section Term	Peak Spread (Mb)	Average Peak (Mb)
$3p$	^1S	^3S	1000	1400
$4p$	^1S	^3S	3100	6300
$5p$	^1S	^3S	6600	15000
$3d$	^1D	^3P	300	6200
$4d$	^1D	^1P	800	16500
$4f$	^3F	^3D	300	17500

lowest respectively for each *np* cross section, deviated the most from the average of the term-resolved peaks per configuration. The singlet terms almost always had higher cross sections, with the exception of the $4f(^3F)$ and (^1F), though the difference between the two was very small.

Figure 3.13 shows cross sections for the $2p^5$*np* and *nd* term ionizations for selected terms, ^3D and ^1D for the former and ^3F and ^1F for the latter. Also included is an n^4-scaled cross section for comparison for the $4d$ and $5p$. Classically, the ionization cross sections are expected to exhibit an n^4-scaling for high nl states [85], such that the ionization cross section of a higher $n_f l$ electron, $\sigma^+_{n_f l}$, can be scaled from a lower $n_i l$ ionization cross section as $n_f^4/n_i^4 \times \sigma^+_{n_i l}$. A similar comparison was made of the higher excited states of B, B^+, and B^{2+}, to test for convergence [103]. The cross sections of the second-highest calculated n_i, 3 for d and 4 for p, were used to generate the scaled results of the highest n_f, and the incident energy was scaled by the ratio of the ionization potentials.

Overall, the term-resolved cross sections show good agreement with the *n*-scaled cross sections. The $4d$ valence orbital cross sections match everywhere for all terms except at the peak, at which the *n*-scale is roughly 10% higher. The $5p$ cross sections all exhibit the same pattern, in which the RMPS-545 cross sections fall about 10% lower than the *n*-scaled ones throughout all energy ranges. These results suggest our calculation is converged and that higher *n*'s can be extrapolated.

Of particular interest to future electron-impact ionization calculations is how high in pseudo orbital angular momentum is required to converge the cross section for all of the excited states. Figure 3.14 depicts the contribution of each set of final state pseudo orbitals of a

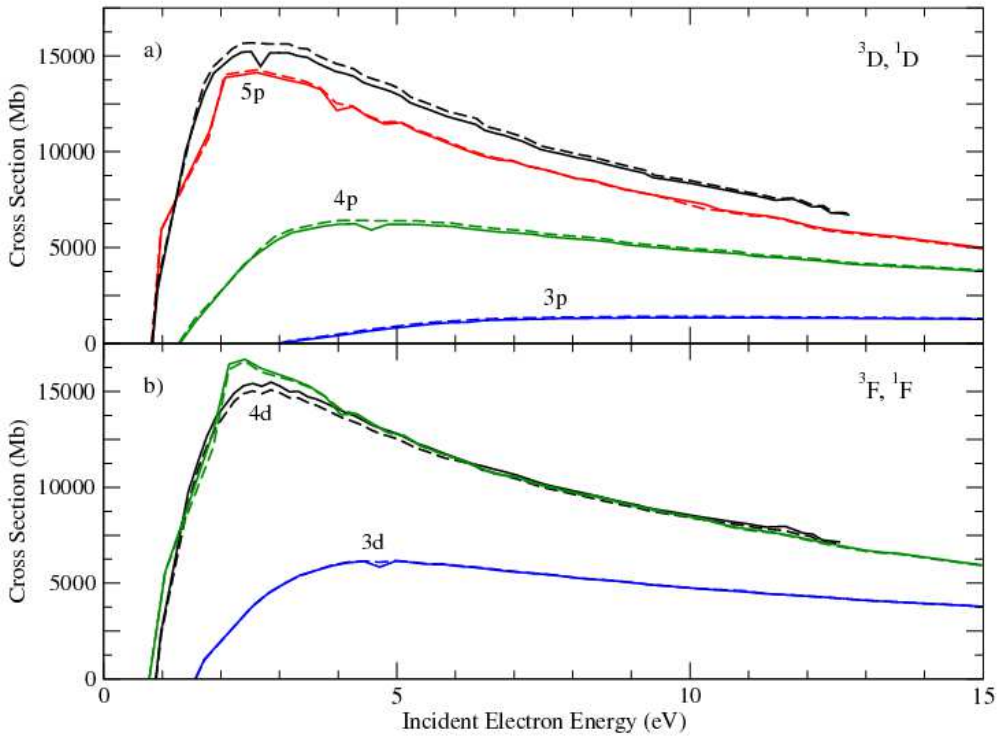

Figure 3.13: Ionization cross sections from the a) $2p^5$ *np* (^3D) and (^1D) states, as well as the b) $2p^5 3d(^3F)$ and (^1F) states. Solid and dashed lines represent triplet and singlet states respectively. Theoretical cross sections (black) are included for the higher $2p^5 5p$ and $4d$ states, derived from an n^4 scaling with the lower $2p^5 4p$ and $3d$ state cross sections respectively.

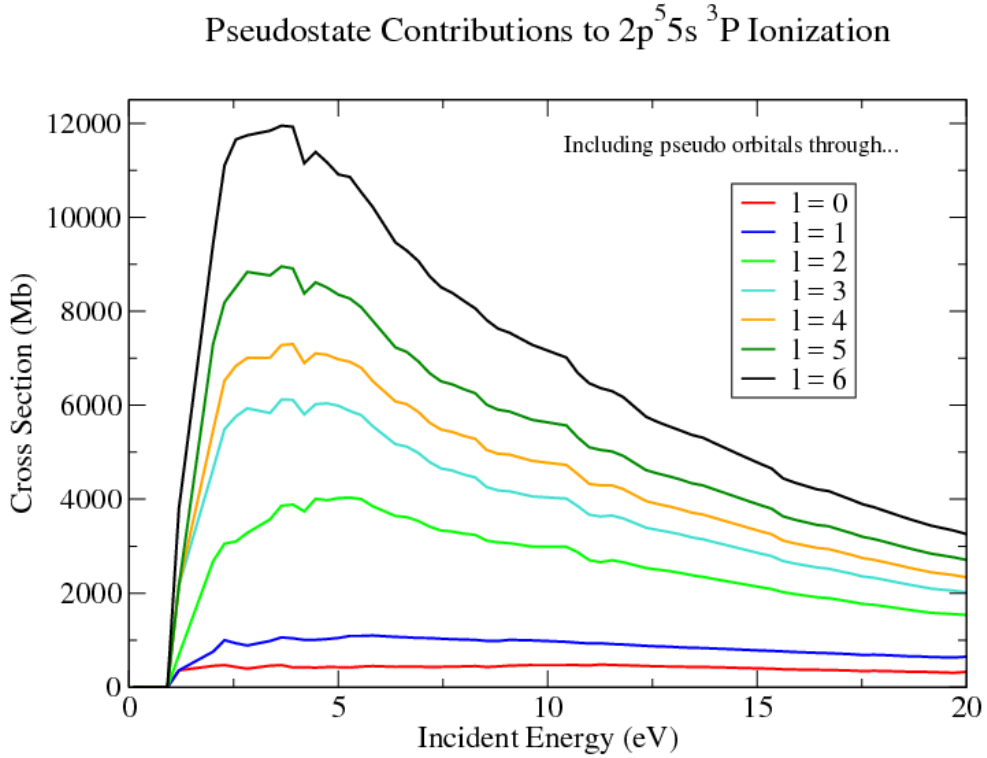

Figure 3.14: Breakdown by angular momentum $\bar{l}$ of the final state pseudo orbital contribution to the 5s valence shell ionization cross section. Each curve shows the contributions of $\leq \bar{l}$.

given angular momentum, through $\bar{l} = 6$ to the valence shell 5s ionization cross section. While previous calculations have typically limited the pseudo orbital angular momentum range from $\bar{l} = 0$ to 5, the ionization to the $\bar{l} = 6$ states contributes over 20% to the total cross section at the peak.

3.5 Generalized-Collisional Radiative Modeling and the Effective Ionization Rate

The main consideration in the GCR modeling reported here is to determine which states contributed most to the effective ionization at relevant densities. GCR modeling of neutral neon was performed using these new electron-impact excitation and ionization data. Rate coefficients were included for all excitation and ionization transitions (based on the cross sections reported earlier in this chapter), and radiative and dielectronic recombination rate coefficients were included as well. The dielectronic and radiative recombination rate coefficients were taken from Zatsarinny *et al.* [104] and Badnell [105] respectively. The calculation of infinite energy

points for the excitation transitions and ionization fits to high energies enabled rate coefficients to be calculated up to electron temperatures beyond the range of the R-matrix calculations.

LS-resolution has traditionally been used for light elements. Neutral neon represents a transition point where *LSJ*-resolution may be required. Proton collisions can efficiently redistribute populations of the levels within an *LS* term. For elements below neon, proton collisions redistribute level populations such that the relative populations of the *J*-levels within an *LS* term are given by the relative statistical weights of each level. Thus for neon, we made both an *LS* and an *LSJ* dataset.

While the *LS*-resolved ionization rate coefficients considered only ionization to the Ne II ground term $2p^5$ (^2P), the LSJ-resolved rate coefficients were split by the Ne II ground term's two J-values, 1.5 (ground) and 0.5. This *LSJ*-resolution was achieved from the *LS* ionization cross sections by using the variation of the Sampson branching ratios [77] given by Equation 2.48.

Ionization of the $2s$ subshell occurs 26.91 eV higher than the $2p$ subshell [86], and a configuration-averaged distorted wave calculation suggested the cross-section from this stage was negligible compared to the valence shell ionization, in agreement with the findings of [55]. Therefore, $2s$ ionization was not considered in our model. Likewise with the excitation, the LSJ-resolved calculations were term-averaged to generate LS excitation rate coefficients for the LS-resolved dataset. To make the atomic dataset as accurate as possible, we further replaced our A-values with those of NIST [86]. Both LS and LSJ datasets will be made available to the community in a standard ADAS format known as an adf04 file [36].

Figure 3.15 gives an example comparison between the original *LS*-resolved cross section of the valence shell 4d (^3P) ionization, being *LSJ*-resolved via branching ratios. Of the three initial J values, 0, 1, and 2, all ionization transitions to either a $2p^5$ (^2P) J = 0.5 or 1.5 (ground) state are possible, except initial J = 0 to final J = 1.5. For all but initial J = 1, transition into the metastable final J = 0.5 has a much greater, or non-zero, cross section.

Figure 3.16 shows the effective ionization rate coefficient as a function of (Maxwellian-averaged) electron temperature through 25 eV, using the *LS*-resolved dataset. Included are rate coefficients at both low and high electron densities, 10^4 and 10^{14} cm^{-3}. As expected, the

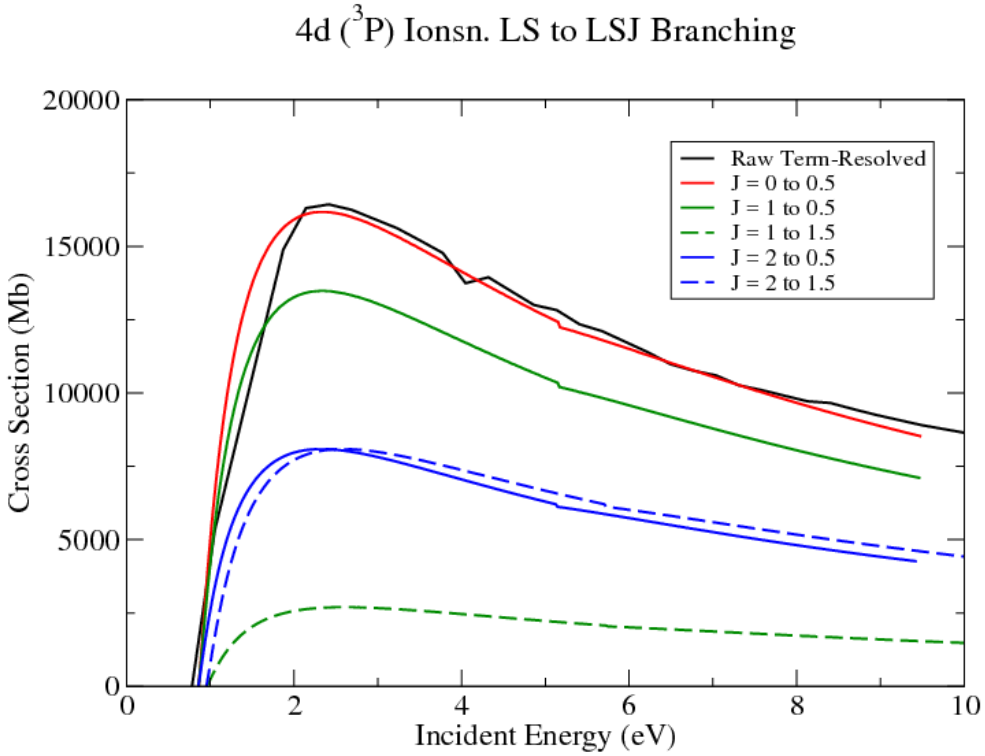

Figure 3.15: Demonstration of the *LS*- to *LSJ*- branching ratios for valence shell 4d ($^3P_{0,1,2}$) ionization. Each level can ionize either to $2p^5$ (^2P) J = 0.5 or 1.5, except initial J = 0 for which final J = 1.5 is forbidden.

low-density effective ionization rate coefficient (dashed black) nearly matches that of just the ground (solid green), slightly diverging with increasing electron temperature. This reflects that most of the population is in the ground state at low densities.

At high electron density, excited-state ionization has a greater contribution to the SCD than ground-state ionization in the 0 - 25 eV electron temperature range. The ratio of the SCD when including all excited states and ground ionization (solid black line) compared to the SCD from including only ground-state ionization (SCD_{gr}) declines exponentially, reaching roughly three times SCD_{gr} at 25 eV. The solid blue line, omitting the $2p^5$*np*, *nd*, and $4f$ ionizations, further suggests most of the excited-state contribution comes from the *ns* series, while the solid red line, omitting the *nd* and $4f$ ionizations, suggests the *nd* and $4f$ ionizations contribute less than one percent to the SCD. At 25 eV, the $4s$ ionization contributes the most to the effective ionization, followed by the ground and $3s$ ionizations. Given the strong dipole-allowed radiative rates that depopulate the *ns* states, one might think that they may not contribute significantly to the ionization. Yet, the populations of the *ns* states is quite large, due to cascades from higher *np* states and direct excitation from the ground, leading to a larger contribution to the SCD.

The Exchange Classical Impact Parameter (ECIP) method [32], a semi-classical approach, was used for comparison with the new RMPS-545 ionization data. The ECIP method has been recommended in the past over configuration-averaged distorted-wave for use in accounting for excited states when non-perturbative data is not available [55]. We replaced the RMPS-545 rate coefficients for ionization from the *np*, *nd*, and $4f$ orbitals with ECIP rate coefficients, and the resulting SCD matched what would be obtained from excluding these higher excited state rate coefficients from modeling. Ionization cross sections from *n*-scaling of the *R*-matrix data for the $4d$ and $5p$ orbitals converged with calculated ones (see Fig. 3.13) suggesting that *n*-scaling of the R-matrix data would be more accurate than using semi-classical or distorted-wave data for these states.

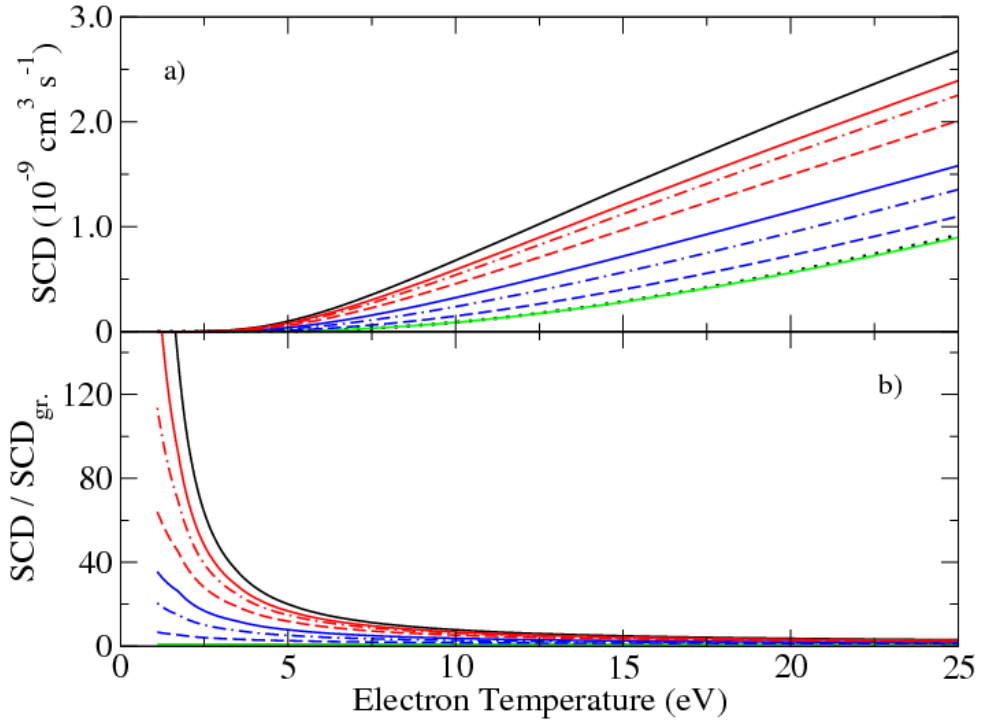

Figure 3.16: a) The effective ionization rate coefficient (SCD) (cm^3 s^{-1}) versus electron temperature (eV). The dotted and solid black lines show the SCD including all possible states at electron densities of 10^4 and 10^{14} cm^{-3} respectively. The ionization rate coefficient of the ground only (solid green) is roughly a factor of three lower at 25 eV and 10^{14} cm^{-3}. The dashed, dot-dashed, and solid blue lines show the SCD if including the ground as well as the $2p^5 3s$; $3s$ and $4s$; and $3s$, $4s$, and $5s$ states respectively. The dashed, dot-dashed, and solid red lines include the ground and *ns* states, as well as the $3p$; $3p$ and $4p$; and $3p$, $4p$, and $5p$ states respectively. b) The ratio of the SCDs to the SCD if only the ground state ionization rate coefficient is included (SCD$_{gr}$).

3.5.1 Infinite-energy point extrapolation and additional rate coefficient processing

Though the neon atomic data is to be used primarily in the divertor region, it can also serve useful in other plasma situations, such as in the presence of Edge Localized Modes, or ELMs, during which the electron temperature in parts of the edge region can suddenly reach $>$ 100 eV citeelms. For the electron-impact ionization data, in which the extracted cross sections all

extended past the ionization peaks, higher temperature rates could be properly extracted from Younger fits. Extrapolation of electron-impact excitation rates for higher temperatures requires a more thorough treatment based on the classification of transition, i.e., whether it is dipole-allowed, optically forbidden, etc.

Burgess and Tully [78] outline a method for extrapolating electron-impact cross sections using infinite energy points dependent on transition type. The procedure, assuming a Maxwellian electron distribution, requires scaling of the energy (electron temperature) to a dimensionless variable from 0 (threshold energy) to 1 (infinite energy), and of the effective collision strengths from 0 to value y in a unique Burgess-Tully. The manner of scaling is distinguished by transition type as follows:

Type 1 - dipole-allowed transitions, non-zero oscillator strengths f_{ij}

$$x = 1 - \frac{lnC}{ln(\frac{kT}{E_{ij}} + C)}$$

$$y(x) = \frac{\Upsilon_{ij}}{ln(\frac{kT}{E_{ij}} + e)} \tag{3.1}$$

Type 2 - optically-forbidden (multipole) transitions

$$x = \frac{(\frac{kT}{E_{ij}})}{(\frac{kT}{E_{ij}} + C)}$$

$$y(x) = \Upsilon_{ij} \tag{3.2}$$

Type 3 - change in ion spin with negligible magnetic interactions

$$x = \frac{(\frac{kT}{E_{ij}})}{(\frac{kT}{E_{ij}} + C)}$$

$$y(x) = (\frac{kT}{E_{ij}} + 1)\Upsilon_{ij} \tag{3.3}$$

Type 4 - dipole-allowed transitions, but with small f_{ij}

$$x = 1 - \frac{lnC}{ln(\frac{kT}{E_{ij}} + C)}$$

$$y(x) = \frac{\Upsilon_{ij}}{ln(\frac{kT}{E_{ij}} + C)} \tag{3.4}$$

E_{ij} represents the difference in energies between the final and initial levels, kT the electron temperature, and C an adjustable parameter. A good test of the quality of the higher-energy electron-impact excitation data is whether the extrapolation with the above scaling trends towards the expected infinite energy points, defined as follows:

Types 1 and 4:

$$y(1) = \frac{4w_i f_{ij}}{E_{ij}} \tag{3.5}$$

Type 2:

$$y(1) = \text{high energy limit of } \Omega \tag{3.6}$$

Type 3:

$$y(1) = \int_0^\infty \Omega d(\frac{E_j}{E_{ij}}) \tag{3.7}$$

Ω represents the collision strength, E_j the incident electron energy, and w_i the statistical weight of the lower level. The infinite energy points for Types 1 and 4, 2, and 3 can be derived from the Bethe [106], Born, and Ochkur approximations respectively [78]. Types 1 - 3 have an initial $x(0) = \Omega(0)$, while $x(0) = \frac{\Omega(0)}{ln(C)}$ for Type 4.

We therefore extrapolate the electron-impact excitation cross section rate coefficients for electron temperatures greater than 25 eV and use the infinite energy points as an accuracy check. Extrapolation of higher temperatures was performed using the most recent version

of adasexj.f, which includes extrapolation towards infinite energies. Prior to running adasexj.f, the 20% threshold on adjacent energy points was applied to the *R*-matrix cross-sectional OMEGA file. A separate OMEGA file, as well as an input file for adasexj.f, was generated for the infinite energy points from AUTOSTRUCTURE [83]. Through setting "BORN=INF" and "RAD=ALL", AUTOSTRUCTURE will calculate infinite energy points with a Breit-Pauli structure using the above approximations based on their transition type [107]. Prior to running adasexj.f, three pre-processing steps must be performed. 1) Transitions involving levels corresponding to pseudo orbitals must be removed from each OMEGA file prior to running adasexj.f. For neon, the first 79 levels were therefore retained. 2) The infinite energy OMEGA file must be reordered such that its levels correspond to the *R*-matrix file. This processing step can be accomplished from the utility code "omorder.f" The input file for adasexj.f generated from AUTOSTRUCTURE must similarly be reordered. This task was accomplished by a custom suite of Python code, "adf04utility.py", discussed in Appendix refpycodes. 3) The OMEGA files from the *R*-matrix and AUTOSTRUCTURE infinite energy runs must then be combined into one OMEGA file. Removal of energy points via a threshold must be done on the *R*-matrix OMEGA file without the infinite energy point.

Figures 3.17 - 3.20 show Burgess-Tully plots for each type from selected transitions, using the set of effective rate coefficients generated from the adasexj.f code. The variables follow the x and y relations defined in the previous discussion. The plots include the infinite energy points, indicated by a triangle, for Types 1 and 4, the dipole-allowed types. The other triangle on the indicates the point where extrapolation begins. Extrapolated effective rate coefficients in the Burgess-Tully space are indicated by the dotted line for types 2 and 4. A few hundred of the 3081 total transitions were examined, including transitions from higher excited states. In general, the infinite energy points and high temperature extrapolation show reasonable agreement with the trends of the rate coefficients.

Following high temperature excitation rate coefficient extrapolation, additional adf04 processing needed to be performed. Both level energies and A_{ij}-values for spontaneous emission were replaced with those of NIST [86]. Due to the rounding of energies in the OMEGA files,

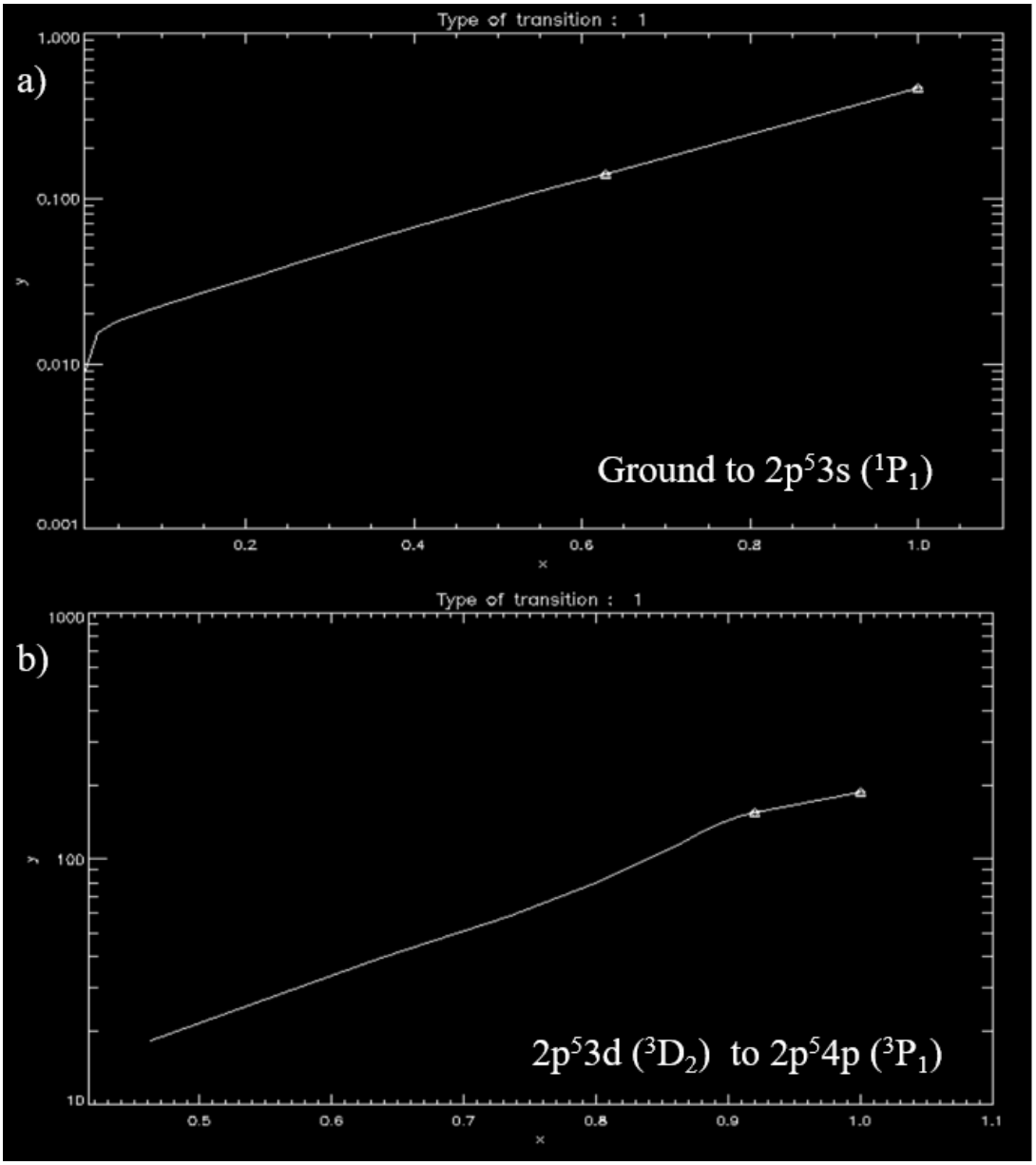

Figure 3.17: Selected Type 1 (dipole-allowed) transitions in Burgess-Tully space. a) and b) are transitions from the ground and higher excited states respectively. The first triangle indicates where the extrapolation begins and the second the infinite energy point.

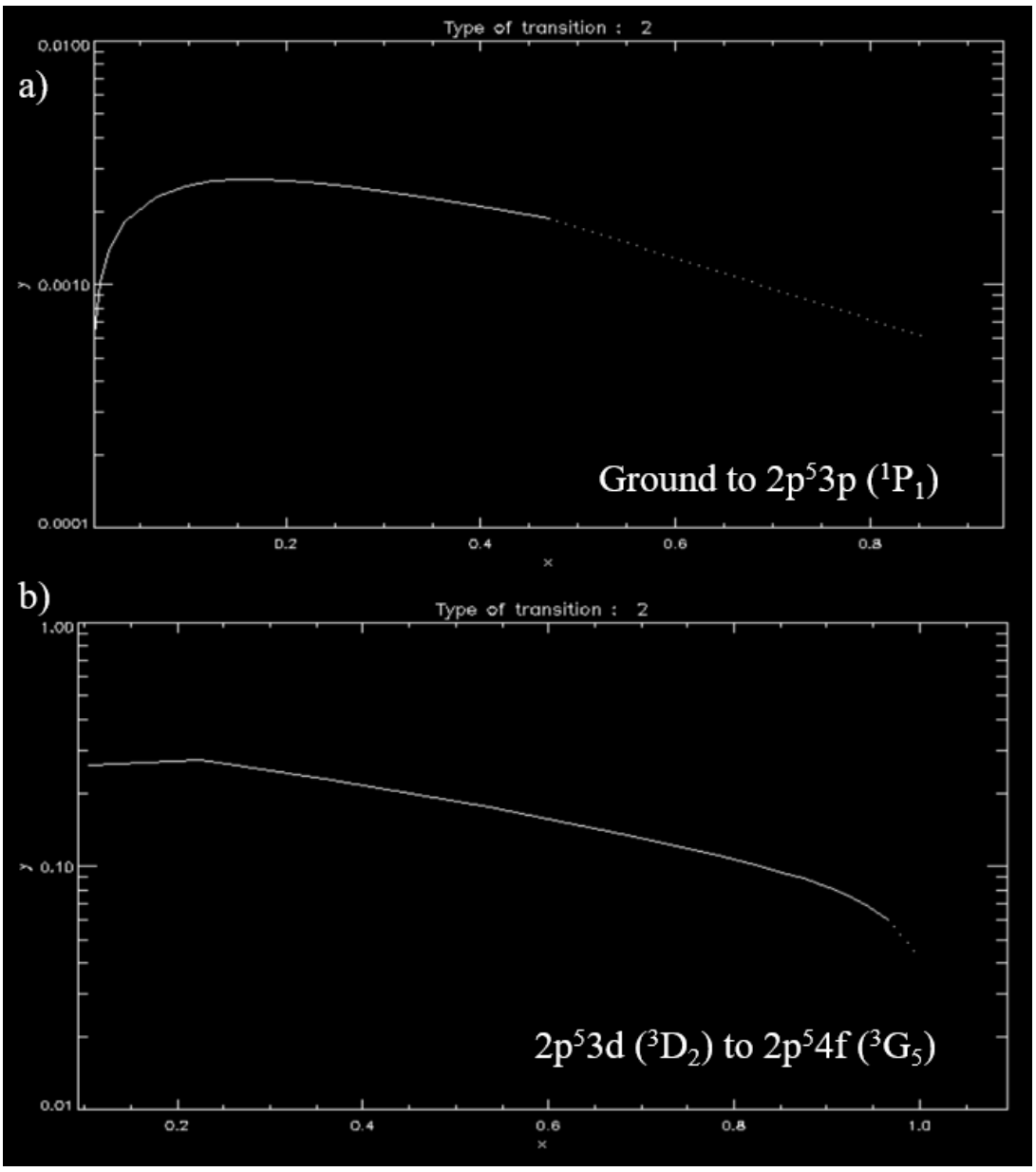

Figure 3.18: Selected Type 2 (optically-forbidden) transitions in Burgess-Tully space. a) and b) are transitions from the ground and higher excited states respectively. The dotted lines indicate extrapolated rate coefficients.

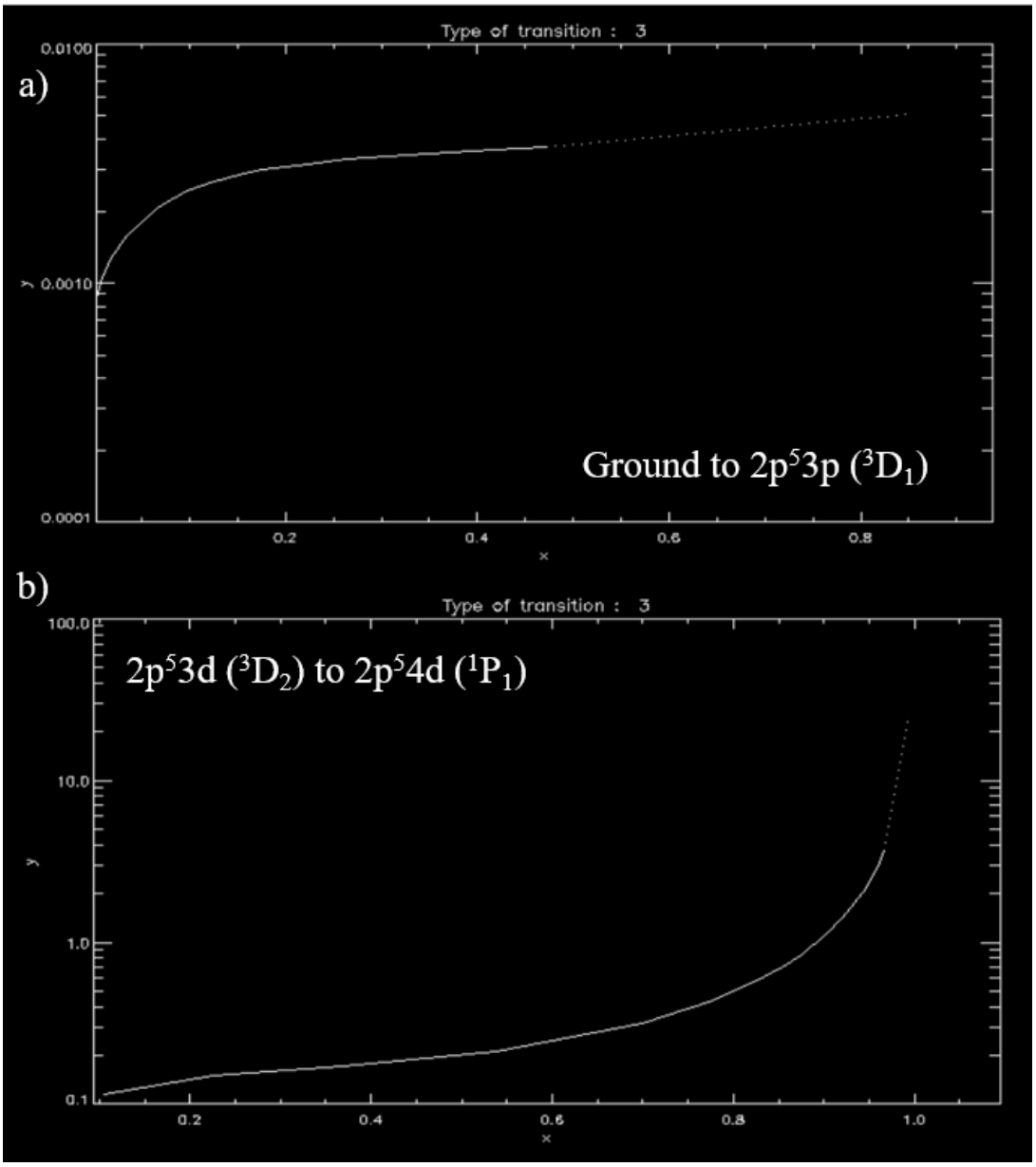

Figure 3.19: Selected Type 3 (spin-change) transitions in Burgess-Tully space. a) and b) are transitions from the ground and higher excited states respectively. The dotted lines indicate extrapolated rate coefficients.

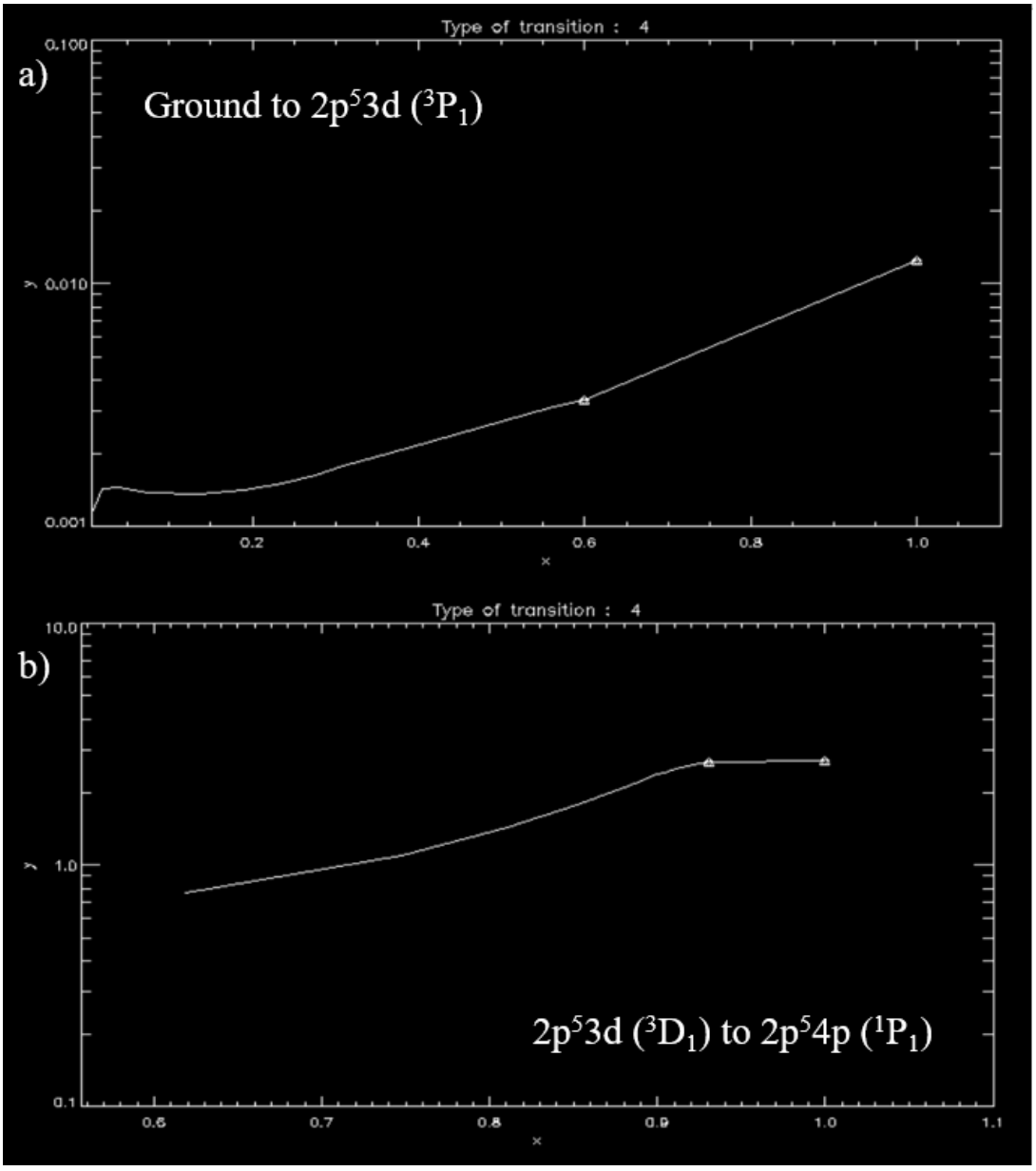

Figure 3.20: Selected Type 4 (dipole-allowed, small f_{ij}) transitions in Burgess-Tully space. a) and b) are transitions from the ground and higher excited states respectively. The first triangle indicates where the extrapolation begins and the second the infinite energy point.

this switch resulted in a couple of levels being out of order. These levels were therefore re-ordered throughout the OMEGA file using the Python utility code "adf04utility.py". As a result, two transitions corresponding to the switched levels (58/59 and 73/74) were now in reverse order, such excitation was assumed from the higher level down to the lower level (58 - 59 and 73 - 74). These were manually switched around, and the A-values were converted by the ratio of the statistical weights.

Recombination rates were also added, using the ADAS codes for the latter [36].

3.6 Summary and Conclusions

Using new semi-relativistic non-perturbative RMPS calculations for the electron-impact excitation and ionization of neon, we obtained cross sections that generally agreed with previous ones and that were then used to generate reliable spectral data for any range of temperatures and densities. We performed new electron-impact excitation and ionization calculations for neutral neon at low energies that included more pseudostates than previous calculations and showed convergence for ionization from all excited states through $2p^5 5p$.

The $2p5ns(^3P)$ series in comparison to Ballance *et al.* [55] demonstrated the increased pseudostate coverage of our calculation at higher *n*'s, in which the $5s$ (^3P) ionization cross section experienced a 20% increase across all energies. Ionization of valence electrons from the $4d$ and $5p$ orbitals both fit well to an n^4 scaling using the $3d$ and $4p$ cross sections. This follows the trend expected classically, as also seen with B, B^+, and B^{2+} [103].

The effect of excited-state ionization on the effective ionization rate coefficient, in which the excited states contributed as much as three times the ground state at high density (10^{14} cm^{-3}) and 25 eV electron temperature, highlights its importance in proper GCR modeling throughout all temperature ranges. Most of the excited state contribution comes from the $2p^5ns$ series, despite being dipole-allowed to the ground state. This can be explained by the low electron-impact excitation rates to the *nd* levels, as indicated by their cross sections, as well as by the dipole-allowed spontaneous emission from the *np* levels to the *ns* levels. For divertor applications, the effective ionization rate becomes increasingly significant from T_e = 5 to 10 eV. The differences in the SCD from a divertor temperature range to the edge region temperature

range (T_e = 20 to 25 eV [47]) will impact comparisons made at W7-X between He and Ne lines in the two regions [47].

We further tested the effectiveness of the semi-classical ECIP ionization rate coefficients for higher excited states. ECIP rates usually fall below non-perturbative approaches, whereas the configuration-averaged distorted-wave (CADW) perturbative method leads to diverged cross sections for higher excited states for near neutral systems. The ECIP rate coefficients underestimated the contribution of $2p^5$*np* and *nd* valence shell ionization to the SCD. However, R-matrix ionization cross sections of the higher *n* states showed good agreement with *n*-scaling of the lower *n*-shell *R*-matrix data. **This work therefore indicates a pattern that can be used for other elements: perform non-perturbative calculations to achieve cross sections for as high in *n* as possible or until *n*-scaling is attained and then use *n*-scaling for higher excited-state ionization rate coefficients.**

There is also a question on what level of resolution in the angular momentum coupling is appropriate for the final datasets. For elements below neon, it is normal to use LS-resolved data with the assumption that the J-levels are statistically populated due to proton-ion collisions. For elements above Ne, one normally uses J-resolution, since the splitting in the level energies is making ion collisions less efficient at redistributing in J. For neon, we generated both LS and LSJ files, along with a recommendation for line ratios to determine which is appropriate for a particular plasma. They involve transition pairs of different J-values going to the same final state. The two transition pairs are:

$2p^5 3p(^3D_3)$ - $2p^5 3s(^3P_2)$, λ = 640.225 nm;
$2p^5 3p(^3D_2)$ - $2p^5 3s(^3P_2)$, λ = 633.443 nm

and

$2p^5 3p(^3P_2)$ - $2p^5 3s(^1P_1)$, λ = 667.828 nm;
$2p^5 3p(^3P_1)$ - $2p^5 3s(^1P_1)$, λ = 659.896 nm.

LS-resolution is appropriate when the ratio of the statistically weighted A-values of each transition pair is close to the observed line ratio. Both LS- and LSJ-resolved atomic

data were thus compiled, containing the most accurate set of electron-impact excitation and ionization as well as dielectronic and radiative recombination rate coefficients to date.

In summary, we have generated new electron-impact excitation and ionization data for neutral Ne and investigated the contributions to the effective ionization rate coefficient from the excited states. The datafiles have been made available to the community through the ADAS database.

Chapter 4

Electron-Impact Ionization R-matrix with Pseudostates Calculations for Neutral Tungsten

4.1 Introduction

The aim of this chapter is to calculate and investigate the electron-impact ionization of the ground and metastable states of neutral tungsten using the non-perturbative R-matrix with psueodstates method. At present, only a small number of non-perturbative electron-impact collision calculations have been performed for high-Z neutral atoms, except molybdenum [108, 109] and the recent electron-impact excitation Dirac *R*-matrix calculation and ionization TDCC calculation by Smyth *et al.* [41] and Pindzola *et al.* [71] respectively. Modeling of high-Z elements presents a challenge in that they are relativistic and can contain open $d-$ and $f-$ subshells.

Unlike previous neutral tungsten electron-impact ionization calculations, the RMPS method allows for coupling between all sets of channels, including those of different ionization pathways. Aside from the present work, the only other non-perturbative electron-impact ionization calculation of neutral tungsten was performed by Pindzola *et al.* [71] using the Time-Dependent Close-Coupling (TDCC) method [68] for the $5d$ and $6s$ ionization out of the $5d^4 6s^2$ ground state configuration. The calculation, which uses orbitals derived from a semi-relativistic Hartree Fock structure [61], solves the close-coupling equation for a configuration-averaged case and considers each orbital ionization separately (i.e., no coupling between different channels). The TDCC results were compared to relativistic Distorted Wave (R-DW) calculations, for which the $6s$ ionization cross section is systematically slightly below R-DW and about three-fifths below R-DW for $5d$ ionization. The TDCC's $5d$ ionization peaked much higher in

incident electron energy than R-DW: 75 eV compared to 40 eV. The configuration-averaged TDCC calculation had a distorted wave top-up applied for partial-waves beyond l = 5. Ionization from the metastable $5d^5 6s$ ($^7S_3$) state, 0.37 eV above the ground state [29], was also not considered.

Other calculations, all either perturbative or semi-classical, similarly do not include channel-coupling effects and for the most part assume configuration-resolved collisions. This includes the two datasets, ECIP from ADAS [31, 32] and the Born and Born-Ochkur ground state calculations by Beigman *et al.* [11], that have been used for generating and comparing S/XB ratios. Kwon *et al.* [110] calculate the $5d^4 6s^2$ (^5D) and metastable $5d^5 6s$ (^7S) ionization cross sections using the semi-classical binary-encounter Bethe (BEB) model. Their calculation uses a binding energy, kinetic energy (involving the momentum expectation value), and occupation number of the orbital derived from a relativistic multiconfiguration Dirac-Fock (MCDF) structure [111]. Unlike these calculations, the R-DW method of the HULLAC codes, employed by Purohit *et al.* [112], uses a fully relativistic LSJ- rather than configuration-averaged basis set to represent the continuum orbitals. $LS-$ or $LSJ-$ resolved non-perturbative results that include both the ground and metastable states, as well as account for the expected high amount of configuration mixing, would enhance the ionization data available for neutral W.

As discussed in Chapter 1, the primary motivation of the present work is therefore to provide a complementary calculation to the excitation calculation by Smyth *et al.* [41] that can yield accurate electron-impact cross sections for ionization out of the ground, metastable, and excited states in order to obtain an accurate S/XB. The generation and specifications of the neutral tungsten target structure used in the electron-impact ionization calculation are described in Section 4.2. Computational details are provided in Section 4.3. This is followed in Section 4.4 by results from convergence checks on the highest spin set of partial-waves, the octets, which contain many less coupled channels than the sextet or quartet partial wave sets. Metastable and ground state cross sections are reported and analyzed in Sections 4.5 and 4.6. An approximation supported by the metastable cross sections, that the two coupling spin sets contribute roughly equally to a term's ionization cross section, is used to generate the ground state cross section, in which the sextet partial wave contribution is doubled rather than calculate

the quartet partial-waves. The results from both the ground and metastable ionizations suggest the importance of incorporating a complete list of configuration series corresponding to each single-electron ionization pathway and, further, that the ionization processes out of the ground ^5D and metastable ^7S terms are interfering with each other, leading to behavior distinguished from previous methods where coupling between channels was neglected.

4.2 Neutral Tungsten Atomic Structure Details

As explained in Section 1.3, the atomic structure of neutral tungsten is challenging due to the high level of mixing present between the three open $d-$shell configuration series, 5d^{4}6s*nl*, 5d^5 *nl*, and $5d^36s^2nl$. Figure 1.3 also depicted the four possible ionization pathways from the $5d^46s^2$ (^{5}D) ground and $5d^56s$ (^{7}S) metastable states arising from $5d$ and $6s$ ionizations. It will be shown in Section 4.4 that all three of the main series must be included in the structure for proper convergence of ionization cross sections. Before proceeding further, it is important to note the use of the words "ground" and "metastable" as they are used in the present discussion regarding neutral tungsten. It is likely that additional excited states of neutral tungsten are behaving like metastable states. However, a general analysis of which states are metastable is beyond the scope of this dissertation, and a method to determine which states are metastable has discussed by Johnson *et al.* [41]. For this work, the ^5D ground, ^7S metastable, and excited state ionization cross sections are calculated and labeled thus. The user of the data is then free to include some of the excited states as metastables in their collisional-radiative modeling.

Another challenge in obtaining an accurate neutral tungsten structure is a lack of available data regarding energy levels and A-values. Based on the set of experimentally measured W I energy levels and transitions compiled by Kramida and Shirai [42], many gaps still persist in neutral tungsten energy level identification, particularly for the $5d^36s^2nl$ series. Quinet *et al.* 2010 and 2011 [113, 114] performed HFR parametric fits similar to that of Wyart [59], but with expanded sets of configurations. Both Quinet *et al.* [114] and Wyart show good agreement with both experimental level energies and transition probabilities. Though Wyart used a limited number of configurations and thus agrees less well, the mean error of his energy levels is 131 cm^{-2}, or around 0.016 eV.

Smyth *et al.* iteratively refined their relativistic structure in tandem with spectral observations from a tungsten probe inserted into the Auburn University Compact Toroidal Hybrid (CTH) [41]. Their structure calculation utilized the relativistic multiconfigurational Dirac-Fock (MCDF) method, which optimizes the $(2J + 1)$-weighted trace of the Dirac-Coulomb Hamiltonian. Their final 25 configurations included $5d^4\{6s^2, 6p^2, 6d^2, 6s6p, 6s6d, 7s^2, 7p^2\}$; $5d^5\{6s, 6p, 6d, 7s, 7p\}$; $5d^3\{6d^3, 6s^27s\}$; $5d^6$; $5p^5\{5d^7,5d^66s\}$; $5p^4\{5d^8, 5d^66s^2, 5d^76s\}$; and $5s5p^65d^7$, leading to 7,825 levels. These configurations were chosen to cover the 200 - 500 nm range of fine-structure lines observed by the CTH tungsten probe, which includes the range of lines being considered for the S/XB diagnostic. This structure was further employed in their electron-impact excitation Dirac *R*-Matrix calculation. To fit their DARC calculation within computational constraints, they were unable to include pseudostates in their structure and therefore excluded core polarization and continuum coupling effects. Nevertheless, their structure shows good agreement with Kramida and Shirai [42], with an average error of 11% in their 250 level energies. After shifting to these experimental energies, their transition rates show agreement anywhere from 0.02% to 35% for select strong dipole transitions and those relevant to a possible S/XB diagnostic. The excitation data, when used in collisional-radiative models has been shown to produce good agreement with CTH spectral measurements of W I emission. Thus, it seems likely that the electron-impact excitation data is of good quality. The Smyth *et al.* [41] calculation was for electron-impact excitation and did not include pseudostates. Thus no ionization cross sections could be extracted. In this chapter we use the RMPS method to calculation ionization data to supplement the available excitation data from Smyth *et al.* [41].

To keep the current electron-impact ionization calculation within RAM and I/O constraints, certain compromises to the structure had to be made while still preserving an accurate representation of neutral tungsten's ionization. Similar to the previous electron-impact ionization *R*-matrix calculation for W^{3+} [67], the calculation was constrained to *LS*-resolution, though structure was optimized from the levels obtained through intermediate coupling. Optimization of an *LS*-resolved structure based on the level-averaged term energies of NIST [29] had also been considered; however, these level-averaged energies would not properly represent

the *J*-resolved nature of neutral tungsten. That is, the assumption of a statistically weighted population between an *LS* term's levels may no longer be valid. Furthermore, the term-resolved $5d^5 6s$ (^7S) is 0.186672 eV below $5d^4 6s^2$ (^5D), reversing the order of the ground and metastable terms compared to their levels. To best reflect the *LSJ* resolution of tungsten while still fitting the ionization calculation into modern computational resources, an *LS*-resolved RMPS calculation optimized by the levels expected from intermediate coupling is thus performed, and the final *LS* cross sections are recoupled back into *LSJ* using a modified version of the Sampson branching ratios [77], described in the next section.

The atomic structure package AUTOSTRUCTURE [83] was employed, using a Thomas-Fermi-Dirac-Amaldi (TFDA) statistical potential to generate wavefunctions for the radial spectroscopic orbitals. Non-orthogonal Laguerre pseudo orbitals were also included to represent the continuum in the structure. These pseudo orbitals are important not only because they represent ionized states for energy levels above the ionization potential, but also because they can account for configuration interaction between the spectroscopic and continuum states, a particularly strong effect for neutral atoms.

The addition of these pseudostates significantly increases the number of terms and levels in the calculation. It was therefore important to limit the number of pseudostates to be just enough for convergence of the final electron-impact ionization cross section. Limitations on the pseudo orbitals were further imposed due by the orthogonality constraints imposed by the continuum orbitals in the *R*-matrix calculation and also the *R*-matrix box size. A suitable structure could not be found such that pseudo orbitals beyond $\bar{n}$ = 11 were included while orthogonality with the continuum orbitals was attained, and that the wave-functions attenuated to an acceptably small value inside the *R*-matrix box. Similar issues also required making the 4f and 4g into pseudo orbitals. Further convergence checks were made on what angular momentum range would lead to RMPS convergence, described in the next section, and convergence was seen for $\bar{l}$ = 5, similar to the findings of [67]. Pseudo states thus extended from $6\bar{f}$ to $1\bar{1}h$, including also $4\bar{f}$ and $4\bar{g}$, and they included 5d^{4}6s$\bar{nl}$, $5d^3 6s^2 \bar{nl}$, and $5d^5\ \bar{nl}$ configurations, reflecting $6s$ and $5d$ ionization from both the ground and metastable levels.

Table 4.1: Neutral tungsten orbital scaling parameters that were held consistent between competing structure models.

1s	2s	2p	3s	3p	3d
1.39098	1.1317	1.0844	1.07701	1.05743	1.04124
4s	4p	4d	4f	5s	
1.03131	1.02228	1.00507	0.99319	1	

Choosing a concise set of spectroscopic configurations required further trade-offs regarding optimization of the energy levels and transition rates. We limited the number of spectroscopic configurations compared to those used by Quinet *et al.* [114] and Smyth *et al.* [41], which were more targeted towards a high accuracy of the fine structure. Because the cross sections going into states above the ionization potential are summed over, less fine structure accuracy is required. Therefore, our structure followed a similar direction to Wyart [59], who obtained relatively good agreement for both level energies and transition rates, in that we primarily considered spectroscopic configurations from the $5d^4 6snl$, $5d^5$ *nl*, and $5d^3 6s^2 nl$ series.

Over one hundred structure runs were performed that varied additional configurations and lambda parameters, and each selection carried with it both benefits and costs. Table 4.1 lists the orbital scaling parameters that were not in general changed during structure runs. These parameters were obtained from a general structure run optimizing for the lowest energy levels. Most of the structure optimization were performed through modifying the $5p$, $5d$, $6s$, and $6p$ orbital scaling parameters. Table 4.2 shows these orbital scaling parameters for five considered structures. Out of these, Structure No. 1 was the final one that was used to generate the orbital wavefunctions used in the R-matrix calculation. Structures No. 4 and 5 contain additional configurations $5d^4 6p^2$ and $5p^5 5d^7$.

Evaluating structures based on energy and A-value accuracy proved challenging, as no single structure stood out prominently from the rest; each candidate structure had costs associated with any gains. The best target structure for electron-impact ionization was chosen based on the following criteria: 1) agreement of the ground and metastable level energies to NIST values and 2) agreement of the highest level dipole transition rates to those available in NIST and Smyth *et al.* [41], giving preference to NIST. The largest contribution to the ionization cross sections should be from dipole transitions into states above the ionization potential. The

Table 4.2: Orbital scaling parameters for a sample of candidate structures of the neutral tungsten electron-impact ionization *R*-matrix calculation. Structure No. 1 corresponds to the one chosen. Configurations include $5p^4 5d^6 6s^2$ and $5d^6$ for mixing effects in addition to the $5d^4 6s$ *nl*, $5d^5$ *nl*, and $5d^3 6s^2$ *nl* series. Structures No. 4 and 5, starred, contain additional configurations $5d^4 6p^2$ and $5p^5 5d^7$.

Structure No.	$5p$	$5d$	$6s$	$6p$
1	1	0.96978	0.985	1.12
2	1	0.9689	1	1.12
3	1.02	0.9631	1	1.125
4*	1	0.9646	0.985	1.107
5*	1	0.9644	0.985	1.107

transition rate with the highest upper level energy from NIST is $5d^4 6s6p$ ($^5P_1$) - $5d^4 6s^2$ ($^5D_0$) and from the structure of Smyth *et al.* is $5d^5 6p$ ($^5P_1$) - $5d^4 6s^2$ ($^5D_0$).

Tables 4.3 and 4.2 show comparisons of the first 15 energy levels and selected A-values. The candidate structure are all within reasonable agreement with NIST, each less than 13% average difference across all levels and with the correct ground state. Because we do not attempt to calculate ionization from the triplet states, prioritization is given to ground and metastable state accuracy, for which structures 1 and 2 show the best agreement, within a 3% average difference.

The A-value comparison shown in Table 4.2 demonstrates much more sensitivity to small changes in the orbital scaling parameters. Included also is a comparison with the DARC calculation's set of A-values [41]. The transitions are all dipole-allowed, and include strong transitions of ground and metastable lower levels. Experiments at CTH were performed in tandem with the DARC calculation [41], resulting in the identification and classification of new neutral tungsten lines. As a result, some of the labeling between NIST and the DARC calculation differs. The higher level configuration labels of the first two transitions, for example, are switched for the DARC calculation. Matching of A-values was therefore performed using the actual energies recorded for both NIST and DARC, and the configurations listed correspond to those from the DARC calculation.

For these transitions, Structure No. 1 has the best average percent difference with both NIST and DARC. A tradeoff can be observed with the $5d^4 6s6p$ ($^7P_2$) - $5d^5 6s$ ($^7S_3$) A-value, for which Structure 1 differs with NIST by 153.29%. Although this is a strong transition, its

Table 4.3: Comparison of the first 15 energy levels of sample candidate structures with NIST. The average percent differences are only from the levels shown in the table.

			Level Energies by Structure No.				
Configuration	J	NIST	1	2	3	4	5
$5d^46s^2(^5D)$	0	0.0000	0.0000	0.0000	0.0000	0.0000	0.0000
	1	0.0152	0.0146	0.0141	0.0113	0.0125	0.0124
	2	0.0303	0.0305	0.0294	0.0243	0.0266	0.0265
	3	0.0440	0.0455	0.0440	0.0372	0.0405	0.0403
	4	0.0567	0.0597	0.0580	0.0499	0.0541	0.0538
$5d^56s(^7S)$	3	0.0269	0.0269	0.0266	0.0265	0.0282	0.0271
$5d^46s^2(^3P)$	0	0.0868	0.1059	0.1037	0.0977	0.1016	0.1014
	1	0.1213	0.1459	0.1436	0.1341	0.1378	0.1375
	2	0.1755	0.1692	0.2043	0.1906	0.1983	0.1975
$5d^46s^2(^3H)$	4	0.1108	0.1361	0.1345	0.1266	0.1303	0.1301
	5	0.1373	0.1649	0.1631	0.1517	0.1561	0.1558
	6	0.1550	0.1835	0.1819	0.1690	0.1742	0.1739
$5d^46s^2(^3G)$	3	0.1216	0.1505	0.1480	0.1384	0.1430	0.1426
	4	0.1497	0.1864	0.1829	0.1691	0.1699	0.1695
	5	0.1807	0.2117	0.2084	0.1919	0.1981	0.1975
Avg. % Diff.			12.38	12.33	11.55	11.72	11.41
% Diff, Gr. and Meta.			2.21	2.88	11.06	6.81	6.27

upper level, at 3.25 eV, is far from the ionization potential. Agreement with the two highest transitions in DARC and on NIST is overall best for Structure 1 as well. Although Structure 2 agrees better with DARC for $5d^56p$ ($^5P_1$) - $5d^46s^2$ ($^5D_0$), at 33.51%, it shows much more disagreement for the other highest transition, $5d^46s6p$ ($^5P_1$) - $5d^46s^2$ ($^5D_0$). In general, all of the candidate structures show highly varying amounts of agreement for different A-values. Furthermore Structures 4 and 5, in which additional mixing configurations were added, showed worse agreement for nearly all of the transitions compared to Structure 1.

Table 4.4: A-value comparison with both NIST and those from the Dirac structure of [41] for select transitions. No. 1, the one chosen, agreed the most for these transitions.

Initial	$6s6p(^7P_2)$	$d^56p(^7P_2)$	$6s6p(^7D_1)$	$6s6p(^5F_1)$	$6s6p(^7D_1)$	$6s6p(^5F_2)$	$6s6p(^5P_1)$	$d^56p(^5P_1)$	
Final	$5d^56s(^7S)$	$d^56s(^7S)$	$6s^2(^5D_0)$	$6s^2(^5D_0)$	$6s^2(^5D_1)$	$6s^2(^5D_1)$	$6s^2(^5D_0)$	$6s^2(^5D_0)$	
NIST A Value	44800000	161000000	2290000	10300000	37600000	13300000	6900000	87800000	
DARC A Value	12400000	108000000	NA	830000	1900000	2140000	3200000	NA	
No. 1	31408100	203000000	2432000	857550	276552	94507.5	2776600	26492800	**Average %**
DARC %	29.89	26.09	6.20	91.67	99.26	99.29	59.76	69.83	60.25
NIST %	153.29	87.96	NA	3.32	85.44	95.58	13.23	NA	73.14
No. 2	23529000	354780000	820225	299500	282670	157241	16485600	117220000	**Average %**
DARC %	47.48	120.36	64.18	97.09	99.25	98.82	138.92	33.51	87.45
NIST %	89.75	228.50	NA	63.92	85.12	92.65	415.18	NA	162.52
No. 3	52762700	803122	58452.5	277100	564000	1187290	1811100	124440000	**Average %**
DARC %	17.77	99.50	97.45	97.31	98.50	91.07	73.75	41.73	77.14
NIST %	325.51	99.26	NA	66.61	70.32	44.52	43.40	NA	108.27
No. 4	1969600	332050000	1425650	354700	1829890	1398800	5211500	41009600	**Average %**
DARC %	95.60	106.24	37.74	96.56	95.13	89.48	24.47	53.29	74.82
NIST %	84.12	207.45	NA	57.27	3.69	34.64	62.86	NA	75.00
No. 5	1692200	338540000	1423600	372200	1827300	1340110	5665240	16638300	**Average %**
DARC %	96.22	110.27	37.83	96.39	95.14	89.92	17.90	81.05	78.09
NIST %	86.35	213.46	NA	55.16	3.83	37.38	77.04	NA	78.87

The final structure included $5p^4 5d^6 6s^2$ and $5d^6$ for configuration-mixing effects in addition to the $5d^4 6s$ *nl*, $5d^5$ *nl*, and $5d^3 6s^2$ *nl* series. Because including $5d^4 6p^2$ and $5d^5 5d^7$ led to larger differences in A-values compared to NIST and Smyth *et al.* [41], these configurations were left out. Table 1 shows a selected level and transition rate comparison of this structure with NIST and Smyth *et al.* [41].

A more complete list of level and term energy comparisons for the structure is provided in Appendix C. The final structure included 15,960 terms, which leads to 40,994 levels. Energies differed an average of 15.91% and 31.23% from terms and levels respectively for those available on NIST.

4.3 Computational Details

Similar to the electron-impact ionization calculation of neutral neon outlined in Section 3.2.2, the *R*-Matrix with Pseudostates (RMPS) method was used to determine the electron-impact ionization cross sections of the metastable and ground state of neutral tungsten. The RMATRX I suite of codes, including stages 1, 2, 3, and f, were once again used [60], described in Section 2.4.3. The ionization cross sections were obtained from summing transitions into pseudostates above the ionization potential.

Recall, a general constraint on an *R*-matrix calculation is that the target radial wavefunctions must become vanishingly small at the *R*-matrix box radius. To satisfy these constraints, a solution to the target and continuum orbitals could only be obtained if the $5f$ and $5g$ orbitals were pseudo-orbitals and if the pseudo-orbitals did not extend past n = 11. A structure calculation extending to n = 12 indicated the $1\bar{2}l$ pseudostate terms all occurred above 16.5 eV. We therefore chose a basis set size of 29 to fully cover the incident electron energy range up to this point. The *R*-matrix box radius was set to 69 atomic units.

Stage 2, which sets up and calculates the upper triangle of the inner region Hamiltonian for the N and N + 1 system, required code development both to allow for neutral tungsten's closed f-subshell and to increase computational efficiency. The codes currently allow for only up to 2 electrons in shells where l >2. The H_{N+1}, due to its making the continuum electron indistinguishable from the other N electrons, requires up to two active electrons in the f-subshell. The

Table 4.5: Neutral tungsten term energy comparison with NIST.

Configuration	Term	NIST Energy (Ryd)	Present Work Energy (Ryd)	Percent Difference
$5d^46s^2$	^5D	0.0000	0.0000	0.00
$5d^5(^6S)6s$	^7S	-0.0137	-0.0488	71.91
$5d^46s^2$	$^3P2$	0.1069	0.1136	5.88
$5d^46s^2$	^3H	0.0964	0.1313	26.52
$5d^46s^2$	^3G	0.1144	0.1290	11.28
$5d^46s^2$	$^3F2$	0.1099	0.1223	10.16
$5d^46s^2$	^3D	0.1036	0.1318	21.43
$5d^5(^4G)6s$	^5G	0.1350	0.1378	2.08
$5d^5(^6S)6s$	^5S	0.1260	0.1244	1.30
$5d^46s(^6D)6p$	^7F	0.1918	0.3412	43.78
$5d^5(^4P)6s$	^5P	0.1447	0.1652	12.42
$5d^46s^2$	$^1S2$	0.1432	0.1403	2.09
$5d^46s(^6D)6p$	^7D	0.2078	0.3414	39.13
$5d^5(^4D)6s$	^5D	0.1718	0.1750	1.80
$5d^46s^2$	$^1G2$	0.1676	0.1608	4.26
$5d^46s^2$	^1I	0.1734	0.1905	8.99
$5d^46s^2$	^1F	0.1837	0.2184	15.90
$5d^46s^2$	$^1D2$	0.1853	0.2175	14.81
$5d^46s(^6D)6p$	^5F	0.2380	0.3888	38.78
$5d^5(^6S)6p$	^7P	0.2087	0.6038	65.43
$5d^46s(^6D)6p$	^5D	0.2367	0.4324	45.27
$5d^5(2F1)6s$	^3F	0.2099	0.2890	27.38
$5d^5(^4F)6s$	^5F	0.2202	0.2344	6.06
$5d^5(2I)6s$	^3I	0.2205	0.2371	7.02
$5d^46s(^6D)6p$	^5P	0.2301	0.3548	35.14
$5d^5(^4P)6s$	^3P	0.2211	0.2965	25.44
$5d^46s^2$	$^3P1$	0.2227	0.2448	9.01
$5d^46s^2$	$^3F1$	0.2309	0.2350	1.74
$5d^5(^4G)6s$	^3G	0.2485	0.2621	5.20
$5d^5(2D3)6s$	^3D	0.2544	0.2788	8.73
$5d^5(2G2)6s$	^3G	0.2665	0.2950	9.68
$5d^5(2I)6s$	^1I	0.2628	0.2964	11.36
$5d^5(^4D)6s$	^3D	0.2688	0.3013	10.79
$5d^46s(^4H)6p$	^5H	0.3212	0.3980	19.29
$5d^46s(^6D)7s$	^7D	0.3903	0.4036	3.29
$5d^46s(^6D)7s$	^5D	0.4087	0.4039	1.20
			Average:	17.35

TERMS array in pstg2r.f and stglib.f were thus extended to incorporate terms for f^{12}, and its coefficient of fractional parentage was inserted using its Racah recursion relation to f^2 found in Cowan [61]. A detailed description of the code modifications required for the closed f-subshell can be found in Section 6.3.1.

The continuum-continuum elements of the Hamiltonian presented the largest impediment to the calculation. The pstg2r.f code currently available is parallelized as one partial-wave calculation per processor. For most of the partial-waves, the duration of the calculation would exceed several months. Recent code development was completed by Ballance *et al.* [67] that exploits the target atom's sets of $LS\Pi$ symmetries, parallelizing as one target symmetry per partial-wave per processor. Our structure, for example, led to 81 possible symmetries, each of which would be associated with a certain set of channels based on its quantum numbers. Splitting the calculation in this way reduces the amount of time required from a matter of months to weeks or days. Two limitations of this approach are that it requires both a large amount of RAM, over 60 Gb per processor in some cases, and a sizeable number of processors to run simultaneously, here multiples of 81. Furthermore, for any given partial-wave, many if not most of the target symmetries will have no coupled channels with the continuum electron, resulting in many of the processors sitting idle throughout the calculation. Thus, this code was further modified such that it was separated into two parts. First, the bound-bound and bound-continuum elements are calculated, and a file containing all target symmetries with at least one coupled channel, as well as the size of the Hamiltonian block of each symmetry, is printed. Then, the continuum-continuum elements are calculated in batches, using manually chosen target symmetries. This enables symmetries with larger Hamiltonian blocks to be calculated separately, allowing for more RAM on cluster machines, while excluding processor allotment for symmetries with no channels.

Another Stage 2 modification allowed unrestricted access to RAM throughout runtime. Previously, the majority of integers were written in single precision, including the variables governing Hamiltonian matrix allocation. As a result, an artificial cap had been placed on how much of the Hamiltonian could be stored at once. In cases where this cap was exceeded, large pieces of the Hamiltonian must be written into and read from a temporary space before finally

being written to file. The code was modified throughout, such that the user can now choose the precision of integers, e.g., double, removing the RAM cap. This change reduced the runtime from several weeks to less than a week per partial-wave.

An incident electron coupling with the ground and metastable terms, ^5D and ^7S respectively, will result in a total $2S_{N+1}$ + 1 = 4, 6, or 8 for the N + 1 system. The ^7S metastable state can couple to the octets and sextets, and the ground state can couple to the sextets and quartets. Other excited states of the three nl series are singlets and triplets, such that a set of doublet partial-waves would be needed to obtain their cross sections. These lower spin states were not pursued at the present time.

Table 4.3 shows a comparison of the number of channels per partial-wave, split by the $2S + 1$ spin states: the octets, sextets, and quartets. They reach a maximum of 738; 11,201; and 44,756 respectively. The calculation included partial-waves spanning from L = 0 to 9 both even and odd parities. A Burgess 'top-up' was applied [66] after L = 9, though in principle the calculation was converged after L = 7. The dimensions of the N + 1 Hamiltonians, including the continuum-continuum, bound-continuum, and bound-bound elements, ranged from 1,909 - 21,655 and 42,856 - 329,677 for the octets and sextets respectively. The quartets, whose continuum-continuum dimensions alone would have ranged from 149,437 - 1,298,098, were not feasible for direct calculation with modern computational resources. Instead, an approximation for their contribution is provided for all quintet terms, including the ground state, as discussed in the next section.

4.4 Convergence Checks with the Octet partial-waves

The small number of channels for the octet spin-state set of partial-waves was a tremendous benefit in assessing the size and convergence of the neutral W electron-impact ionization R-matrix calculation. Despite the large differences in the number of channels between spin states, each state contributes a comparable amount to the total cross sections. For the $5d^5 6s$ (^7S) ionization, for example, the set of octets and set of sextets will be shown to contribute roughly half to the total cross section each. This can be explained physically in part from the use of *LS*-resolved Hamiltonians for the target and N + 1 systems, which, unlike the relativistic

Table 4.6: Comparison of the number of N + 1 channels split by $2S_{N+1} + 1$ states, i.e., octets, sextets, and quartets, for each $L\Pi_{N+1}$.

	No. Channels		
partial-wave ($L\Pi$)	Octets	Sextets	Quartets
0, Even	134	1366	5153
0, Odd	60	1359	5159
1, Even	242	3967	15083
1, Odd	316	3974	15077
2, Even	472	6267	23904
2, Odd	398	6260	23910
3, Even	516	8098	31153
3, Odd	590	8105	
4, Even	668	9443	36601
4, Odd	594	9436	36607
5, Even	639	10310	40349
5, Odd	713	10317	40343
6, Even	732	10820	42657
6, Odd	658	10813	42663
7, Even	664	11062	43930
7, Odd	738	11069	43924
8, Even	738	11170	44523
8, Odd	664	11163	44529
9, Even	664	11194	44762
9, Odd	738	11201	44756

Hamiltonians, contain no spin or total J dependence. Convergence and structure checks were thus performed using the much less computationally expensive octet set.

To reduce the size of the calculation, running separate *R*-matrix calculations for electron-impact ionization of each of the three series had been considered. Figure 4.1 shows how splitting the calculation by nl series would affect the octet metastable $6s$ ionization cross section. While excluding $5d^3 6s^2 nl$ does not change the cross section significantly, excluding $5d^4 6snl$ greatly increases the size of the cross section, by a factor of more than 2 at certain energy ranges. This behavior can be understood in part by the ability of each series to form octet N + 1 channels. Whereas the spin of the $5d^4 6snl$ configurations can add to 7, such that octet channels can be formed, the highest possible spin for the $5d^3 6d^2 nl$ configurations is 5. For the sextets and quartets, therefore, for which all configuration series can contribute, all configurations are necessary to account for mixing in both the target and the N + 1 states. Thus, it was not possible to split the calculation into separate calculations for the ground and metastable states. They had to be evaluated in a single, larger, calculation.

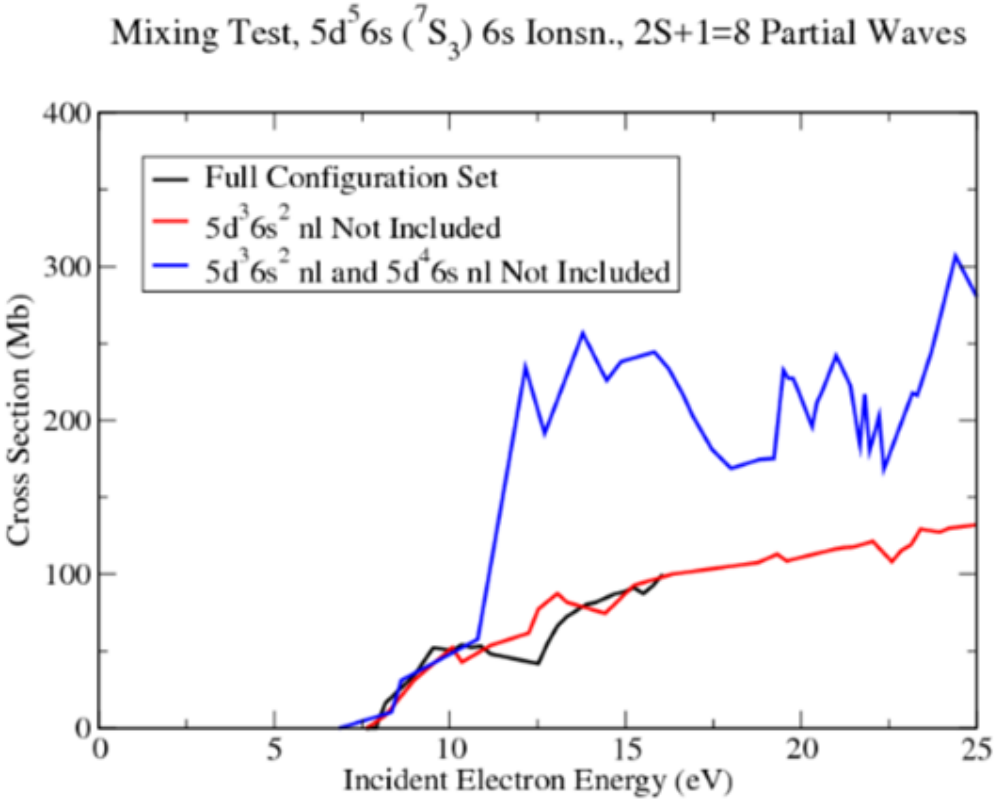

Figure 4.1: Test of the necessary configuration series required to obtain an accurate cross section of the electron-impact $6s$ ionization from the metastable $5d^5 6s$ ($^7S_3$) term. The cross sections shown are from including octet partial-waves only. The blue, red, and black lines indicate the cross section if including in the target structure and *R*-matrix calculation only the $5d^5nl$ series; the $5d^5nl$ and $5d^4 6snl$ series; and the $5d^5nl$, $5d^4 6snl$, and $5d^3 6s^2nl$ series respectively.

Figure 4.2 shows a further check of the octets on both the angular momentum range $\bar{l}$ of the pseudostates needed to converge the cross section and on how sensitive the cross section is to changes in the structure. $\bar{l} = 4$ or 5 have been used in past electron impact ionization calculations, such as for W^{3+} [67] and neutral neon [55, 56]. A test structure was made including up to $\bar{l}$ = 6 pseudo orbitals using the same orbital scaling parameters from the final structure and resulted in 18,960 total terms. For the total metastable (^7S) cross section, including $5d$ and $6s$ ionization, the cross sections from including through $\bar{l} = 5$ and 6 agree well up to 14 eV, at which point the latter cross section experiences a 20% increase from the former. Given that this increase occurs only within the last couple eV of our calculation range, the decision was

made to run the sextets using pseudo orbitals through $\bar{l} = 5$. Another question when deciding on a final structure was whether to set the structures such that the ^7S metastable term energy would equal its level energy, 0.02698 eV. The green line, representing a structure run optimized in this way, shows good agreement through 10 eV and within 20% for higher incident energies. For reference, the metastable term energy of the final structure is -0.0137 relative to the ground term energy. This preliminary structure and RMPS run therefore suggested that the cross section is not sensitive to changes in the metastable structure, within the kind of parameter space we were exploring during optimization.

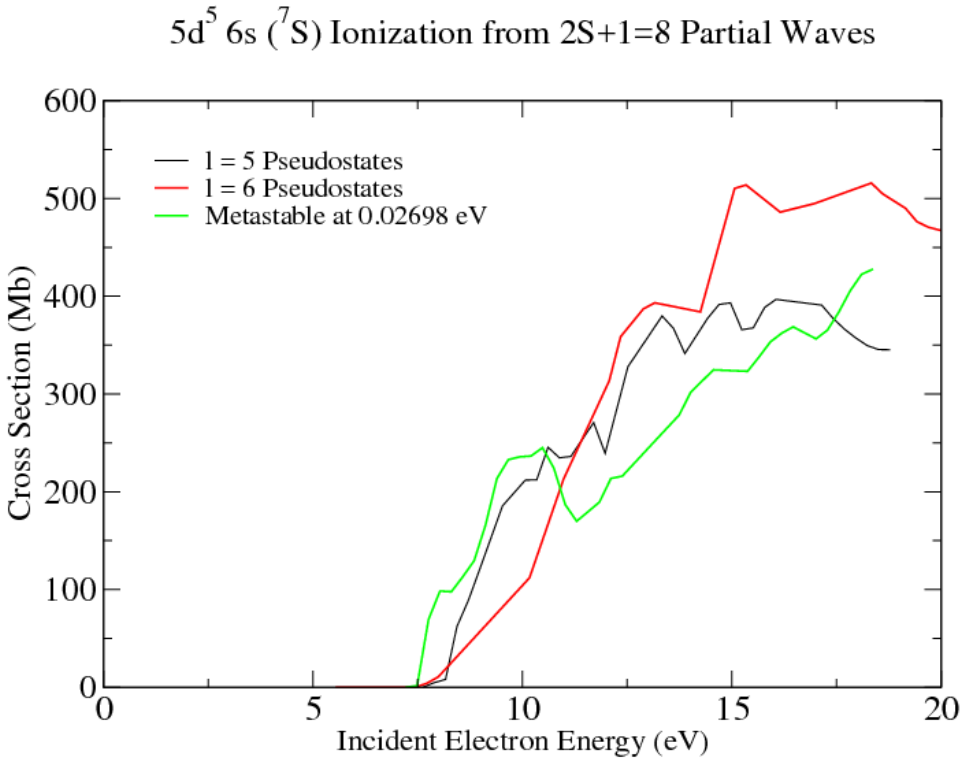

Figure 4.2: Pseudostate and structure convergence check with the $5d^5 6s$ (^7S) total ionization from the octet partial-wave set. The black line indicates the cross section from the final structure used, which includes pseudo orbitals through $\bar{l} = 5$. The red line is the resulting cross section if adding $\bar{l} = 6$ pseudo orbitals. The two agree up to about 14 eV, at which point the cross section with more pseudo orbitals experiences a 20% increase. The green line is the cross section from a structure run in which the metastable ^7S term energy was optimized to equal its level energy, and it suggests the cross section is not sensitive to changes in the structure.

4.5 Metastable $5d^5 6s$ (^7S) electron-impact ionization cross section results

Figure 4.3 shows the RMPS results of the metastable $5d^5 6s$ (^7S) ionization cross sections, including the separate contributions from the octet (dotted) and sextet (dashed) partial-waves. The total cross section (black) does not reach its peak within the range of the calculation, but it starts to plateau around 850 - 900 Mb. The individual $5d$ and $6s$ ionization cross sections, red and blue respectively, are themselves nearly equivalent. For the total cross section, the octets and sextets are within 10% of each other, such that each contributes roughly half. The same trend can be observed for the ionization from the $6s$ and $5d$ orbitals.

Figure 4.4 shows the metastable $5d$ and $6s$ cross sections from direct ionization, excluding excitation autoionization. Comparing to the full cross sections, there is almost no excitation autoionization contribution to the $5d$ cross section and a nearly 100 Mb contribution to the $6s$ cross section. The octets (dotted) and sextets (dashed) are each still nearly equivalent, although the $5d$ cross octet cross section is nearly 50 Mb higher at some incident energies.

The combined direct and excitation autoionization results of the two partial-wave spin sets suggest the suitability of doubling the sextet ground state $5d^4 6s^2$ (^5D) cross section to account for the quartet contribution.

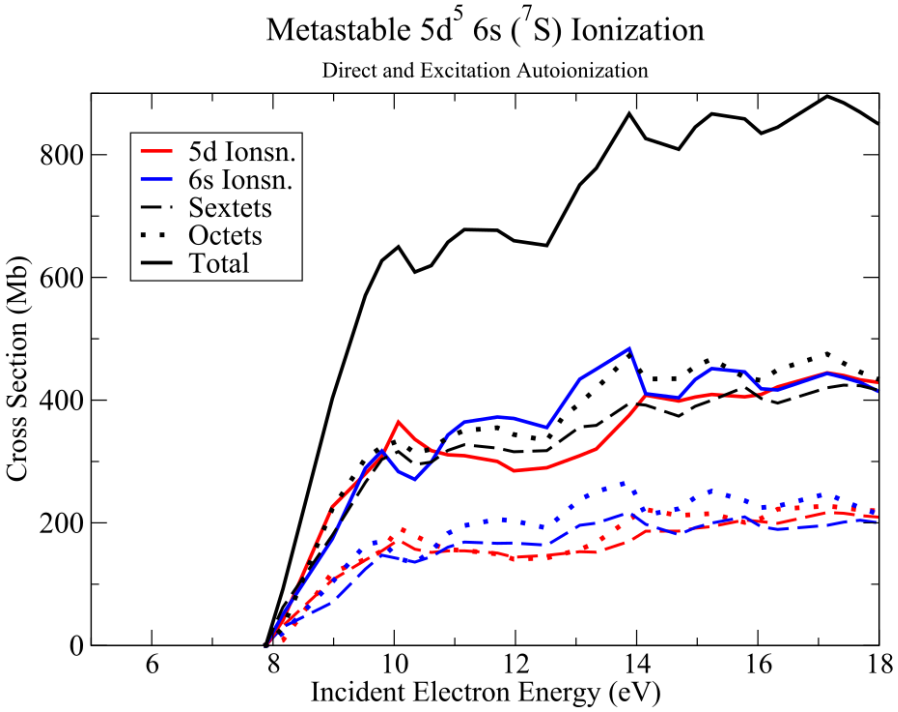

Figure 4.3: RMPS $5d^5 6s$ (^7S) results, including $5d$ (red), $6s$ (blue), and total ionization. Cross sections include contributions from both direct ionization and direct ionization. Also shown is the separate contributions from the octet (dotted) and sextet (dashed) spin state sets of partial-waves. For $5d$, $6s$, and total ionization, the contributions of these two spin states are within 10% of each other.

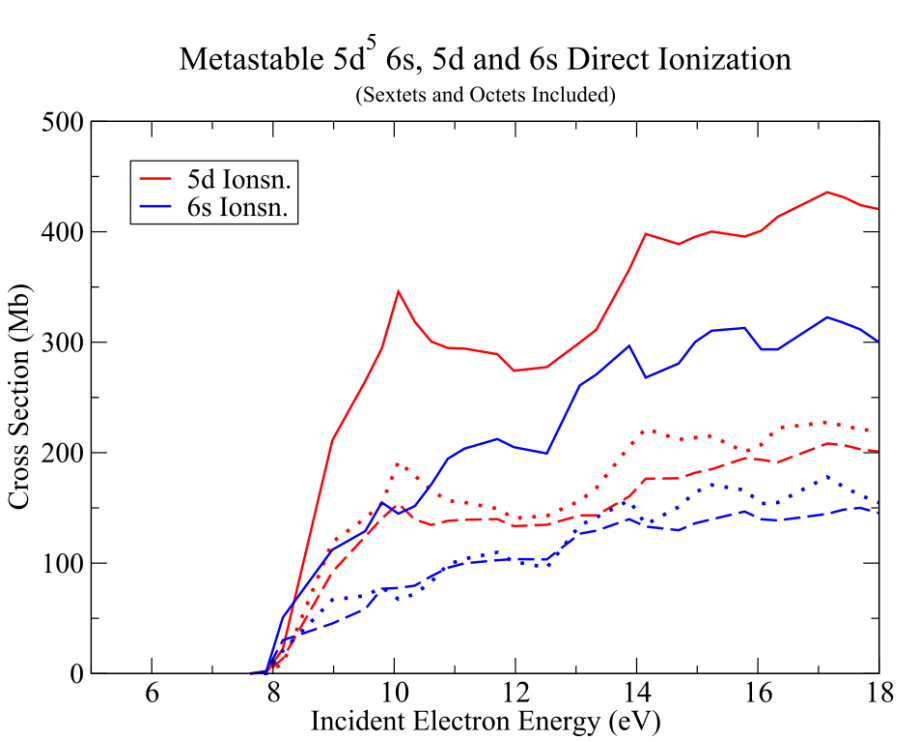

Figure 4.4: RMPS $5d^5 6s$ (^7S) direct $5d$ (red) and $6s$ (blue) ionization results. The contributions from both the octet and sextet spin state partial-wave sets, dotted and dashed respectively, are within 10% for $6s$ and 25% for $5d$ ionization across all calculated incident electron energies.

Figure 4.5 compares the RMPS total, $6s$,and $5d$ electron-impact direct ionization cross sections from the metastable $5d^5 6s$ (^7S) term, with $6s$ and $5d$ ionization comparisons to configuration-averaged distorted wave (CADW) calculations. None of the RMPS cross sections have reached their peaks by the end of the calculation's valid energy range. The calculation would have to extend to 25 eV to reach up to the CADW $5d$ ionization peak. The RMPS $5d$ ionization cross section is a factor of five reduced compared to CADW. Yet, the $6s$ cross sections agree well.

The configuration-averaged distorted wave method is appropriate for a fast-moving electron, and it does not account for exchange, continuum coupling, or configuration mixing effects. The former two effects will reduce the cross section and are factored into RMPS. The metastable $5d$ and $6s$ ionization cross sections might further be explained by considering mixing of the ionization pathways from the $5d^5\bar{n}l$ and $5d^4 6s\bar{n}l$ terms that also lead to the possible

W^+ lowest energy states. Ionization of $6s$, represented by the $5d^5\bar{n}l$ series, can only result in $5d^5$ (^6S), whose level is 0.0676 Ryd above the ground state. The $5d$ ionization, represented by the $5d^46s\bar{n}l$ series, can result in either the W^+ ground state ^6D or any of the $^4(PDFG)$ states. The ^6D state is also possible from $5d^46s^2$ (^5D) $6s$ ionization, in addition to ^4D. The distorted wave results assume ionization from either $5d^56s$ or $5d^46s^2$, but not their simultaneous possibility. Therefore, a more accurate comparison will be the sum of the RMPS $5d^56s$ $5d$ and $5d^46s^2$ $6s$ cross sections, compared to the sum of their respective distorted wave results.

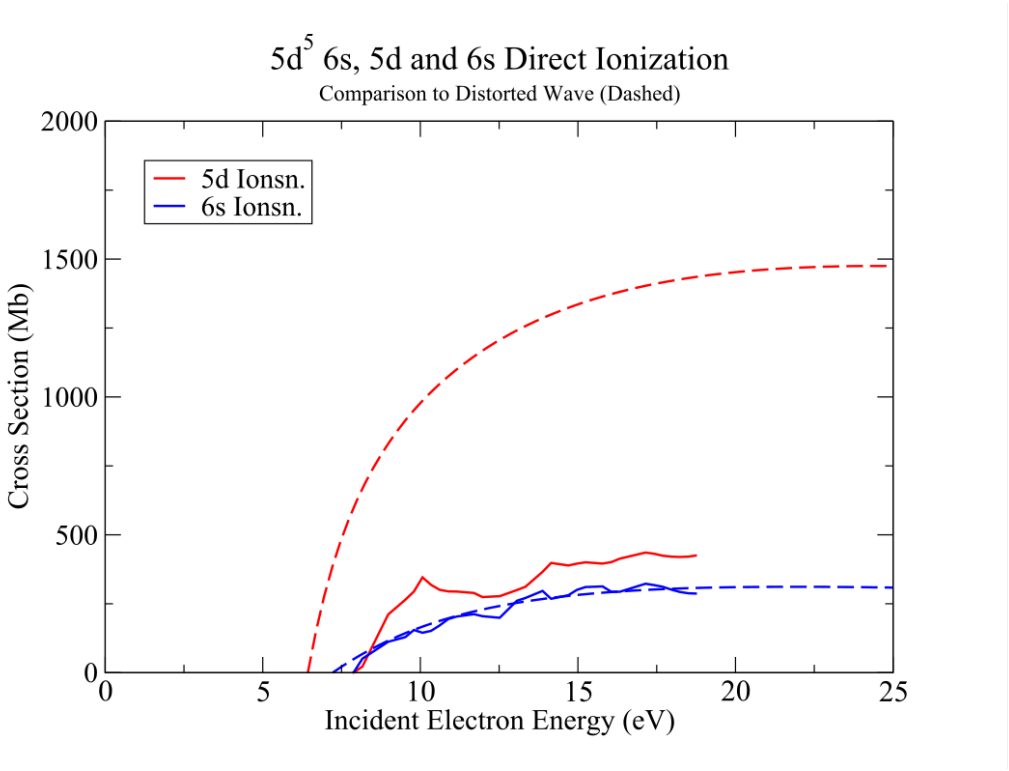

Figure 4.5: RMPS $5d^56s$ (^7S) direct ionization cross sections compared with configuration-averaged distorted wave (CADW), including the total term-resolved (black) and from $6s$ (blue) and $5d$ (red). The RMPS $5d$ ionization cross section is a factor of five below CADW, while the $6s$ cross section matches.

4.6 Ground $5d^46s^2$ (^5D) electron-impact ionization cross section results

Sextet ionization cross sections were also obtained for the ground $5d^46s^2$ (^5D) term. Complete cross sections would require the quartet spin set of partial-waves as well. Due to their large number of channels and corresponding N + 1 Hamiltonian sizes, the quartets could not be

calculated. Instead, the $5d$, $6s$, and total ground state cross sections are approximated as twice their respective sextet cross sections, an approximation supported by the octet and sextet partial contributions to the $5d^5 6s$ cross sections.

Figure 4.6 shows the RMPS ground state ionization cross sections resulting from the sextet partial-waves. Direct ionization, represented by the dashed lines, comprises about 90% of the total. About two-thirds of the total comes from $5d$ ionization, whereas the $6s$ ionization is less than 10% of the total.

A consequence of the heavy mixing between the three configuration series is the presence of a $5d^5 nl$ cross section (purple), reaching about 150 Mb. For traditional lighter systems ionizing from ns and np orbitals, the configuration series are more pure and therefore represent distinct ionization pathways. The $5d^5 nl$ cross section, an excitation and an ionization of the $6s$ electrons, arises from the large $5d^4 6s\bar{nl}$ mixing coefficients present in terms labeled as $5d^5\bar{nl}$. In calculating the close-coupling Hamiltonian, configurations are calculated separately and summed for each bra and ket channel. So, while pure $5d^4 6snl$ and $5d^5 nl$ states would be orthogonal, the $5d^4 6s\bar{nl}$ percentage present in technically $5d^5\bar{nl}$ terms would yield a non-zero contribution.

In further corroboration of this result, the mixing coefficients were examined for the ground state and a pseudostate, $5d^5 9\bar{p}$ (^5F). This pseudostate was the largest contributor to the total ground ionization cross section at 14 eV. 89.88% of the ground state corresponded to the lowest $5d^4 6s^2$ term. The highest percentage for the pseudostate was only 10.14%. The other highest four percentages, ranging from 8.23% to 5.58%, came from both $5d^4 6snl$ and $5d^5 nl$ configurations. Most of the $5d^5 nl$ contribution therefore likely corresponds to transitioning into $5d^4 6snl$ configurations, whose majority percentage is from a $5d^5 nl$ configuration.

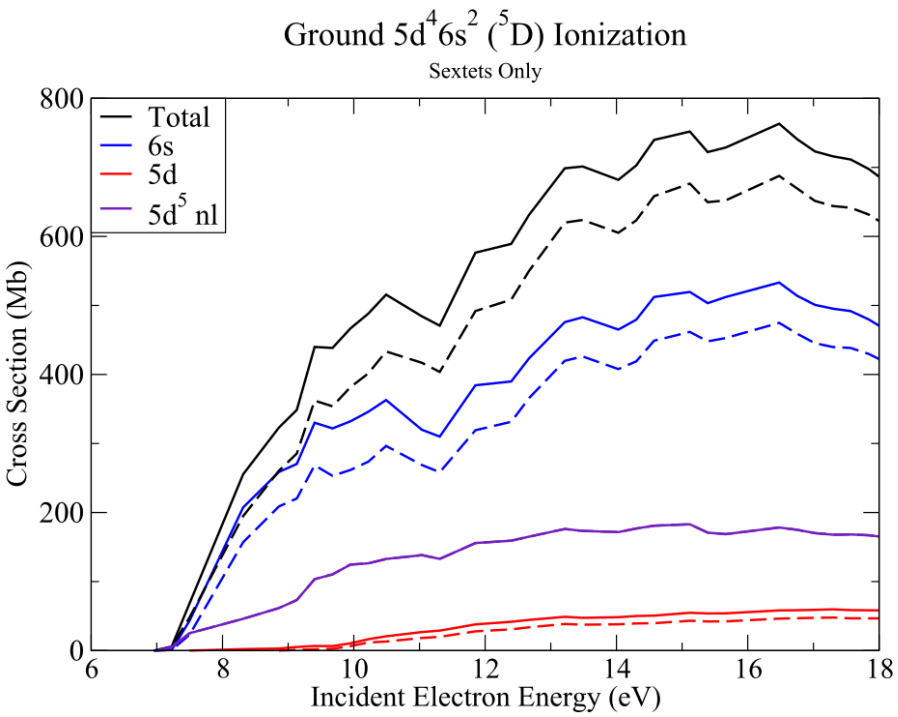

Figure 4.6: RMPS $5d^4 6s^2$ (^5D) results for the sextet spin state partial-wave set. The full cross sections require the quartet set also. The solid lines include both direct ionization and excitation autoionization, while the dashed lines include only direct ionization. $6s$ ionization (blue) represents the largest contribution to the overall cross section, while the $5d$ ionization (red) contributes less than 10%. A nonzero contribution representing ionization into the $5d^5\bar{n}l$ series is also present (purple), accounting for roughly 20% of the total cross section.

Comparisons of $5d$ and $6s$ direct ionization from the ground to previous calculations reveal further differences from configuration-averaged results. Figures 4.7 and 4.8 show the $5d$ and $6s$ direct ionization cross sections from the ground state if assuming the quartet contribution will be approximately equal to that of the sextet. The RMPS $5d$ direct ionization, less than 100 Mb, is much smaller than HULLAC [112], R-DW [71], ECIP, and the non-perturbative time-dependent close-coupling (TDCC) [71] cross sections. All of the cross sections share a similar shape in that they do not reach their peak in the 0-25 eV incident range. Yet, the RMPS $6s$ direct ionization is larger by more than a factor of two past 10 eV incident energy range for R-DW and TDCC, and by more than a factor of four for ECIP. The RMPS ground $6s$ results

reach nearly 1000 Mb in the calculated energy range and has clearly not reached its peak, which occurs around 20 eV for the other methods. The total RMPS ground ionization cross section is about equal to the total HULLAC ground ionization cross section, however.

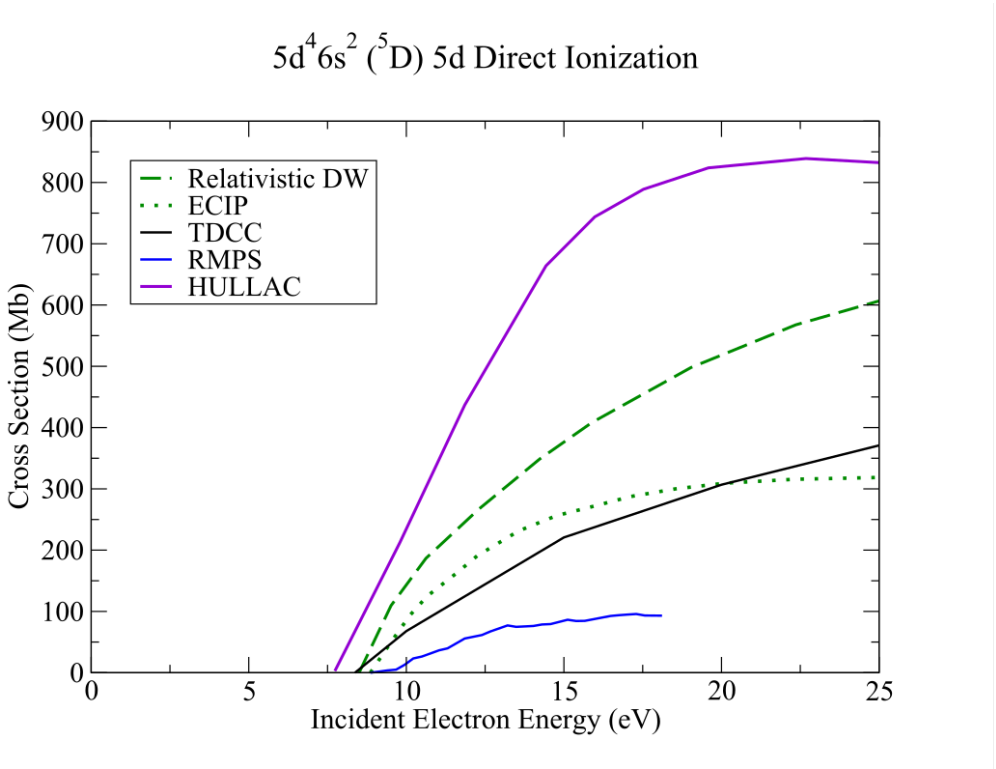

Figure 4.7: RMPS $5d^4 6s^2\ (^5D)\ 5d$ direct ionization (blue) comparison with relativistic distorted wave (R-DW, dashed green) [71], exchange classical impact parameter (ECIP, dotted green), time-dependent close coupling (TDCC, solid black) [71], and HULLAC (solid purple) [112]. The RMPS represent the sextet partial-wave set doubled, i.e., an equal contribution from the sextet and quartet partial-waves.

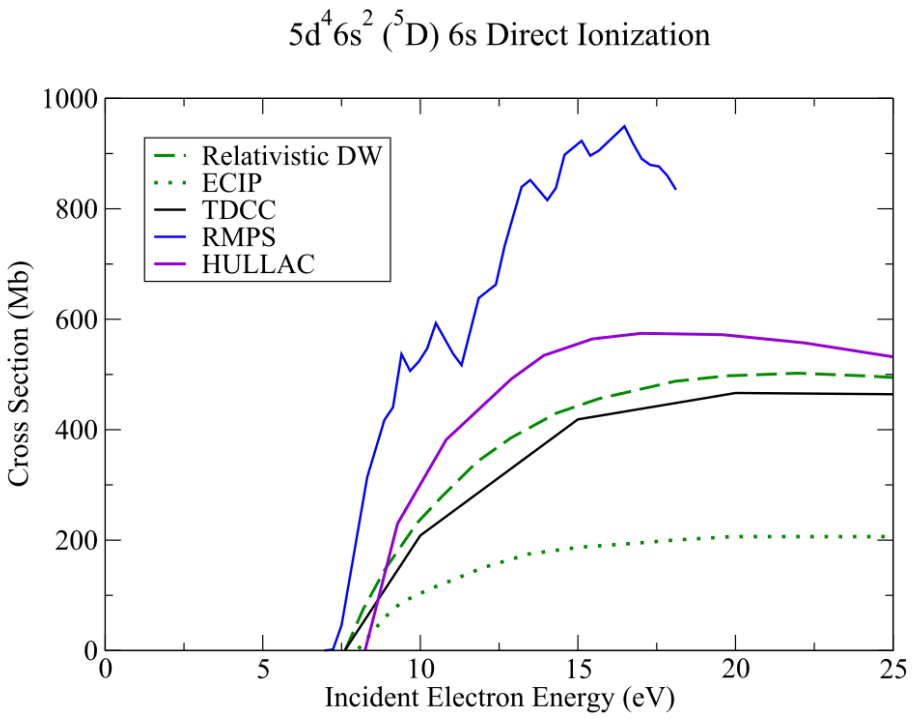

Figure 4.8: RMPS $5d^4 6s^2\ (^5D)\ 6s$ direct ionization (blue) comparison with relativistic distorted wave (R-DW, dashed green) [71], exchange classical impact parameter (ECIP, dotted green), time-dependent close coupling (TDCC, solid black) [71], and HULLAC (solid purple) [112].

Overall, the total RMPS ground ionization of the $6s$ subshell is nearly twice that of the total relativistic distorted wave, which, due its neglective exchange and correlation effects, often overestimate the cross section for neutral systems. Further attention is therefore required to determine 1) the validity of the assumption that the sextet and quartet contribution are about equal, 2) if any additional configuration series are missing that would further reduce the cross section, and 3) if the larger RMPS cross section can be understood through quantum mechanical effects.

The possibility of additional configuration series to fully account for mixing was also explored. The $5d^4 6pnl$ series should mix with both the $5d^5 nl$ and the $5d^4 6snl$ series, and this series might reduce the ground state cross section. This effect was witnessed with the metastable cross section by the addition of the $5d^4 6snl$ series. Because a full structure with the $5d^4 6pnl$ series and including through the same $\bar{nl}$ pseudo orbitals would result in over

30,000 terms, a check on the $5d^46pnl$ series was performed using a reduced set of pseudo orbitals, through $\bar{l}$ = 3. The octet partial-waves were calculated and the metastable cross section extracted. This result was compared to a control calculation, which included the same pseudo orbital reduction through $\bar{l}$ = 3 but did not include the $5d^46pnl$ series. Both the $5d^46pnl$ and the control structures used the same orbital scaling parameters as the structure used to obtain the final results. The $5d^46pnl$ structure had 19,652 terms, while the control structure had 8,176 terms. Figure 4.9 shows the $5d^56s$ (^7S) total ionization results from the octet partial-waves. Good agreement is shown between the cross section from the control structure and *R*-matrix run compared to the cross section if including the $5d^46pnl$ series in the structure, suggesting a convergence on configuration mixing without the $5d^46pnl$ series.

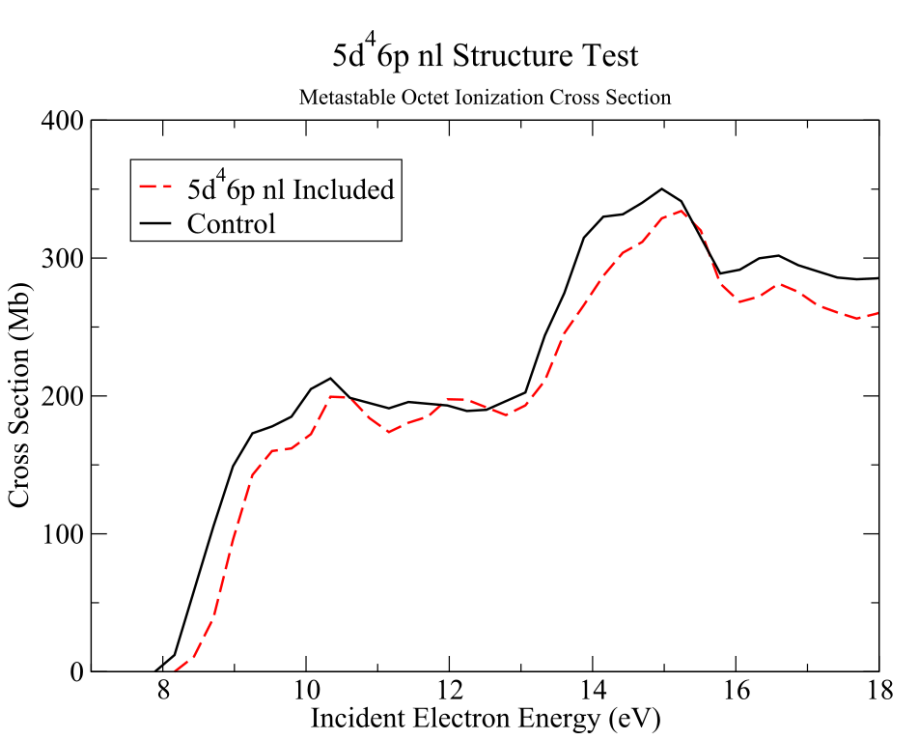

Figure 4.9: $5d^56s$ total ionization results for the octet partial-waves from a structure including the $5d^46pnl$ series (red dashed). This structure and *R*-matrix calculation as well as the control structure (solid black), did not include pseudostates beyond $\bar{l} = 3$. The two exhibit close agreement.

The metastable $5d$ and $6s$ ionization cross sections might further be explained by considering mixing which ionization pathways from the $5d^5\bar{n}l$ and $5d^46s\bar{n}l$ terms that also lead to the possible W^+ lowest energy states. Ionization of $6s$, represented by the $5d^5\bar{n}l$ series, can only result in $5d^5$ (^6S), whose level is 0.0676 Ryd above the ground state. The $5d$ ionization, represented by the $5d^46s\bar{n}l$ series, can result in either the W^+ ground state ^6D or any of the $^4(PDFG)$ states. The ^6D state is also possible from $5d^46s^2$ (^5D) $6s$ ionization, in addition to ^4D. The distorted wave results assume ionization from either $5d^56s$ or $5d^46s^2$, but not their simultaneous possibility. That is, mixing between the N + 1 states would not be included. A more accurate comparison should therefore be the sum of the RMPS $5d^56s$ and $5d^46s^2$ direct ionization cross sections, compared to the sum of their respective distorted wave results.

Figure 4.10 shows the total direct ionization from the ground and metastable states, $5d$ and $6s$, of RMPS (red) compared to previous configuration-averaged results. The configuration-averaged distorted wave total (blue), which includes the relativistic results from [71] for the ground and the non-relativistic results for the metastable, exhibits the same shape as RMPS and is consistently about 20 - 20% higher. No metastable ionization cross sections from the TDCC (black) and ECIP (green) methods currently exist. A scaling of the metastable to the ground non-relativistic distorted wave results suggests an approximate ratio of slightly less than 2:1, and this approximate scaling applied to the TDCC would bring its total cross section to around 10% of the RMPS results. The RMPS total ionization results are therefore consistent with previous ionization results for lighter systems, for which RMPS agrees reasonably well with TDCC and is less than distorted wave.

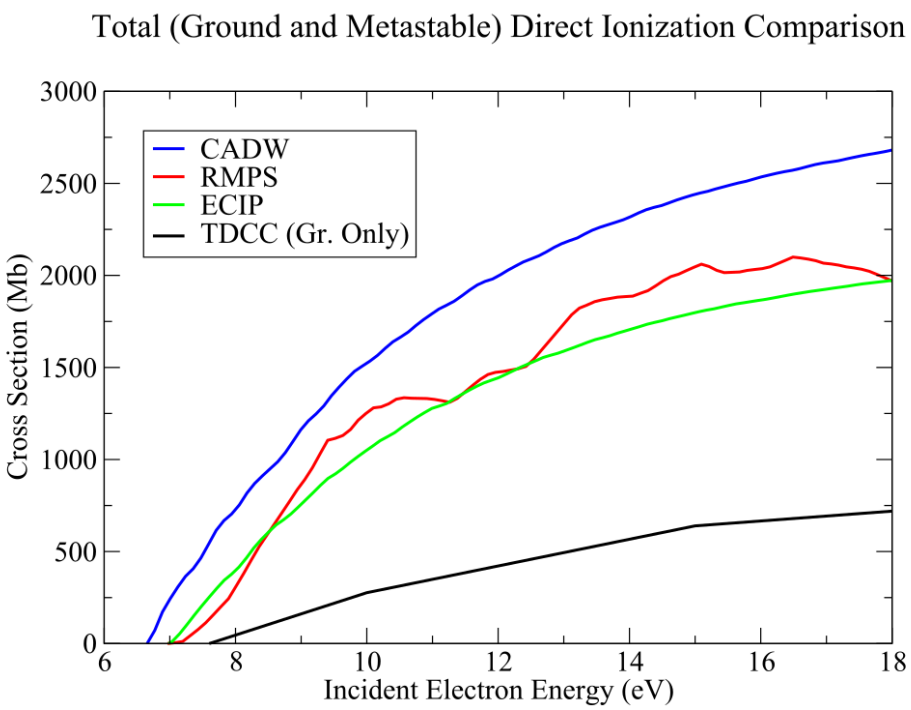

Figure 4.10: Comparison of the RMPS total direct electron-impact ionization from the ground and metastable states (red) with the total from configuration-averaged distorted wave (CADW, blue). The ground state cross sections from TDCC (black) and ECIP (green), $5d$ and $6s$ ionizations summed, are also shown. Despite a large ground state $6s$ ionization, the RMPS falls below CADW at all energy ranges.

4.7 Discussion

For purposes of accurate collisional radiative modeling of tungsten as a plasma facing component, a new *R*-matrix with Pseudostates electron-impact ionization calculation has been performed for neutral tungsten. The calculation improves upon previous data by being non-perturbative and also *LS*-resolved, allowing for configuration mixing between the three main ionization configuration series of neutral tungsten, both in the target N and the N + 1 electron system. The calculation also includes contributions due to excitation auto-ionization. Furthermore, the RMPS calculation allows for the extraction of cross sections for ionization from excited states, which has been shown to contribute more than ionization from the ground state in lighter systems such as Ne [115], He [37], Li [38], and B [39].

Neutral tungsten differs from previously studied lighter elements in that, not only does it require a relativistic treatment, but its configuration series both share ionized states and are heavily mixed. The importance of considering all of the these mixing configurations together into the N + 1 Hamiltonian were observed by the dramatic reduction in the metastable $5d^5 6s$ (^7S) $6s$ ionization cross section when the $5d^4 6snl$ series was added to the structure.

The results from the new RMPS calculation differed from previous electron-impact results of lighter systems in that the ground state and metastable $6s$ direct ionization cross section were respectively about twice as high as (for the ground) and equivalent to (for the metastable) configuration-averaged distorted wave (CADW) results. CADW does not account for correlation and continuum coupling effects, such that RMPS typically has a reduced cross section compared to CADW. The need for additional configuration series for convergence was ruled out through a test run with the $5d^4 6pnl$ series.

The total direct ionization cross section of both the ground and metastable states falls within range, though below, that of CADW, and this suggests that the shared ionization series between the ground and metastable, as well as configuration mixing, are likely the reason for the uniqueness of the RMPS ground and metastable cross sections with respect to perturbative methods. This can be observed chiefly from the ionizations of $6s$ from $5d^4 6s^2$ and $5d$ from $5d^5 6s$, both found by summing over the $5d^4 6s\bar{nl}$ pseudostates above the ionization potential. The cross sections for these two ionizations differ the most from previous results, with the $5d$ being much lower and the $6s$ much higher. One way of interpreting the results might be: if both metastable $5d$ and ground $6s$ ionizations are possible, mixing effects mean that nature prefers the $6s$ ionization from the ground.

The importance of term or level-specific resolution of electron-impact ionization in collisional radiative modeling is still an open question. That is, given that the total cross sections including the ground and metastable states show reasonable agreement with more approximate configuration-averaged methods, it is unclear if the term-specific differences revealed in the RMPS cross sections will lead to significant differences in tungsten plasma modeling. The next logical step will therefore be to examine the effect of these new RMPS electron-impact ionization cross sections for the ground and excited states on the collisional radiative modeling

of tungsten. In the next chapter we consider the excited state ionization of neutral W and the effects on SCD and S/XB coefficients.

Chapter 5

Excited-State Ionization and GCR Modeling of Neutral Tungsten

The previous chapter reported on ground and metastable cross section results for neutral tungsten. Given the likely importance of excited states ionization to the effective ionization of neutral W, this chapter addresses both the calculation of excited state ionization cross sections and possible scaling laws for the ionization rate coefficients. As with neon, the RMPS calculation discussed in the previous chapter yields cross sections for all possible target structure transitions. Other methods such as configuration-averaged TDCC require separate calculations for each configuration and do not account for configuration mixing and interference between the configurations and ionization processes (i.e., the target-continuum electron channels).

With the exception of the ECIP results used in ADAS [31], no other calculations exist for excited state ionization cross sections of neutral tungsten. Figure 5.1 illustrates the contribution of excited state ionization to the effective ionization rate coefficient using rate coefficients derived from ECIP cross sections. The ratio of the SCD if including all excited states to the SCD of ground-only ionization, $\mathrm{SCD}_{gr.}$, suggests excited states contribute about a factor of 200 more than the ground state to the SCD at $n_e = 10^{14}$ cm^{-3} in the 0 - 30 eV temperature range, and by a factor of more than 1,000 around 1 eV. Ground in this case is referring to the lowest $5d^4 6s^2\ ^5D_0$ level and does not include ionization contributions from other ^5D_J levels. The SCD ratio is still not yet 1.0 at $n_e = 10^4$ cm^{-3}, suggesting these other low-lying levels as well as the metastable $5d^5 6s\ ^7S_3$ have a significant population even at very low densities.

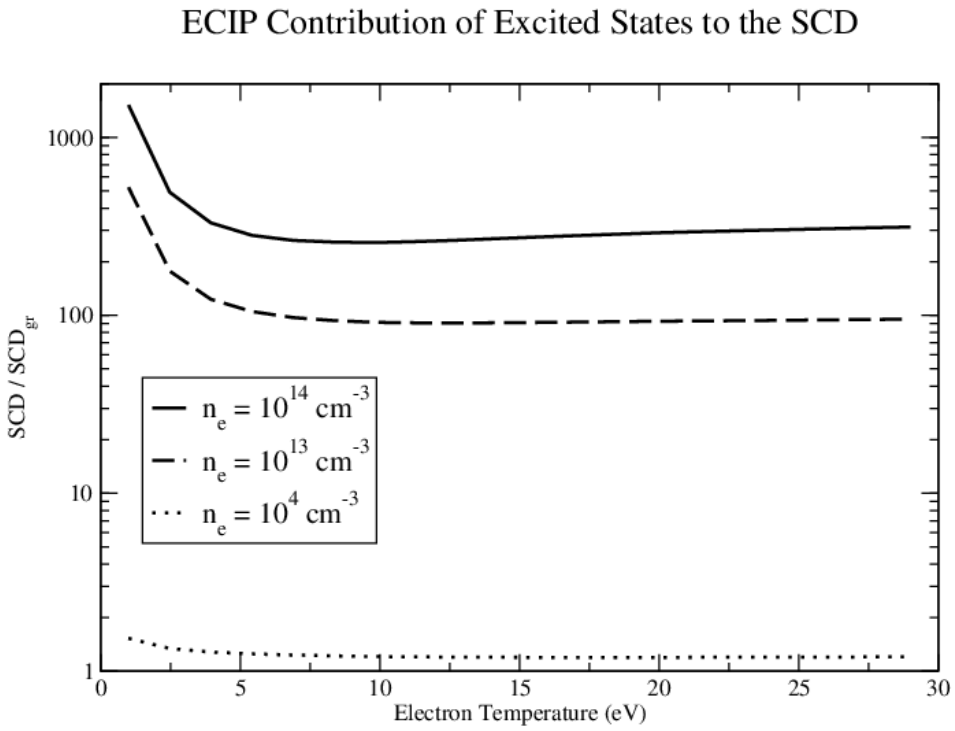

Figure 5.1: Comparison of the excited-state ionization contribution from ECIP to the effective ionization rate at different electron densities, as measured by the ratio to the SCD if including only the ground ECIP ionization rate (SCD$_{gr}$).

The discussion proceeds as follows: excited state cross sections from the $5d^46s6p$, $5d^46s6d$, $5d^56s$, $5d^56d$, $5d^6$, and $5d^36s^26p$ configurations are presented in Section 5.1. Their pseudostate convergence and ionization potential scaling behavior is analyzed. In Section 5.2, results are presented for fitting all of the cross sectional results, including ground and metastable, to include higher energies. Maxwellian rate coefficients are additionally evaluated from these fits. ECIP scaling of the data is shown to be effective for purposes of better fits and for obtaining cross sections of ionizations from excited states not included the *R*-matrix calculation. A strong correlation is observed between ECIP scale factors and a state's specific ionization potential, and this correlation is distinct relative to the parity of the state. Finally, in 5.4, the set of neutral tungsten *R*-matrix and ECIP scaling results are used in GCR modeling of the SCD, PEC, and S/XB coefficients.

5.1 Neutral Tungsten Excited-State Ionization Cross Sections

The aim in extracting excited state ionization cross sections is to add ionization rate coefficients to the excitation data file produced by the DARC calculation of Smyth *et al.* [41]. Thus, it was necessary to map the cross sections presented in this chapter against level and term information in the adf04 file produced from Smyth *et al.* [41]. Excited neutral tungsten terms present in the DARC calculation by Smyth *et al.* [41] were extracted from the new RMPS OMEGA file; however, there was not a one-to-one correspondence between the sets of terms. A full list of the terms and levels from the DARC calculation are recorded in the final neutral tungsten adf04 file, which will be made freely available via the open-adas online database [31]. 139 of the 250 levels lacked a corresponding term-resolved RMPS electron-impact ionization cross section.

Most notably, the constraints on the electron-impact ionization RMPS calculation required that the $7s$ be a pseudo orbital. So, cross sections for $5d^4 6s 7s$ terms and levels could not be obtained. Further, all $5d^5 6p$ terms in the ionization calculation were above the ionization potential, while $5d^5 6d$ terms were not and showed reasonable agreement with NIST term energies (note that both the $6p$ and $6d$ orbitals were optical). Regarding spin states, only cross sections for septet and quintet terms could be obtained as a result of limiting the calculation to the octet and sextet N + 1 spin sets. Singlets and triplets could therefore not be extracted. Similar to the ground ^5D term, cross sections for excited state quintet terms were extracted through an OMEGA file containing the sextet contribution and assuming the total cross section (quartets plus sextets) could be obtained by doubling the sextet cross section contributions.

To begin, a check on pseudostate convergence was performed. It was shown in Section 3.4 with neutral neon that pseudo orbitals up to $\bar{l}$ = 6 were required to converge all excited state-ionization cross sections. Limits on the size of the neutral tungsten RMPS calculation prevented adding pseudo orbitals beyond $\bar{l}$ = 5. Figure 5.2 shows the results of a $\bar{l}$ = 6 pseudo orbital convergence check on the septet excited states including only the octet partial-waves. Three $5d^4 6s 6p$ and one $5d^4 6s 6d$ septet state were extracted. The same test structure is used as that for the metastable convergence in Figure 4.2. Across all incident energy ranges, the cross

sections for all of the excited states are about 10 - 25% higher for the structure including $\bar{l}$ = 6 pseudostates (dashed).

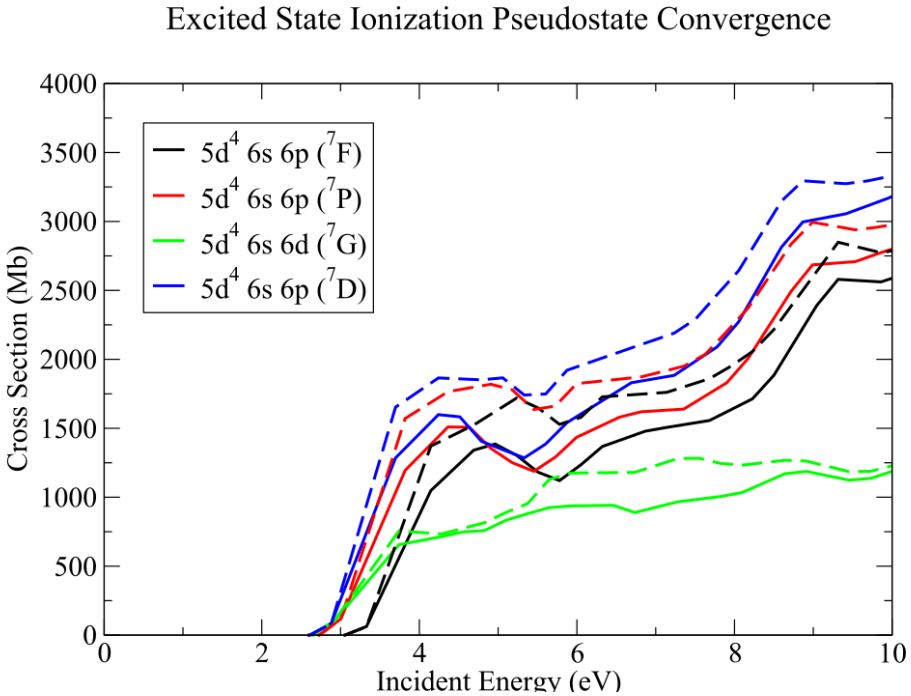

Figure 5.2: A pseudostate convergence check for the septet excited state ionizations using the octet partial-wave set. A structure of the same orbital parameters but with $\bar{l}$ = 6 pseudostates included (dashed lines) is 10 - 25% higher than the structure used in the RMPS calculation (solid lines) for all septet states across all incident energies.

Another check similar to the n^4-scaling of the neon excited state cross sections was also performed. Cross sections should increasingly resemble the classical solution with increasing energy of the excited term. Figure 5.3 shows both the full raw septet cross sections as well corresponding classically scaled cross sections. For the scaling a term's ionization cross section is multiplied by its ionization potential squared. A ratio of the incident energy to the term's ionization potential is used on the x-axis. These cross sections have close to the same ionization potential. So since 3 of the 4 cross sections are close to each other, it indicates that there is a connection between the magnitude of the neutral W ionization cross sections and their ionization potentials. The $6s6p$ terms are tending towards the same scaled cross section (blue)

as term energy increases. Further, the closeness in their shapes supports the overall consistency of the *R*-matrix calculation and also that the cross sections themselves were properly extracted from the OMEGA file.

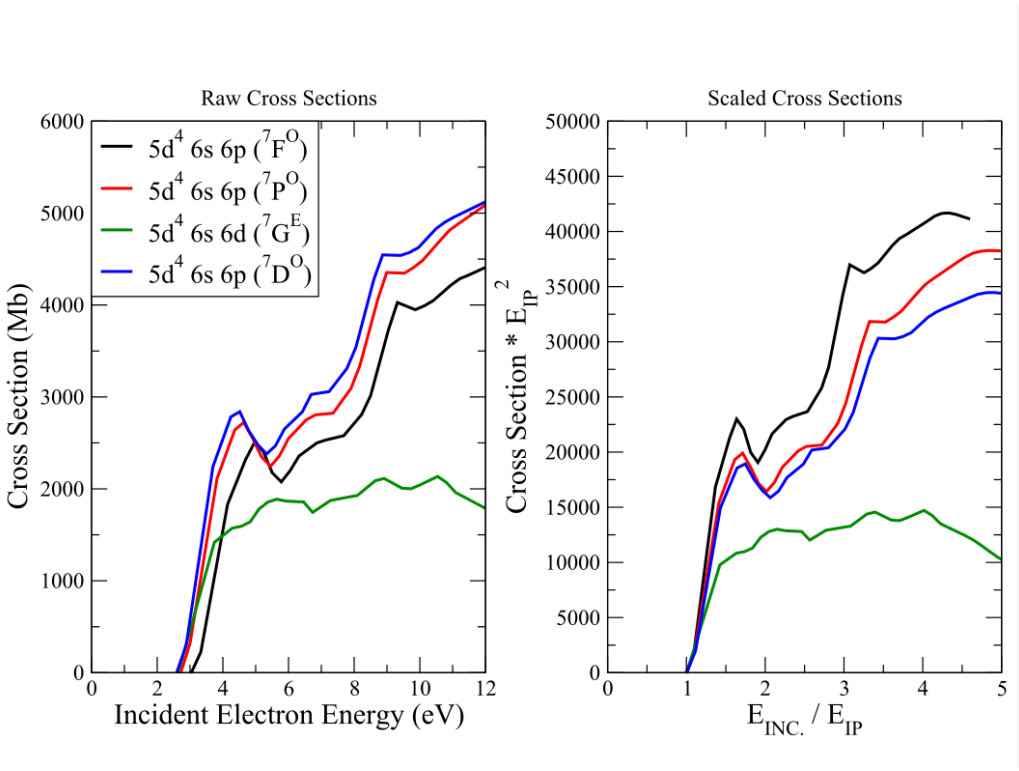

Figure 5.3: Both raw and scaled ionization cross sections for the extracted excited states. Each term's specific ionization potential squared is used for the scale factor, and the ratio of the incident energy to the ionization potential is used for the horizontal axis. The $6s6p$ cross sections all exhibit similar shape and show closer agreement with increasing term energy (decreasing ionization potential).

Figures 5.4 - 5.6 show total ionization results for the quintet excited states that were extracted. The results seem reasonable in terms of shape and also consistency with each other and with the ground and metastable cross sections. The $5d^5 6s$ quintets are all almost identical, their heights slightly increasing as ionization potential decreases. Both their shapes and trends in height are additionally consistent with the metastable (^7S) cross section (dashed line). Ionization cross sections from the $6s6p$ are shown in Figure 5.5. As the $5d^4 6pnl$ series could not be included in the structure due to computational size, $6s$ ionization is not considered; although,

the test calculation that included this series, demonstrated in Figure 4.9, indicated a negligible contribution from the $6s$ ionization. The $6s6p$ Cross sections are generally smooth and tend to peak at incident energies greater than twice the ionization potential. The ^5F state closest to 0 eV (dashed magenta) peaks at roughly 37 times its ionization potential. The ^5P cross section closest to 0 eV (solid black) never reaches its peak, through to the last energy point around 10 eV. Figure 5.6 suggests the $5d^5 6d$, $5d^3 6s^2 6p$, and $5d^6$ configurations share similar trends in overall shape and farther away ionization peaks as the $6s6p$ configurations. The cross sections further seem to be consistent across configurations regarding the heights of the peaks relative to their ionization potentials.

Similar to the septet analysis, an examination of the $6s6p$ quintet classical scaling was performed, in part motivated by the need to account for other excited states not extractable from the *R*-matrix data. Figure 5.7 shows a subset of the $6s6p$ scaling. The diffuseness of the lines, solid versus dashed versus dotted, designates the term energy order: the solid and dotted lines represent the lowest energy term (^5P at 5.54 eV) and highest energy term (^5G at 7.78 eV). The heights of the scaled cross sections thus decrease with increasing term energy and decreasing ionization potential. Furthermore, many of the cross sections, especially in the middle of the term energy range, converge at higher incident energies. This convergence in particular suggests that a scaling might be reasonable for obtaining cross sections of terms missing from the RMPS calculation.

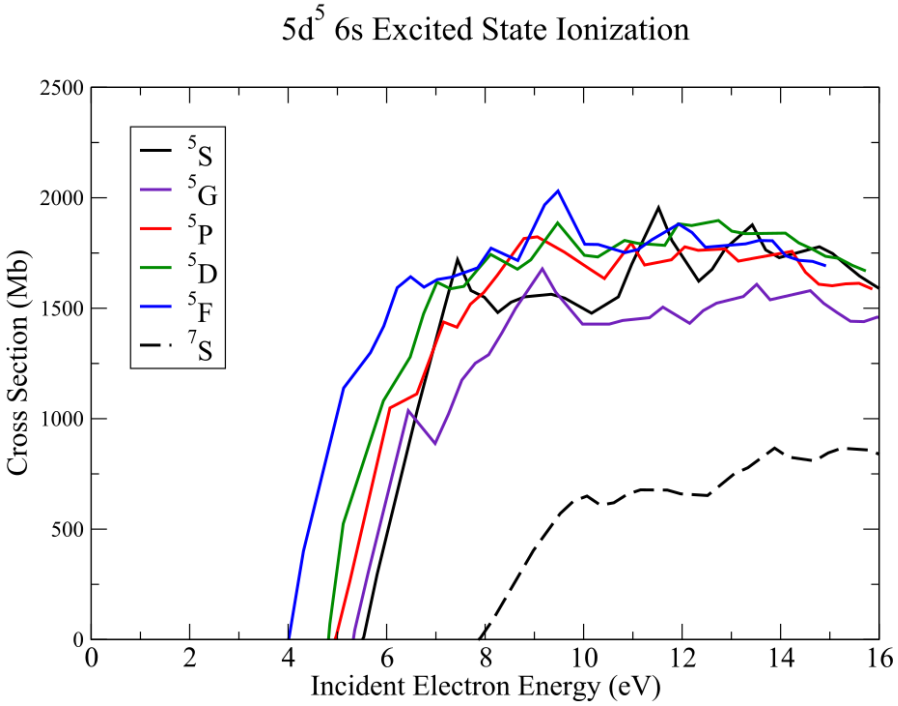

Figure 5.4: Raw cross sections of the $5d^5 6s$ quintet excited states. They all exhibit similar shapes and, compared with the metastable (dashed) and each other, match the trend of an increasing height with decreasing ionization potential.

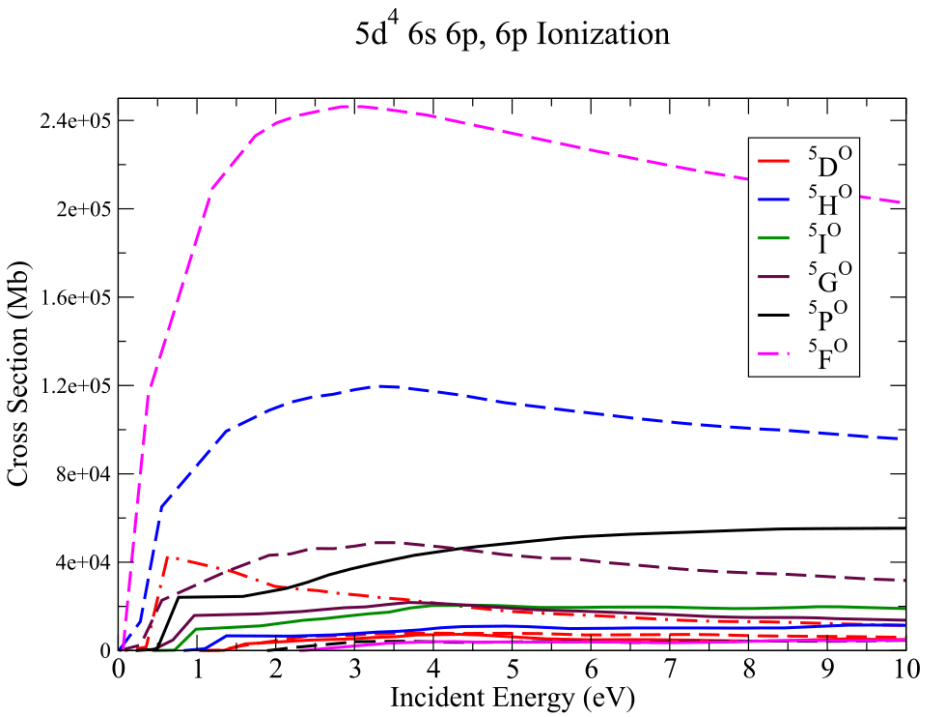

Figure 5.5: Raw cross sections of $6s6p$ ionization from the quintet states. Direct ionization of the $6s$ was not considered.

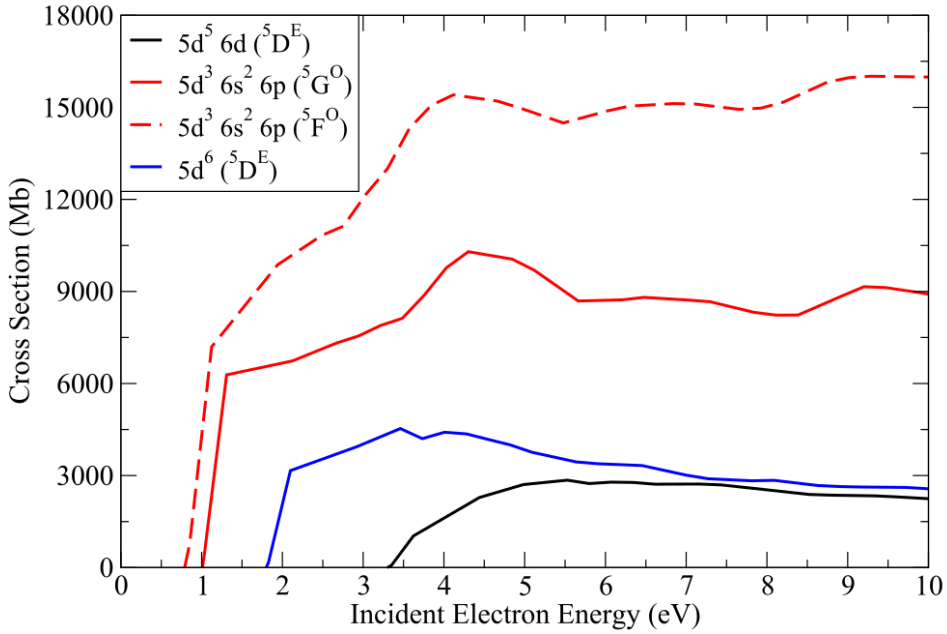

Figure 5.6: Raw cross sections of $5d^5 6d$, $5d^3 6s^2 6p$, and $5d^6$ ionization. The cross sections are overall smooth and follow similar trends regarding ionization potential versus height.

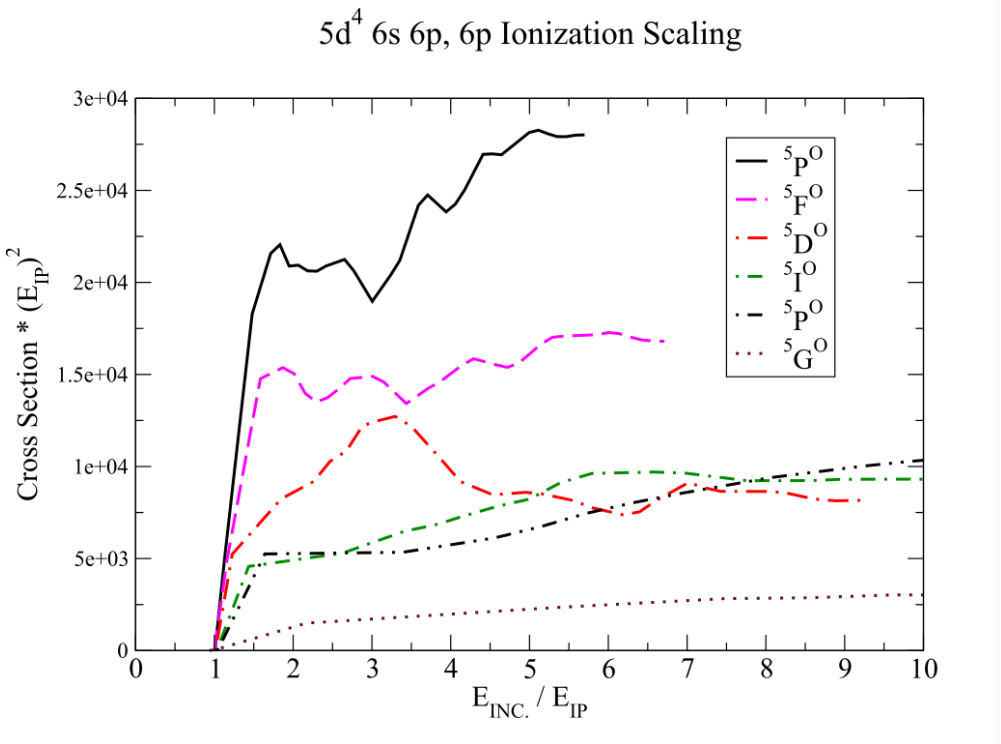

Figure 5.7: Scaled cross sections for quintet $6s6p$ ionization. The cross sections are multiplied by their ionization potentials squared and are plotted versus the ratio of the incident energy to their ionization potential. The diffuseness of the lines indicate the term's energy: the solid line represents the term lowest in energy (highest ionization potential), while the dotted line represents the term highest in energy (lowest ionization potential).

5.2 Fitting the Cross Sections and ECIP Scaling

Similar to neutral neon, all of the cross sections were fit using Rost-Pattard and Younger fits in the lower and higher incident energy regions respectively. Unlike neon, issues arose particularly for the ground and metastable cross sections in that the Bethe energy limit did not correspond to the proper high energy behavior of the cross sections in *LS*- or *LSJ*-resolution. The Bethe points are derived from a configuration-averaged distorted wave approach and therefore do not account for the configuration mixing effects observed in the cross sections. The Rost-Pattard fits as well tended to overestimate the cross sections, in part due to the small energy ranges of the ground and metastable cross sections; they clearly have not reached the peak of their cross sections yet in the available 0 - 16.5 eV incident energy span.

A related issue to fitting the cross sections was also deriving scaled cross sections for missing excited states. Among the missing excited state cross sections were singlet and triplet terms as well as those arising from configurations included in the DARC structure but not in the RMPS. An alternative to Rost-Pattard and Younger fits was therefore employed involving a least-squares fit to the Exchange-Classical Impact Parameter (ECIP) cross sections of the respective term's ionization. The fit involved a single scale factor multiplied by the ECIP result and often gave better results than the Rost-Pattard and Younger fits. Furthermore, the scale factors can be applied directly to target levels in an adf04 file and utilized by the ADAS GCR suite of collisional-radiative codes, allowing for a reasonable approximation for the ionization rate coefficients for the missing excited states.

Figures 5.8 and 5.9 show a comparison of scaled ECIP results with the raw RMPS cross sections for both $6s$ and $5d$ ionization. For $6s$ ground ionization and $5d$ metastable ionization in particular, the high energy Younger fit (red) is producing a much higher cross section than the general trend of the raw data. For both the ground and metastable ionizations, therefore, the decision was made to use the scaled ECIP cross sections when making rates, rather than the Rost-Pattard and Younger fits.

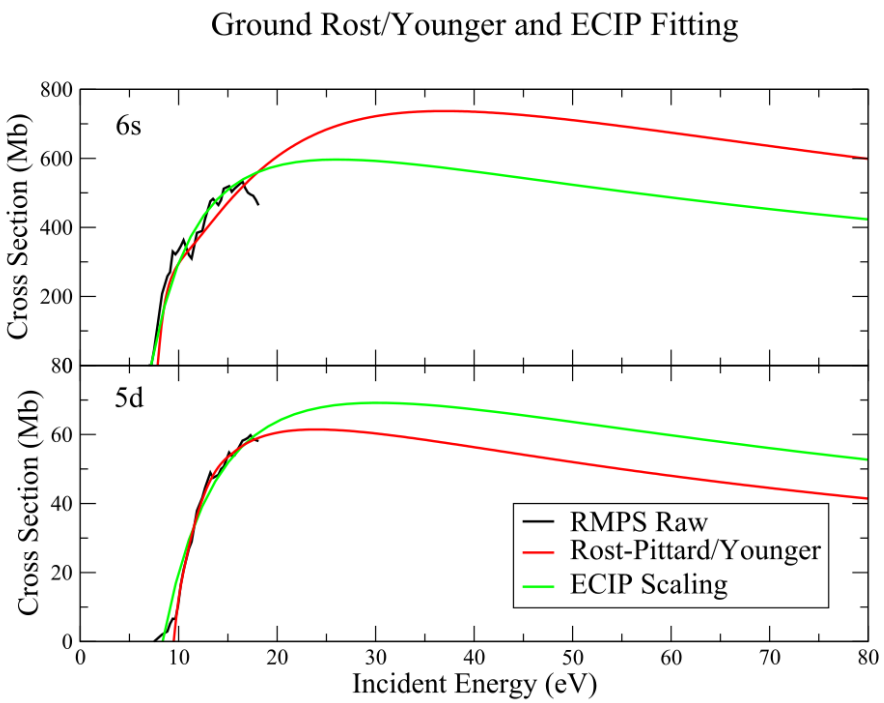

Figure 5.8: Scaled ECIP (green) versus Rost-Pattard/Younger (red) fitting of the ground state $6s$ and $5d$ raw cross sections (black).

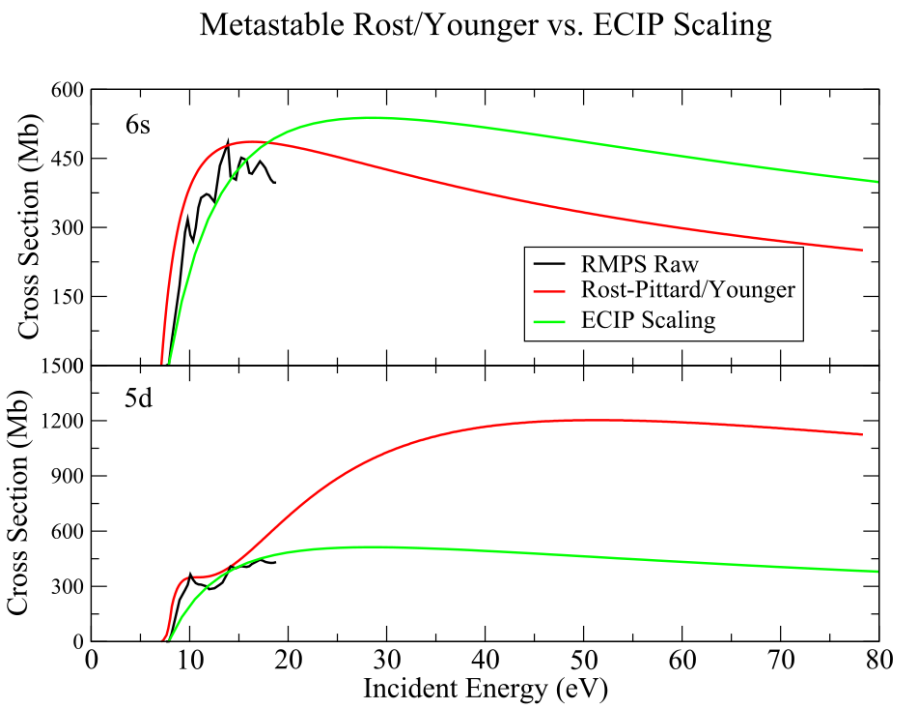

Figure 5.9: Scaled ECIP (green) versus Rost-Pattard/Younger (red) fitting of the metastable state $6s$ and $5d$ raw cross sections (black).

Rost-Pattard and Younger fits proved more reliable overall for the excited state cross sections compared to ECIP. The combination of two separate equations allows for more accurate coverage of idiosyncrasies in the cross sections, such as extra smaller peaks prior to the overall peak. Further, their cross sections, starting at lower energies, cover a broader cross section range and are less sensitive to the configuration-averaged Bethe point. The Rost-Pattard and Younger fits were therefore used when deriving rates for extractable excited states, while the scaled ECIP cross section was used for the ground and metastable states. ECIP scaling was still useful in determining cross sections from excited states not present in the RMPS calculation, however.

Figures 5.10 and 5.11 show select examples of ECIP scaling for the $5d^4 6s6p$ and miscellaneous excited state configurations respectively. Results for the fitting were mixed (pardon the pun). In some cases the scaled ECIP result agrees well with both the raw data and its higher energy trend. In other cases, e.g. the $5d^4 6s6p$ (^5H) and the $5d^5 6d$ (^5D), both the peak height

and high energy trend clearly do not match the raw results. To make the ECIP and raw results match as closely as possible, the ionization potential was shifted during the ECIP calculation for some cross sections, such as with $5d^4 6s6p$ (^7F).

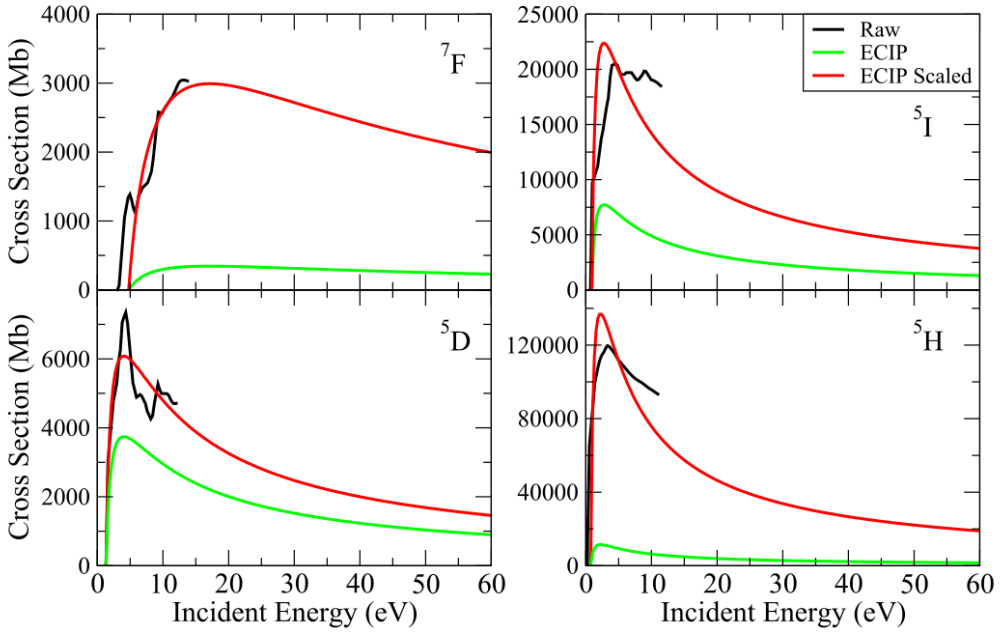

Figure 5.10: ECIP scaling shown for select $5d^4 6s6p$ terms. In some cases, such as the (^7F) cross section (top left), the ECIP ionization potential was shifted from that used with the RMPS in order to produce better fits.

Cross sections from configurations and terms excluded from the RMPS calculation were then obtained through fits to the ECIP scale factors, and these fits revealed interesting patterns regarding parity and configuration mixing. Figure 5.11 shows a plot of the ECIP scale factors obtained from each cross section versus ionization potential and includes the ground and metastable terms, as well as terms rising from the $5d^5 6s$, $5d^4 6s6p$, $5d^3 6s^2 6p$, $5d^5 6d$, $5d^4 6s6d$, and $5d^6$ configurations. Overall, the data appears to form two unique and possibly parallel lines showing a positive correlation between ionization potential and the ECIP scale factor. This trend makes physical sense in that terms with lower ionization potentials involve less

interaction with the overall target system, and are therefore more likely to correspond to semi-classical results. A similar result was seen with the neutral neon 4d, 4p, and 5p excited states when n^4-scaling was applied. A few exceptions are much higher than these two trend lines, including the ^5F, ^5H, and ^5P terms of $5d^46s6p$ (with scales of 21.037, 11.942, and 8.116 respectively) as well as $5d^36s^26p$ (^5F) (13.275 scale). The metastable scale factor shown is lower than the two lines, though this can be explained by the choice of "1" for the occupation number of the ECIP calculation shown. Recall, $5d$ and $6s$ ionization each contributed about half of the total metastable (^7S) cross section. The ECIP scales shown assumed ionization of only singly occupied orbitals, namely $6s$, $6p$, or $6d$. For ECIP, the final cross section is multiplied by the occupation number. The large contribution of $5d$ ionization to the metastable, which really should have an occupation number of 5, therefore skews its data point.

Two linear fits were thus applied to the ECIP scaling results, excluding the five outlier terms mentioned above. Interestingly, the linear fits extended across different configurations. The black line naturally included scale factors from $5d^46s6p$ and $5d^36s^2$, while the green line included those from $5d^56s$, $5d^46s^2$, $5d^56d$, $5d^46s6d$, and $5d^6$. The key difference between these two configuration sets is their parities: *the black and green lines correspond to ionization from configurations of odd and even parities respectively*. The odd parity fit is less precise, $y = (21.26 \pm 2.78)x + (1.4295 \pm 0.5415)$ with $R^2 = 0.9175$, compared to the even parity fit, $y = (21.427 \pm 0.804)x - (1.922 \pm 0.268)$ with $R^2 = 0.9951$. The two slopes are further within 0.05 standard deviations of each other, suggesting a potential equivalence. The ECIP method is blind to parity, and the shift between the two lines might suggest a deeper role for the target configuration's parity in its RMPS ionization cross section. Additionally, the three $5d^46s6p$ configurations lying between the two lines are all ^5D, a term also possible for all of the shown even-parity configurations. Configuration mixing might therefore play a role in the shift of these configurations closer to the green line, although another $6s6p$ (^5D) term does not exhibit this same shift.

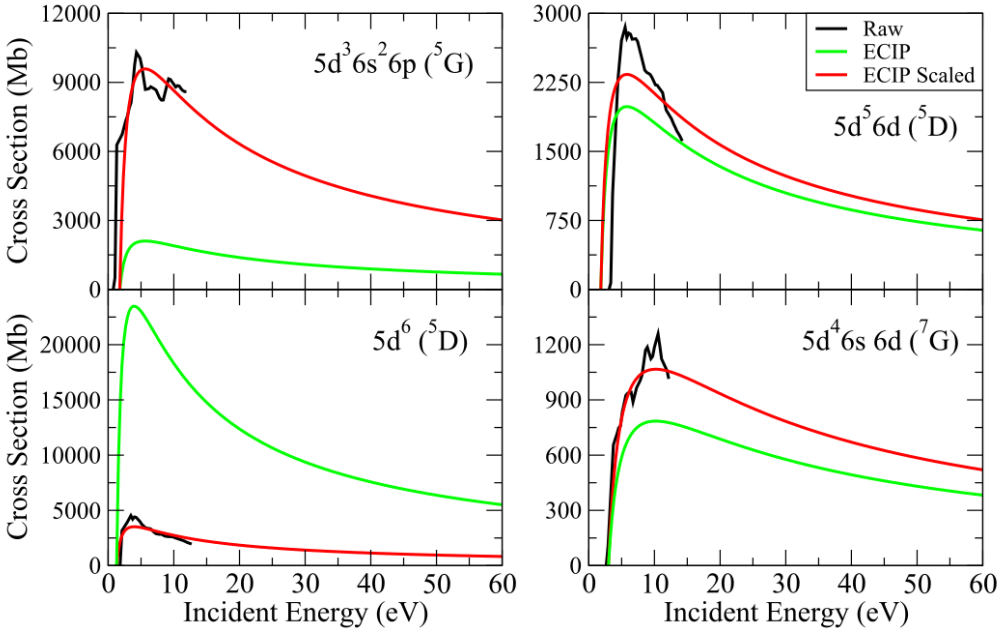

Figure 5.11: ECIP scaling shown for select configurations.

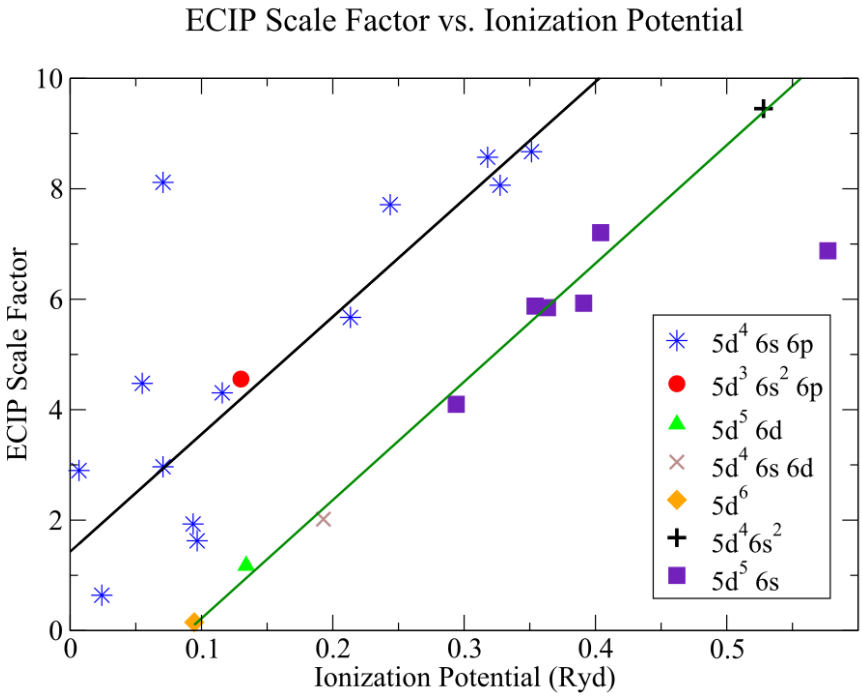

Figure 5.12: ECIP scale factors for each extracted term cross section versus ionization potential. Two linear fits were generated, which seem to correspond to odd (black) and even (green) parity configurations and for which $R^2 = 0.9175$ and 0.9951 respectively, if neglecting outliers.

Cross sections and rate coefficients for ionization out of the excited states present in the DARC calculation but not the RMPS were therefore generated using ECIP with scale factors calculated from one of the two linear fits of the scaling data, choosing whichever fit corresponded with the excited state's parity. A full set of ionization rates for all states of neutral tungsten was therefore compiled from the RMPS calculation and stored in an adf04 file to be made available to the public.

5.3 On the $5d^4 6snl$, $5d^5 nl$, and $5d^3 6s^2 nl$ contributions to excited state ionization cross sections and possible W^+ final state resolution

An important assumption was made in generating the rate coefficients, whose validity will be examined further in the succeeding section: *the final W^+ states were left unresolved*. In keeping with the raw cross sections, all of the ionization rate coefficients assume the W^+ ground

ionization potential, corresponding to $5d^46s$ at 7.8640 eV. Configuration-averaged and *LSJ* resolution of the W^+ final states had been considered, including $5d^5$ and $5d^36s^2$ at 8.784 eV and 8.844 eV from the W ground state respectively. Resolving the final states would have the effect of increasing the overall average ionization potential from each level, which would lead to proportionately smaller cross sections and ionization rate coefficients. Yet, resolution of the final ionized state is problematic for neutral tungsten due to both excitation autoionization and configuration mixing typically present with both the initial and final states, which shall be the topic of the present discussion.

Similar to the ground and metastable term-resolved ionization cross sections, the excited state cross sections are the results of several effects related to configuration-mixing, shared ionization pathways, and excitation autoionization. Resolution of the final W^+ states would require separate accounts of the contributions from each of these processes, including which final W^+ state would result. Neutral tungsten can be ionized to $5d^46s$, $5d^5$, or $5d^36s^2$, whose lowest levels and energies are ${}^6D_{1/2}$ at 0.00 eV, ${}^6S_{5/2}$ at 0.92 eV, and ${}^4F_{3/2}$ at 1.08 eV respectively. As will be shown, the $5d^36s^2nl$ series contributed almost nothing to the excited state ionization cross sections. The following discussion will therefore only consider ionization to $5d^46s$ or $5d^5$. Furthermore, a preliminary W^+ structure calculation suggests that the lowest $5d^46s$ and $5d^5$ terms are highly pure, with leading percentages of 99.1% and 97.8% respectively. If the final W^+ states can be discriminated, their configurations will therefore be assumed as the entire, rather than as a configuration contributing from a smaller mixing percentage.

The following processes related to W ionization can result in the $5d^5$ final state:

1. For W states that are predominantly $5d^5nl$, direct ionization out of the nl orbital into the $5d^5n'l'$ contributions of states above 0.92 eV. This includes any where the $5d^5n'l'$ series are an appreciable percentage, major or otherwise.
2. For W states that are predominantly $5d^46snl$, direct ionization from the lesser $5d^5nl$ percentage into the $5d^5n'l'$ contributions of final states above 0.92 eV. This includes any where the $5d^5n'l'$ series are an appreciable percentage of the final state, major or otherwise.

For processes resulting in the $5d^46s$ final state, the converse of the above processes are possible in addition to a couple of others:

1. For W states that are predominantly $5d^46snl$, direct ionization out of the nl orbital into the $5d^46sn'l'$ contributions of states. This includes any where the $5d^46sn'l'$ series are an appreciable percentage, major or otherwise.
2. For W states that are predominantly $5d^5nl$, direct ionization from the lesser $5d^46snl$ percentage into the $5d^46sn'l'$ contributions of final states. This includes any where the $5d^46sn'l'$ series are an appreciable percentage, major or otherwise.
3. For $5d^5nl$ contributions of W states, major or otherwise, direct ionization of the $5d$ orbital from the $5d^5nl$ contribution.
4. For $5d^5nl$ contributions of W states, major or otherwise, excitation autoionization from a $5d^5n'l'$ contribution, possible below 0.92 eV.

The above processes cover a wide range of possibilities for the crossing over from one configuration series to another between initial and final states. For the general case of an excited state term with appreciable configuration mixing, able to transition into a wide range of heavily mixed pseudostates, one must therefore ask whether the ionization constraints upheld in a configuration-resolved modeling of the atom are still valid. That is, for a given incident electron energy, some of the above processes might be more favorable than others, whereas in configuration-averaged resolution, a smaller number of processes, namely $5d$ and $6s$ direct ionization and excitation autoionization, are possible. In both classical and quantum mechanics, the motion and processes of a (closed) system correspond to minimizing the system's total energy. Ionization cross sections defined according to the ground state ionization potential of W^+ might therefore better reflect this precept of energy minimization.

As an illustration of the appropriateness of a W^+ ground state resolution to the ionization potential and also of the complications of resolving the final states, Figure 5.13 shows the contributions of the $5d^46snl$, $5d^5nl$, and $5d^36s^2nl$ series to a representative sample of excited states. Both the $5d^46snl$ and $5d^5nl$ contributions are significant for nearly all of the excited states, shown or otherwise. Some exceptions include ionization from the $5d^46s6p$ (^5I) term, for which there is only a $5d^46snl$ contribution. The exclusion of other contributions for this

term can be explained by the fact that the term can only arise from a $5d^4 6s$ (^4H) core. In general, the $5d^4 6snl$ series contributes the most to cross sections. Some exceptions include the $5d^6$ (^5D) and $5d^4 6s6p$ (^5F), both shown in Figure 5.13 for which the $5d^5 nl$ series contributes the most.

The $5d^3 6s^2 nl$ contributes less than 1% for all of the extracted cross sections, surprisingly including for the $5d^3 6s^2 6p$ ionized terms. The cross sections of both of the extracted $5d^3 6s^2 6p$ terms, the ^5F shown in Figure 5.13 are composed primarily of transitions to $5d^4 6snl$ states, with almost no contribution from the $5d^3 6s^2 nl$ states. The $5d^3 6s^2 6p$ results contrast a configuration-averaged picture, for which the system would be constrained to the much higher $5d^3 6d^2$ ionization potential. They also further emphasize a breakdown in configuration-based physical concepts of ionization: the $5d^5 nl$ contribution would correspond to an ionization, double-excitation.

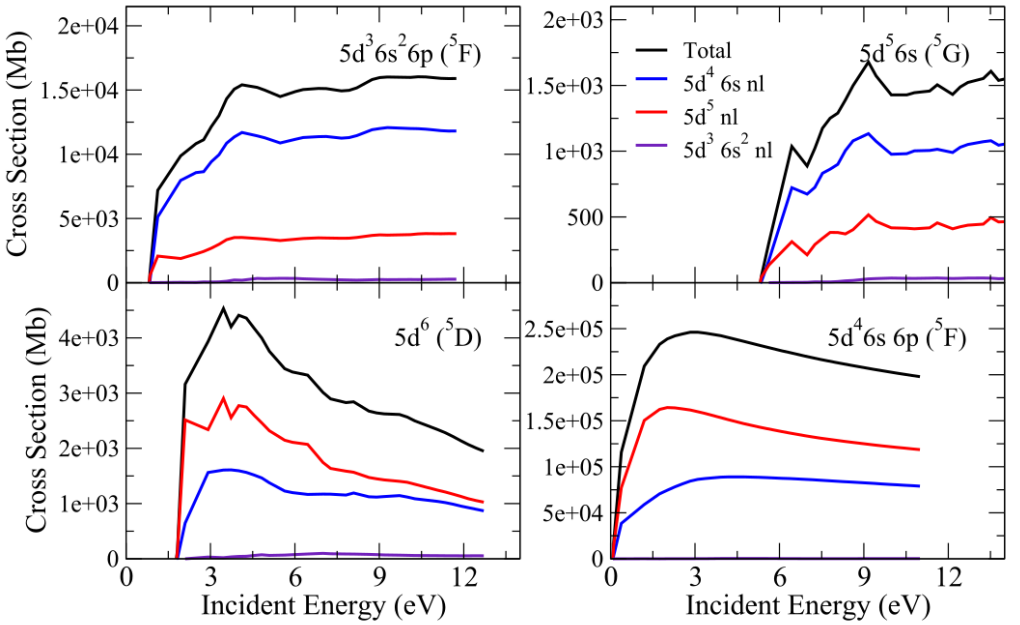

Figure 5.13: Contributions of the $5d^46snl$, $5d^5nl$, and $5d^36s^2nl$ final state series to select excited state ionization cross sections. For most of the excited state cross sections overall, including for terms arising from $5d^36s^26p$ (top left, e.g.), $5d^46snl$ is the leading contributor. For $5d^36s^2nl$ contributes less than a percent for all of the cross sections, including for those cross sections not shown.

Given that the excited-state ionization cross sections look fully-formed for all extracted configurations relative to the ground state ionization potential and that the breakdown of contributions in general strongly favors the lower energy $5d^46s$ final state, ionization cross sections and rates, including for missing terms requiring ECIP scaling, were obtained relative to the W^+ ground state. Whether results would further be improved from full *LSJ*-resolution also seems unlikely, despite most transitions not being possible to the LSJ ground level. The effect of an potential overall shift in the ionization potential as a result of *LSJ*-resolution is considered in the next section.

Figure 5.14 shows the resultant ground-resolved SCD from GCR modeling at electron densities of 10^{13} and 10^{14} cm^{-3} of the full new tungsten dataset (red), including the DARC electron-impact excitation results [41], the RMPS electron-impact ionization results, and ECIP scaling of the RMPS for missing excited state ionization cross sections. The full atomic data uses ionization results from branching ratios of the TDCC for the higher $5d^4 6s^2$ excited states. It should be noted that these results are still the subject of investigation and may be subject to change (see the work in Section 5.5 on the sensitivity of the $6s6p$ excited state cross sections to changes in the orbital wavefunctions). This SCD is nearly a factor of five and twelve higher at 25 eV at lower and higher electron densities respectively compared to the SCD if only including the RMPS ground ionization rate (green). The RMPS SCD from ground only ionization is slightly more than half the TDCC ground only SCD across all electron temperatures from 0 to 26 eV and both low and high electron densities. The SCD if not including ECIP, scaled or otherwise, for missing excited states (blue) is within 20% of the results with all excited states included, indicating that these additional excited states are not dominating the effective ionization rate coefficient. The same trend is observed at high electron density, but the SCD without ECIP is 60% that with scaled ECIP. As expected, therefore, the scaled ECIP rate coefficients, used predominantly for higher excited states, contribute a larger percentage to the SCD at higher densities, in keeping with a larger population in these states. Similarly, the TDCC and RMPS SCDs for ionization from the ground only are further reduced at higher density. Compared to results from unscaled ECIP rates (orange), which would correspond to the default ionization rates in ADAS, the effective ionization rate from the new RMPS/scaled ECIP rates is increased by about a factor of 5 or 6 at both shown electron densities.

An additional check on the importance of W^+ final state resolution was performed (purple), for which the ionization potential in the adf04 file was increased by 0.5 eV. Given that $5d^4 6s$ (^6D) and $5d^5$ (^6S) W^+ levels range from 0.00 to 0.9199 eV, this seemed like a reasonable approximation for a possible shift in the ionization potential due to final state resolution. The shifted ionization potential was used to calculate the ECIP rates. The rates directly from the

RMPS and TDCC calculation are stored in the adf04 file as being multiplied by exp(E_{IP}/k_BT) for greater numerical stability. Upon GCR modeling, these rates were thus divided by this factor, except the ionization potential E_{IP} was now the shifted ionization potential. The SCD decreased 6% and 15% for low and high densities respectively as a result of this shift.

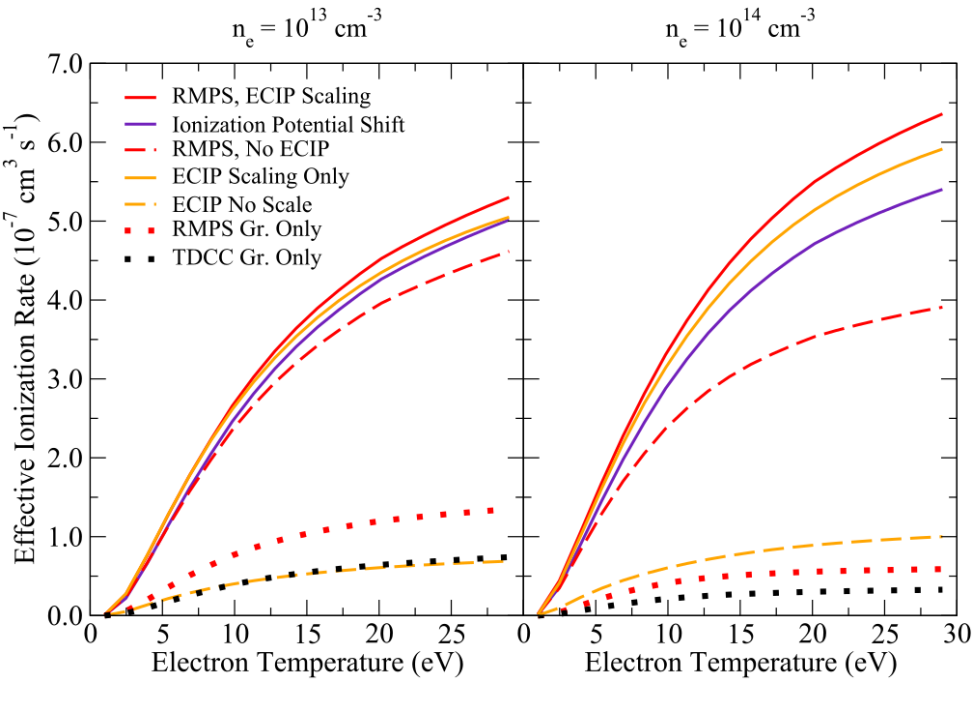

Figure 5.14: Ground-resolved effective ionization rate coefficient results at electron densities of 10^{13} and 10^{14} cm^{-3} from GCR modeling with the new tungsten atomic data. The difference between the SCD from the full dataset (red) and those of not including ECIP for missing states (blue), RMPS ground ionization only (green), and TDCC ground ionization only (black), illustrates the contribution of excited-state ionization at both low and high densities. The ground-only results include ionization from all of the levels arising from the $5d^46s^2\ ^5D$ term. Further, the SCD was not sensitive to increasing the ionization potential by 0.5 eV (purple).

A similar study of the 400.9 nm photon emissivity coefficient, the denominator of the S/XB, was performed, shown in Figure 5.15. For both 10^{13} and 10^{14} electron densities, the full PEC, here assuming the metastable states are in steady-state with the ground population, experiences a large reduction at higher electron temperatures, more than a factor of three and

increasing for n_e = 10^{14} cm^{-3}, compared to the ones from including only ground state ionization. Similarly, the PEC at 10^{14} cm^{-3} from unscaled ECIP ionization rates is reduced by almost a factor of two compared to the ground only PECs. As electron-impact excitation is the main driving force behind population of excited states, thus also of the PECs, the fact that ionization is reducing the PEC is a significant result. Compared to ionization rates of lower levels, greater ionization out of both the upper levels of the transitions and higher excited states that might spontaneously emit down to the upper level are a plausible explanation. Compared to ionization from the ground only, ionization from excited states reduces the population of the upper level. Similar to the SCD, increasing the ionization potential by 0.5 eV has almost no effect on the lower density PEC and a slight effect, about a third increase, on the higher density PEC.

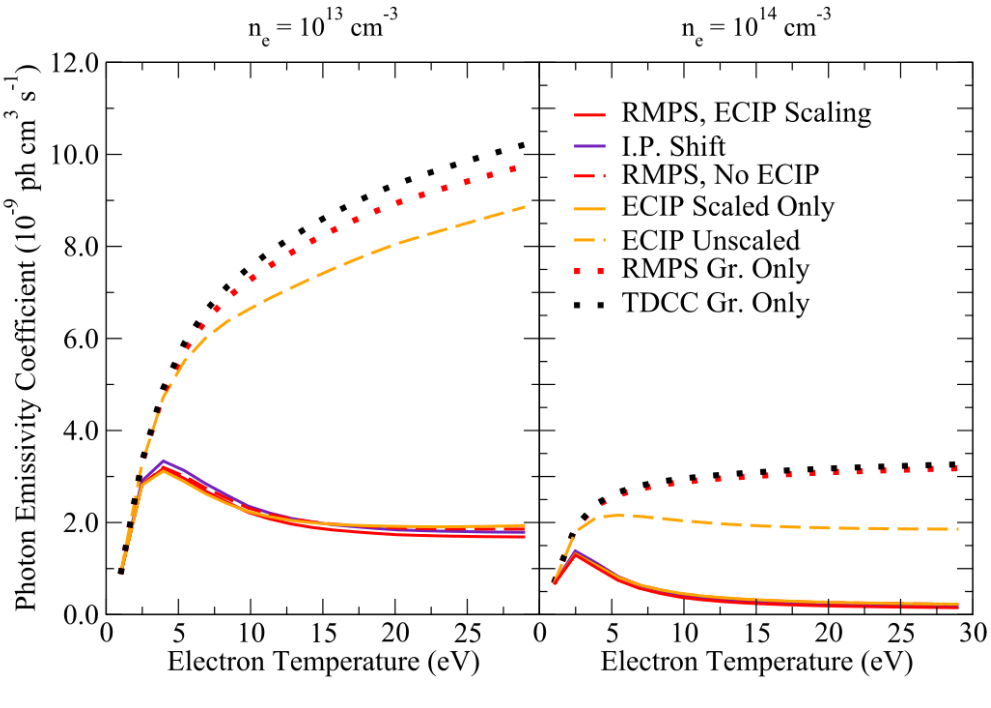

Figure 5.15: Ground-resolved 400.9 nm ($5d^5 6p\ ^7P_4$ - $5d^5 6s\ ^7S_3$) photon emissivity coefficient results at electron densities of 10^{13} and 10^{14} cm^{-3} from GCR modeling with the new tungsten atomic data. The PEC from the full dataset (red) is reduced relative to those of not including ECIP for missing states (blue), RMPS ground ionization only (green), and TDCC ground ionization only (black). The ground-only results include ionization from all of the levels arising from the $5d^4 6s^2\ ^5D$ term. Further, the PEC experienced negligible change to a third of a ph cm^3 s^{-1} at low and high densities as a result of increasing the ionization potential by 0.5 eV (purple).

So far, non steady-state metastables other than the ground state have been neglected in GCR modeling. The ratio of the above SCD to PEC further suggests that the 400.9 nm S/XB would be several orders of magnitude higher than those from experimental measurements across all electron temperatures and densities. A ground-resolved S/XB using only unscaled ECIP is similarly orders of magnitude above experimental measurements, suggesting the discrepancy is independent of the ionization data being used. In corroborotion with the

metastable population modeling of Beigman *et al.* [11], then, metastable resolution might resolve the discrepancy of the 400.9 nm S/XB. The generalization of GCR modeling to include multiple metastables was discussed in Section 2.6.

If metastable resolution is required for an accurate S/XB, the fraction of each metastable population, which is unique to each plasma, must be also determined. Knowledge of these neutral tungsten's metastable population within plasmas such as at DIII-D is beyond the scope of this dissertation. Another issue with metastable-resolved GCR modeling of tungsten is the presence of a large excited state population, for which the GCR results must be appropriately normalized. At present, a rough normalization of excited state populations is implemented in ColRadPy [84], using a factor of the sum of the excited state populations + 1. A more complete account of the excited state normalization will not be attempted here; however, metastable-resolved GCR modeling with the rough population normalization used in ColRadPy might help assess how many metastables are needed to represent plasma conditions, as well as the relative importance of each metastable.

Figures 5.16 and 5.17 show the results of metastable resolution, performed with ColRadPy [84], of the neutral tungsten atomic data on the SCD and 400.9 nm PEC respectively (solid lines), at an electron density of 10^{14} cm^{-3}. The first six levels, including the five arising from $5d^46s^2$ (^5D) and the one from $5d^56s$ (^7S), are used as metastables in GCR modeling. The SCD and PEC results from GCR modeling with unscaled ECIP only is also shown (dashed lines). Per metastables, the SCDs and PECs from modeling of the new RMPS atomic data are about 3.33 times as large and the same order of magnitude respectively of those from modeling with unscaled ECIP. For both cases, all of the metastable-resolved SCDs are within the same range as each other for all electron temperatures, the RMPS/scaled ECIP SCDs slightly more spread at higher electron temperatures. Further, the SCDs from both datasets are all higher than their respective ground-resolved SCDs (black, diamond, and solid and dashed for the RMPS and unscaled ECIP respectively). Overall, the metastable-resolved 400.9 nm PECs agree well between RMPS and unscaled ECIP, with the latter being slightly higher at electron temperatures above 5 eV for all metastables. The ground-resolved 400.9 PEC is not shown in Figure 5.17 for comparison, because it is much smaller than the metastable-resolved PECs. The small

magnitude of the ground-resolved PEC explains why the ground-resolved S/XB appears much larger than previous measurements.

The metastable 400.9 nm PEC plot hints at a possible way to obtain the metastable population fractions: the PEC is driven almost entirely by $5d^5 6s$ (^7S). This level is also the lower level of the 400.9 nm line. The 400.9 nm upper level is thus populated mainly from its own lower level, the same to which it also spontaneously emits. If other spectral lines exhibit similar behavior, being driven primarily by one of the metastables, a diagnostic for each metastable population might then be obtained by measuring a series of lines, each being driven from a different metastable. Collisional-radiative modeling for Mo has shown this to be the case [84], with W showing similar behavior.

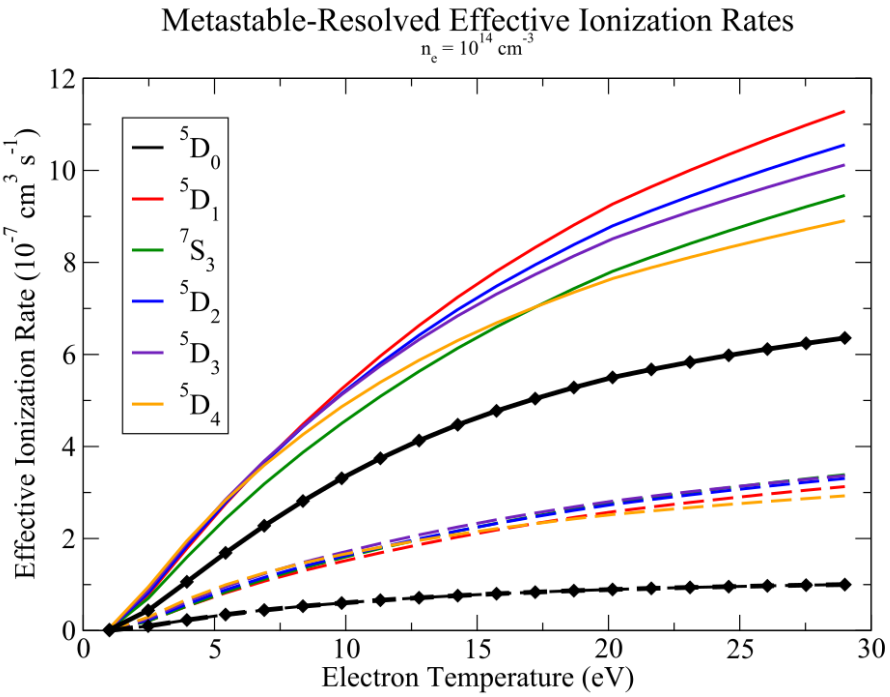

Figure 5.16: The effective ionization rate coefficients modeled with the first six levels as metastables, at 10^{14} cm^{-3}. Across the 0 to 30 eV electron temperature range, the metastable SCDs from the combined RMPS tungsten ionization and ECIP scaling data (solid lines) are roughly each twice as large as their respective metastable SCDs generated using unscaled ECIP ionization rate coefficients only (dashed lines). The ground-resolved SCDs for the full RMPS (black, solid, diamonds) and unscaled ECIP only datasets (black, dashed, diamonds) are also shown for comparison, which are both lower than each of their metastable-resolved counterparts. A rough excited state normalization factor, equal to the sum of the excited state populations + 1, is used.

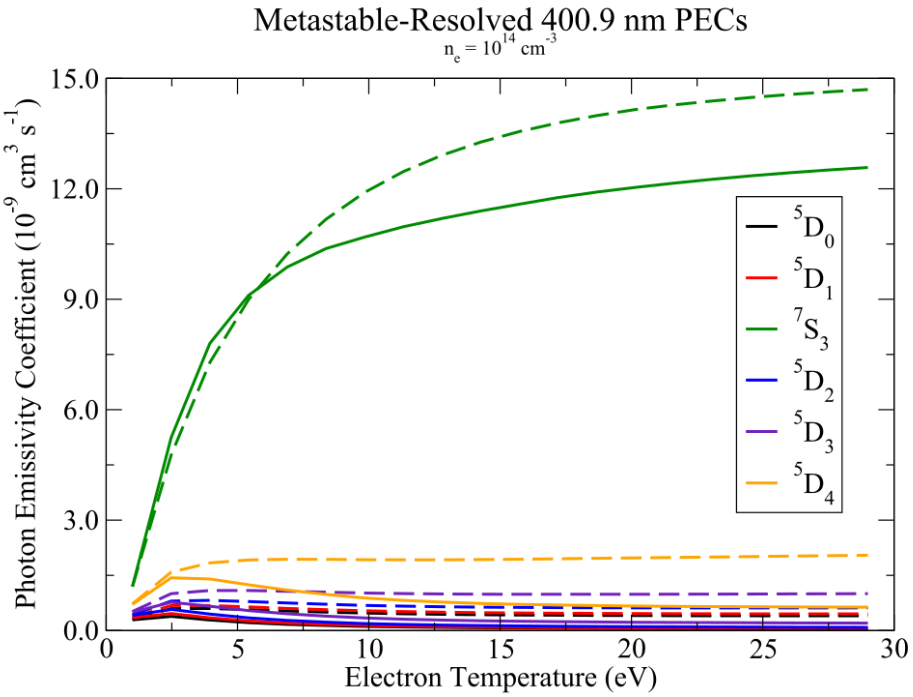

Figure 5.17: The 400.9 nm photon emissivity coefficients modeled with the first six levels as metastables, at 10^{14} cm^{-3}. Across the 0 to 30 eV electron temperature range, the metastable PECs from the combined RMPS tungsten ionization and ECIP scaling data (solid lines) are roughly each half their respective metastable PECs generated from using unscaled ECIP ionization rate coefficients only (dashed lines)). The ground-resolved PECs for the full RMPS and unscaled ECIP only datasets, not shown, are much smaller. In both cases, most of the PEC is driven by the $5d^5 6s$ (^7S) metastable population. A rough excited state normalization factor, equal to the sum of the excited state populations + 1, is used.

Figure 5.18 shows the lower bound of the metastable-resolved 400.9 m S/XBs resulting from the full RMPS atomic data compared with previous measurements. Without knowledge of the metastable populations, an exact line cannot be determined. Instead, the shown lower bound (blue, triangles) is taken from the average of the metastable-resolved SCDs and solely from the metastable ^7S state, the highest PEC. It represents the S/XB if this metastable state comprised the entire population of tungsten in the plasma. The upper bound, which would correspond to the lowest PEC (the ground), is not shown, because it reaches into the hundreds

across all shown electron densities at low electron temperatures. Three electron densities are shown: 10^{12} (dot-dashed), 10^{13} (dashed), and 10^{14} (solid) cm^{-3} respectively. The 10^{13} and 10^{14} cm^{-3} lower bounds fall below previous measurements of the same density range. Yet, because the upper bounds and the ground-resolved S/XBs are so much higher, it is hard to determine the accuracy of the DARC/RMPS rate coefficients.

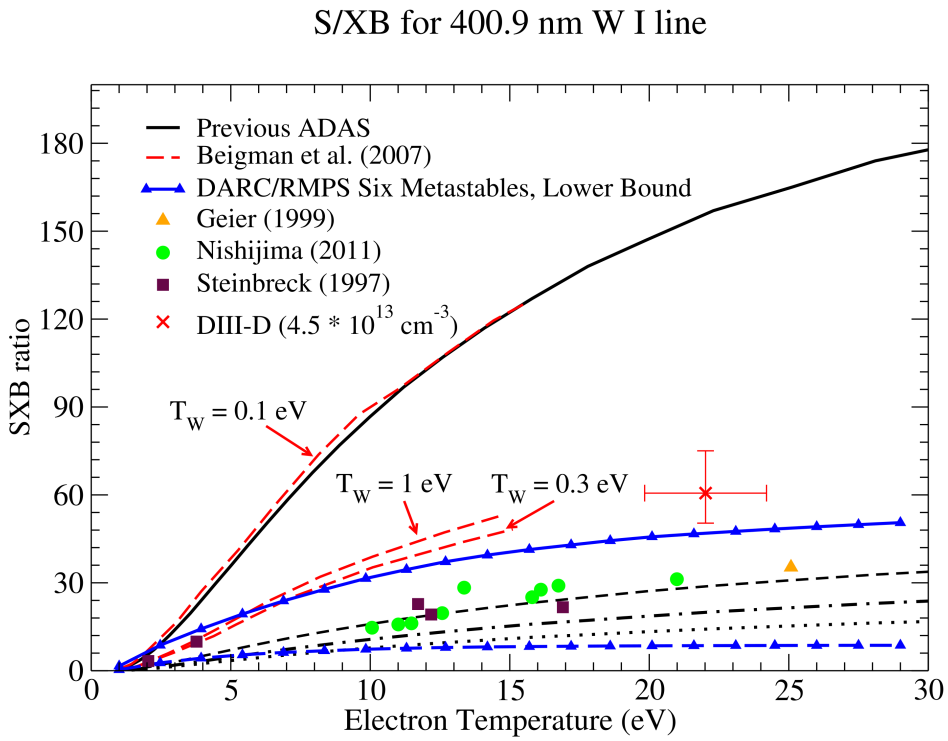

Figure 5.18: The 400.9 nm S/XB ratio from the DARC [41]/RMPS dataset compared to previous calculations and measurements [8, 11, 25, 26, 28]. Six metastables were used, and the S/XB shown (blue, triangles) corresponds to the lower bound of the S/XB, the result of assuming all of the population is in the $5d^5 6s$ (^7S) state. The ground resolved S/XB, which reaches into the hundreds at low temperatures, is not shown. The upper bound of the S/XB with six metastables reaches a similar high value. A rough excited state normalization factor, equal to the sum of the excited state populations + 1, is used.

5.5 *6p* orbital study to assess the accuracy of the RMPS ionization rates

A greater understanding of the accuracy of the neutral tungsten structure and RMPS calculations would help narrow the possibilities in understanding the high 400.8 nm ground-resolved S/XB. Recall from Section 4.2 that the orbital scaling parameters were optimized primarily on agreement of the ground and metastable energies as well as A-values for transitions with upper levels close to the ionization potential. Most of the optimization involved adjustments to the $5d$ and $6s$ orbitals. From observation, the $6p$ orbital produced little effect on the energies of the levels arising from $5d^46s^2$ and $5d^56s$. Levels arising from $6p$-occupied configurations were sensitive to changes in the $6p$ lambda scaling parameter, however. The energies of the lowest lying (septet) $6s6p$ states showed good agreement for $\lambda_{6p} \approx 1.12$ or 0.95. For the latter parameter, the A-values for emissions both from higher-lying excited states and from the 400.9 nm transition showed significantly worse agreement. On the other hand, the ground-resolved S/XB results suggest that the RMPS ionization rates might be too high.

Gauging the accuracy of the atomic structure along with the size of the odd parity cross sections and rates is complicated by the presence of heavy configuration mixing between the odd parity configurations and by the shifts in ionization potentials between configurations and their LSJ-resolved levels. The odd parity study by Wyart [59] suggested only one odd parity configuration has a $5d^56p$ majority; that is, the presence of the $5d^56p$ in the atomic structure is primarily as a lesser percentage of $5d^46s6p$ configurations.

A comparison of the RMPS $6s6p$ scaled ionization cross sections to CADW cross sections relevant to N + 1 channel coupling are is shown in Figure 5.19, featuring the same term-specific ionization potential E_{IP} scaling as Figures 5.3 and 5.7. Recall, the sum of the ground and metastable cross sections showed good agreement with the sum of the configuration-averaged $5d^46s^2$ and $5d^56s$ cross sections for DW and ECIP. The ground and metastable cross sections exhibited a case of coupling between N + 1 channels, which one can think of as essentially "N + 1 configuration mixing." This kind of mixing arises from identical spectator electron sets ($5d^46s$ for ground and metastable) leading to interference between Coulomb matrix elements from otherwise orthogonal configurations. Configuration mixing is strongest between terms

of similar energies. Similarly for the $6s6p$ cross sections, the septets are all within 0.04 Ryd of each other (0.355 - 0.388 Ryd) and should therefore yield a similar comparison to the sum of configuration-averaged cross sections corresponding to terms of similar energies. Configurations relevant to the septets are $5d^4 6s\{6s, 6d\}$, $5d^5\{6p, 6d\}$, and $5d^3 6s^2 6p$ terms. The $6s6p$ terms are heavily mixed with terms from all of these configurations, so N + 1 channel coupling effects similar to those seen with the ground and metastable states are therefore possible. Juxtaposition between the $6s6p$ RMPS and the DW scaled cross sections suggests the septets and quintets demonstrate interference similar in shape to the different configuration-averaged cross sections. A small dip in the cross sections is present around $E_{INC.}/E_{IP}$ = 2 for both the CADW and RMPS septets. The RMPS quintets and septets further share peaks, in some cases local ones only, in common with CADW. A large global peak occurs primarily for the septets around 4.5 * E_{IP} that significantly increases their cross sections. Ionization from all of the configurations represented by CADW should be possible within this region, and the large increase might be attributed to the $5d^3 6s^2 6p$ cross section. The sum over the cross sections all of the configurations should be greater than the sum of the RMPS septet cross sections; however, the RMPS septet sum would be slightly larger near this peak. On its own, this result does not invalidate the RMPS odd ionization results. Both the sum of $6s6p$ cross sections and the high ground-resolved S/XB do, however, raise the question of how reliable the RMPS results are, particularly regarding odd parity configurations.

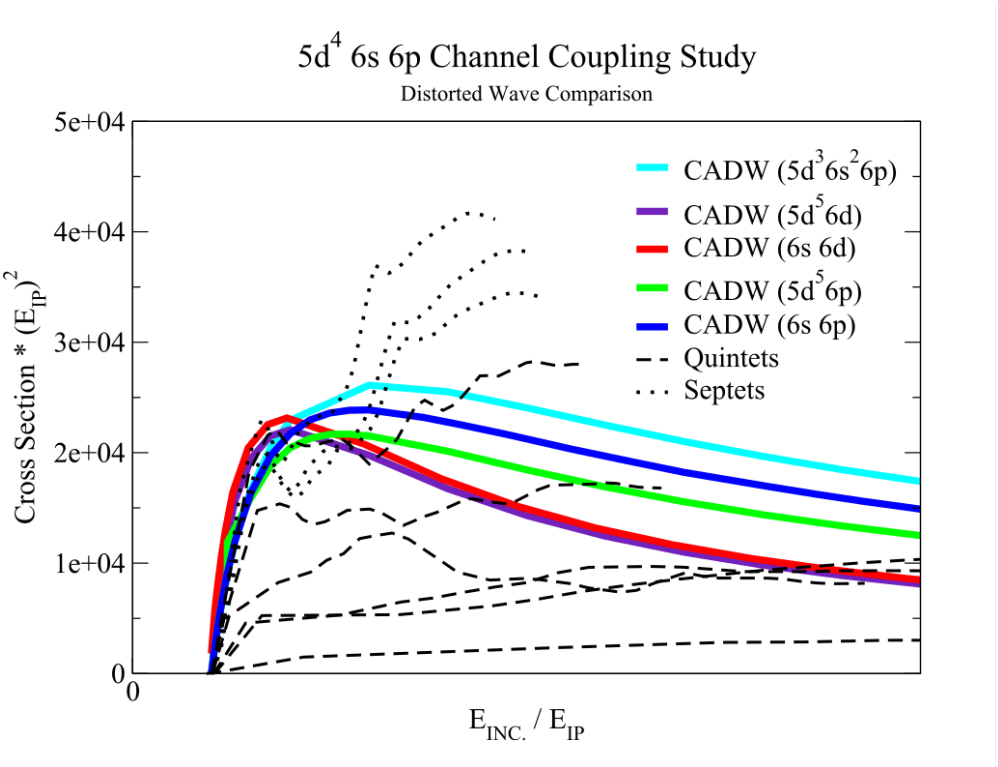

Figure 5.19: Comparison of CADW $6s6p$ (blue), $5d^56p$ (green), $6s6d$ (red), $5d^56d$ (purple), $5d^36s^26p$ (cyan) with RMPS $6s6p$ term-resolved quintet (dashed) and septet (dotted) cross sections. Cross sections are scaled by their ionization potentials E_{IP}, and plotted over the ratio of the incident energy $E_{INC.}$ with E_{IP}.

Because adjustments to the $6p$-orbital scaling parameter was primarily responsible for shifting the $6s6p$ levels during optimization, an additional study was performed to gauge the effect of the $6p$-orbital scaling parameter on the ionization cross sections and rates. Atomic structures resulting from different λ_{6p} values between 1.12 and 0.95 were calculated along with their cross sections resulting from the octet partial-waves. These cross sections were then doubled, similar to the quintets in the full calculation, to approximate their entire cross sections, and the same ECIP scaling technique was applied as described in Section 5.12.

Figure 5.20 shows ECIP scaling results for septet cross sections corresponding to structures with different $6p$-orbital scaling parameters: 0.95, 1.00, 1.06, and 1.09. The black and green lines represent the original fits to the even and odd parity configuration cross sections

respectively. With the exception of λ_{6p} = 0.95, cross sections for extracted even parity ionization cross sections agree well with the original calculation, suggesting that the $6p$ orbital does not have a significant effect on this set of cross sections. Uncertainty is present in generating new fits for the datasets, as each set only has up to 5 points that are relatively close together. Further, points corresponding to cross sections likely to experience stronger channel coupling, as observed with the ^5D terms from odd parity configurations, are likely to be apart from the fit line and closer to the even parity data points. For example, the λ_{6p} = 1.06 (stars) data point that is closest to the even parity configurations is of the $6s6p$ (^7S) term.

Some λ_{6p} datasets suggest the odd parity configuration line should be parallel to the even parity line, particularly for λ_{6p} = 0.95 and 1.09. The λ_{6p} = 1.00 and 1.06 data sets, on the other hand, leave open the possibility that the odd and even parity configuration lines are not parallel. Both contain an outlier point corresponding to the $5d^56p$ (^7P) ionization cross section. The $5d^46s6p$ (^7P) data point from the original calculation is not an outlier, however. Linear fitting of the λ_{6p} = 1.06 dataset if excluding the last $6s6p$ (^7S) point leads to an R^2 value of 0.9992. Furthermore, using a parallel slope for this dataset, such that the three points highest in ionization potential are closest to the line, results in negative ECIP scale factors for levels of lower ionization potentials.

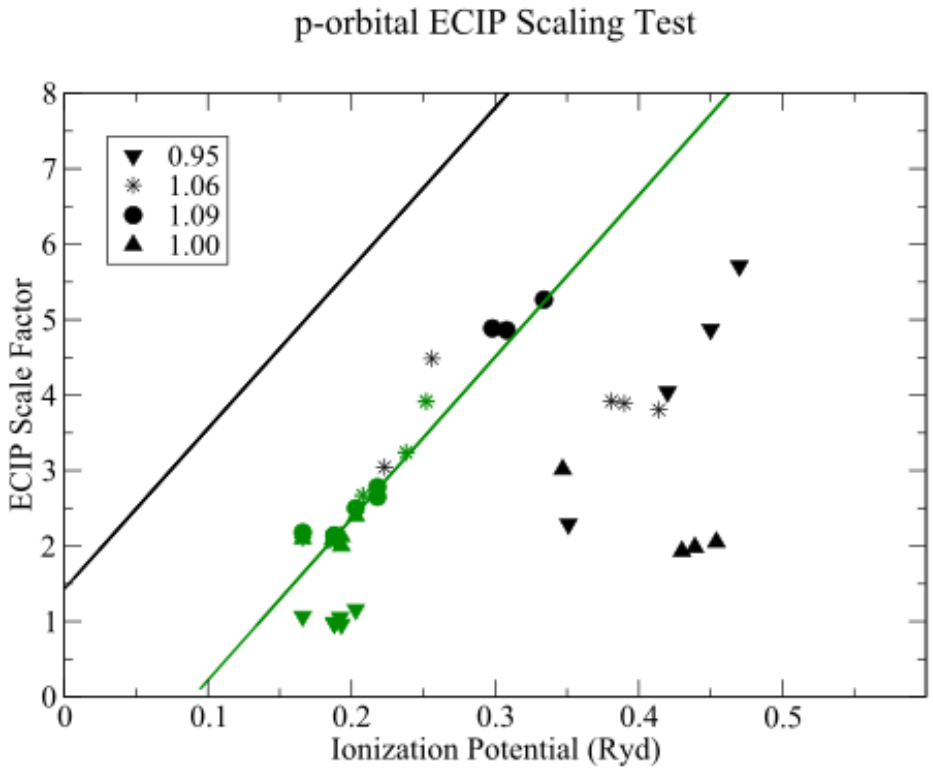

Figure 5.20: Results from a series of RMPS octet partial wave calculations to study the effect of varying λ_{6p}. Each point represents fitted ECIP scale factor of a septet term cross section doubled (to approximate the sextets). Datasets for λ_{6p} = 0.95 (down triangle), 1.06 (star), 1.09 (circle), and 1.00 (up triangle) are further distinguished by even (green) and odd (black) parity configurations. The original even and odd parity fits from the original calculation are also shown.

A-values were further examined, the same transitions as those in Section 4.2, and a full comparison can be found in the appendix. Some structures were clearly better than others, though none gave good agreement for all A-values. Best overall agreement with NIST A-values was seen in the range λ_{6p} = 1.03 to 1.065. Agreement with A-values for higher energy levels was reached its lowest for λ_{6p} = 1.3, at around 3% with NIST for the two highest. Agreement with DARC was worse than the original structure, however. It should also be emphasized that the lowest septet energy levels became lower as λ_{6p} was decreased, by over an 1 eV compared

to NIST for λ_{6p} = 1.03 for example. Therefore, values of λ_{6p} closer to the original 1.12 would be preferred in cases where A-values show similar agreement.

A compromise between better higher-term A-values and accurate septet energies was seen with λ_{6p} = 1.09, whose data points coincided with the even parity line fit. A GCR test was therefore performed corresponding to this λ_{6p}, for which the odd parity fit line was assumed equal to the even parity fit line. Changes in the 400.9 nm PEC and the SCD from the original calculation are shown in Figures 5.21 and 5.22. A 30% reduction in the SCD is seen at n_e = 10^{14} cm^{-3}; however, the SCD is still over four times higher than the SCD from unscaled ECIP GCR modeling. The 400.9 nm PEC shows similar results: slight increases from the original calculation at lower and higher densities and also several factors lower than ECIP.

Another test was performed to examine the effects of a level's *individual* ionization rate coefficient. For this test (solid green in Figure 5.22), the ionization rate coefficient of the upper level of the 400.9 nm line was set to the unscaled ECIP rate coefficient, a reduction of over a factor of 8. No effect was observed for the SCD, but the PEC increases by the same amount as the λ_{6p} = 1.09 test from 0 to 15 eV, after which it slowly becomes smaller.

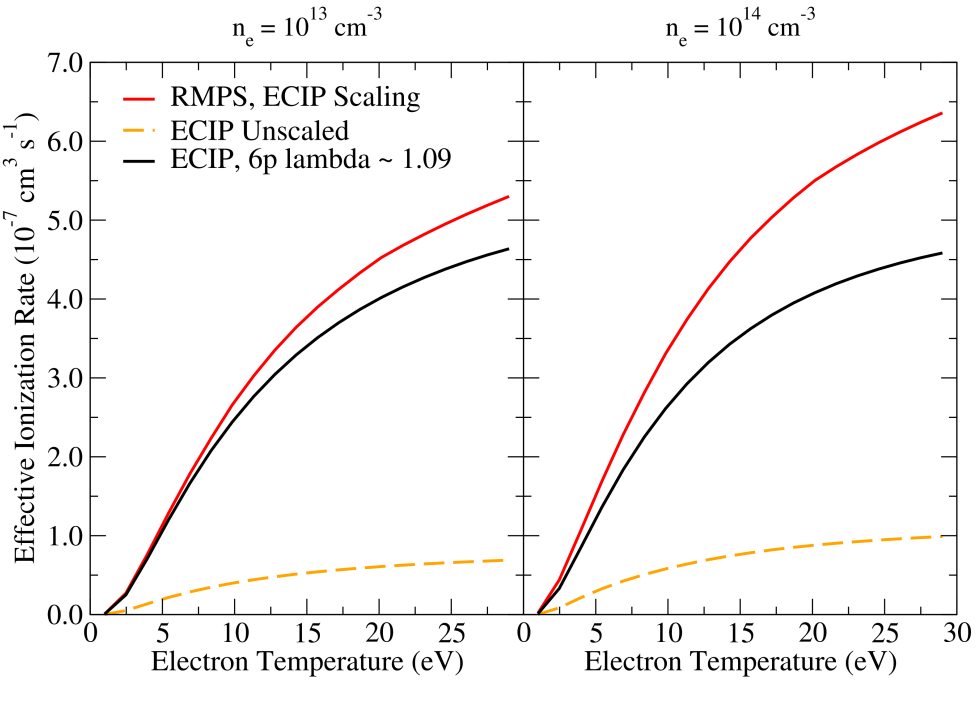

Figure 5.21: Comparison of the SCD if changing λ_{6p} from 1.12 (red) to 1.09 (black) at 10^{13} and 10^{14} cm^{-3} electron densities. The unscaled ECIP SCD (dashed orange) is also shown.

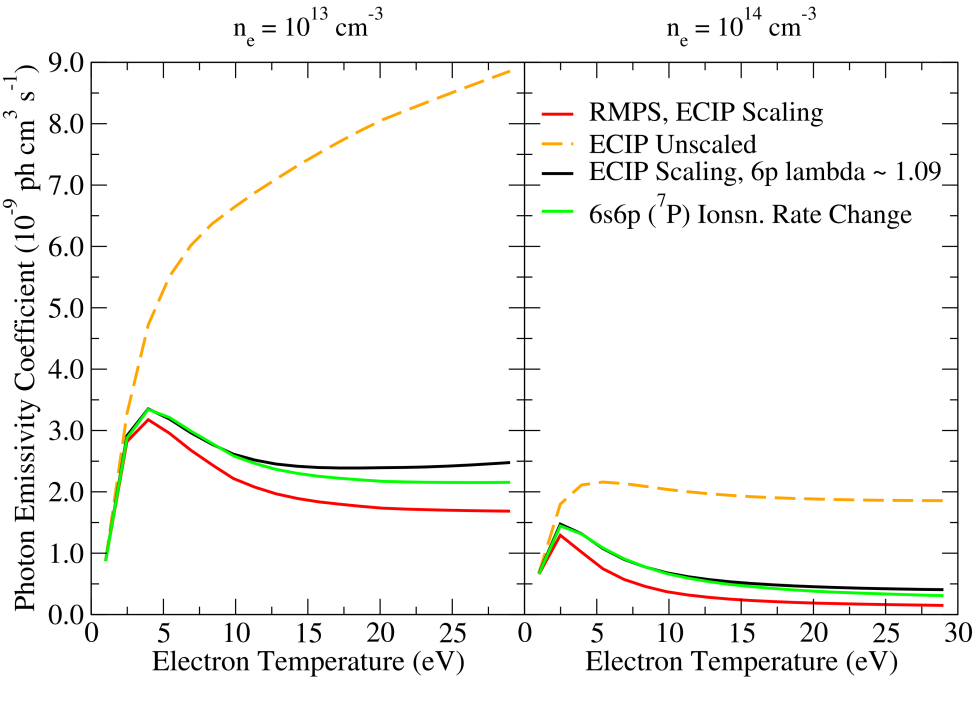

Figure 5.22: Comparison of the PEC if changing λ_{6p} from 1.12 (red) to 1.09 (black) at 10^{13} and 10^{14} cm^{-3} electron densities. Results from switching only the ionization rate coefficient of $6s6p$ (^7P) (green), the upper level of the 400.9 nm line, yield similar results to the $6p$ orbital switch. The unscaled ECIP SCD (dashed orange) is also shown.

As Figure 5.23 shows, the ground-resolved S/XB from λ_{6p} (red) experiences a large reduction from the original calculation (blue), up to 80% at n$_e$ = 10^{13} (dashed) and 90% for n$_e$ = 10^{14} cm^{-3} (solid). The S/XB is still several factors above measurements, however.

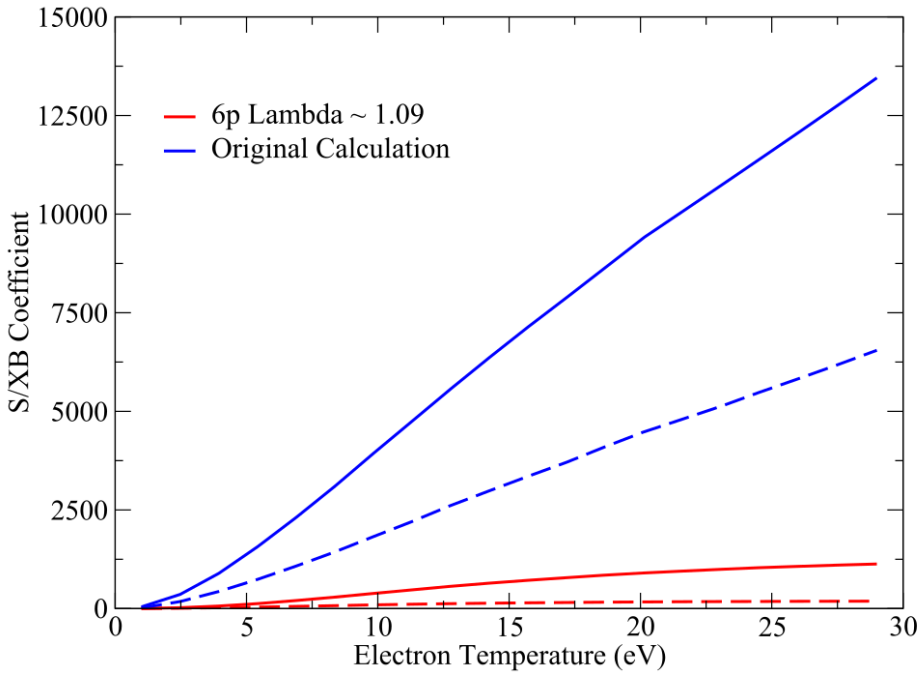

Figure 5.23: Comparison of the S/XB coefficient from GCR modeling with the λ_{6p} = 1.09 structure and preliminary RMPS calculation (blue) with the original calculation (red) at n_e = 10^{13} (dashed) and 10^{14} cm^{-3} (solid). The S/XBs from modeling with λ_{6p} = 1.09 at 30 eV are 41 and 12 times lower than the original ground-resolved S/XBs at 10^{13} and 10^{14} cm^{-3} respectively.

5.6 Conclusions

Excited state ionization cross sections were extracted for the RMPS neutral tungsten electron-impact ionization calculation that suggested separate even and odd parity configuration scaling to the semi-classical ECIP method. Mixing of the target configurations and channel coupling was found to play a significant role for odd parity terms with ionization potentials less than 0.15 Ryd. Configuration mixing at this energy range is of similar amounts to that observed by Wyart [59]. The ground-resolved S/XB is orders of magnitudes too high from previous measurements; however, the lower bound of the S/XB from GCR modeling with six metastables suggests the S/XB is within range if assuming a high metastable population. A study on the $6p$ orbital suggests that the S/XB is sensitive to this orbital's scaling parameter but that the ground-resolved S/XB still would not agree with experiment for all electron densities.

Chapter 6

New Insights and Future Directions in High-Z Electron-Impact Ionization, GCR Modeling, and Code Development

6.1 Introduction

The work presented in this dissertation for neutral W represents the largest non-perturbative RMPS calculation to date, and is focused on diagnostically important quantities. This has allow a new understanding of important atomic effects expected to be important for other high-Z open d-shell atoms, in addition to quantifying the role of excited state ionization and producing new computational advancements. We reiterate and summarize these advancements. This chapter is organized as follows:

1. Conclusions from the new R-matrix electron-impact ionization calculation of neutral tungsten are summarized, with an emphasis on the unexpectedly strong importance of configuration mixing and the possibility of scaling ECIP cross sections.
2. Excited state ionization effects on GCR modeling are examined for both neutral neon and tungsten. A discussion on the effects of the new data on the SCD, PEC, and S/XB coefficients is presented.
3. An overview is given of new code development required for the neutral tungsten electron-impact calculation, including attempted changes that were not beneficial. Computational limitations and future directions of code development are discussed.

6.2 Configuration-mixing and Channel Coupling Effects and Excited-State Ionization Scaling in the Electron-Impact Ionization of Neutral Tungsten

For open d-shell elements, all strongly contributing ionization pathways are required for accurate configuration and term-resolved ionization cross sections. This was observed when running tests with the octet set of partial-waves on the metastable $5d^5 6s$ (^7S) cross section. Running each ionization pathway, $5d^4 6s\bar{nl}$, $5d^5\bar{nl}$, and $5d^3 6s^2\bar{nl}$, separately would have been beneficial for limiting the size of the RMPS electron-impact ionization calculation. A dramatic decrease in the metastable $6s$ ionization cross section was observed upon adding the $5d^4 6s\bar{nl}$ series to the $5d^5\bar{nl}$ series, despite the former ionization not being extracted. In terms of the N + 1 Hamiltonian, this effect can be attributed to configuration mixing of the final excited states rather than the mixing between the ground and metastable state. Recalling the rules governing configuration mixing detailed in Section 2.2, mixing can only occur if two configurations have the same parity and differ in at most two orbitals, such as is the case between all of the $5d^4 6snl$, $5d^5 nl$, and $5d^3 6s^2 nl$ series. Furthermore, mixed configurations must share LS or LSJ total angular momentum quantum numbers. Open d-shell configurations are therefore more susceptible to mixing than open $s-$ and $p-$shell configurations in that, not only can open d-shells result in many terms, but identical quantum numbers can be generated for many combinations of d-shell occupation numbers when other occupied shells, such as the $6s$ and $6p$ with tungsten, are present. As discussed in Section 4.6, the ground $5d^4 6s^2$ (^5D) LS state had an 89.88% purity, while the highest percentage of the largest contributing final state for the ground ionization cross section was only 10.14%, suggesting most of the mixing effects are attributable to the upper states. These correspond to pseudostates for direct ionization and optical states for excitation autoionization. Mixing to the continuum is present in both the N-electron Hamiltonian between optical and pseudostates, as well as in the N + 1 Hamiltonian, between combinations of target-continuum orbital states.

Configuration mixing led to both 1) contributions from unexpected configuration series and 2) changes in relative contributions between expected configuration series. The $5d^5 nl$ series contributed to the $5d^4 6s^2$ (^5D) ionization cross section. A similar finding was noted previously

with C^+ ionization [116], whose ionic core is Be-like and more prone to mixing. Contributions from other configuration series are not considered in perturbative approaches such as distorted wave and in configuration-averaged methods that do not allow for coupling between target-continuum electron channels. *LS*- and *LSJ*-resolved *R*-matrix, by comparison, calculates the Hamiltonian across all possible channels and includes possible interference between them in the off-diagonal elements of the N + 1 Hamiltonian. For the *LS*-resolved Hamiltonian used in the present work, the off-diagonal elements arise from the Coulomb operators, representing mutual repulsion between electrons. In the calculation of the Coulomb operators, described in detail in Fano [117], "active" electrons are distinguished from "spectator" electrons. It can be shown [61] that the spectator electrons do not contribute to the Coulomb matrix elements except for imposing an orthogonality constraint between the bra and ket. In other words, the spectator configurations must match on both sides for the overall matrix element to be non-zero.

Interference due to the Coulomb matrix elements can be generated in two ways: 1) from configuration elements representing lesser percentages of states in either or both the bra and the ket, and 2) from two different configurations sharing the same set of spectator electrons. The $5d^5nl$ contribution to the ground $5d^46s^2$ ionization cross section, for example, can be seen as a case of 1) in that the relatively pure ground state nevertheless has a non-zero contribution resulting from the lesser $5d^46snl$ percentages of the $5d^5nl$ upper levels.

In the context of ionization, 2) can be understood as the presence of shared ionization pathways. For the N + 1 Hamiltonian, only Coulomb elements associated with an active continuum orbital are considered. The other active electron in a bra or ket comes from the target. Coulomb elements in which the spectator and active electrons represent the W^+ core and ionized electron respectively are of particular significance to ionization. Interference between ionization pathways can therefore originate from Coulomb matrix elements in which the bra and ket correspond to different ionization pathways (configuration series). The discrepancies in the ground and metastable ionization cross sections can be attributed to this interference. The metastable $5d$ and ground $6s$ ionizations, which share the same $5d^46s$ core, were much lower and higher respectively than previous calculations. Yet, the total cross section of ionization out

of the summation of the ground or metastable states was in between distorted wave and ECIP, in support of the overall validity of the ionization results.

Configuration mixing and channel coupling played an even more prominent role for excited states. An analysis of configuration series contributions to cross sections from $5d^36s^26p$ states revealed almost none of the cross section was to the actual $5d^36s^26p$ series, which in a configuration-averaged viewpoint would correspond to direct ionization. The relative contributions of the series seemed to reflect the energy level ordering of the resulting W^+ core: the $5d^46snl$ series leading to the W^+ $5d^46s$ ground configuration generally contributed the most, while the $5d^36s^2nl$ series leading to the W^+ configuration highest in energy contributed almost nothing.

The neutral tungsten ionization results therefore suggest that at least *LS*-resolution is necessary for proper term-resolved ionization cross sections: the total term-resolved ground state cross section is distinctly higher than even distorted wave, while the total metastable cross section is distinctly lower than even ECIP. Whether the *total* ionization from all states yields different results than perturbative and configuration-averaged methods remains unclear. That is, configuration-averaged TDCC calculations for all tungsten configurations might still yield roughly the same total ionization as *R*-matrix. The total ground and metastable ionization cross section, essentially summing over all possible states for a given energy range, suggested that the total ionization cross section might still be preserved. However, the available data is too approximate to make definitive conclusions, and the ionization potential in the calculation was assumed at the W^+ ground, 7.864 eV, rather than trying to resolve the final W^+ states. One might propose that configuration mixing actually increases ionization, because it allows states of higher associated configuration series to ionize at lower energies. For example, the lowest possible W^+ core configuration of the $5d^36s^26p$ state is 1.08 eV above the W^+ ground state. Yet, as was seen in the relative series contributions to the cross section, the $5d^46snl$ and $5d^5nl$ series, which would correspond to W^+ cores lower in energy, comprised almost the entire cross section. It is therefore difficult to say for certain the effect of configuration mixing on total ionization from a high-*Z* open-d shell atom, although the results of this work do suggest that at

the very least *all* configurations resulting in the lowest in energy ionic cores must be calculated for full convergence of the total ionization.

Possible scaling of excited state cross sections for both neutral neon and tungsten further revealed interesting patterns that might help diminish the need for large calculation in the future. Excited state cross sections for neutral neon exhibited a classical scaling of 1/(ionization potential)^2 (i.e., an n^4-scaling for screened hydrogenic systems). This scaling was particularly suitable for higher l orbitals, possibly related to the incoming electron having a higher angular momentum and thus being farther away from the atom. Classical scaling for a range of valence n-shells could not be examined for neutral tungsten due restrictions on how high in n optical orbitals could be used in the structure. Instead, classical scaling with the ionization potential was investigated. Fits of the extracted cross sections to their respective ECIP cross sections were performed, and the scaling of these fits showed strong correlation with respect to the term/level-specific ionization potentials. Two linear fits to these scaling parameters versus ionization potential were rendered, seeming to correspond to sets of even and odd parity target configurations respectively. This result is being investigated and will be the subject of future work. The lines were effectively parallel; it would be interesting to do such a study of other complex systems to see if this trend is repeated. Further, all of the odd parity configurations included the 6p orbital, so difference between the two lines may also be related to that orbital instead. The even parity configurations consisted of different combinations of the $5d$, $6s$, and $6d$ orbitals. The ECIP method, while approximating exchange effects, is blind to parity. Yet, parity can play an important role in Hamiltonian elements, where both the bra and ket must have the same parity for any nonzero element. The source of this ECIP scaling therefore warrants further investigation, though it is reasonable to assume ionization cross sections of other atoms may also scale with ECIP.

Another approximation aside from ECIP scaling proved invaluable, nay a *deus ex machina*, for the success of the neutral tungsten calculation: that the upper and lower N + 1 spin sets contribute equally to ionization cross sections. Separate octet and sextet cross sections agreed within 10% across all incident energy ranges for the metastable $5d^5 6s$ (^7S) cross section.

Other approximations in the tungsten calculation gave reasonable results regarding limiting the pseudo orbital range to $\bar{l} = 5$ and neglecting relativistic correction terms such as mass-velocity, Darwin, and spin-orbit interaction in calculating the Hamiltonian. The last would have required recoupling to *LSJ*, which, as seen with the neutral neon excitation, required much more computational power to perform. Further, whereas the neon excitation calculation recoupled to 400 levels, the tungsten calculation would require nearly 41,000 levels, over 100 times the size. The neon ionization calculation further was converged upon including pseudostates through $\bar{l} = 6$. The octet tests on the tungsten calculation suggested cross section convergence at the same $\bar{l}$; however, it was shown in Section 4.4 that the reduction in cross sections from mass-velocity and Darwin effects were of the same magnitude as the increase in cross sections due to including $\bar{l} = 6$ pseudostates. Also, while relativistic effects were not included in the N + 1 Hamiltonian, they were used in optimizing the target structure prior to the RMPS run. So, the target orbitals themselves have radial positions that reflect the relativistic nature of the tungsten atom, even if it is assumed relativistic effects are small for the actual collisional process.

Recall the original questions posed in Section 1.3:

(1) Do all ionization pathways need to be considered in a single calculation for accurate electron-impact ionization cross section results, or can they be treated separately?

This question is in essence referring to the simultaneous inclusion of Hamiltonian elements from configuration series corresponding to different ionization pathways. For accurate term-resolved cross sections, yes, if the pathways/configuration series exhibit high degrees of mixing between their configurations and/or if the pathways share a common ionic core. Configuration series whose ionic core begins much farther from the ionic core's ground state may not be necessary, but should be tested. Whether ionization pathways can be treated separately for total ionization from all states is still an open question.

(2) What is the effect of configuration mixing on term- and level-resolved electron-impact ionization cross sections?

Configuration mixing results in 1) contributions from configuration series other than that of the initial state that may not correspond to a direct ionization pathway, and 2) changes

in the sizes of term- and level-resolved cross sections, due in particular to shared ionization pathways.

6.3 *R*-Matrix and GCR Current and Future Code Modification, Expansion, Development, and Scaling Graphs for high-Z Atomic Species

Recall the third question posed in Section 1.3: **(3) how can the size or computational burden of more expansive non-perturbative calculations be reduced while maintaining accuracy in the results?**

The standard (unmodified) RMATRX I [72] as it stands is not sufficient for handling the entirety of electron-impact calculations as large and complex as those involving tungsten's low charge states. The present work, if all possible partial-wave spin sets had been calculated, represented the most computationally expensive *R*-matrix calculation to date, in terms of RAM, I/O, and required runtime. As has been previously discussed, much of this burden was alleviated 1) by assuming the lower spin sets yielded equal contributions to cross sections as the higher spin sets and 2) that the ionization cross sections scaled well with ECIP. In addition to the octet and sextet contributions being within 10% across all calculated energy ranges for the metastable $5d^5 6s$ cross section, it can be observed from Figure 5.12 that the ECIP scale factors obtained from the septet configurations fall onto the same lines as those of the quintet configurations, whose cross sections were obtained from doubling the sextets. Further GCR testing in which the ECIP scale factors are used for *all* ionizations reveals that the SCDs and PECs agree well with those obtained from using both RMPS and ECIP scaling. *In other words, nearly identical GCR results could have been obtained from calculating only the octet contributions, doubling the octets for the septet states, generating ECIP scale factors for the septet cross sections, and applying a fit to the scale factors for the remaining cross sections.* The ECIP scaling was not without its limitations, however. It yielded no information regarding relative contributions of the different configuration series to the cross sections, and the shapes of the scaled ECIP cross sections did not always match the RMPS cross sections, as demonstrated in Figure 5.10.

While the approximations used here can serve as a strong point of reference for future calculations, additional code development to the *R*-matrix codes and to the processing of atomic

data remains important, not only for ensuring accurate results, but also to allow for full utilization of modern supercomputer architectures. For example, Summit, the new supercomputer at Oak Ridge and whose smaller development cluster was in part utilized in this work, is a CPU-GPU architecture: each node is comprised of two CPUs with 21 processors and 6 GPUs each. As will be discussed, GPUs can result in considerable speedup for linear algebra computations [118–120], such as the eigendecomposition and matrix-matrix multiplications present in the *R*-matrix codes. This section contains a summary of the code development performed in the current work, as well as some scaling graphs related to GPUs to illustrate the performance of Stage 3 and f on the Oak Ridge Titan and Rhea supercomputers. Certain possibilities for limiting the size of the calculation had also been explored but ultimately were not used, and these attempts are also briefly discussed.

To summarize the code development undertaken in the present work:

1. A set of modifications to RMATRX I [72] involving Stage 2 and calculation of the N + 1 Hamiltonian was completed in order to 1) account for additional physics present in high-Z atom collisions but absent in low-Z collisions, 2) to allocate computer resources more efficiently during runtime (e.g., reducing I/O at the expense of RAM), and 3) to reduce overall runtime.
2. Other modifications were explored as well, particularly for Stage 3 with Hamiltonian diagonalization and for Stage f with the *R*-matrix matrix multiplication, which was not suitable to be performed for the large neutral tungsten quartet partial-wave Hamiltonians at the present time. Scaling graphs of Stages 3 and f are included, with a comparison to a new GPU version of Stage f.
3. Finally, various Python and Fortran codes are described that process collisional data and generate properly *LSJ*-resolved rate coefficients. Most notably, 1) a much more memory efficient Python code for cross section extraction from OMEGA files (the Stage f and final *R*-matrix output), as well as 2) a code to split *LS*- into *LSJ*-resolved ionization cross sections via branching ratios were developed.

6.3.1 Stage 2 Modifications

Stage 2, which calculates the N and N + 1 Hamiltonians, was modified in many ways related to compensating for the the closed f-shell of tungsten, maximizing RAM usage, and reducing I/O and runtime. Further modifications, such as streamlining the Hamiltonian element calculations and usage of GPUs over the last configuration loops, could help reduce Stage 2 runtime and the need for human oversight.

Fix allowing for closed f-shells

Both pstg2r.f and stglib.f, the latter of which contains many subroutines and functions related to linear and angular algebra, required modification to allow for the presence of the closed f-subshell of tungsten. Prior to modification, the code allows only up to 2 electrons in subshells with $l \geq 3$. This 2-electron constraint stems from a lack of angular algebra data written into the code regarding both terms and coefficients of fractional parentage related greater occupation of higher *l* subshells.

The original f-subshell problem was identified based on the values of the *R*-matrix poles, or eigenvalues of the N + 1 Hamiltonian, following Stage 3 diagonalization. A calculation displaying proper atomic collisional physics would result in the range of *R*-matrix poles being higher in absolute energy than the ground state of the N + 1 bound system. For example, in a bare *R*-matrix calculation run with only the W^{6+} ground state configuration, $6s$, an AUTOSTRUCTURE run of the N + 1 configuration, $6s^2$, results in an absolute ground state energy of -15292.3950 Ryd. Yet, the range of *R*-matrix poles from just the $6s$ configuration extended lower. Upon modifying the code as described below, the poles properly started above the N + 1 ground states for all ions and configurations tested, including with more than one configuration.

The coefficients of fractional parentage are required with the one- and two-electron operators for distinguishing "active" and "spectator" electrons, the rules regarding which are defined in [117]. The N + 1 Hamiltonian includes direct Coulomb interaction operators between the continuum electron and each bound/pseudostate orbital.

The following changes were made related to the f-subshell:

stglib.f:

1) The TERMS array was extended to include the seniority, angular momentum, and spin quantum numbers arising from f^{12}, and FUNCTION NTAB1 was modified to call the new terms when the spectator electrons of a Coulomb matrix element include f^{13}. The size of the TERMS array and its indexing arrays were correspondingly changed throughout the code.

2) A SUBROUTINE CFPF was added, which yields the coefficient of fractional parentage arising from the f^{12} terms, i.e., with f^{13} spectator electrons. Although the CFP for an orbital with two electrons is 1.0, the CFP for an orbital with two electrons missing is not. The CFP for f^{12} is calculated through the following Racah recursion relation [61]:

$$(l^{4l+2-w}v\bar{L}S|\}l^{4l+3-w}vLS) = (-1)^{L+S+\bar{L}+\bar{S}-l-1/2}$$
$$\times[\frac{w(2\bar{L}+1)(2\bar{S}+1)}{(4l+3-w)(2L+1)(2S+1)}]^{1/2}(l^{w-1}vLS|\}l^{w}v\bar{L}S), \tag{6.1}$$

where w and l are the number of electrons and orbital angular momentum, and vLS and $v\bar{L}S$ represent the quantum numbers of terms arising from l^w and l^{w-1} orbitals respectively.

pstg2r.f:

1) In SUBROUTINE CONFIG, the constraint of no more than 2 electrons was relaxed to allow for fully occupied f-subshells.

2) The size of the TERMS array and its indexing arrays were changed throughout the code to reflect the additional f^{12} terms.

Importantly, these changes specifically considered only closed f-shells. Further modification for open f^w subshells where $w > 2$ would require extending the TERMS array to include f^{w-1} terms and writing arrays into SUBROUTINE CFPF to include the (numerous) CFPs from each f^{w-1} term.

Memory and I/O Improvements

Two other major changes were made to pstg2r.f and stglib.f related to improving user flexibility and reducing I/O, and these changes were discussed in Section 4.3. A sample of the code modifications, SUBROUTINE SETMX1 that calculates the N + 1 Hamiltonian elements, has been provided in Appendix B, along with a list of pstg2r.f variables and their definitions. To recapitulate, an effective cap on the RAM allocated for calculation of the N + 1 Hamiltonian elements was lifted through changing the integer precision from int*4 to *8 throughout the code, including for the variable responsible for RAM.

The user can also now manually choose for which target symmetries to calculate N + 1 Hamiltonian elements in a given program execution. A prior print-off can be generated, through setting "idimcheck = 1" in the dstg2 namelist, that lists the number of Hamiltonian elements for a given target $SL\Pi$ symmetry bra (including all of its channels) and each of its kets, as well as the total size of all of its kets. Recall that pstg2r.f has been parallelized as one processor per partial-wave per target symmetry [67]. Prior knowledge of the number of Hamiltonian elements per target symmetry allows the user to avoid running symmetries with no channels and also to run symmetries of similar sizes together, increasing computational efficiency. To manually choose target symmetries, the user must supply a list, "symlist", which is simply a file with a different symmetry number on each line. The symmetry number corresponds to the one from the prior printoff. The first number of the file must equal the number of symmetries in each file.

Beyond parallelization as *one processor per partial-wave per bra target symmetry*, Stage 2 could further be streamlined to automatically fetch N + 1 Hamiltonian blocks left to calculate upon a processor finishing its symmetry; that is, a calculation stack could be implemented. This would reduce the need for humans to manually submit batches of symmetries. In addition, the code could further be parallelized as *one processor per partial-wave per bra target symmetry per ket target symmetry*.

Use of GPUs is currently not allowed in Stage 2, and while they are not critical for the stage, they likely would further reduce runtime. Runtime for the tungsten sextet partial-waves

was around two weeks each prior to the RAM cap removal modifications and one to three days after. Most of the remaining runtime was consumed in for loops over the set mixed configurations of the bra and ket target states. For reference, the maximum number of mixing configurations for a given target state of the neutral tungsten calculation was 706. For a given N + 1 Hamiltonian matrix element, the contributions of all the configurations of the bra and ket target symmetries are summed over. This step could instead be cast as a matrix multiplication step, consisting of a matrix of all separate term-term elements, multiplied by another matrix of the same dimensions, consisting of the outer product between the bra and ket sets of mixing coefficients.

6.3.2 Stages 3 and f: scaling graphs and future directions

With the new Stage 2 improvements, no technical limitations now exist on the size of the N and N + 1 Hamiltonians that can be calculated and written to file for electron-impact calculations of large ions and with many pseudostates: as long as one has enough RAM to store (# Configurations per Target Symmetry * # Channels per Target Symmetry) * (Basis Set)^2 * # Channels per partial-wave Symmetry) elements at a time per processor and target symmetry. Stages 3 and f, responsible for N + 1 Hamiltonian diagonalization and the *R*-matrix matrix multiplication respectively, are much less scalable as the Hamiltonian and channel sizes increase.

At Stage 3, the Hamiltonian matrix, stored as its upper triangle, is partitioned over processor blocks: each processor stores only a part, and the global eigenvectors need not be calculated. ScaLAPACKs PDSYEVD, a parallel divide and conquer algorithm for real Hermitian matrices, is used to diagonalize the partitions. Figure 6.1 shows the both diagonalization and overall runtime for Stage 3 as a function of Hamiltonian size. Also included is a partition comparison between 32 x 32 blocks (1024 processors) and 50 x 50 blocks (2500 processors). As expected, a larger proportion of the overall runtime is spent diagonalizing the matrix for the 32 x 32 compared to greater partitioning. For larger Hamiltonians, processing, organizing and message passing between processors becomes increasingly time-consuming for the 50 x 50 partitioning.

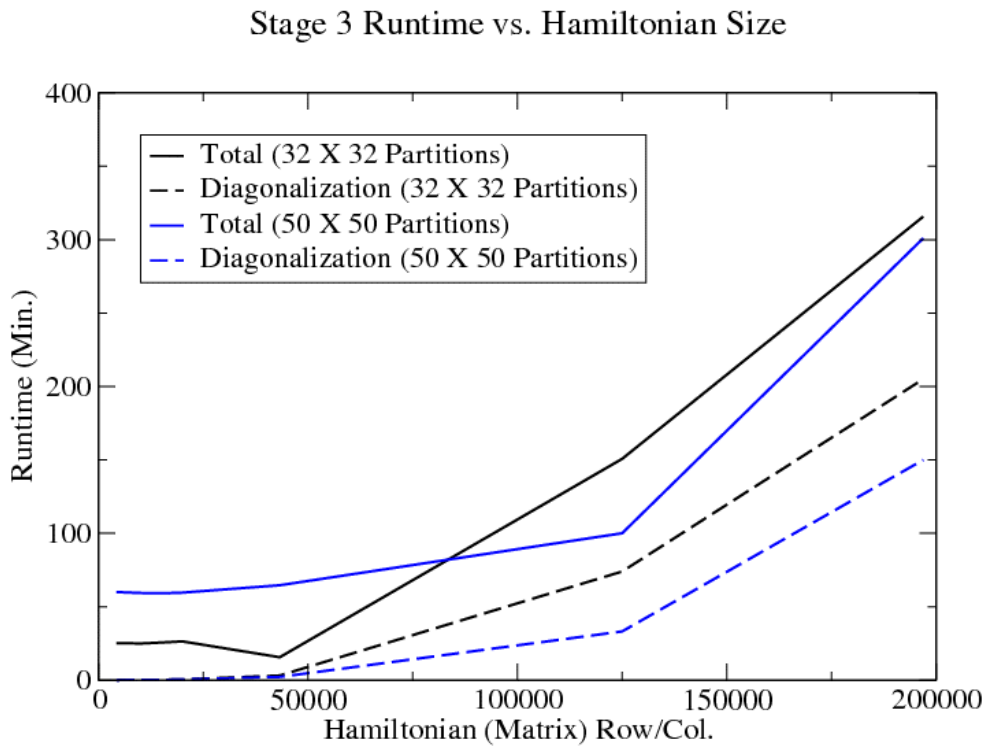

Figure 6.1: Stage 3 diagonalization and total times versus Hamiltonian size. The black and blue lines represent 32 X 32 and 50 X 50 partitioning respectively. The data points were collected using neutral tungsten octet and sextet partial-waves run on Supercomputer Hazel Hen.

For neutral tungsten, the quartet partial-waves reach up to 45000 channels, so, with a basis set size of 29, diagonalization of matrices beyond 1,300,000 rows/columns would be required. Based on an exponential least squares fit of the total runtime versus Hamiltonian size with 50 X 50 partitions (the blue line in Figure 6.1), such a calculation under the same partitions would require 8,500,000 hours, well beyond modern computational resources.

Future large-scale calculations of smaller size than neutral tungsten might still benefit from a hybrid CPU-GPU code suite such as MAGMA [119]. MAGMA offers a hybrid eigensolver, in which different steps of the eigendecomposition problem occur on either the CPU or GPU [121]. Scaling tests shown by Tomov *et al.* show a 12x speedup from using 3 GPUs versus 12 cores on the tridiagonalization step of the eigendecomposition problem. The MAGMA routines

require relatively small changes to existing code to implement and would therefore be worth exploring.

To recall, Stage f calculates the R-matrix and solves the outer region, resulting in cross sections for all possible target transitions over a set of supplied energy points. Recent code development has allowed for the R-matrix matrix-matrix multiplication step to be performed on GPUs, resulting in a considerable speedup.

The R-matrix matrix multiplication step described by Equation 2.38 is an ideal case for utilizing GPUs. In recent code development [122], the previously used DGEMM has been replaced by a CUDA Fortran subroutine. The reduced radial orbital matrices are copied to the GPU, where the matrix multiplication is performed. The results are then copied back to the CPU. Figure 6.2 shows a logscale comparison of Stage f runtimes on Rhea. Using the regular Stage f, the R-matrix multiplication becomes almost the entirety of the runtime as the size of the problem, the number of channels, increases. At 6000 channels, the GPU code runs 10 times faster, with the matrix multiplication roughly 100 times faster.

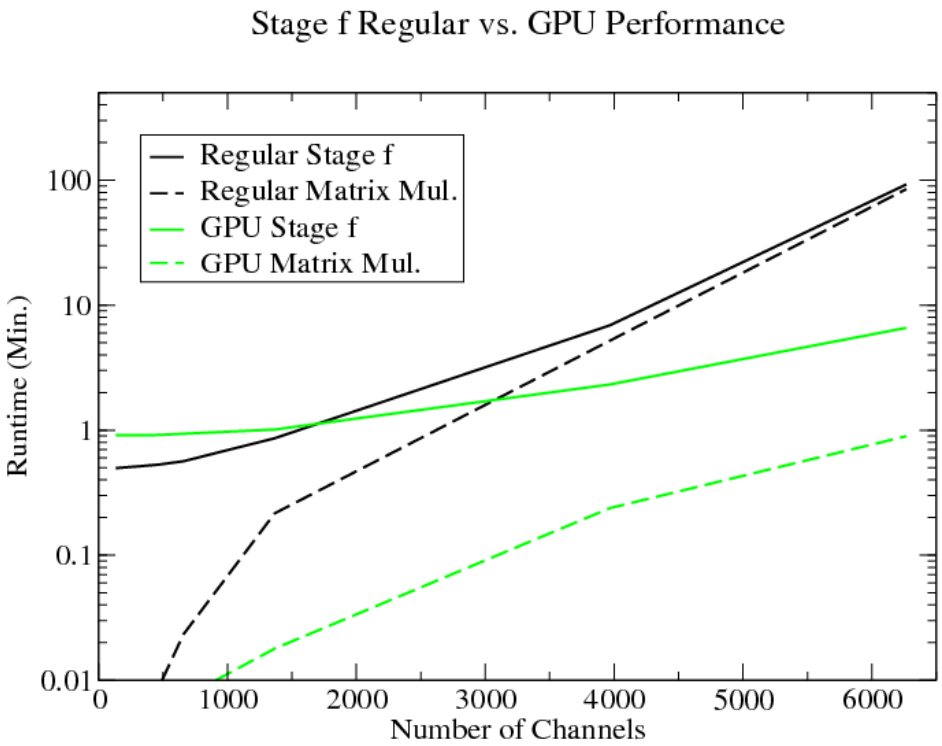

Figure 6.2: Stage f runtime comparison using CUDA Fortran (green) versus the original non-GPU DGEMM from BLAS (black) for the *R*-matrix multiplication. The solid and dashed lines indicate the total Stage f and *R*-matrix multiplication runtimes respectively.

Further modifications have been made to allow the R-matrix multiplication step to fit onto GPU memory [122]. For the quartets, if keeping a basis set of 29 and with NCHAN = 45,000, the matrix-matrix multiplication would require nearly a terabyte of RAM. To reduce memory requirements, the code now splits the reduced radial matrices into smaller partitions, which are sequentially copied over to the GPU for smaller matrix-matrix multiplications. The last point in Figure 6.2, with NCHAN = 6,267 and MNP1 = 196,887, was obtained using this updated GPU code, partitioning the reduced radial matrices into fourths. It suggests surprisingly small overhead from copying back and fourth between GPU and CPU.

Partitioned R-matrix for Stages 3 and f

Another possibility exists to limit the size of Stage 3 and f for electron-impact ionization calculations: compute only a smaller subset of eigenvalues/eigenvectors and approximate the contribution of the others within the *R*-matrix. The theory for this idea was first described by Berrington and Ballance [123]. This method had been explored for the neutral tungsten calculation, but it ultimately suffered problems related to the accuracy of the SCALAPACK algorithms [76] for computing only a subset of eigenvalues rather than all of them.

Partitioned *R*-matrix begins with the assumption that only a subset of the N + 1 Hamiltonian H_{ij} eigenvalues, the lowest in energy, are known [123]. The unknown eigenvalues are approximated as one degenerate eigenvalue, E_0. Let $X_{k'k}$ denote the matrix containing the full stack of N + 1 eigenvectors and j the number of the l eigenvectors known. The assumption of partitioned *R*-matrix can therefore be expressed as,

$$\sum_{k=1}^{m} H_{ik} X_{kj} = X_{ij} E_0 \qquad\qquad j > l \tag{6.2}$$

From a least-squares fit of Equation 6.2, an expression for E_0 and for the *R*-matrix containing E_0 can be obtained [123]. RMATRX I [72] previously included an option to run Stage 3 and f via the partitioned *R*-matrix, done by setting "IPRCENT" in the namelist equal to the percentage of eigenvectors to be calculated. This option still works in Stage 3 for finding the subset of eigenvectors; however, in Stage f, the partitioned *R*-matrix is deprecated in the most recent versions and requires some code reversions.

Accuracy in calculating only a subset of eigenvalues/eigenvectors remains questionable if using SCALAPACK's PDSYEVX and PDSYEVR algorithms and routines [76], particularly given the large clustering of eigenvalues present in Hamiltonians with many pseudostates. The two algorithms depend on first tridiagonalizing the matrix and on the present of sufficiently large gaps in between eigenvalues [124]. Tests were run using an electron-impact excitation calculation of O^{6+} with 72 partial-waves and on the neutral tungsten octet partial-waves to determine the reliability of the partitioned *R*-matrix results . The older versions of pstg3r.f and pstgf.f, for which the partitioned *R*-matrix code is not deprecated, were used for the O^{6+} test,

while a recent pstg3r.f version was used for the octet tests. The total cross sections for O^{6+} if keeping 50% of the eigenvalues and eigenvectors were almost completely identical to the cross sections from regular *R*-matrix, except for a nearly 25% drop in the cross section over a 0.111 eV energy range for the transition from the ground state to the last included energy level. In another test with the neutral tungsten octets, PDSYEVX, the algorithm used by the partitioned code to calculate only a subset of eigenvalues and eigenvectors, crashed the code. When PDSYEVX was replaced with the more recent PDSYEVR [124], however, the resultant eigenvalues were consistent with those of the full calculation. For all octet partial-waves, if calculating only 1% of the eigenvalues and eigenvectors, the first pole (eigenvalue) was equal to that from the full diagonalization through the 9th decimal place. Further, the last pole was suitably shifted closer to the first, and was also less than the last pole from full diagonalization. This trend in the last pole is what should occur if the higher eigenvalues are being approximated. The tests on the partitioned *R*-matrix were preliminary, and the overall effectiveness of the method at reducing the size of an ionization calculation requires further analysis. PDSYEVR generates "Multiple Relatively Robust Representations" of clusters of eigenvalues and relies upon finding large gaps in values between clusters [124]. Further testing on larger partial-wave sets and reverting the Stage f code to once again allow for partitioned *R*-matrices is therefore required to gauge the effectiveness of PDSYEVR for much denser Hamiltonian eigenvalue sets and also of how many eigenvalues/eigenvectors are necessary for accurate ionization cross sections.

6.3.3 Other code development (Python) related to efficient OMEGA file processing and utilities

The size of the neutral tungsten calculation as well as the need for LS- to LSJ-resolution also prompted the need for new code development related to processing the OMEGA file, cross sections, rates, and adf04 files. A summary of these utility codes and their testing is provided in Appendix C. The most important of these new codes was a new cross section extractor for OMEGA files. The neutral tungsten OMEGA files were each over 67 GB. The new "pystgsig.py" holds only one line of the file, corresponding to six transition cross sections

at one incident energy, in an array at one time, as opposed to all transitions at all energies. Codes and scripts were also made to automate transition number calculation and batching of excited state cross section extraction. Another important new code allows for the calculation of LS- to LSJ- Sampson branching ratios [77] for cross sections and rate coefficients, as discussed in Section 2.5.

6.3.4 Conclusions regarding ionization approximations and code development

As discussed, while the lower-spin state and ECIP scaling approximations utilized for the neutral tungsten calculation proved effective, improvements can still be made to improve the *R*-matrix code to reduce runtime, RAM, and I/O usage. These changes are particularly important for Stage 3, which currently is the bottleneck for large calculations. The GPU code development introduced by Connor Ballance [122] greatly reduced the time required to run Stage f, while enabling larger matrix-matrix multiplications to fit onto the smaller GPU RAM. Hybrid CPU-GPU code suites such as MAGMA or the partitioned *R*-matrix approach may similarly help reduce Hamiltonian diagonalization time.

6.4 The importance of excited-state ionization and non-perturbative *LS* or *LSJ*-resolved electron-impact data for GCR modeling of high-Z elements

(4) How important is excited-state ionization for accurate GCR modeling, particularly as concerns the effective ionization rate coefficient?

Excited-state ionization raised the effective ionization rate by factors of 3 and 12 for neutral neon and tungsten respectively at 10^{14} cm^{-3} electron densities and electron temperatures relevant to divertors. For neutral tungsten, contributions to the SCD from excited-state ionization are still predicted at extremely low electron densities, as shown in Figure 5.1 at $n_e = 10^4$ with ECIP rates coefficients. Ground state ionization cross sections and rates are nevertheless important in developing an understanding of the quantum mechanical properties of an atomic species, such as with the $5d^5nl$ contribution to the neutral tungsten ground state.

For neutral tungsten, excited-state ionization rate coefficients also result in a significant drop in PECs compared to GCR modeling with ground-only rate coefficients (Figure 5.15).

This result was also observed with the smaller unscaled ECIP rate coefficients, where the 400.9 nm PEC was reduced 60% at $n_e = 10^{14}$ cm^{-3}.

(5) How important is LSJ- and LS-resolved electron-impact data for accurate GCR modeling of high-Z elements?

The RMPS neutral tungsten cross section results, particularly in light of the total ground/metastable ionization and the demonstrated scaling of the ECIP cross sections, leave open the possibility that more approximate methods, such as configuration-averaged TDCC for all configurations, might still generate an accurate effective ionization rate coefficient; however, the reduction in the 400.9 nm PECs also suggests the importance of accurate level-specific ionization rates, for which approximate methods may not be as well-suited.

Regarding level-specific accuracy, LSJ-resolved over LS-resolved rates are most likely not necessary, due to the rules governing LS- to LSJ- branching ratios (See 2.5). Because the low levels of W^+ contain many possible final J values within a 0.762 eV energy range [29], the total ionization rate coefficient out of an LSJ-state, summing over all possible J values, is unlikely to change. Recall, the ionization potentials of the RMPS and scaled ECIP results were all relative to the W^+ groud. The heights of the cross sections themselves reflect an LS-resolved electron-atom collision. The effect of LS-resolution of the final W^+ states was explored in Section 5.4, where GCR modeling was performed with the ionization potential shifted by 0.5 eV. The SCD and PEC from this ionization potential shift still agreed well with the original RMPS results across all electron temperatures and densities.

Future work related to GCR modeling with a full set configuration-averaged excited state cross sections, such as from TDCC, would be helpful in clarify whether they yield different results without the configuration-mixing and channel coupling effects present in *R*-matrix.

Regarding the S/XB more experimental work related to modeling metastable populations with different measured W I lines would help quantify the reliability of the new RMPS/DARC atomic data. The ground-resolved 400.9 nm S/XB was much higher than previous measurements across relevant electron densities and temperatures. GCR modeling with six metastables, including the $5d^5 6s$ (^7S), suggests the 400.9 PEC is mostly driven by the ^7S state. It was demonstrated that if the metastable fraction was entirely composed of the ^7S state, a lower

bound for the S/XB in other words, the S/XB is lower than previous measurements. As was seen in Chapter 4, the target neutral tungsten structure was far from perfect, however, and the possibility remains that a structure more tailored to the excited states is needed. The structure used in the present work was based on the best available data, showing good agreement with the first 100 levels and the best agreement on available A-values. The available excited state data, particularly of A-values close to the ionization potential, is still fairly limited, however. The reliability of the scaling of the ECIP cross sections opens the possibility of refining the RMPS calculation with an updated structure with relative ease. Some other complications to S/XB modeling not considered here include sheath and other possibilities related to plasma transport effects and non-Maxwellian electrons. New experimental measurements, particularly S/XB measurements in combination with high resolution spectral observations of multiple W I spectral lines, might therefore help distinguish calculation-specific effects from plasma-specific S/XB effects stemming from metastable populations, plasma transport modeling, and a non-Maxwellian electron distribution.

6.5 Concluding Remarks and Future Directions

The work presented here has illustrated the importance of excited-state ionization and configuration-mixing for accurate atomic data and generalized collisional-radiative modeling. The configuration mixing effects seen in the neutral tungsten results are original: with the exception of one C^+ term ionization cross section in Pearce [116], the effects of configuration mixing on electron-impact ionization have never been studied. This work therefore serves as a benchmark for electron-impact and GCR modeling of future high-Z open d-shell atomic species. Analysis is still required for generating an accurate S/XB diagnostic for neutral tungsten, particularly regarding metastable population and plasma transport modeling, although all of the necessary electron-impact data is now available. Additional work on electron-impact ionization of other atomic species with large configuration mixing in the ionic core should further clarify whether mixing effects change the *total* ionization rates, beyond just the configuration- and term-resolved ionization rates.

The next logical extension of this work is with GCR modeling of W^+ and W^{2+}. Once tungsten is ionized, its net negative charge makes it susceptible to the forces from the magnetic field, which can lead to its redeposition. GCR modeling of the lowest charge states of tungsten should therefore provide a way to measure redeposition rates in addition to the erosion rates. Preliminary electron-impact ionization calculations suggest that the RMPS ground state cross section of W^{2+} converges with distorted wave, suggesting the usability of more approximate theoretical methods for higher charge states. Considerable work has already been done for these charge states [125–138]. A full set of rate coefficients for the atomic processes of all of tungsten's charge states will then enable a full account of tungsten's populations in the plasma through ionization balance and impurity transport.

References

[1] B. P. Abbott, R. Abbott, T. D. Abbott, F. Acernese, K. Ackley, C. Adams, T. Adams, P. Addesso, R. X. Adhikari, V. B. Adya, C. Affeldt, M. Afrough, B. Agarwal, M. Agathos, K. Agatsuma, N. Aggarwal, O. D. Aguiar, L. Aiello, A. Ain, P. Ajith, B. Allen, G. Allen, A. Allocca, P. A. Altin, A. Amato, A. Ananyeva, S. B. Anderson, W. G. Anderson, S. V. Angelova, S. Antier, S. Appert, K. Arai, M. C. Araya, J. S. Areeda, N. Arnaud, K. G. Arun, S. Ascenzi, G. Ashton, M. Ast, S. M. Aston, P. Astone, D. V. Atallah, P. Aufmuth, C. Aulbert, K. AultONeal, C. Austin, A. Avila-Alvarez, S. Babak, P. Bacon, M. K. M. Bader, S. Bae, M. Bailes, P. T. Baker, F. Baldaccini, G. Ballardin, S. W. Ballmer, S. Banagiri, J. C. Barayoga, S. E. Barclay, B. C. Barish, D. Barker, K. Barkett, F. Barone, B. Barr, L. Barsotti, M. Barsuglia, D. Barta, S. D. Barthelmy, J. Bartlett, I. Bartos, R. Bassiri, A. Basti, J. C. Batch, M. Bawaj, J. C. Bayley, M. Bazzan, B. Bécsy, C. Beer, M. Bejger, I. Belahcene, A. S. Bell, B. K. Berger, G. Bergmann, S. Bernuzzi, J. J. Bero, C. P. L. Berry, D. Bersanetti, A. Bertolini, J. Betzwieser, S. Bhagwat, R. Bhandare, I. A. Bilenko, G. Billingsley, C. R. Billman, J. Birch, R. Birney, O. Birnholtz, S. Biscans, S. Biscoveanu, A. Bisht, M. Bitossi, C. Biwer, M. A. Bizouard, J. K. Blackburn, J. Blackman, C. D. Blair, D. G. Blair, R. M. Blair, S. Bloemen, O. Bock, N. Bode, M. Boer, G. Bogaert, A. Bohe, F. Bondu, E. Bonilla, R. Bonnand, B. A. Boom, R. Bork, V. Boschi, S. Bose, K. Bossie, Y. Bouffanais, A. Bozzi, C. Bradaschia, P. R. Brady, M. Branchesi, J. E. Brau, T. Briant, A. Brillet, M. Brinkmann, V. Brisson, P. Brockill, J. E. Broida, A. F. Brooks, D. A. Brown, D. D. Brown, S. Brunett, C. C. Buchanan, A. Buikema, T. Bulik, H. J. Bulten, A. Buonanno, D. Buskulic, C. Buy, R. L. Byer, M. Cabero, L. Cadonati, G. Cagnoli, C. Cahillane,

J. Calderón Bustillo, T. A. Callister, E. Calloni, J. B. Camp, M. Canepa, P. Canizares, K. C. Cannon, H. Cao, J. Cao, C. D. Capano, E. Capocasa, F. Carbognani, S. Caride, M. F. Carney, G. Carullo, J. Casanueva Diaz, C. Casentini, S. Caudill, M. Cavaglià, F. Cavalier, R. Cavalieri, G. Cella, C. B. Cepeda, P. Cerdá-Durán, G. Cerretani, E. Cesarini, S. J. Chamberlin, M. Chan, S. Chao, P. Charlton, E. Chase, E. Chassande-Mottin, D. Chatterjee, K. Chatziioannou, B. D. Cheeseboro, H. Y. Chen, X. Chen, Y. Chen, H.-P. Cheng, H. Chia, A. Chincarini, A. Chiummo, T. Chmiel, H. S. Cho, M. Cho, J. H. Chow, N. Christensen, Q. Chu, A. J. K. Chua, S. Chua, A. K. W. Chung, S. Chung, G. Ciani, R. Ciolfi, C. E. Cirelli, A. Cirone, F. Clara, J. A. Clark, P. Clearwater, F. Cleva, C. Cocchieri, E. Coccia, P.-F. Cohadon, D. Cohen, A. Colla, C. G. Collette, L. R. Cominsky, M. Constancio, L. Conti, S. J. Cooper, P. Corban, T. R. Corbitt, I. Cordero-Carrión, K. R. Corley, N. Cornish, A. Corsi, S. Cortese, C. A. Costa, M. W. Coughlin, S. B. Coughlin, J.-P. Coulon, S. T. Countryman, P. Couvares, P. B. Covas, E. E. Cowan, D. M. Coward, M. J. Cowart, D. C. Coyne, R. Coyne, J. D. E. Creighton, T. D. Creighton, J. Cripe, S. G. Crowder, T. J. Cullen, A. Cumming, L. Cunningham, E. Cuoco, T. Dal Canton, G. Dálya, S. L. Danilishin, S. D'Antonio, K. Danzmann, A. Dasgupta, C. F. Da Silva Costa, V. Dattilo, I. Dave, M. Davier, D. Davis, E. J. Daw, B. Day, S. De, D. DeBra, J. Degallaix, M. De Laurentis, S. Deléglise, W. Del Pozzo, N. Demos, T. Denker, T. Dent, R. De Pietri, V. Dergachev, R. De Rosa, R. T. DeRosa, C. De Rossi, R. DeSalvo, O. de Varona, J. Devenson, S. Dhurandhar, M. C. Díaz, T. Dietrich, L. Di Fiore, M. Di Giovanni, T. Di Girolamo, A. Di Lieto, S. Di Pace, I. Di Palma, F. Di Renzo, Z. Doctor, V. Dolique, F. Donovan, K. L. Dooley, S. Doravari, I. Dorrington, R. Douglas, M. Dovale Álvarez, T. P. Downes, M. Drago, C. Dreissigacker, J. C. Driggers, Z. Du, M. Ducrot, R. Dudi, P. Dupej, S. E. Dwyer, T. B. Edo, M. C. Edwards, A. Effler, H.-B. Eggenstein, P. Ehrens, J. Eichholz, S. S. Eikenberry, R. A. Eisenstein, R. C. Essick, D. Estevez, Z. B. Etienne, T. Etzel, M. Evans, T. M. Evans, M. Factourovich, V. Fafone, H. Fair, S. Fairhurst, X. Fan, S. Farinon, B. Farr, W. M. Farr, E. J. Fauchon-Jones, M. Favata, M. Fays, C. Fee, H. Fehrmann, J. Feicht, M. M. Fejer, A. Fernandez-Galiana, I. Ferrante, E. C. Ferreira, F. Ferrini, F. Fidecaro, D. Finstad, I. Fiori, D. Fiorucci, M. Fishbach, R. P.

Fisher, M. Fitz-Axen, R. Flaminio, M. Fletcher, H. Fong, J. A. Font, P. W. F. Forsyth, S. S. Forsyth, J.-D. Fournier, S. Frasca, F. Frasconi, Z. Frei, A. Freise, R. Frey, V. Frey, E. M. Fries, P. Fritschel, V. V. Frolov, P. Fulda, M. Fyffe, H. Gabbard, B. U. Gadre, S. M. Gaebel, J. R. Gair, L. Gammaitoni, M. R. Ganija, S. G. Gaonkar, C. Garcia-Quiros, F. Garufi, B. Gateley, S. Gaudio, G. Gaur, V. Gayathri, N. Gehrels, G. Gemme, E. Genin, A. Gennai, D. George, J. George, L. Gergely, V. Germain, S. Ghonge, Abhirup Ghosh, Archisman Ghosh, S. Ghosh, J. A. Giaime, K. D. Giardina, A. Giazotto, K. Gill, L. Glover, E. Goe. GW170817: Observation of Gravitational Waves from a Binary Neutron Star Inspiral. *Phys. Rev. Lett.*, 119:161101, Oct. 2017.

[2] E. Pian, P. D'Avanzo, S. Benetti, M. Branchesi, E. Brocato, S. Campana, E. Cappellaro, S. Covino, V. D'Elia, J. P. U. Fynbo, F. Getman, G. Ghirlanda, G. Ghisellini, A. Grado, G. Greco, J. Hjorth, C. Kouveliotou, A. Levan, L. Limatola, D. Malesani, P. A. Mazzali, A. Melandri, P. Møller, L. Nicastro, E. Palazzi, S. Piranomonte, A. Rossi, O. S. Salafia, J. Selsing, G. Stratta, M. Tanaka, N. R. Tanvir, L. Tomasella, D. Watson, S. Yang, L. Amati, L. A. Antonelli, S. Ascenzi, M. G. Bernardini, M. Boër, F. Bufano, A. Bulgarelli, M. Capaccioli, P. Casella, A. J. Castro-Tirado, E. Chassande-Mottin, R. Ciolfi, C. M. Copperwheat, M. Dadina, G. De Cesare, A. Di Paola, Y. Z. Fan, B. Gendre, G. Giuffrida, A. Giunta, L. K. Hunt, G. L. Israel, Z.-P. Jin, M. M. Kasliwal, S. Klose, M. Lisi, F. Longo, E. Maiorano, M. Mapelli, N. Masetti, L. Nava, B. Patricelli, D. Perley, A. Pescalli, T. Piran, A. Possenti, L. Pulone, M. Razzano, R. Salvaterra, P. Schipani, M. Spera, A. Stamerra, L. Stella, G. Tagliaferri, V. Testa, E. Troja, M. Turatto, S. D. Vergani, and D. Vergani. Spectroscopic identification of r-process nucleosynthesis in a double neutron-star merger. *Nature*, 551:67 EP –, Oct. 2017.

[3] H.-S. Bosch, R. Brakel, T. Braeuer, V. Bykov, P. van Eeten, J.-H. Feist, F. Fllenbach, M. Gasparotto, H. Grote, T. Klinger, H. Laqua, M. Nagel, D. Naujoks, M. Otte, K. Risse, T. Rummel, J. Schacht, A. Spring, T. Sunn Pedersen, R. Vilbrandt, L. Wegener, A. Werner, R.C. Wolf, J. Baldzuhn, C. Biedermann, H. Braune, R. Burhenn, M. Hirsch, U. Hfel, J. Knauer, P. Kornejew, S. Marsen, T. Stange, and H. Trimino Mora and. Final

integration, commissioning and start of the wendelstein 7-x stellarator operation. *Nuclear Fusion*, 57(11):116015, Aug. 2017.

[4] T. Hirai, S. Panayotis, V. Barabash, C. Amzallag, F. Escourbiac, A. Durocher, M. Merola, J. Linke, Th. Loewenhoff, G. Pintsuk, M. Wirtz, and I. Uytdenhouwen. Use of tungsten material for the ITER divertor. *Nuclear Materials and Energy*, 9:616 – 622, 2016.

[5] M Mayer, V Philipps, P Wienhold, H.G Esser, J von Seggern, and M Rubel. Hydrogen inventories in nuclear fusion devices. *Journal of Nuclear Materials*, 290293:381 – 388, 2001. 14th Int. Conf. on Plasma-Surface Interactions in Controlled Fusion Devices.

[6] G Pintsuk. Tungsten as a plasma-facing material. *Comprehensive Nuclear Materials*, 4:551–581, 12 2012.

[7] S. Krat, Yu Gasparyan, A. Pisarev, I. Bykov, M. Mayer, G. de Saint Aubin, M. Balden, C.P. Lungu, and A. Widdowson. Erosion at the inner wall of {JET} during the discharge campaign 20112012 in comparison with previous campaigns. *Journal of Nuclear Materials*, 456:106 – 110, 2015.

[8] Tyler Abrams, Rui Ding, Houyang Y. Guo, Dan M. Thomas, Christopher P. Chrobak, Dmitry L. Rudakov, Adam G. McLean, Ezekial A. Unterberg, Alexis R. Briesemeister, Peter C. Stangeby, J. D. Elder, W. R. Wampler, and Jonathan G. Watkins. The inter-ELM tungsten erosion profile in DIII-D H-mode discharges and benchmarking with ERO+OEDGE modeling. *Nuclear Fusion*, 57(5), 4 2017.

[9] R.E. Nygren, D.L. Rudakov, C. Murphy, J.D. Watkins, E.A. Unterberg, J.L. Barton, and P.C. Stangeby. Thermal management of tungsten leading edges in DIII-D. *Fusion Engineering and Design*, 124:271 – 275, 2017. Proceedings of the 29th Symposium on Fusion Technology (SOFT-29) Prague, Czech Republic, September 5-9, 2016.

[10] Sebastijan Brezinsek, M Laengner, Jan Coenen, M G OMullane, Albrecht Pospieszczyk, Gennady Sergienko, and U Samm. Spectroscopic determination of inverse photon efficiencies of W atoms in the scrape-off layer of TEXTOR. T170:014052, 12 2017.

[11] I Beigman, A Pospieszczyk, G Sergienko, I Yu Tolstikhina, and L Vainshtein. Tungsten spectroscopy for the measurement of W-fluxes from plasma facing components. *Plasma Physics and Controlled Fusion*, 49(11):1833, 2007.

[12] S. Brezinsek. Plasma-surface interaction in the Be/W environment: Conclusions drawn from the JET-ILW for ITER. *Journal of Nuclear Materials*, 463:11 – 21, 2015. PLASMA-SURFACE INTERACTIONS 21.

[13] J.W. Coenen, K. Krieger, B. Lipschultz, R. Dux, A. Kallenbach, T. Lunt, H.W. Mueller, S. Potzel, R. Neu, and A. Terra. Evolution of surface melt damage, its influence on plasma performance and prospects of recovery. *Journal of Nuclear Materials*, 438:S27 – S33, 2013. Proceedings of the 20th International Conference on Plasma-Surface Interactions in Controlled Fusion Devices.

[14] B. Lipschultz, J.W. Coenen, H.S. Barnard, N.T. Howard, M.L. Reinke, D.G. Whyte, and G.M. Wright. Divertor tungsten tile melting and its effect on core plasma performance. *Nuclear Fusion*, 52(12):123002, 2012.

[15] R. Neu, A. Kallenbach, M. Balden, V. Bobkov, J.W. Coenen, R. Drube, R. Dux, H. Greuner, A. Herrmann, J. Hobirk, H. Hhnle, K. Krieger, M. Koan, P. Lang, T. Lunt, H. Maier, M. Mayer, H.W. Mller, S. Potzel, T. Ptterich, J. Rapp, V. Rohde, F. Ryter, P.A. Schneider, J. Schweinzer, M. Sertoli, J. Stober, W. Suttrop, K. Sugiyama, G. van Rooij, and M. Wischmeier. Overview on plasma operation with a full tungsten wall in ASDEX Upgrade. *Journal of Nuclear Materials*, 438:S34 – S41, 2013. Proceedings of the 20th International Conference on Plasma-Surface Interactions in Controlled Fusion Devices.

[16] R. Neu, R. Dux, A. Kallenbach, T. Ptterich, M. Balden, J.C. Fuchs, A. Herrmann, C.F. Maggi, M. O'Mullane, R. Pugno, I. Radivojevic, V. Rohde, A.C.C. Sips, W. Suttrop, A. Whiteford, and the ASDEX Upgrade team. Tungsten: an option for divertor and main chamber plasma facing components in future fusion devices. *Nuclear Fusion*, 45(3):209, 2005.

[17] G. J. Hartwell, S. F. Knowlton, J. D. Hanson, D. A. Ennis, and D. A. Maurer. Design, construction, and operation of the compact toroidal hybrid. *Fusion Science and Technology*, 72(1):76–90, 2017.

[18] J.W. Coenen, G. Arnoux, B. Bazylev, G.F. Matthews, A. Autricque, I. Balboa, M. Clever, R. Dejarnac, I. Coffey, Y. Corre, S. Devaux, L. Frassinetti, E. Gauthier, J. Horacek, S. Jachmich, M. Komm, M. Knaup, K. Krieger, S. Marsen, A. Meigs, Ph. Mertens, R.A. Pitts, T. Puetterich, M. Rack, M. Stamp, G. Sergienko, P. Tamain, V. Thompson, and JET-EFDA Contributors. ELM-induced transient tungsten melting in the JET divertor. *Nuclear Fusion*, 55(2):023010, 2015.

[19] T. Hirai, F. Escourbiac, V. Barabash, A. Durocher, A. Fedosov, L. Ferrand, T. Jokinen, V. Komarov, M. Merola, S. Carpentier-Chouchana, N. Arkhipov, V. Kuznetcov, A. Volodin, S. Suzuki, K. Ezato, Y. Seki, B. Riccardi, M. Bednarek, and P. Gavila. Status of technology R and D for the ITER tungsten divertor monoblock. *Journal of Nuclear Materials*, 463:1248 – 1251, 2015.

[20] T. Sugie, A. Costley, A. Malaquias, and C. Walker. Spectroscopic Diagnostics for ITER. *Journal of Plasma and Fusion Research*, 79(10):1051–1061, 2003.

[21] K Behringer, H P Summers, B Denne, M Forrest, and M Stamp. Spectroscopic determination of impurity influx from localized surfaces. *Plasma Physics and Controlled Fusion*, 31(14):2059, 1989.

[22] M. Laengner, S. Brezinsek, J.W. Coenen, A. Pospieszczyk, D. Kondratyev, D. Borodin, H. Stoschus, O. Schmitz, V. Philipps, and U. Samm. Penetration depths of injected/sputtered tungsten in the plasma edge layer of TEXTOR. *Journal of Nuclear Materials*, 438, Supplement:S865 – S870, 2013. Proceedings of the 20th International Conference on Plasma-Surface Interactions in Controlled Fusion Devices.

[23] S Brezinsek, D Borodin, J W Coenen, D Kondratjew, M Laengner, A Pospieszczyk, U Samm, and the TEXTOR team. Quantification of tungsten sputtering at W/C

twin limiters in TEXTOR with the aid of local WF 6 injection. *Physica Scripta*, 2011(T145):014016, 2011.

[24] D. Nishijima, R. P. Doerner, M. J. Baldwin, A. Pospieszczyk, and A. Kreter. Experimental determination of S/XB values of W I visible lines. *Physics of Plasmas*, 16(12):122503, 2009.

[25] D. Nishijima, R. P. Doerner, M. J. Baldwin, A. Pospieszczyk, and A. Kreter. Erratum: Experimental determination of S/XB values of WI visible lines [Phys. Plasmas 16, 122503 (2009)]. *Physics of Plasmas*, 18(1):019901, 2011.

[26] A. Geier, K. Asmussen, A. Bard, R. Neu, and K. Krieger. A sublimation probe for the injection of high-Z impurities into fusion devices. *Review of Scientific Instruments*, 70(1):63–67, 1999.

[27] A Geier, H Maier, R Neu, K Krieger, and the ASDEX Upgrade Team. Determination of the tungsten divertor retention at ASDEX Upgrade using a sublimation probe. *Plasma Physics and Controlled Fusion*, 44(10):2091, 2002.

[28] J Steinbrink and U Wenzel. Sputtered Tungsten Atoms Investigated in a Linear Plasma Generator. Europhysics Conf. Abstracts vol 21A, 1997.

[29] A. Kramida, Yu. Ralchenko, J. Reader, and and NIST ASD Team. NIST Atomic Spectra Database (ver. 5.3), [Online]. Available: `http://physics.nist.gov/asd` [2017, March 14]. National Institute of Standards and Technology, Gaithersburg, MD., 2015.

[30] H C Skinner. Applications of EBIT to magnetic fusion diagnostics. *Can. J. Phys.*, 86(1):285, 2008.

[31] ADAS: Atomic Data and Analysis Structure.

[32] Alan Burgess and Hugh P. Summers. The Recombination and Level Populations of Ions: I HYDROGEN AND HYDROGENIC IONS. *Monthly Notices of the Royal Astronomical Society*, 174(2):345–391, 1976.

[33] Shevelko V P and Vainshtein L A. *Atomic Physics for Hot Plasmas*. Institute of Physics Publishing, Bristol, 1993.

[34] H. van Regemorter. Rate of Collisional Excitation in Stellar Atmospheres. *The Astrophysical Journal*, 136:906, Nov. 1962.

[35] M. Laengner. PhD thesis, Forschungszentrum Jlich, 2017.

[36] The ADAS User Manual.

[37] S D Loch, C Ballance, M S Pindzola, and Daren Stotler. The role of excited state ionization data on H and He generalized collisionalradiative coefficients. *Plasma Physics and Controlled Fusion*, 51:105006, 09 2009.

[38] S. D. Loch, J. Colgan, M. C. Witthoeft, M. S. Pindzola, C. P. Ballance, D. M. Mitnik, D. C. Griffin, M. G. O'Mullane, N. R. Badnell, and H. P. Summers. Generalised collisional-radiative model for light elements. A: Data for the Li isonuclear sequence. *Atomic Data and Nuclear Data Tables*, 92:813–851, Nov. 2006.

[39] Bastiaan J Braams and Hyun-Kung Chung. Light element atom, molecule and radical behaviour in the divertor and edge plasma regions. *Journal of Physics: Conference Series*, 576(1):011001, 2015.

[40] J. P. Allain, D. G. Whyte, and J. N. Brooks. Lithium erosion experiments and modelling under quiescent plasma conditions in DIII-D. *Nuclear Fusion*, 44(5):655–664, 5 2004.

[41] R. T. Smyth, C. P. Ballance, C. A. Ramsbottom, C. A. Johnson, D. A. Ennis, and S. D. Loch. Dirac R-matrix calculations for the electron-impact excitation of neutral tungsten providing noninvasive diagnostics for magnetic confinement fusion. *Phys. Rev. A*, 97:052705, May 2018.

[42] A.E. Kramida and T. Shirai. Compilation of Wavelengths, Energy Levels, and Transition Probabilities for W I and W II. *Journal of Physical and Chemical Reference Data*, 8:423–683, 2006.

[43] T Morel and K Butler. The neon content of nearby B-type stars and its implications for the solar model problem. *Astronomy and Astrophysics*, 487, June 2008.

[44] Enrique Prez-Montero, Guillermo Hagele, T Contini, and ngeles Daz. Neon and Argon optical emission lines in ionized gaseous nebulae: Implications and applications. *Monthly Notices of the Royal Astronomical Society*, 381:125 – 135, 10 2007.

[45] M. Meléndez, T. M. Heckman, M. Martínez-Paredes, S. B. Kraemer, and C. Mendoza. Theoretical modelling of emission-line galaxies: new classification parameters for mid-infrared and optical spectroscopy. *Monthly Notices of the Royal Astronomical Society*, 443:1358–1369, September 2014.

[46] L. L. Alves, K. Bartschat, S. F. Biagi, M. C. Bordage, L. C. Pitchford, C. M. Ferreira, G. J. M. Hagelaar, W. L. Morgan, S. Pancheshnyi, A. V. Phelps, V. Puech, and O. Zatsarinny. Comparisons of sets of electron-neutral scattering cross sections and swarm parameters in noble gases: II. Helium and neon. *Journal of Physics D Applied Physics*, 46:334002, August 2013.

[47] T. Barbui, M. Krychowiak, R. König, O. Schmitz, J. M. Muñoz Burgos, B. Schweer, and A. Terra. Feasibility of line-ratio spectroscopy on helium and neon as edge diagnostic tool for Wendelstein 7-X. *Review of Scientific Instruments*, 87(11):11E554, Nov. 2016.

[48] D. G. Whyte, T. C. Jernigan, D. A. Humphreys, A. W. Hyatt, C. J. Lasnier, P. B. Parks, T. E. Evans, M. N. Rosenbluth, P. L. Taylor, A. G. Kellman, D. S. Gray, E. M. Hollmann, and S. K. Combs. Mitigation of tokamak disruptions using high-pressure gas injection. *Physical Review Letters*, 89(5):055001, July 2002.

[49] J. R. Martín-Solís, A. Loarte, and M. Lehnen. Formation and termination of runaway beams in ITER disruptions. *Nuclear Fusion*, 57(6):066025, June 2017.

[50] X. Bonnin, R.A. Pitts, V. Komarov, F. Escourbiac, M. Merola, L. Bo, L. Wei, L. Pan, and A.S. Kukushkin. ITER divertor plasma response to time-dependent impurity injection. *Nuclear Materials and Energy*, 12:1100 – 1105, 2017. Proceedings of the 22nd International Conference on Plasma Surface Interactions 2016, 22nd PSI.

[51] Daoyuan Liu, Chaofeng Sang, Liang Wang, and Dezhen Wang. The impact of neon-seeding location on the divertor plasma in EAST. *Fusion Engineering and Design*, 136:324 – 329, 2018. Special Issue: Proceedings of the 13th International Symposium on Fusion Nuclear Technology (ISFNT-13).

[52] Oleg Zatsarinny and Klaus Bartschat. Electron-impact excitation of neon at intermediate energies. *Phys. Rev. A*, 86:022717, Aug. 2012.

[53] M. S. Pindzola, J. Colgan, F. Robicheaux, and D. C. Griffin. Time-dependent close-coupling calculations for the electron-impact ionization of carbon and neon. *Phys. Rev. A*, 62:042705, Sep. 2000.

[54] Philip L. Bartlett and Andris T. Stelbovics. Calculation of electron-impact total-ionization cross sections. *Phys. Rev. A*, 66:012707, Jul. 2002.

[55] C P Ballance, J A Ludlow, M S Pindzola, and S D Loch. Electron-impact ionization of ground and metastable neon. *Journal of Physics B: Atomic, Molecular and Optical Physics*, 42(17):175202, 2009.

[56] Oleg Zatsarinny and Klaus Bartschat. Large-scale pseudostate calculations for electron scattering from neon atoms. *Phys. Rev. A*, 85:062710, Jun. 2012.

[57] C P Ballance, D C Griffin, J A Ludlow, and M S Pindzola. Electron-impact ionization of metastable neon. *Journal of Physics B: Atomic, Molecular and Optical Physics*, 37(24):4779, 2004.

[58] C P Ballance and D C Griffin. Electron-impact excitation of neon: a pseudo-state convergence study. *Journal of Physics B: Atomic, Molecular and Optical Physics*, 37(14):2943, 2004.

[59] Jean-Franois Wyart. Interpretation of the odd parity energy levels in the spectrum of neutral tungsten. *Journal of Physics B: Atomic, Molecular and Optical Physics*, 43(7):074018, 2010.

[60] N S Scott and P G Burke. Electron scattering by atoms and ions using the Breit-Pauli Hamiltonian: an R-matrix approach. *Journal of Physics B: Atomic and Molecular Physics*, 13(21):4299, 1980.

[61] R. D. Cowan. *The Theory of Atomic Structure and Spectra*. University of California, Berkeley, 1981.

[62] C. Fischer, Brage T., and Jonsson P. *Computational Atomic Structure: An MCHF Approach*. Institute of Physics Publishing, 2000.

[63] Klaus Bartschat and Igor Bray. Electron-impact ionization of atomic hydrogen from the 1S and 2S states. *Journal of Physics B: Atomic, Molecular and Optical Physics*, 29(15):L577–L583, Aug. 1996.

[64] Philip G. Burke. *R-Matrix Theory of Atomic Collisions: Applications to Atomic, Molecular, and Optical Processes*. Springer, 2011.

[65] Anthony Chak Tong Chan. Distorted Wave Born Approximation For Inelastic Atomic Collision. Master's thesis, University of Waterloo, 2007.

[66] A. Burgess, D. G. Hummer, and J. A. Tully. Electron impact excitation of positive ions. *Philosophical Transactions of the Royal Society of London Series A*, 266:225–279, April 1970.

[67] C Ballance, S D Loch, M S Pindzola, and D C Griffin. Electron-impact excitation and ionization of W^{3+} for the determination of tungsten influx in a fusion plasma. *Journal of Physics B: Atomic, Molecular and Optical Physics*, 46:055202, 2 2013.

[68] J. Colgan and M. S. Pindzola. Application of the time-dependent close-coupling approach to few-body atomic and molecular ionizing collisions. *The European Physical Journal D*, 66(11):284, Nov. 2012.

[69] Cleanthes A. Nicolaides and Donald R. Beck. The variational calculation of energies and widths of resonances. *Physics Letters A*, 65(1):11 – 12, 1978.

[70] Magnus Rittby, Nils Elander, and Erkki Brndas. Exterior complex scaling - a calculation of shape resonances in the A1 state of CH+ using a realistic numeric potential. *Chemical Physics*, 87(1):55 – 62, 1984.

[71] M S Pindzola, S D Loch, and A R Foster. Electron-impact single and double ionization of W. *Journal of Physics B: Atomic, Molecular and Optical Physics*, 50(9):095201, 2017.

[72] Patrick H. Norrington Keith A. Berrington, Werner B. Eissner. RMATRX1: Belfast atomic R-matrix codes. *Computer Physics Communications*, 92(2-3):290–420, 1995.

[73] P. J. A. Buttle. Solution of Coupled Equations by R-Matrix Techniques. *Phys. Rev.*, 160:719–729, Aug. 1967.

[74] Oleg Zatsarinny. BSR: B-spline atomic R-matrix codes. *Computer Physics Communications*, 174(4):273 – 356, 2006.

[75] O Zatsarinny and K Bartschat. B-spline BreitPauli R-matrix calculations for electron collisions with neon atoms. *Journal of Physics B: Atomic, Molecular and Optical Physics*, 37(10):2173, 2004.

[76] L.S. Blackford, Jinhee Choi, A. Cleary, Ed DAzevedo, J. Demmel, I. Dhillon, Jack Dongarra, S. Hammarling, Gwendolyn Henry, Antoine Petitet, Kathryn Stanley, David Walker, and R.C. Whaley. Scalapack users guide. incl. 1 cd-rom. 01 1997.

[77] Douglas H. Sampson. Branching ratios for excitation to highly excited levels or ionization of complex ions. *Phys. Rev. A*, 34:986–1006, Aug. 1986.

[78] A. Burgess and J. A. Tully. On the analysis of collision strengths and rate coefficients. *Astronomy and Astrophysics*, 254:436, Feb. 1992.

[79] H P Summers, W J Dickson, M G O'Mullane, N R Badnell, A D Whiteford, D H Brooks, J Lang, S D Loch, and D C Griffin. Ionization state, excited populations and emission of impurities in dynamic finite density plasmas: I. The generalized collisionalradiative model for light elements. *Plasma Physics and Controlled Fusion*, 48(2):263, 2006.

[80] Paul Bryans. *On the Spectral Emission of Non-Maxwellian Plasmas*. PhD thesis, University of Strathclyde, 2005.

[81] D.R. Bates, A.E. Kingston, and McWhirter R.W.P. Recombination between electrons and atomic ions, I. Optically thin plasmas. *Proceedings of the Royal Society of London A: Mathematical, Physical and Engineering Sciences*, 267(1330):297–312, 1962.

[82] HP Summers and MB Hooper. On radiative power from impurities in plasmas. *Plasma Physics*, 25(12):1311, 1983.

[83] N R Badnell. On the effects of the two-body non-fine-structure operators of the Breit - Pauli Hamiltonian. *Journal of Physics B: Atomic, Molecular and Optical Physics*, 30(1):1, 1997.

[84] C.A. Johnson, S.D. Loch, and D.A. Ennis. ColRadPy: A Python collisional radiative solver. *Nuclear Materials and Energy*, page 100579, 2019.

[85] T. Topçu, M. S. Pindzola, C. P. Ballance, D. C. Griffin, and F. Robicheaux. Electron-impact ionization of highly excited hydrogenlike ions in a collinear s-wave model. *Phys. Rev. A*, 74:062708, Dec. 2006.

[86] A. Kramida, Yu. Ralchenko, J. Reader, and and NIST ASD Team. NIST Atomic Spectra Database (ver. 5.3), [Online]. Available: `http://physics.nist.gov/asd` [2017, April 16]. National Institute of Standards and Technology, Gaithersburg, MD., 2015.

[87] V Zeman and K Bartschat. Electron-impact excitation of the $2p^5 3s$ and $2p^5 3p$ states of neon. *Journal of Physics B: Atomic, Molecular and Optical Physics*, 30(20):4609, 1997.

[88] M. A. Khakoo, J. Wrkich, M. Larsen, G. Kleiban, I. Kanik, S. Trajmar, M. J. Brunger, P. J. O. Teubner, A. Crowe, C. J. Fontes, R. E. H. Clark, V. Zeman, K. Bartschat, D. H.

Madison, R. Srivastava, and A. D. Stauffer. Differential cross sections and cross-section ratios for the electron-impact excitation of the neon $2p^5 3s$ configuration. *Phys. Rev. A*, 65:062711, Jun. 2002.

[89] J. Ethan Chilton, M. D. Stewart, and Chun C. Lin. Electron-impact excitation cross sections of neon. *Phys. Rev. A*, 61:052708, Apr. 2000.

[90] M. Hoshino, H. Murai, H. Kata, Y. Itikawa, M. J. Brunger, and H. Tanaka. Resolution of oa significant discrepancy in the electron impact excitation of the 3s[3/2] and 3s'[1/2], low-lying electronic states in neon. *Chemical Physics Letters*, 585:33–36, 2013.

[91] I Kanik, J M Ajello, and G K James. Electron-impact-induced emission cross sections of neon in the extreme ultraviolet. *Journal of Physics B: Atomic, Molecular and Optical Physics*, 29(11):2355, 1996.

[92] Mark H. Phillips, L. W. Anderson, and Chun C. Lin. Electron excitation cross sections for the metastable and resonant levels of Ne($2p^5$3s). *Phys. Rev. A*, 32:2117–2127, Oct. 1985.

[93] D. F. Register, S. Trajmar, G. Steffensen, and David C. Cartwright. Electron-impact-excitation cross sections for electronic levels in neon for incident energies between 25 and 100 ev. *Phys. Rev. A*, 29:1793–1810, Apr. 1984.

[94] T. Y. Suzuki, H. Suzuki, S. Ohtani, B. S. Min, T. Takayanagi, and K. Wakiya. Measurements of cross sections and oscillator strengths for Ne by electron-energy-loss spectroscopy. *Phys. Rev. A*, 49:4578–4584, Jun. 1994.

[95] M Allan, K Franz, H Hotop, O Zatsarinny, and K Bartschat. Absolute angle-differential cross sections for electron-impact excitation of neon within the first 3.5 ev above threshold. *Journal of Physics B: Atomic, Molecular and Optical Physics*, 42(4):044009, 2009.

[96] John B. Boffard, M. L. Keeler, Garrett A. Piech, L. W. Anderson, and Chun C. Lin. Measurement of electron-impact excitation cross sections out of the neon $^3P_2$ metastable level. *Phys. Rev. A*, 64:032708, Aug. 2001.

[97] R. Rejoub, B. G. Lindsay, and R. F. Stebbings. Determination of the absolute partial and total cross sections for electron-impact ionization of the rare gases. *Phys. Rev. A*, 65:042713, Apr. 2002.

[98] E Krishnakumar and S K Srivastava. Ionisation cross sections of rare-gas atoms by electron impact. *Journal of Physics B: Atomic, Molecular and Optical Physics*, 21(6):1055, 1988.

[99] M Johnston, K Fujii, J Nickel, and S Trajmar. Ionization of metastable neon by electron impact. *Journal of Physics B: Atomic, Molecular and Optical Physics*, 29(3):531, 1996.

[100] Oleg Zatsarinny and Klaus Bartschat. B-spline calculations of oscillator strengths in noble gases. *Physica Scripta*, 2009(T134):014020, 2009.

[101] Jan M. Rost and Thomas Pattard. Analytical parametrization for the shape of atomic ionization cross sections. *Phys. Rev. A*, 55:R5–R7, Jan. 1997.

[102] S.M. Younger. Electron impact ionization cross sections and rates for highly ionized atoms. *Journal of Quantitative Spectroscopy and Radiative Transfer*, 26(4):329 – 337, 1981.

[103] Teck-Ghee Lee, S. D. Loch, C. P. Ballance, J. A. Ludlow, and M. S. Pindzola. Electron-impact-ionization cross sections for excited states of B^{q+} ($q = 0-2$) and an investigation into n scaling of ionization cross sections. *Phys. Rev. A*, 82:042721, Oct. 2010.

[104] Oleg Zatsarinny, T W. Gorczyca, J Fu, K T. Korista, N R. Badnell, and D W. Savin. Dielectronic recombination data for dynamic finite-density plasmas. IX. The fluorine isoelectronic sequence. *Astronomy & Astrophysics - ASTRON ASTROPHYS*, 447:379–387, 02 2006.

[105] N. R. Badnell. Radiative recombination data for modeling dynamic finite-density plasmas. *Astrophysical Journal Shortcut Series*, 167:334–342, Dec. 2006.

[106] A. Burgess and J. A. Tully. *Journal of Physics B: Atomic and Molecular Physics*, 11:4271, 1978.

[107] N.R. Badnell. A BreitPauli distorted wave implementation for autostructure. *Computer Physics Communications*, 182(7):1528 – 1535, 2011.

[108] R. T. Smyth, C. A. Johnson, D. A. Ennis, S. D. Loch, C. A. Ramsbottom, and C. P. Ballance. Relativistic R-matrix calculations for the electron-impact excitation of neutral molybdenum. *Phys. Rev. A*, 96:042713, Oct. 2017.

[109] J. A. Ludlow, S. D. Loch, and M. S. Pindzola. Electron-impact ionization of mo^{+}. *Phys. Rev. A*, 72:032729, Sep. 2005.

[110] Duck-Hee Kwon, Yong-Joo Rhee, and Yong-Ki Kim. Ionization of W and W^{+} by electron impact. *International Journal of Mass Spectrometry*, 252(3):213 – 221, 2006.

[111] I.P. Grant. Relativistic calculation of atomic structures. *Advances in Physics*, 19(82):747–811, 1970.

[112] Ghanshyam Purohit, Daiji Kato, and Izumi Murakami. Electron impact ionization cross sections of tungsten atoms and tungsten ions. *Plasma and Fusion Research*, 13:3401026–3401026, 2018.

[113] P Quinet, P Palmeri, and Bimont. Spectroscopic data for atomic tungsten transitions of interest in fusion plasma research. *Journal of Physics B: Atomic, Molecular and Optical Physics*, 44(14):145005, 2011.

[114] P Quinet, V Vinogradoff, P Palmeri, and Bimont. Radiative decay rates for W I, W II and W III allowed and forbidden transitions of interest for spectroscopic diagnostics in fusion plasmas. *Journal of Physics B: Atomic, Molecular and Optical Physics*, 43(14):144003, 2010.

[115] C J Favreau, C A Johnson, D A Ennis, and S D Loch. The role of excited-state ionization on the effective ionization of neutral neon using non-perturbative atomic data. *Journal of Physics B: Atomic, Molecular and Optical Physics*, 52(9):095203, Apr. 2019.

[116] Jonathan Pearce. *The role of atomic excited states in laboratory plasmas and a study in finestructure diagnostics for far infra-red astrophysical observations*. PhD thesis, Auburn University, 2016.

[117] U. Fano. Interaction between Configurations with Several Open Shells. *Physical Review*, 140:67–75, Oct. 1965.

[118] Brian Caulfield. What's the Difference Between a GPU and a CPU?, 2009.

[119] Jack Dongarra, Mark Gates, Azzam Haidar, Jakub Kurzak, Piotr Luszczek, Stanimire Tomov, and Ichitaro Yamazaki. Accelerating Numerical Dense Linear Algebra Calculations with GPUs. *Numerical Computations with GPUs*, pages 1–26, 2014.

[120] Tingxing Dong, Azzam Haidar, Piotr Luszczek, Stanimire Tomov, Ahmad Abdelfattah, and Jack Dongarra. MAGMA Batched: A Batched BLAS Approach for Small Matrix Factorizations and Applications on GPUs. Technical report, August 2016.

[121] Stanimire Tomov, Jack Dongarra, Azzam Haidar, Ichitaro Yamazaki, Tingxing Dong, Thomas Schulthess, and Raffaele Solcà. MAGMA: A Breakthrough in Solvers for Eigenvalue Problems. 2012-05 2012.

[122] Connor Ballance, 2019. private communication.

[123] Keith A Berrington and Connor P Ballance. Partitioned R-matrix theory. *Journal of Physics B: Atomic, Molecular and Optical Physics*, 35(10):2275–2282, May 2002.

[124] Thomas Auckenthaler, V. Blum, Hans-Joachim Bungartz, Thomas Huckle, R. Johanni, Lukas Krmer, Bruno Lang, Hermann Lederer, and P.R. Willems. Parallel solution of partial symmetric eigenvalue problems from electronic structure calculations. *Parallel Computing*, 37:783–794, 12 2011.

[125] A. V. Demura, M. B. Kadomtsev, V. S. Lisitsa, and V. A. Shurygin. Electron impact ionization of tungsten ions in a statistical model. *JETP Letters*, 101(2):85–88, Jan. 2015.

[126] S. D. Loch, J. A. Ludlow, M. S. Pindzola, A. D. Whiteford, and D. C. Griffin. Electron-impact ionization of atomic ions in the W isonuclear sequence. *Phys. Rev. A*, 72:052716, Nov 2005.

[127] M Stenke, K Aichele, D Harthiramani, G Hofmann, M Steidl, R Volpel, and E Salzborn. Electron-impact single-ionization of singly and multiply charged tungsten ions. *Journal of Physics B: Atomic, Molecular and Optical Physics*, 28(13):2711–2721, July 1995.

[128] D. Schury, Jr. A. Borovik, B. Ebinger, F. Jin, K. Spruck, A. Mller, and S. Schippers. Electron-impact single ionisation of W^{q+} ions: Experiment and theory for $\mathbf{11 \leq q \leq 18}$, 2019.

[129] Deng-Hong Zhang and Duck-Hee Kwon. Theoretical electron-impact ionization of W^{17+} forming W^{18+}. *Journal of Physics B Atomic Molecular Physics*, 47(7):075202, Apr. 2014.

[130] Alexander Borovik Jr, Daniel Schury, Barbara Ebinger, K Spruck, A Becker, Mohammad Gharaibeh, J Rausch, S Schippers, and Alfred Mller. Electron-impact ionization of tungsten ions. *Journal of Physics: Conference Series*, 635:052040, 09 2015.

[131] Valdas Jonauskas, A. Kyniene, and arnas Masys. Electron-impact ionization of W^{26+} ion. volume 635, page 052058, 9 2015.

[132] X. Ding, I. Murakami, D. Kato, H. A. Sakaue, F. Koike, and C. Dong. Collisional-radiative modeling of W^{27+}. *Plasma and Fusion Research*, 7:2403128–2403128, 2012.

[133] A.A.A. Hussein, Abdel-Haleem Abdel-Aty, Udai Al-Juboori, and El Sayed Yousef. Cross sections by electron impact excitation and ionization of tungsten ions, W^{39+}. *Journal of Electron Spectroscopy and Related Phenomena*, 234:86 – 90, 2019.

[134] C P Ballance and D C Griffin. Electron-impact excitation of W^{44+} and W^{45+}. *Journal of Physics B: Atomic, Molecular and Optical Physics*, 40(2):247–258, Jan. 2007.

[135] M M Bluteau, M G O'Mullane, and N R Badnell. Dirac R-matrix and Breit-Pauli distorted wave calculations of the electron-impact excitation of W^{44+}. *Journal of Physics B: Atomic, Molecular and Optical Physics*, 48(19):195701, Aug. 2015.

[136] A.A. El-Maaref, M.M. Abou halaka, Mahmoud Tammam, E.R. Shaaban, and El Sayed Yousef. Electron impact excitation and ionization cross section of tungsten ions, W^{44+}. *Journal of Quantitative Spectroscopy and Radiative Transfer*, 224:147 – 153, 2019.

[137] Duck-Hee Kwon and Wonwook Lee. Dielectronic recombination of Ni-, Cu-, and +Zn-like tungsten ions. *Journal of Quantitative Spectroscopy and Radiative Transfer*, 179:98 – 104, 2016.

[138] Duck-Hee Kwon and Wonwook Lee. Dielectronic recombination of Cu-like W^{45+}. *Journal of Quantitative Spectroscopy and Radiative Transfer*, 170:182 – 188, 2016.

Appendix A

Complete list of neutral tungsten structure term energies

Configuration	Term	J Value	Energy (Ryd)	NIST	Percent Difference
$5d^4 6s^2$	^5D	0	0.0000	0.0000	0.00
$5d^4 6s^2$	^5D	1	0.0146	0.0153	3.87
$5d^4 6s^2$	^5D	2	0.0305	0.0304	0.51
$5d^4 6s^2$	^5D	3	0.0455	0.0441	3.39
$5d^4 6s^2$	^5D	4	0.0597	0.0567	5.39
$5d^5(6S)6s$	^7S	3	0.0269	0.0269	0.06
$5d^4 6s^2$	$^3P2$	0	0.1059	0.0869	21.97
$5d^4 6s^2$	$^3P2$	1	0.1459	0.1213	20.29
$5d^4 6s^2$	$^3P2$	2	0.1692	0.1755	3.56
$5d^4 6s^2$	^3H	4	0.1361	0.1109	22.79
$5d^4 6s^2$	^3H	5	0.1649	0.1374	20.09
$5d^4 6s^2$	^3H	6	0.1835	0.1550	18.39
$5d^4 6s^2$	^3G	3	0.1505	0.1217	23.69
$5d^4 6s^2$	^3G	4	0.1864	0.1498	24.49
$5d^4 6s^2$	^3G	5	0.2117	0.1807	17.19
$5d^4 6s^2$	$^3F2$	2	0.1559	0.1256	24.20
$5d^4 6s^2$	$^3F2$	4	0.1800	0.1559	15.46
$5d^4 6s^2$	$^3F2$	3	0.1931	0.1614	19.73
$5d^4 6s^2$	^3D	2	0.2139	0.1365	56.75

Configuration	Term	J Value	Energy (Ryd)	NIST	Percent Difference
$5d^4 6s^2$	^3D	3	0.1804	0.1409	28.02
$5d^4 6s^2$	^3D	1	0.2031	0.1648	23.24
$5d^5(^4G)6s$	^5G	2	0.2069	0.1651	25.34
$5d^5(^4G)6s$	^5G	3	0.2146	0.1730	24.12
$5d^5(^4G)6s$	^5G	4	0.2175	0.1755	23.95
$5d^5(^4G)6s$	^5G	5	0.2211	0.1781	24.18
$5d^5(^4G)6s$	^5G	6	0.2203	0.1791	23.05
$5d^5(6S)6s$	^5S	2	0.2024	0.1666	21.51
$5d^4 6s(^6D)6p$	^7F	0	0.1859	0.1767	5.23
$5d^4 6s(^6D)6p$	^7F	1	0.1939	0.1829	6.02
$5d^4 6s(^6D)6p$	^7F	2	0.2074	0.1955	6.14
$5d^4 6s(^6D)6p$	^7F	3	0.2253	0.2101	7.27
$5d^4 6s(^6D)6p$	^7F	4	0.2474	0.2257	9.63
$5d^4 6s(^6D)6p$	^7F	5	0.2770	0.2431	13.95
$5d^4 6s(^6D)6p$	^7F	6	0.3656	0.2702	35.33
$5d^5(^4P)6s$	^5P	3	0.2293	0.1807	26.92
$5d^5(^4P)6s$	^5P	1	0.2386	0.1862	28.20
$5d^5(^4P)6s$	^5P	2	0.2354	0.1913	23.11
$5d^4 6s^2$	$^1S2$	0	0.2259	0.1839	22.87
$5d^4 6s(^6D)6p$	^7D	1	0.3421	0.1956	74.98
$5d^4 6s(^6D)6p$	^7D	2	0.2474	0.2184	13.27
$5d^4 6s(^6D)6p$	^7D	3	0.3510	0.2387	47.07
$5d^4 6s(^6D)6p$	^7D	4	0.3683	0.2714	35.76
$5d^5(^4D)6s$	^5D	4	0.2562	0.2049	25.10
$5d^5(^4D)6s$	^5D	0	0.2597	0.2076	25.13
$5d^5(^4D)6s$	^5D	1	0.2689	0.2138	25.79
$5d^5(^4D)6s$	^5D	3	0.2736	0.2181	25.47

Configuration	Term	J Value	Energy (Ryd)	NIST	Percent Difference
$5d^5(^4D)6s$	^5D	2	0.2760	0.2186	26.27
$5d^46s^2$	$^1G2$	4	0.2497	0.2083	19.89
$5d^46s^2$	^1I	6	0.2533	0.2141	18.35
$5d^46s^2$	^1F	3	0.2781	0.2243	24.02
$5d^46s^2$	$^1D2$	2	0.2741	0.2259	21.32
$5d^46s(^6D)6p$	^5F	1	0.3171	0.2368	33.94
$5d^46s(^6D)6p$	^5F	2	0.3222	0.2521	27.81
$5d^46s(^6D)6p$	^5F	3	0.3708	0.2656	39.65
$5d^5(^6S)6p$	^7P	2	0.3452	0.2391	44.44
$5d^5(^6S)6p$	^7P	3	0.2715	0.2505	8.39
$5d^5(^6S)6p$	^7P	4	0.2892	0.2542	13.79
$5d^46s(^6D)6p$	^5D	0	0.2978	0.2427	22.74
$5d^46s(^6D)6p$	^5D	1	0.3229	0.2532	27.57
$5d^46s(^6D)6p$	^5D	2	0.3377	0.2661	26.92
$5d^46s(^6D)6p$	^5D	4	0.3897	0.2992	30.26
$5d^5(^2F1)6s$	^3F	2	0.3060	0.2448	25.00
$5d^5(^2F1)6s$	^3F	4	0.3134	0.2480	26.39
$5d^5(^4F)6s$	^5F	2	0.3887	0.2571	51.23
$5d^5(^4F)6s$	^5F	5	0.3229	0.2573	25.49
$5d^5(^4F)6s$	^5F	3	0.3241	0.2584	25.47
$5d^5(^4F)6s$	^5F	4	0.3275	0.2721	20.38
$5d^5(^2I)6s$	^3I	5	0.3136	0.2538	23.55
$5d^5(^2I)6s$	^3I	6	0.3186	0.2588	23.13
$5d^5(^2I)6s$	^3I	7	0.3276	0.2685	22.04
$5d^46s(^6D)6p$	^5P	1	0.2211	0.2570	13.97
$5d^46s(^6D)6p$	^5P	3	0.3909	0.2788	40.23
$5d^46s^2$	$^3P1$	2	0.3203	0.2634	21.63

Configuration	Term	J Value	Energy (Ryd)	NIST	Percent Difference
$5d^5(^4G)6s$	^3G	5	0.3485	0.2861	21.85
$5d^5(^4G)6s$	^3G	4	0.3378	0.2929	15.36
$5d^5(^2D3)6s$	^3D	1	0.3700	0.2951	25.40
$5d^5(^2G2)6s$	^3G	5	0.3763	0.3026	24.37
$5d^5(^2G2)6s$	^3G	4	0.3793	0.3126	21.36
$5d^5(^2I)6s$	^1I	6	0.3724	0.3034	22.74
$5d^5(^4D)6s$	^3D	3	0.3652	0.3095	18.04
$5d^46s(^4H)6p$	^5H	7	0.4220	0.3619	16.63
$5d^46s(^6D)7s$	^7D	1	0.4260	0.3960	7.57
$5d^46s(^6D)7s$	^7D	2	0.6104	0.4094	49.13
$5d^46s(^6D)7s$	^7D	5	0.3813	0.4498	15.22
$5d^46s(^6D)7s$	^5D	0	0.4646	0.4122	12.74
$5d^46s(^6D)7s$	^5D	1	0.4764	0.4234	12.54
$5d^46s(^6D)7s$	^5D	2	0.4906	0.4382	11.97
$5d^46s(^6D)7s$	^5D	3	0.5050	0.4525	11.61
$5d^46s(^6D)7s$	^5D	4	0.5193	0.4659	11.46
				Average:	31.23

Appendix B

R-Matrix Stage 2 variable definitions and selected code segment

Definitions of select Stage 2 variables:

1. **MZMEG:** Variable governing the max memory for storing N+1 Hamiltonian elements. Memory is in general stored per bra target symmetry. If the memory cap set by MZMEG is exceeded, then Hamiltonian elements will be written to scratch space, and read back out in chunks (TAKES MUCH LONGER).
2. **L2P:** The angular momentum l of a channel incident electron.
3. **NCONAT:** The number of channels for a given target term.
4. **LRGL, NSPN, NPTY:** The N + 1 total L, S, and Parity respectively
5. **NCHAN:** The number of channels of a partial-wave.
6. **NCFG:** The number of N + 1 bound states of a partial-wave.
7. **ENAT:** Target state energies.
8. **NTYP:** A unique number per term per configuration.
9. **HNPS:** Where Hamiltonian elements are stored if RAM is exceeded.
10. **ARRAY:** Where Hamiltonian elements are stored during their calculation.
11. **HNP1:** Where Hamiltonian elements are stored to be written out to file (STG2###.DAT).
12. **ITSYM:** Total number of target symmetries.
13. **ISYM:** Array returning the number of configurations per target symmetry.
14. **LENGTH:** Number of matrix blocks stored in memory.

Appendix C

Python OMEGA cross section extractor and other utility codes

The following is a list of atomic utility codes available at https://github.com/cjf0019/Physics/tree/master/AtomicPhysics:

1. **pystgsig.py**: Extract cross sections from an OMEGA file, given initial and final transition numbers. Can optionally return cross sections as collision strengths.
2. **pydstgsig.py**: Same as 'pystgsig.py' but takes a dstgsig file (same format as original stgsig code) and can be used to extract specific transitions through a list of 0's and 1's after the namelist: one value on each succeeding line, with 0 and 1 designating not to include and to include respectively. Can use "generatestgsiglist.py" to generate this list.
3. **omegautility.py**: Includes OMEGA and XSEC classes, the former a wrapper for OMEGA files, storing their basic information, and the latter for cross sections. The OMEGA class can be used to extract cross sections (see pystgsig.py and pydstgsig.py). Rost-Pattard and Younger fits as well as both fit and raw plots can be performed using the XSEC class (see ionsnfitandplot.py for such usage). Cross sections reflecting an n$\hat{4}$ scaling (for ionization of high n states) can also be generated.
4. **fitecip_winfile.py**: Generate scaled ECIP fits to raw cross sections from a file 'scale_ecip_input' that includes sets of configuration, term, or level-specific ionization potentials, the occupation number of the ionized shell, the cross section file name, and the output file names for the fit, graph, and raw ECIP cross section.
5. **fitecip.py**: the base code for generating scaled ECIP fits to raw cross sections. A least squares fit is applied to a raw cross section to determine a multiplying constant, 'a' for 'a unscaled_ecip.'

6. **ionsnfitandplot.py**: Generate Rost-Pattard and Younger fits to raw cross sections in lower and higher incident energies respectively.
7. **generatestgsiglist.py**: See the "pydstgsig.py" description. Reads in a TERMS file from AUTOSTRUCTURE.
8. **xsec.py**: Contains the base class XSEC for reading, writing and fitting cross sections.
9. **adf04utility.py**: Contains various functions related to processing adf04 files (which store the rate coefficients of various atomic processes like electron-impact and recombination.)
10. **gettransnums.py**: Get the transition numbers for OMEGA extraction of ionization cross sections. NOTE: Assumes elastic collisions are not included. Needs modification if they are present (one extra transition per level).
11. **convertatomicunits.py**: Contains a list of functions for converting between atomic units (eV, Ryd, cm-1).